THÈSE

Pour obtenir le grade de

**DOCTEUR DE L'UNIVERSITÉ GRENOBLE ALPES**

École doctorale : ISCE - Ingénierie pour la Santé la Cognition et l'Environnement
Spécialité : MBS - Modèles, méthodes et algorithmes en biologie, santé et environnement
Unité de recherche : Translational Innovation in Medicine and Complexity

# Approche expérimentale et numérique pour la modélisation biomécanique des tissus mous du sacrum dans un contexte de prévention des escarres

# Experimental and numerical approach for the biomechanical modeling of the sacral soft tissues in the context of pressure ulcer prevention


Présentée par :

**Ekaterina MUKHINA**


Direction de thèse :

| | |
|---|---|
| **Yohan PAYAN**<br>Université Grenoble Alpes | Directeur de thèse |
| **Pierre-Yves ROHAN**<br>ENSAM | Co-encadrant de thèse |
| **Nathanaël CONNESSON**<br>UGA | Co-encadrant de thèse |

Rapporteurs :

**XUGUANG WANG**
Directeur de recherche, UNIVERSITE GUSTAVE EIFFEL
**STEPHANE AVRIL**
Professeur, ECOLE NAT SUP MINES ST ETIENNE

Thèse soutenue publiquement le **25 novembre 2022**, devant le jury composé de :

| | |
|---|---|
| **YOHAN PAYAN**<br>Directeur de recherche, CNRS DELEGATION ALPES | Directeur de thèse |
| **XUGUANG WANG**<br>Directeur de recherche, UNIVERSITE GUSTAVE EIFFEL | Rapporteur |
| **STEPHANE AVRIL**<br>Professeur, ECOLE NAT SUP MINES ST ETIENNE | Rapporteur, Président du jury |
| **HELENE PILLET**<br>Professeur, ENSAM CER PARIS | Examinatrice |
| **CELINE FOUARD**<br>Maître de conférences HDR, UNIVERSITE GRENOBLE ALPES | Examinatrice |

Invités :

**PIERRE-YVES ROHAN**
Maitre de Conférence HDR, ENSAM CER PARIS
**NATHANAEL CONNESSON**
Maitre de Conférence, UNIVERSITE GRENOBLE ALPES

# General Summary

A Pressure Ulcer (PU) is defined, according to National and European Pressure Ulcer Advisory Panels (NPUAP and EPUAP) as: "*a localized injury to the skin and/or underlying tissue usually over a bony prominence, as a result of pressure, or pressure in combination with shear*." Pressure Ulcers (PUs) have, for a long time, been considered to be a Cinderella subject. Since it mostly affects bed-ridden population, it was assumed to be part of the patient's disease for a long time until it was recognized as a challenge of the nursing process.

According to epidemiology studies, a PU is a complication primarily related to the care and treatment of individuals who have difficulty moving or changing positions: for example, people with a disability and the elderly (based on the study conducted in the hospitals from five European countries, PU prevalence of 18% was observed (Vanderwee et al. 2007)). Currently, with the development of healthcare and treatments, life expectancy of the average person is increasing worldwide meaning also an increase in the elderly population.

In the worst case, untreated PU or its complications could lead to death; from 1990 to 2001, PU was reported as a cause of death for 114380 persons in the United States (Redelings, Lee, and Sorvillo 2005) and from 1999 to 2016 in Spain, PU was listed as a cause of death for 11238 people over 65 years old (Verdú-Soriano, Berenguer-Pérez, and Quesada 2021). PUs also have an important impact on the psychological state of the person affected (Upton and South 2011). They can potentially lead to social isolation and worsening of the existing medical condition.

The clinical management of PUs also represents a financial burden for the society. A study by Dealey et al. estimated that the cost of PU treatment in United Kingdom could be as high as £14108 for a grade 4 PUs (Dealey, Posnett, and Walker 2012). Treatment of the advanced PU requires surgery and a long rehabilitation period. Depending on the region of the damaged tissue, the treatment could be complicated by the potential risk of incontinence or any challenges associated with the full unloading of the affected tissues (in case of the lower back, ischium or heel PU). Meanwhile, latest research by Downie et al. (Downie et al. 2013) based on a 12 months-long study in five UK hospitals suggests that 43% of the grades 3 and 4 PUs could be preventable.

Current research oriented on the development of PU prevention strategies include the development of new risk assessment protocols, sensors, research on pressure injury biomarkers and mechanical parameters that could help in the decision-making process. The main scientific evidence and the main findings are outlined and discussed in the corresponding section of the literature review. In brief, it has been shown, in a rat model, that there exists a correlation between compression-induced tissue damage and mechanical strain (Ceelen, Stekelenburg, Loerakker, et al. 2008). Based on this evidence, several numerical models, mostly based on Finite Element Analysis, have been proposed in the literature to estimate tissue deformations resulting from the mechanical interaction of the body with external devices. Moreover, according to figures reported in a National Prevalence Study in French Hospital patients, sacral 29% and heel 53% regions have been reported to be the two most common anatomical sites for PU development (B. Barrois et al. 2008). Sacrum was therefore chosen in this study as the investigation location because of the high risk of PUs development at this location.

As shown in several studies, the mechanical response is very sensitive to the input data (geometry (Moerman et al. 2017), material properties (Luboz et al. 2014a) and boundary conditions). Building patient-specific mechanical models for the prediction of strain localization is a long and tedious task but seems necessary to accurately evaluate the risk factors. It is clear that, to bring the research findings to the clinical environment, an accessible minimally time-consuming techniques should be employed. 3D MRI is often considered as a benchmark technique for collecting the geometrical data of Finite Element (FE) models, but it remains a costly and not easily accessible exam. On the other hand, 2D B-mode Ultrasound (US) was investigated as a promising image modality in relation to PU (Akins et al. 2016a; Swaine et al. 2018). The main objective of this PhD project is to evaluate the possible biases introduced by using 2D US-derived FE models in place of 3D MRI-derived FE models for the analysis of strain intensities and localizations in relation to personalized sacral PU risk assessment.

The PhD project is part of the H2020 European Training Network "Skin Tissue INTegrity under Shear" (H2020-MSCA-ITN-2018 STINTS). The aim of the STINTS project is to get a better understanding of complex biomechanical and biochemical factors responsible for the skin damage in reaction to prolonged pressure, shear forces and friction. My PhD project focuses on the development of subject-specific FE models of buttock soft tissues to evaluate the intensities and localizations of strains when the body interacts with supporting surfaces. The manuscript is organized as follows:

**Chapter I** summarizes and discusses the literature review on PU condition, its aetiology and possible consequences. A review of existing FE models of the buttock region reported in the literature was performed to summarize the assumptions generally made in these studies. This analysis allowed to identify the gap in the existing research and frame the objective of this PhD project, which focuses on the development and the evaluation of the reliability of 2D US-based FE model as an alternative to 3D MRI-based FE model.

**Chapter II** focuses on the experimental work conducted to collect data for the development and the evaluation of the FE models. Two experiments were conducted. The first one was an MRI pilot study to experimentally quantify the in-plane and out-of-plane soft tissue displacements in the sacrum area under a realistic US transducer-like compressive loading with a 3D printed copy of an ultrasound probe. 3D MRI acquisitions were performed at the IRMaGe research platform (Univ. Grenoble Alpes) in 5 configurations: one unloaded (L0) and 4 loaded (L1-L4) in decreasing order of loads from 1.2 kg to 400 g. The second experiment described in **chapter II** is related to material data collection with the use of the VLASTIC local aspiration device (Kappert et al. 2021). Pressure-volume curves were collected for future identification of Young's moduli for skin and adipose tissue.

**Chapter III** details the methodology employed to develop and evaluate a personalized 3D FE model of the buttock from data collected on a healthy volunteer (**chapter II**). The model was used to simulate the soft tissue vertical displacements under a realistic US transducer-like compressive loading and to compute the maximum shear strains in the sacrum area. Digital Volume Correlation (DVC) based on 3D MR image registration was explored to estimate soft tissue displacements and strains from the experimental data previously collected in **chapter II**. This allowed to define a dataset for the evaluation of the FE model prediction for each of the four defined load cases.

**Chapter IV** details the methodology employed to develop and evaluate a personalized 2D FE model of the sacral region based on the experimental geometrical and loading data collected in **chapter II**. The same four load cases as the ones used with the 3D FE model are defined here. In the end, a results section provides a quantitative comparison between the results of 2D and 3D simulations.

**Chapter V** focuses on the experimental assessment of the out-of-plane tissue motion under the compressive load, as a step towards addressing the possibility of using US in place of MRI for data collection for sacral risk assessment. First, the process of US plane construction is described. The parameters used for quantification of in-plane and out-of-place tissue displacements are then defined and two regions of interest are introduced. A results section provides the calculation of the uncertainty in the US plane definition and a quantification of in-plane and out-of-plane tissue motion.

This manuscript ends with a summary of the main contributions of this work and outlines some of the perspective work that are envisaged.

# Acknowledgements

First of all, I would like to express my deepest appreciation to my supervisor DR Yohan Payan and co-supervisors Dr Pierre-Yves Rohan and Dr Nathanaël Connesson for their support, enthusiasm, patience and reassurance. This research project would not have been possible without their continuous guidance and I am extremely grateful that I had a chance to learn from their vast knowledge and experience.

Besides my supervisors, I am deeply indebted to Prof. Stéphane Avril and DR Xuguang Wang for devoting their time to reviewing my manuscript and I would like to extend my gratitude to the rest of my thesis committee, Prof. Hélène Pillet and Dr Céline Fouard for kindly accepting to examine my doctoral work.

Indeed, I am grateful to Prof. Hélène Pillet and Dr Sandra Loerakker for taking the time to follow my research project over these years and providing me with their thoughtful suggestions on how it could be improved.

This project has received funding from the European Union's Horizon 2020 research and innovation programme under the Marie Skłodowska-Curie grant agreement No. 811965. And I would also like to thank all the members of the STINTS project for our exchanges over the years. Unfortunately, we didn't get to meet in person as often as I would have liked, but each time it happened, our interactions were filled with insightful scientific exchanges and great friendliness.

Special thanks to my fellow PhD student Alessio Trebbi for all research exchanges and laughs we shared over these 3 years.

I would be remiss in not mentioning all of my friends and climbing buddies in Grenoble and Paris for all the good times and adventures that made my life full.

Last but not least, a very special thanks belongs to my life partner Anatolii for his constant support through all ups and downs of this journey.

## Table of contents

# List of figures

# CHAPTER I. Literature review: Clinical and scientific context of pressure ulcers development and prevention

To introduce the overall research topic, this chapter first summarizes the existing knowledge on the etiological pathways, risk factors, staging current prevention and risk assessment techniques for the reader.

Prevention of Pressure Ulcers (PUs) currently relies on labour-intensive vigilance in nursing care. In many hospitals and community settings, risk assessment scores, regular skin assessment and clinical judgments are used to develop an individualized prevention plan for each patient. However, the interpretation and the development of these individualized prevention strategies is limited by the extremely large range of descriptors that contribute to PU development and the complex interplay between them. To assist the clinician in developing such individualized prevention plans, objective measurements are required.

Biomechanical indices have been shown to be correlated to the injury risk in animal models. Building upon this, several computational models of load-bearing soft tissue have been reported in the literature. These have shown that bony prominences induce substantial stress concentrations, which explains why these areas are vulnerable to ulceration. In the second section of this chapter, a review of these models is presented and focuses on the tools used and assumptions made to collect both input data to feed the model and experimental data to evaluate the predictive performance of such models.

## *1.1 Clinical context*

### *1.1.1 Pressure ulcer pathways*

When a person interacts with his environment, mechanical loads are transferred from the skin to the bony prominences. On the compression sites at risk (heel, sacrum, ischium, etc), the soft tissues are generally composed of the following layers: the external protective layer - skin, the underlying layer of adipose tissues, fascias, and the muscle layer located over the bony prominence (Figure 3).

There is a consensus that PU can be grouped into two main categories depending on whether they expand inward from the skin surface towards muscle and bone (superficial PU) or from muscle tissue outward (Deep Tissue Injury).

Superficial injuries develop in the skin, as a result of excessive normal pressure combined with shear force, and progress continuing deeper inside. A four-stage PU classification system was developed by the NPUAP (National and European Pressure Ulcer Advisory Panels) and later adapted by the EPUAP (the description of the different stages according to the EPUAP is listed in Table 1 below; the illustration of each stage is shown in Figure 1, adapted from (Bhattacharya and Mishra 2015)). It was additionally stated that PU might not progress orderly from stage to stage, therefore the staging system shall not be used to state the level of improvement (Defloor and Schoonhoven 2004).

Table 1: PU classification (European Pressure Ulcer Advisory Panel (EPUAP). 1999) adapted from (Beeckman et al. 2007)

| | |
|---|---|
| Grade 1 | Non-blanchable erythema of intact skin. Discolouration of the skin, warmth, oedema, induration or hardness may also be used as indicators, particularly in individuals with darker skin*. |
| Grade 2 | Partial thickness skin loss involving epidermis, dermis or both. The ulcer is superficial and presents clinically as an abrasion or blister. |
| Grade 3 | Full thickness skin loss involving damage to or necrosis of subcutaneous tissue that may extend down to, but not through, underlying fascia. |
| Grade 4 | Extensive destruction, tissue necrosis or damage to muscle, bone, or supporting structures with or without full thickness skin loss. |

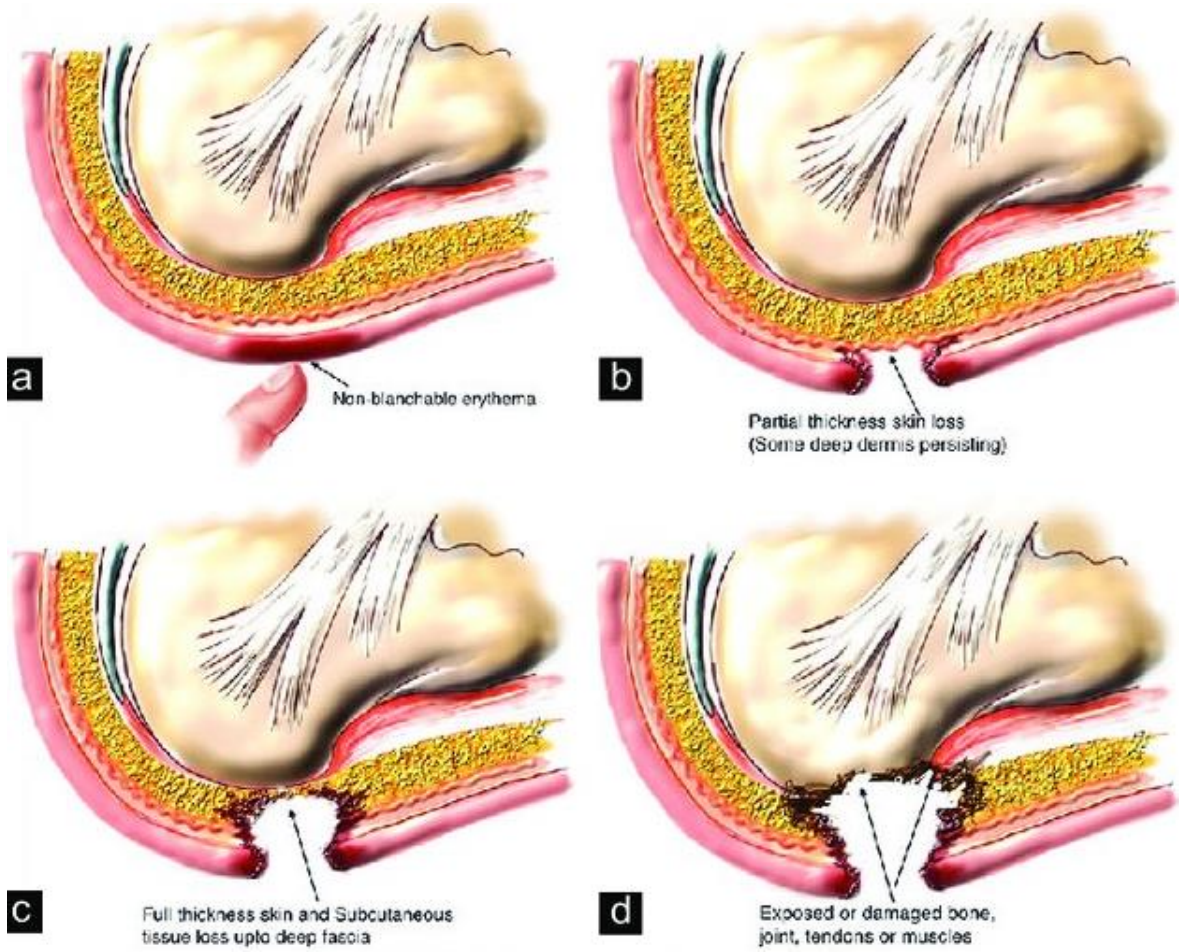


Figure 1: Different grades of pressure ulcers. A) Grade 1 b) Grade 2 c) Grade 3 d) Grade 4 Adapted from (Bhattacharya and Mishra 2015)

The second path of pressure injury is deep tissue injury (DTI). It originates in the muscle tissue around bony prominences as a result of excessive compression or shear strains and propagates to the top layers (C. V. Bouten et al. 2003). DTI is considered to be more dangerous than surface PU due to the difficulty of detection in the early stages. A pressure related injury under intact skin could lead to the development of grade 3-4 PU even with an optimal treatment (Black 2005; Ankrom et al. 2005).

### *1.1.2 Biological soft tissues under consideration*

During the contact of the human body with a supporting surface (cushions, mattresses, shoes, etc.), several biological tissues are being affected. A short description of these tissues and their main functions are provided below.

- **The skin** is the largest organ in the body. It acts as a protective barrier from mechanical and any other external injury. It also plays an important role in the prevention of moisture loss and of the regulation of internal conditions. As shown in Figure 2 below, skin is composed of three main layers. The epidermis is the top layer; it serves as a barrier to infections and regulates the water loss. The dermis is the intermediate layer and consists of irregular connective tissues; it partially absorbs the external mechanical impact. The hypodermis is the lowest layer and acts as a subcutaneous adipose layer. Material properties of the skin are highly dependent on the age, sex, skin handling and ambient conditions (Dąbrowska et al. 2018). The review by Dąbrowska et al. lists three studies where the skin elasticity was assessed on a forearm. Zahouani et al. performed an indentation test on 20 women (55-70 y.o.) *in vivo* resulting in Young's modulus of 8.3±2.1 kPa (Zahouani et al. 2009). Agche et al. performed a torsion test on 138 subjects (3-89 y.o.) *in vivo* resulting in Young's modulus of 0.42-0.85 MPa (Agache et al. 1980). Finally, Diridollou et al. performed a suction test on 10 subjects (20-30 y.o.) *in vivo* resulting in Young's modulus of 129±88 kPa (Diridollou et al. 2000).

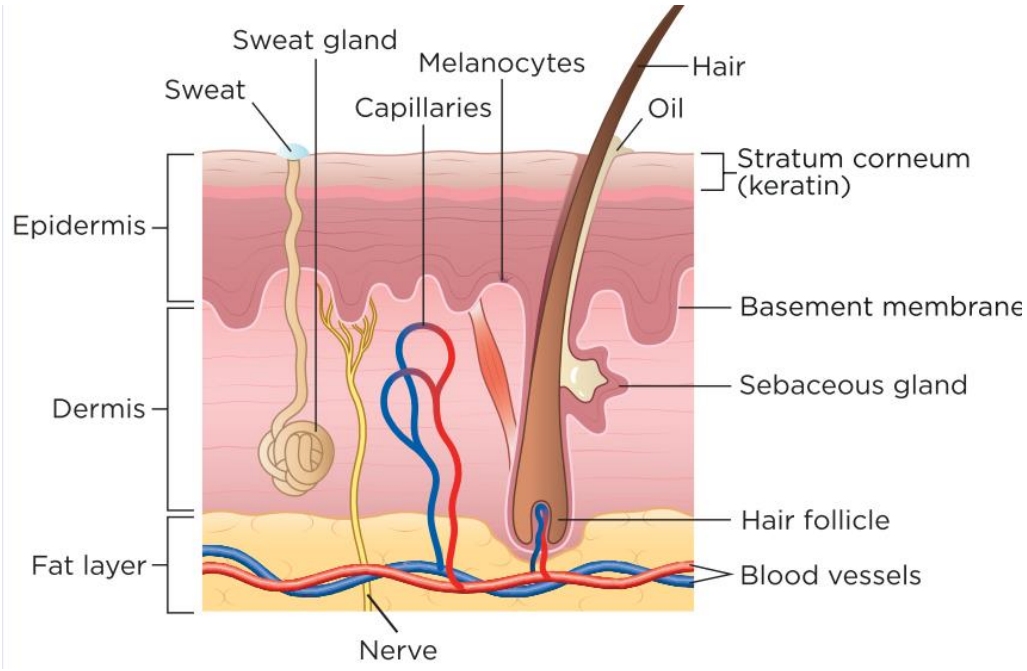


Figure 2: Skin anatomy, image adapted from (Lawton 2019)

- **The adipose tissue** (fat) is a main metabolic organ responsible for the regulation of the body energy homeostasis (Choe et al. 2016). In addition, it provides insulation qualities and cushions the inner organs. Hendriks at al. performed suction test on the forearm hypodermis resulting in the shear modulus of 0.04 kPa (Hendriks et al. 2003). In the indentation test conducted by Pailler-Mattei et al. on the forearm, shear modulus of the hypodermis was calculated to be 2 kPa (Pailler-Mattei, Bec, and Zahouani 2008). Adipose breast tissue was evaluated with the MR elastography by Van Houten et al., the shear modulus was in the range between 0.16 and 8.3 kPa (Van Houten et al. 2003). Another traction test was performed by Sommer et al. on the abdomen hypodermis tissue resulting in the shear modulus values of 0.4 ± 0.2 kPa (Sommer et al. 2013).
- **The fascia** (shown in Figure 3 below) is a layer of connective tissues with a varying thickness whose role is to sustain the integrity of the skin and protect the subcutaneous tissues (Stecco et al. 2011). The superficial fascia divides fat layer into superficial and deep adipose tissues (Stecco et al. 2011). The deep fascia surrounds individual muscles and groups of muscles to separate into fascial compartments. Astruc et al. performed uniaxial tensile tests on the several samples harvested from connective tissues in the abdominal wall with the, experimental data was fitted and the estimated Young modulus was in the range between 0.6 and 6.6 MPa (Astruc et al. 2018).

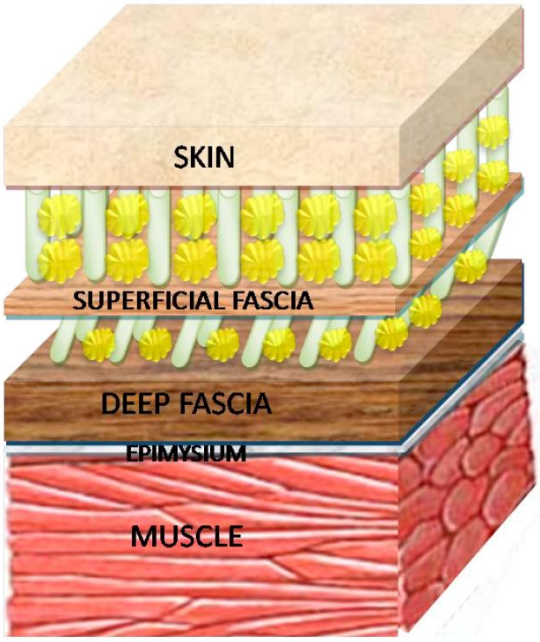


Figure 3: Composition of subcutaneous tissues including the superficial and deep fasciae, image adapted from (Stecco et al. 2011)

- **Skeletal muscles** are attached to the bones by tendons and are responsible together for all body movements. Muscle's roles also include absorbing shocks and shielding bones from the mechanical overloading (Böl et al. 2019). Each muscle is composed of a set of fibers. When a muscle is stretched, passive forces are mostly generated by the muscle fibers connective tissues. However, in the context of pressure ulcer grades 1-3, muscles only serve as a support for the affected tissues. Koppenhaver et al. used Shear Wave Elastography to assess the shear modulus of erector spinae muscle at rest for

two groups of subjects with and without low back pain (N=60 for each group) (Koppenhaver et al. 2020). Shear moduli of 6.4 ± 3.4 kPa and 4.5 ± 1.7 kPa were observed for groups with and without low back pain correspondingly.

- **The Bone** is a constantly remodeling mineralized connective tissue that supports and protects soft tissues and inner organs. The role of the bone also includes production of red blood cells, white blood cells and platelets. However, in the context of pressure ulcers, it plays a role of the rigid support for the soft tissues.

### *1.1.3 Common localizations for PU onset and epidemiology*

PU generally develop at the load bearing areas of the body. The common locations are indicated on the picture depicted in Figure 4 below, adapted from the EPUAP website. They include the areas covering the bony prominences like the occipital bone, shoulders, elbows, knees, buttocks, sacrum, and heels. Bauer et al. analyzed the PU occurrence in inpatient population in the USA concluding that the most common localization for PU was the lower back (lower back/sacral/ coccygeal regions) (47%); 17% were observed on the buttock, 14% on the heel, 5% on the hip and 9% at other locations (including ankle, upper back and elbow each accounted for less than 5% (Bauer et al. 2016)).

The study carried out in 2014 in France throughout various hospital care units showed a PU prevalence of 8.1% in hospital facilities (Brigitte Barrois, Colin, and Allaert 2018). Two most common anatomical sites of the PU development, regardless of the care unit type, were sacral and heel regions (Brigitte Barrois, Colin, and Allaert 2018).

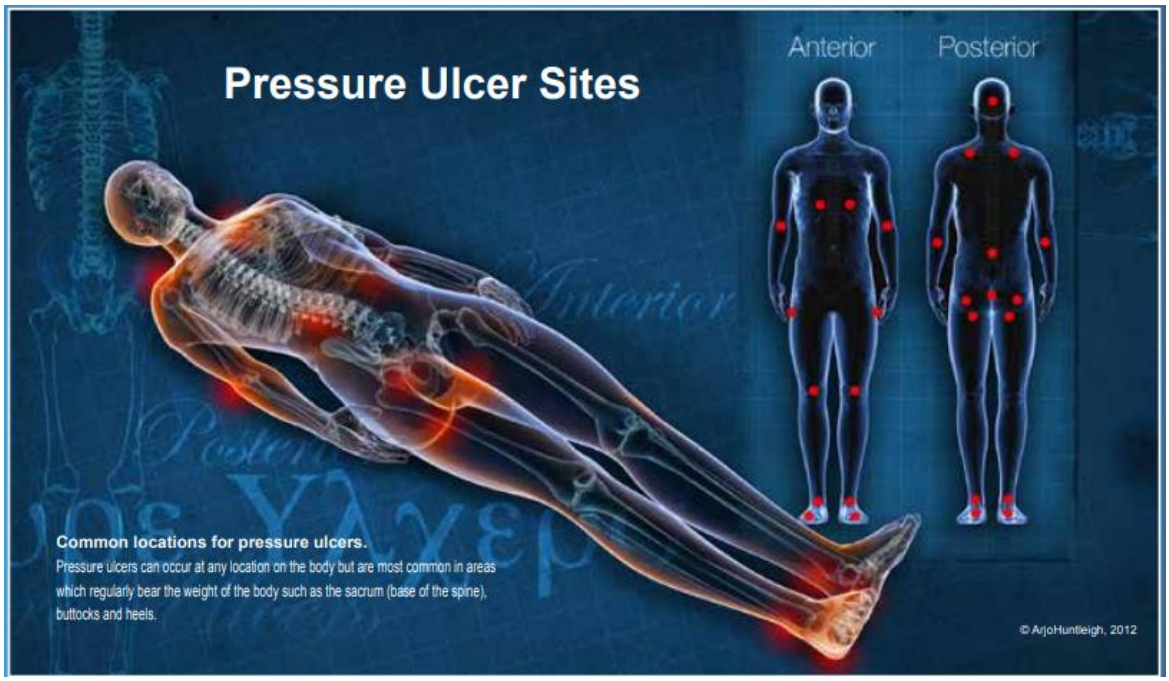


Figure 4: Localizations of PU, image adapted from epuap.org

### *1.1.4 Impact of PU*

Anyone can get a pressure ulcer (including babies in the hospital care units or healthy people undergoing long surgeries), but the following things can make them more likely to form: being over 70 (older people are more likely to have mobility problems, with a skin that can be more easily damaged through dehydration and other factors) and/or being confined to bed.

PU develops over a one-year period in 1 out of 3 adults with spinal cord injury, increasing to 9 of 10 patients over the lifetime (Gefen et al. 2008; Garber et al. 2000; Krause and Broderick 2004). Statistical analysis also associated the 6-month post hip fracture mortality rate in elderly patients with PU (Magny et al. 2017).

PU have been reported to highly affect the patient's health-related Quality of Life (Essex et al. 2009). In the elderly patients with PU, an elevated depression rate was indeed reported in comparison with the control group (Galhardo et al. 2010). Symptoms such as pain, discomfort, exudate and odor can occur, which can further restrict mobility and daily activities as well as lead to disturbed sleep and a general reduced Quality of Life. Patient's psychological well-being can be affected by feelings of anxiety, worry, and dependence. This can lead to social isolation and the inability to participate in activities.

The prevention and management of PUs represent an important financial burden on the healthcare system. According to a recent review, costs of PU prevention per patient was estimated to range between 3€ to 88€ per day (Demarré et al. 2015). According to the same study, the cost of treatment per patient varied between 2€ to 470€ per day. The conclusion of the systematic review performed by Demarré et al. was the following: even with prevention costs being considerable according to some studies, the treatment cost of the severe cases is substantially higher (Demarré et al. 2015).

One of the difficulties is the absence of any unified approach for data collection to evaluate prevalence in population; this leads to hardly comparable results. Barrois et al. reviewed 50 PU prevalence studies and noted the prevalence rate ranging from 3.5% to 29.5% for hospital inpatients. The rate is highly dependent on the studied population, sample size and country where the study was performed (B. Barrois et al. 2008).

### *1.1.5 Etiology*

Several recent studies have established that there are at least two damage mechanisms responsible for the onset of PUs: i) ischemia/reperfusion damage (Loerakker et al. 2011; Jiang et al. 2011; Peirce, Skalak, and Rodeheaver 2000; Gefen et al. 2008) initiated by **sustained moderate tissue deformations** and ii) direct cell damage initiated by excessive direct (local compression and shear) deformations (Gawlitta et al. 2007; Breuls et al. 2003; C. V. Bouten et al. 2003; Loerakker et al. 2011; Gefen et al. 2008; Eran Linder-Ganz et al. 2006).

**Sustained moderate mechanical strains** in soft tissue have been shown to cause partial occlusion of blood and lymph vessels, limiting perfusion (e.g. ischemia) (Loerakker et al. 2011; Jiang et al. 2011; Peirce, Skalak, and Rodeheaver 2000). Because of blood vessels occlusion, the oxygen level is reduced and the muscle tissue changes its metabolism from aerobic to anaerobic, switching from oxygen to one of the weaker oxidants. During the anaerobic respiration, different waste products are formed (depending on the oxidant type used in place of the oxygen). In the well-regulated metabolic process, the waste products should be removed by the blood and lymph vessels. But, due to the vessels' occlusion, waste products are accumulated which decreases the pH level and leads to the cell death (C. V. C. Bouten et al. 2001; Anke Stekelenburg et al. 2007). Stekelenburg et al. performed *in vivo* experiment son rats to study the isolated and combined effects that ischemia and deformations have on tissue damage, showing that a 2-hour pure ischemic loading with inflatable tourniquet results in reversible muscle tissue damage (Stekelenburg et al. 2007).

Consistent results have previously been shown on the skeletal muscle of the mongrel dog. A 2-hour ischemic insult led to minimal damage with complete regeneration on reperfusion, while a 7-hour insult resulted in inability to restore intramuscular phosphagens and glycogen on reperfusion (Harris et al. 1986). These results suggest that the irreversible ischemic injury takes several hours to develop.

Impaired lymph formation and clearance could lead to inflammation (Olszewski 2003; Tabibiazar et al. 2006; Zampell et al. 2012) and have been suggested to be contributing factors to PU development (Reddy, Cochran, and Krouskop 1981). The main functions of the lymphatic system include the removal of the interstitial fluids from the tissues and immune defense with lymphatic fluid being rich with cellular debris. Gray et al. showed that lymph circulation is indeed altered by clinically relevant pressures (Gray, Voegeli, and Bader 2016). Lymphatic system response to different loading scenarios have been estimated for healthy volunteers with Near Infrared Imaging (Worsley et al. 2020). Measurements showed high inter-subject variability in pressure values causing microcirculatory occlusion. The blood microvascular system impairment developed under the higher pressures than blockage of the lymphatic flow.

The reperfusion (resumption of the blood flow) that follows an episode of ischemia has also been linked to the onset of pressure ulcer. Reperfusion injury was investigated in the dorsal skin in rats varying the amount of ischemia-reperfusion cycles, cycles frequency and ischemia duration. Analysis showed that for the same total ischemia duration time, tissue damage increased with the higher number of reperfusion events (Peirce, Skalak, and Rodeheaver 2000). Consistent results have been reported by Houwing et al. in pigs. Pressure indenters were placed on the animal's skin above the greater femoral trochanters. Samples of the muscle and subcutaneous tissue were extracted and analyzed right after ceasing the pressure application and after 1-2 hours of reperfusion time. Histological analysis showed no damage in the specimens taken right after the removal of the load. In specimens taken after a minimum of 2 hours, signs of pathology developing were observed (Houwing et al. 2000). It was hypothesized that reperfusion could reverse the damage only when the duration of ischemia does not exceed a particular subject-specific threshold. In contrast, if this threshold were to be surpassed and the critical amount of the waste products would accumulate and momentarily released into the system, the reperfusion would contribute to tissue damage (Loerakker et al. 2011). In comparison, the damage under high strains could occur within **minutes** (Cees W.J. Oomens et al. 2015).

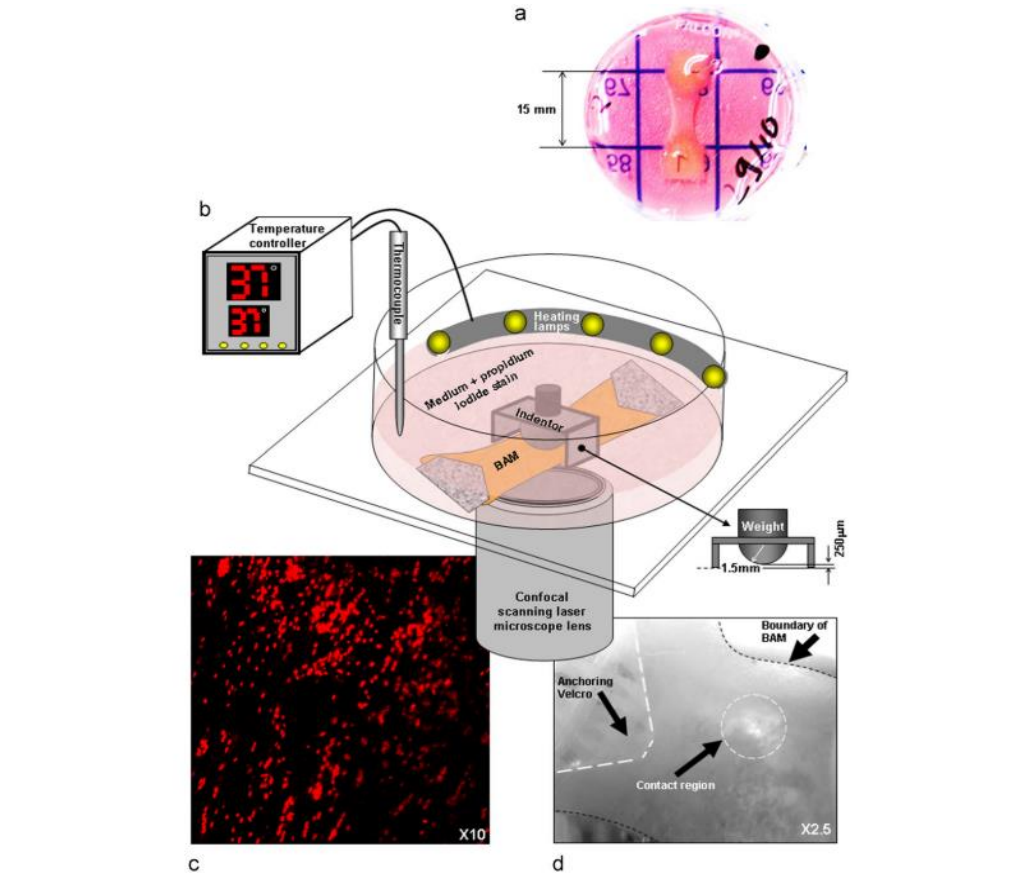


Fig. 2. The experimental apparatus: (a) a mature bio-artificial muscle (BAM) specimen (7-days post molding). (b) BAMs were placed in a specially designed culture dish which fits into the stage of a confocal laser scanning microscope (CLSM) and includes a temperature control system. (c) Red fluorescence images of propidium iodide-stained necrotic cell nuclei were obtained by means of the CLSM (unloaded specimen shown). (d) The indentor–specimen contact region, shown here from below in an optical microscopic view, was monitored over time to determine the radius of deformation-induced cell death.

a

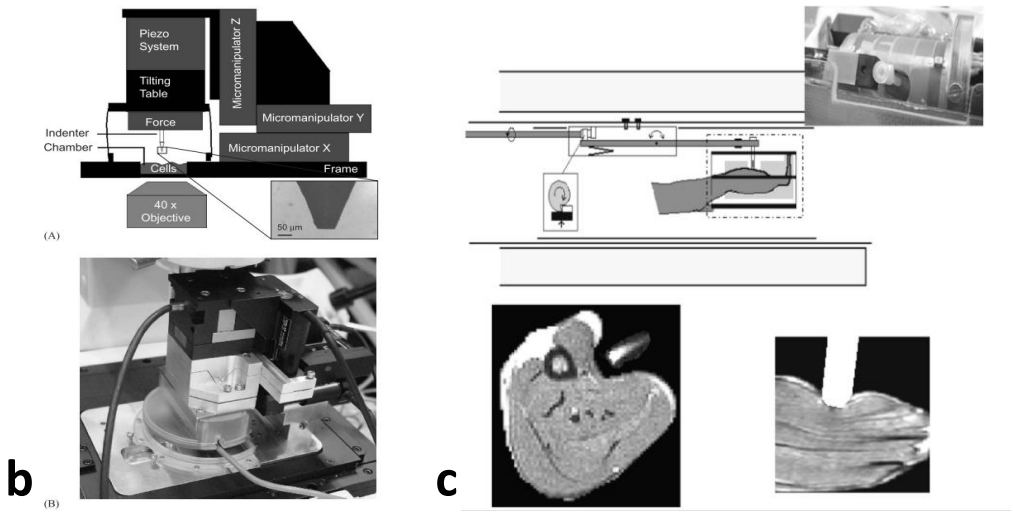


b

c

Figure 5: **a)** Experiment on tissue engineered muscle (Gefen et al. 2008) **b)** Schematic representation (A) and actual realization (B) of the single cell loading device. The inset shows a close-up of the glass indenter. Adapted from (Peeters et al. 2005) **c)** Schematic drawing of experimental set-up (a) Cross sectional T1-Image of the loaded lower leg of a rat (b) Lateral view of the loaded lower leg of a rat (c); adapted from (A. Stekelenburg et al. 2006; Cees W.J. Oomens et al. 2015)

Using a hierarchical approach, starting from single cell studies (C. V. C. Bouten et al. 2001; Breuls et al. 2003; Peeters et al. 2005) (Figure 5, b) to tissue engineered muscle constructs (Gefen et al. 2008),(Figure 5, a) and animal studies (Anke Stekelenburg et al. 2007; Ceelen, Stekelenburg, Loerakker, et al. 2008; Ceelen, Stekelenburg, Mulders, et al. 2008), (Figure 5, c), it was shown that **direct cell damage initiated by excessive direct** deformations (local compression and shear) (C. V. Bouten et al. 2003; Loerakker et al. 2011; Gawlitta et al. 2007; Gefen et al. 2008; Eran Linder-Ganz et al. 2006) is an equally important damage mechanism leading to cell death.

Studies with cells in culture (C. V. C. Bouten et al. 2001; Breuls et al. 2003) suggested that the direct deformation is one of the important factors leading to the cell death. Bouten et al. compared the percentage of the damaged cells in uncompressed constructs and under the moderate strain of 20%. Steady temporal growth of cell death was observed for the strained construct in comparison with the unstrained one (C. V. C. Bouten et al. 2001). Breuls et al. performed a compression test with six constructs of skeletal muscle myotubes embedded in a gel matrix (Breuls et al. 2003). The percentage of the dead cells was then evaluated over time and for various straining regimes in different areas of the construct. It was argued that the cell deformation played a more important role in cell damage than impaired transport of metabolites and waste products. Consistent results were observed by Gawlitta et al. in tissue engineered muscle showing that compression can result in muscle damage, while hypoxia does not add to cell death level within 22 hours (Gawlitta et al. 2007). Later, Gefen et al. evaluated an impact of the load duration and magnitude in tissue engineered muscle under high strains. A half-spherical indenter was used to apply non-inform concentric strains leading to formulation of the sigmoid risk curve shown in Figure 6 separating viable and dead cells with risk of cell damage rapidly growing above the curve (Gefen et al. 2008). The separate and combined roles of deformation and ischemia in the development of deep tissue injury after compressive loading was investigated in rat models. Experiment showed that 2 hours of high compressive loading result in irreversible muscle damage, in contrast with separately applied ischemic loading leading to reversible changes (Anke Stekelenburg et al. 2007). Further analysis showed that the location of damaged tissues corresponds to the area with maximum shear strain (Ceelen, Stekelenburg, Loerakker, et al. 2008).

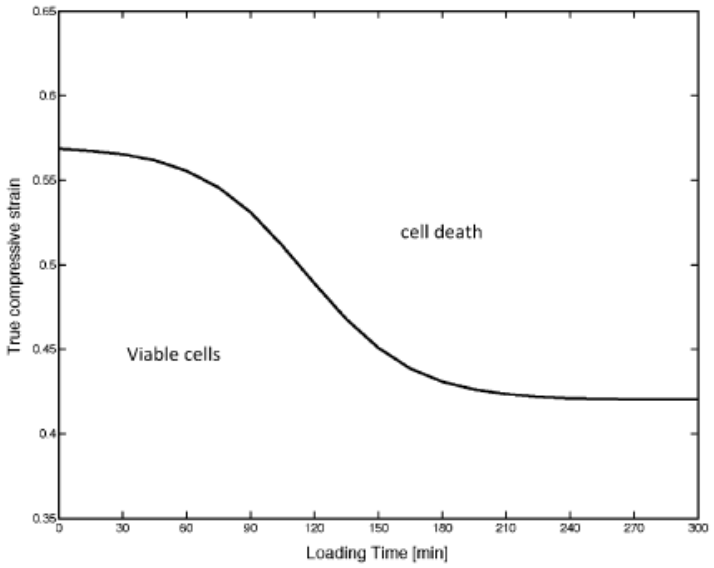


Figure 6: The strain-time cell death threshold for bio-artificial muscle specimens under large compressive strains, image adapted from (Gefen et al. 2008; Cees W.J. Oomens et al. 2015)

In rat models, a relationship between tissue damage and maximum shear strain in excess of 75% and a compressive strain in excess of 45% was observed (Ceelen, Stekelenburg, Mulders, et al. 2008). In the search for a threshold in tissue-engineered muscle, Gefen et al. calculated a 95% probability for cells to withstand the engineering strains below 65% during 1h. It was also shown that a decrease in strain intensity of 40% and less resulted in an increase of the viability period to 285 minutes (Gefen et al. 2008). However, when mechanical loading magnitude was compared to the damage observed in rats in 3D by Traa et al., analysis showed various injury response to the same mechanical loading in different animals. This suggested a subject-specific tolerance to sustaining the mechanical loading in tested rats (Traa et al. 2019).

Existing data (C. V. C. Bouten et al. 2001; Gefen and Weihs 2016; Turner et al. 2014) suggest that soft tissue injury is essentially **a multi-scale and multi-physics process**. The interplay between chemical–biological–mechanical factors is therefore key to understand and eventually predict the initiation and propagation of soft tissue damage. From a **biological and biophysical perspective**, a lot of research has focused on indentifying non-invasive biomarkers capable of discrimining the state of the tissues and predict the subject-specific risk of the PU formation.

Transcutaneous oxygen tension (tcPO2) at the sacrum region was tested as a possible biomarker in twenty debilitated subjects (Bader and Gant 1988). Polliack et al. examined the response of the sweat metabolites to the loading showing an increase of lactate and urea by 39% and 28% accordingly during prolonged loading at low pressure levels (Polliack, Taylor, and Bader 1997). Bronneberg analyzed different cytokines and chemokines as possible biochemical markers for the skin damage under the mechanical load. The inflammatory biomarkers were assumed to show correlation with the tissue deformation, as rupture of cell membranes attracts immune system cells and triggers the inflammatory response. Cytokine IL-1α showed the most promising results in relation with superficial tissue damage. It was also suggested that a combination of several rather than only one biomarker could provide better results (Bronneberg 2007). Soetens et al. confirmed these findings while comparing

intermittent and continuous loading regimes at sacrum region. Normalized IL-1α was found to be an early indicator of the tissue condition after the loading. Cluster analysis also revealed two distinct groups of subjects with either high or low responses to the loading. This could potentially help identifying patients at risk (Soetens, Worsley, Bader, et al. 2019)

Most of the studies focus either only on the evaluation of the mechanical aspect of tissue deformation and its role in the PU formation (Gefen et al. 2008; Anke Stekelenburg et al. 2007; Loerakker et al. 2013; Traa et al. 2019) or the biological markers reflecting the level of tissue damage (Soetens, Worsley, Herniman, et al. 2019; Woodhouse et al. 2015; Worsley et al. 2020). In contrast, multi-scale multi-physics models could account for the transmission of processes happening on the tissue-scale or cell-scale level to the macro-scale model of the structure. Zeevi et al. considered the coupling between the structural and thermal analyses (Zeevi et al. 2018) by incorporating thermal properties of the tissues in their mechanical model to observe the effect of the different supporting surfaces on microclimate of the sacral skin. Sree et al. created a microscale FE skin model with realistic microvascular architecture to investigate the relationship between the tissue deformation and hypoxia (Sree, Rausch, and Tepole 2019).

Multi-physical approach to the modelling gives a new insight into the etiology of tissue damage. However, its use is still mostly limited to research purposes in the lack of possibility to measure subject-specific properties in a clinical environment.

To summarize, ischemia/reperfusion and tissue deformations seem to play an important role in PU development. Damage related to direct deformation could occur within minutes (Cees W.J. Oomens et al. 2015) under high stresses. When the strain exceeds the load threshold that the cell can withstand, that could lead to the failure of the cell membrane and the mechanical disruption, resulting in cell death. In contrast, ischemic damage could be observed even under moderate strains but requires longer loading time (several hours). Occlusion of circulation and lymphatic vessels leads to changes in metabolism and can, over time, result in cell death (Cees W.J. Oomens et al. 2015).

### *1.1.6 Prevention and risk assessment*

Current prevention techniques include the use of specified mattresses, cushions, hydration of the dry or dehydration of the moist skin (depending on the situation), massage and repositioning. Many hospitals combine a visual inspection with risk assessment using different scales in order to provide the patient-specific prevention care.

Various risk assessment scales can be used as a prevention care. For example, Norton scale includes five subscales related to physical and mental conditions, activity, mobility and incontinence. They added together to form a total Norton score. A low score corresponds to a high risk of PU development.

The analysis of the various risk factors related to PU development highlight that there is not a single factor, but rather a complex interplay of several factors that increases the probability of PU (Coleman et al. 2013). This partially explains why some studies performed by different groups and in different settings provide contradicting results. For example, in a study performed in Czech Republic, the repositioning showed the most promising results among other prevention techniques like special mattresses, cushions, massages and skin treatment (Šateková, Žiaková, and Zeleníková 2017). Furthermore, according to the systematic review

of Tayyib and Coyer, only silicone foam dressing showed significant effect in prevention in contrast with the use of supporting surfaces, repositioning and nutritional strategies (Tayyib and Coyer 2016).

Clark et al. evaluated the thickness of the soft tissues covering sacrum in forty elderly patients, nine of whom had visible sacrum PU. They didn't find any correlation between the tissue thickness and Norton score or age of the patients. Measurements showed that all patients with PU as well as five patients without pressure injuries had less than 8.5 mm of soft tissue over the sacrum (Clark et al. 1989).

## *1.2. Scientific context, Mechanical approach*

One of the most important pathways of PU development, as it was described before, is the direct mechanical deformation. To evaluate the damage caused by the load, the external pressure applied by the supporting surfaces to the skin should be related with the tissue internal stress/strain field. In the case of a simple geometry, an analytical solution could be derived. But when it comes to the complex individual geometry of biological tissues, FEA is widely used. FE analysis is a numerical method for solving partial differential equations, based on the idea of breaking up the analyzed domain into a finite number of basic elements and looking for an approximation of the solution on each element. After, the equations for separate elements combined into the global system of equations which represents the entire domain.

The advantages of FEA include the possibility to observe the physical response to the load in any location of the tissue and to simulate load conditions potentially dangerous in real life. The results of the analysis highly depend on the provided input such as linearity/ non-linearity of geometry, material properties, boundary conditions and the load applied. Non-linearity of each of the above parameters adds accuracy to the model predictions but also increases the computational time. Previously used approaches for the building of FE models of the buttock region will be discussed below.

### *1.2.1 State of the art of the FE modelling of the buttock region*

As it was mentioned, most PU localizations include heel and sacrum (Brigitte Barrois, Colin, and Allaert 2018). Over the years, a considerable amount of FE models of the buttock region were developed. This subsection and Table 2, Table 3 and Table 4 provide a summary of different techniques and assumptions used by researchers up until now.

Table 2: Summary of the articles on the FE modelling of the buttock region. Focus on personalization of the geometry using medical imaging.

| | Article | Number of subjects | Position | Type of population | 2D/3D | Imaging | Tissues modeled | | | |
|---|---|---|---|---|---|---|---|---|---|---|
| | | | | | | | Bone | Muscle | Fat | Skin |
| 1 | Dabnichki 1994 | - | Sitting | - | 2D | - | ischium | undifferentiated | | |
| 2 | Todd 1994 | 2 | Lying (Supine) | healthy | 3D | MRI | Ischial tuberosity | undifferentiated | | |
| 3 | Oomens 2003 | 1 | Sitting | - | 2D | MRI | Ischial tuberosity | yes | yes | yes |
| 4 | Lin 2004 | 1 | Sitting | healthy | 2D | US | - | yes | yes | yes |
| 5 | Linder-Ganz 2004 | 1 | Recumbent | healthy | semi-3D | MRI | Pelvis, sacrum | yes | yes | yes |
| 6 | Verver 2004 | 1 | Sitting | not mentioned | 3D | HUMOS database | pelvis, sacrum, femur | undifferentiated | | yes |
| 7 | Makhsous 2007 | 1 | Sitting | healthy | 3D | MRI | pelvis, femur | 5 | yes | yes |
| 8 | Linder-Ganz 2007 | 6 | Sitting | healthy | semi-3D | MRI | ischium | yes | undifferentiated | |
| 9 | Linder-Ganz 2008 | 12 | Sitting | healthy/paraplegic | semi-3D | MRI | ischium | yes | undifferentiated | |
| 10 | Wagnac 2008 | 1 | Sitting | healthy | 3D | CT-scan | pelvis, sacrum | undifferentiated | | |
| 11 | Linder-Ganz 2009 | 6 | Sitting | healthy/paraplegic | semi-3D | MRI | ischium | yes | undifferentiated | |
| 12 | Sopher 2010 | 1 | Sitting | healthy | semi-3D | MRI | ischium | yes | yes | yes |
| 13 | Vogl 2010 | 1 | Lying (Prone) | healthy | 3D | MRI | pelvis, sacrum, femur | yes | undifferentiated | |
| 14 | Bucki 2012 | - | Sitting | - | 3D | CT-scan/EOS | ischium, sacrum | undifferentiated | | |
| 15 | Oomens 2013 | 3 | Lying (Supine) | healthy | 2D | MRI | pelvis, sacrum | yes | yes | yes |
| 16 | Levy 2013 | 1 | Sitting | paraplegic | semi-3D | MRI | ischium | yes | yes | yes |
| 17 | Luboz 2014 | 1 | Sitting | healthy | 3D | CT-scan | pelvis | yes | yes | yes |
| 18 | Al-Dirini 2016 | 1 | Sitting | healthy | 3D | MRI | pelvis, sacrum, femur | 28 | undifferentiated | |
| 19 | Levy 2017 | 1 | Lying (Supine) | healthy | 3D | MRI | sacrum | undifferentiated | | |

| | Article | Number of subjects | Position | Type of population | 2D/3D | Imaging | Tissues modeled | | | |
|---|---|---|---|---|---|---|---|---|---|---|
| | | | | | | | Bone | Muscle | Fat | Skin |
| 20 | Moerman 2017 | 6 | Lying (Supine) | healthy/paraplegic | 3D | MRI | pelvis | yes | yes | yes |
| 21 | Luboz 2018 | 1 | Sitting | not mentioned | 3D | CT-scan | pelvis, sacrum, femur | yes | yes | yes |
| 22 | Macron 2018 | 6 | Sitting | healthy | 3D | EOS+optical scanner+US | pelvis | yes | yes | yes |
| 23 | Zeevi 2018 | 1 | Lying (Supine) | not mentioned | 3D | MRI | pelvis | yes | yes | yes |
| 24 | Wang 2021 | 1 | Sitting | not mentioned | 3D | Visible Human Project | pelvis, sacrum, femur | yes | yes | yes |
| 25 | Fougeron 2022 | 1 | Lying (Supine) | healthy | semi-3D | US | sacrum | no | yes | yes |

Table 3: Summary of the articles on the FE modelling of the buttock region. Focus on personalization of the constitutive parameters.

| | Article | Constitutive law, soft tissues | Material properties | | | | | Source of MP | Viscous behaviour |
|---|---|---|---|---|---|---|---|---|---|
| | | | Bone | Muscle | Fat | Skin | Poisson's ratio, soft tissues | | |
| 1 | Dabnichki 1994 | Mooney-Rivlin | - | A=0.5558 kPa, B=0.0833 kPa | | | 0.495 | Calibration | no |
| 2 | Todd 1994 | Linear elastic | E=17 MPa; ν=0.31 | Female: E=11.9 kPa; Male: E=15.2 kPa | | | 0.49 | Experimental | no |
| 3 | Oomens 2003 | Ogden | rigid | μ=3 kPa, α=30 | μ = 6 - 20 kPa, α = 5 - 30 | μ=8 kPa, α=10 | Not mentioned | Literature + Calibration | no |
| 4 | Lin 2004 | Neo-Hookean | - | G=700 kPa | G=30 kPa | G=90 kPa, 45 kPa | 0.485 | Literature | no |
| 5 | Linder-Ganz 2004 | Non-linear elastic | LE ($E_c$=18 GPa, $E_t$=5 GPa; ν=0.3) | E=75 kPa | E=80 kPa | E=695 kPa | $\nu_{skin}$ = 0.4; $\nu_{fat} = \nu_{muscle}$ =0.5 | Literature + Calibration | no |
| 6 | Verver 2004 | Mooney-Rivlin | rigid | A1=1.65 kPa; A2=3.35 kPa | | LE (E=0.15 MPa; ν=0.46) | 0.49 | Literature + Estimation | no |
| 7 | Makhsous 2007 | Mooney-Rivlin | rigid | Not mentioned | Not mentioned | Not mentioned | 0.485 | Literature | no |
| 8 | Linder-Ganz 2007 | Neo-Hookean | rigid | G=8.5 kPa | G=31.9 kPa | | Not mentioned | Literature | yes |
| 9 | Linder-Ganz 2008 | Neo-Hookean | rigid | G=8.5 kPa | G=31.9 kPa | | Not mentioned | Literature | yes |
| 10 | Wagnac 2008 | Linear elastic | LE (E=17 GPa; ν=0.49) | E=81.5 kPa | | | 0.49 | Literature | yes |
| 11 | Linder-Ganz 2009 | Linear elastic | rigid | G=8.5 kPa | G=31.9 kPa | | 0.49 | Literature | no |
| 12 | Sopher 2010 | Neo-Hookean + Mooney-Rivlin | LE (E=7 GPa; ν=0.3) | G=7.1 kPa | G=0.286 kPa | c10=9.4 kPa; c11=82 kPa | 0.495 | Literature | yes |

| | Article | Constitutive law, soft tissues | Material properties | | | | | Source of MP | Viscous behaviour |
|---|---|---|---|---|---|---|---|---|---|
| | | | Bone | Muscle | Fat | Skin | Poisson's ratio, soft tissues | | |
| 13 | Vogl 2010 | Neo-Hookean | rigid | G=1.025 kPa | G=1.182 kPa | | 0.495 | Literature | no |
| 14 | Bucki 2012 | Mooney-Rivlin | - | c10=1.65 kPa, c11=3.35 kPa, K=500 kPa vs E=9.9 kPa | | | 0.49 | Literature | no |
| 15 | Oomens 2013 | Ogden | LE (E=3.4 GPa; ν=0.36) | μ=0.3 kPa; α=5 | μ=1 kPa; α=5 | μ=8 kPa; α=5 | Not mentioned | Calibration | no |
| 16 | Levy 2013 | Neo-Hookean + Mooney-Rivlin | LE (E=7 GPa; ν=0.3) | G=7.1 kPa; K=708 kPa | G=0.29 kPa; K=28.5 kPa | G=214 kPa, 325 kPa; K=21 kPa, 32 kPa | 0.495 | Literature | no |
| 17 | Luboz 2014 | Neo-Hookean | rigid | E=from 40 to 160 kPa | E=from 5 to 40 kPa | E=from 100 to 500 kPa | 0.49 | Literature | no |
| 18 | Al-Dirini 2016 | Ogden | LE (E=25 MPa; ν=0.3) | μ=1.9 kPa; α =4.6 | μ=1.2 kPa; α=16.2 | | Not mentioned | Calibration | no |
| 19 | Levy 2017 | Neo-Hookean | E=7 GPa; ν=0.3 | G=2 kPa, 2.8 kPa | | | 0.49 | Literature | no |
| 20 | Moerman 2017 | Ogden | rigid | c=0.669 kPa; m=12 | c=1.06 kPa; m=2 | c=49.7 MPa; m=2 | Not mentioned | Literature + Calibration | no |
| 21 | Luboz 2018 | Neo-Hookean | rigid | c10=17 kPa | c10=5 kPa | c10=33 kPa | 0.49 | Literature | no |
| 22 | Macron 2018 | Ogden | rigid | μ=from 2 to 8 kPa; α=5 | μ=from 3.75 to 5 kPa; α=5 | μ=20 kPa; α=5 | 0.49 | Literature + Calibration | no |
| 23 | Zeevi 2018 | Neo-Hookean | E=7 GPa; ν=0.3 | G=0.1125 kPa | G=0.2 kPa | G=2 kPa | 0.494 | Literature | no |
| 24 | Wang 2021 | Ogden | rigid | μ=1.9 kPa; α=4.6 | μ=1.2 kPa; α=16.2 | LE (E=0.15 MPa, ν=0.46) | 0.495 | Literature | no |
| 25 | Fougeron 2022 | Yeoh | - | - | c10=0.13 kPa; c20=0; c30=12.2 kPa | c10=0.27 MPa; c20=1.9 MPa | 0.4999 | Literature | no |

Table 4: Summary of the articles on the FE modelling of the buttock region. Focus on the assessment of interactions and constraints.

| | | Contact type | | | Boundary conditions/Loads | |
|---|---|---|---|---|---|---|
| | **Article** | **Soft tissue/Support** | **Inter soft tissues** | **Soft tissue/Bone** | **Bone** | **Exterior of soft tissues** |
| 1 | Dabnichki 1994 | No friction; Friction, 0.4 | - | - | Body weight on ischium distributed along the thighs | Contact with support |
| 2 | Todd 1994 | No-slip | - | Not mentioned | Half of the weight of the pelvis on ischial tuberosity (m: 6.7% of total; f: 8.6% of total) | Contact with support |
| 3 | Oomens 2003 | Friction coefficient from 0 to 1 | No-slip | No-slip | 50% body weight on ischial tuberosity | Contact with support |
| 4 | Lin 2004 | - | Not mentioned | - | fixed | Uniform pressure (70mmHg) to epidermis |
| 5 | Linder-Ganz 2004 | Friction coefficient 0.4 | Not mentioned | Not mentioned | Tissue weight + Skeletal loads and moments; abdominal pressure of 2 kPa | Contact with support |
| 6 | Verver 2004 | No-slip | No-slip | No-slip | Body weight | Contact with support |
| 7 | Makhsous 2007 | Not mentioned | Not mentioned | Not mentioned | fixed | Uniform contact pressure |
| 8 | Linder-Ganz 2007 | No-slip | No-slip | No-slip | Vertical displacement of ischium and skin from a non-weight-bearing to a weight-bearing posture | |
| 9 | Linder-Ganz 2008 | No-slip | No-slip | No-slip | Vertical displacement of ischium and skin from a non-weight-bearing to a weight-bearing posture | |
| 10 | Wagnac 2008 | No friction | - | Not mentioned | concentrated downward force at centre of sacrum base | Contact with support |
| 11 | Linder-Ganz 2009 | - | No-slip | No-slip | fixed | Continuously recorded pressure patterns |
| 12 | Sopher 2010 | Friction coefficient 0.4 | No-slip | No-slip | Vertical displacement of ischial tuberosities | Contact with support |
| 13 | Vogl 2010 | Not mentioned | Not mentioned | Not mentioned | hip joints fixed | Contact with support |
| 14 | Bucki 2012 | - | - | Not mentioned | fixed | Recorded pressure patterns |
| 15 | Oomens 2013 | Friction coefficient 1 | Not mentioned | Not mentioned | body force | Contact with support |

| | Article | Contact type | | | Boundary conditions/Loads | |
|---|---|---|---|---|---|---|
| | | Soft tissue/Support | Inter soft tissues | Soft tissue/Bone | Bone | Exterior of soft tissues |
| 16 | Levy 2013 | Friction coefficient 0.4 | No-slip | No-slip | Vertical displacement of ischial tuberosities | Contact with support |
| 17 | Luboz 2014 | - | Not mentioned | Not mentioned | fixed | Recorded pressure patterns |
| 18 | Al-Dirini 2016 | Friction coefficient 0.4 | No-slip | Friction coefficient 0.3 | gravity | Vertical displacement of the support |
| 19 | Levy 2017 | Friction coefficient 0.4 | No-slip | No-slip | Downwards displacement on the top of sacrum | Contact with support |
| 20 | Moerman 2017 | No friction | Not mentioned | Not mentioned | fixed | Vertical force (35–45% of body weight) |
| 21 | Luboz 2018 | No-slip | No-slip | No-slip | fixed | Recorded pressure patterns |
| 22 | Macron 2018 | Friction coefficient 0.4 | No-slip | No-slip | Measured force applied to COG of pelvis | Contact with support |
| 23 | Zeevi 2018 | Friction coefficient from 0.4 to 0.9 | No-slip | No-slip | Vertical displacement on the upper part of sacrum | Contact with support |
| 24 | Wang 2021 | Friction coefficient 0.5 | No-slip | No-slip | Gravity + vertical load on the sacrum (50% body weight) | fixed |
| 25 | Fougeron 2022 | Friction coefficient 0.43 | No-slip | - | Vertical displacement of sacrum | fixed |

#### *1.2.1.1 Geometrical data*

The first step to generate such FE models of the buttock region is to acquire the geometrical data, to choose between two- or three-dimensional modality and to decide on the tissues that should be modelled. Table 2 provides a summary about previously used geometrical data in the literature.

Most of the listed articles (17 out of 25) modelled the sitting position which is common for the wheelchair users, while the rest analyzed the tissue deformations in the supine/lying position. Sacrum bone was included in most models of subjects in the lying position to correctly capture the loading in the soft tissues in contact. In the case of sitting, the deformations under the ischial tuberosities were principally investigated.

A two-dimensional model requires much less computation power than a 3D model but doesn't provide the information about the out-of-plane movements of the tissues under the load. Nevertheless, such 2D models allow to get an understanding of the tissue's deformations and were used by many research groups (Dabnichki, Crocombe, and Hughes 1994; C. W.J. Oomens et al. 2003; Lin et al. 2004; C. W.J. Oomens et al. 2013). Another possibility is to use a semi-3D model that represents only one slice of geometry with a given thickness (E. Linder-Ganz and Gefen 2004; Eran Linder-Ganz et al. 2007; 2008; 2009; Sopher et al. 2010; Levy, Kopplin, and Gefen 2013; Fougeron et al. 2022). Nowadays, the computational possibilities are higher; therefore, models used for the research purposes became more complex and detailed. In the model built by Al-Dirini et al., 28 muscles were represented (Al-Dirini et al. 2016). Although separation of the muscle groups might be clinically relevant to observe the response of individual muscles, such a model is time consuming.

However, when it comes to bringing the research findings to the clinical environment, it could be important to be able to build a model and to observe the inner tissues' mechanical state as fast as possible, leading to the search of the possible simplifications of model non-linearities. Macron et al. investigated the possibilities of the local simplified model of the region below the ischium to predict the internal response of the tissues in comparison with the results of the complete FE model. The results of the study were promising, however, with all shear strains being higher for the local simplified model, a possible systematic error was assumed (Macron et al. 2020). Linder-Ganz et al. developed a real-time monitoring of the inner tissues using a simplified semi-3D FE model (Eran Linder-Ganz et al. 2009).

Depending on the region of interest, different types of medical imaging techniques are currently used. For the visualization of the soft tissues in biomedical research, the most commonly used technique, presented in 15 out of 25 reviewed articles, is Magnetic Resonance Imaging (MRI). Five articles relied on data extracted from CT-scans or EOS images. Ultrasound was used in three articles for the acquisition of geometrical data.

MRI provides detailed three-dimensional anatomical images while being a non-invasive technique without any radiation. On the downside, MRI is expensive, time consuming (average scan could take 30-60 minutes) and could cause discomfort to the patient because of the still position in the enclosed space that should be kept throughout the scan. The disadvantages of this method partially explain why the use of FE models built based on this imaging modality is still mostly limited to research purposes.

Lin et al. used another method of geometry data collection, namely ultrasonic imaging, to build a 2D model. Results of this analysis are shown at Figure 7 (Lin et al. 2004). The

feasibility of this method in relation with the assessment of the soft tissues deformations has been also investigated in recent research (Doridam et al. 2018).

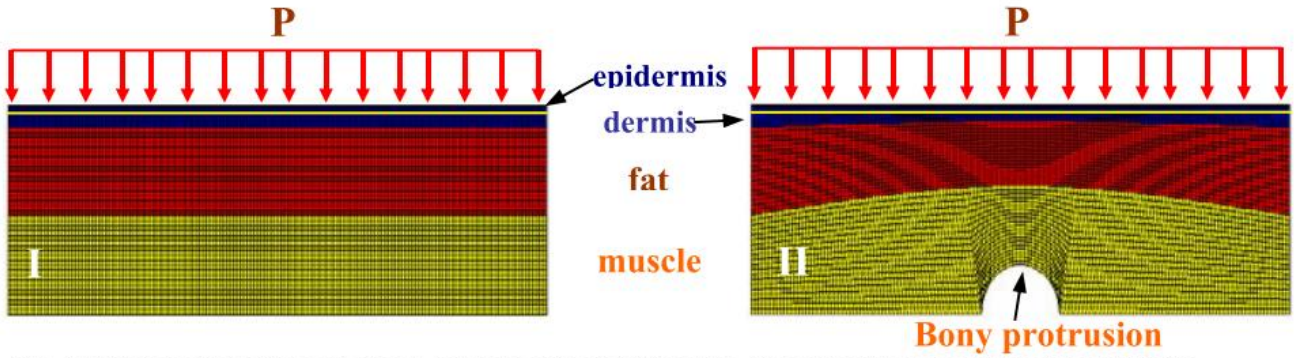


Fig. 4. FEM mesh for the soft-tissue. Case I: without protrusion, Case II: with bony protrusion. Uniform pressures of increasing magnitude were applied to the outer surface of the epidermis.

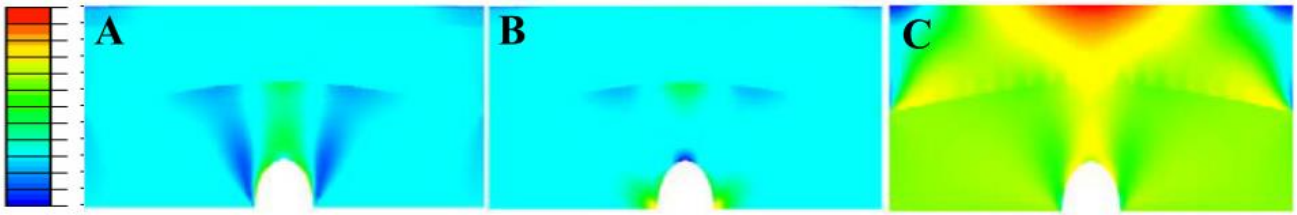


Fig. 5. Contour of stress and strain for model with bony protrusion (**Case II**) at *P*=70 mm Hg. (A) von Mises stress; (B) Stress S1; (C) Strain LE1.

Figure 7: FE model mesh and stress-strain fields for 2D model of soft tissues with and without bony protrusion (Lin et al. 2004).

Ultrasound provides two- or three-dimensional anatomical images, easily accessible in the clinical environment (mostly in 2D modality). It is a non-invasive modality that doesn't use radiation and that is therefore more frequently used. In addition, it takes much less time than MRI and doesn’t require the patient to remain still in the enclosed space which makes it more clinically relevant. Alipour et al. built a FE model of the human gastrocnemius muscle based on the geometrical data from 3D ultrasound (Alipour et al. 2018). Doridam et al. observed a non-negligible out-of-plane movement of the muscle tissues in the region of ischial tuberosity, which shows a possible downside of using 2D modality and points to the necessity of using 3D ultrasound to capture the 3D displacement and strain fields (Doridam et al. 2018).

The mechanical response of soft tissues depends on the anatomical specificities of each subject. Todd et al. included two healthy subjects (male and female) (Todd, B.; Thacker 1994); Linder-Ganz et al. included six healthy subjects (three males and three females), joined by six paraplegic subjects in the next article by the same group (Eran Linder-Ganz et al. 2007; 2008); Oomens et al. included three healthy female subjects (C. W.J. Oomens et al. 2013); Moerman et al. included three healthy subjects (two males and one female) and three subjects with spinal cord injury (two males and one female) (Moerman et al. 2017); Macron et al. included six healthy subjects (five male and one female) (Macron et al. 2018). Several subjects with different geometries were involved in only mentioned above works, while most of the reviewed articles included the FE model based on a single subject for time saving purposes. Moerman et al. investigated the effect of geometry and observed large variations between subjects, confirming the importance of subject-specific modelling (Moerman et al. 2017).

#### *1.2.1.2 Material properties*

Table 2 shows that in most studies, FE models were based on healthy volunteers, while soft tissue elastic properties and their thickness could significantly differ for the paraplegic population. A comparison of stress/strain distributions between healthy and paraplegic population was performed in three studies (Eran Linder-Ganz et al. 2008; 2009; Moerman et al. 2017).

Table 3 provides a summary about previously used constitutive material for each tissue included in the FE models. In the reviewed articles, bones were either considered rigid or linear elastic with modulus varying from 17 MPa (Todd, B.; Thacker 1994) to 18 GPa (E. Linder-Ganz and Gefen 2004).

Soft tissues covering the bony prominences in the buttock region include the layer of muscle, adipose tissues and skin. For simplification purposes and depending on the region of interest, these tissues were undifferentiated in some models. Most often in this case, muscle, fat and skin are considered as a single soft tissue (Dabnichki, Crocombe, and Hughes 1994; Todd, B.; Thacker 1994; Wagnac, Aubin, and Dansereau 2008; Bucki et al. 2012; Levy and Gefen 2017). In other articles, fat and skin were fused (Eran Linder-Ganz et al. 2007; 2008; 2009; Vogl et al. 2010; Al-Dirini et al. 2016). Oomens et al. performed a study including all three separate layers of the soft tissues. A stress-strain field was observed with two areas of the high shear strains, one in the fat just below the bone and another in the deeper muscle. Variation of the fat parameters had a substantial effect on the strains computed in the fat region without any effect in muscle region (C. W.J. Oomens et al. 2003). It was also observed that the change in muscle parameters has considerable effect on the strain's distribution in the model (Luboz et al. 2014b; Macron et al. 2020).

A lot of the reviewed articles considered the viscoelastic properties of soft tissues (Eran Linder-Ganz et al. 2007; 2008; Wagnac, Aubin, and Dansereau 2008; Sopher et al. 2010). Most of them assumed a hyperelastic behaviour arguing that PUs need a long period of time to develop; therefore it is possible to omit the strain rate dependency. The Neo-Hookean material model was used in ten articles, Mooney-Rivlin in six and Ogden in six. The main limitation of such material parameters is the fact that most of them were obtained from the literature and originally often based on data from animal studies. This could be one of the explanations why material parameters vary so much between the listed studies. As an example, elastic modulus of the muscle was assumed to be from 0.1125 kPa (Zeevi et al. 2018) to 700 kPa (Lin et al. 2004). Luboz et al. reported an importance of the fat and muscle stiffnesses for the evaluation of the internal strain field (Luboz et al. 2014b). In other cases, an inverse FE calibration was used (C. W.J. Oomens et al. 2013; Al-Dirini et al. 2016). Such an inverse calibration allows to obtain more controllable data but would not be possible in a clinical environment, since it requires building a FE model and significant computation time to optimize the parameters.

Chen et al. performed the calibration of the human thigh soft tissues and compared different hyperelastic material models. They concluded that the first-order Ogden and Fung orthotropic materials model the mechanical response of soft tissues significantly better than Neo-Hookean and Mooney-Rivlin (Chen et al. 2020) materials.

One of the clinically relevant simplification possibilities is the use of linear material properties. Linder-Ganz et al. used such elastic material for the simulation of all soft tissues (Eran Linder-Ganz et al. 2009). Bucki et al. made a comparison between the non-linear

Mooney-Rivlin material model with the linear one, concluding that the model with linear material underestimates the internal von Mises stresses with an error that is lower than 5% (Bucki et al. 2012).

One of the parameters that has to be specified for the simulation is Poisson's ratio representing the compressibility of the tissues. Human soft tissue are commonly considered as nearly incompressible, but due to the lack of experimental data, values chosen for different studies varied from 0.4 chosen for the skin (E. Linder-Ganz and Gefen 2004) to 0.4999 chosen for both skin and adipose tissues (Fougeron et al. 2022). The most common value (in 9 out of 25 reviewed articles) chosen for Poisson's ratio was 0.49 for most soft tissues.

In addition to the articles listed in Table 3, a brief review of three main groups of easily attainable alternative testing systems proposed in the literature to assess *in vivo* subject-specific constitutive parameters is proposed below.

The first group of systems is based on the principle of *indentation*. The reaction of the soft tissues to a quasi-static compression is assessed via the analysis of the force-displacement data (Sadler et al. 2018; Pathak et al. 1998; Y. P. Zheng and Mak 1999; Moerman et al. 2013; Bell et al. 2016; Fougeron et al. 2020). The use of the Hertz contact model is one of the widely utilized approaches for extracting stiffness parameters from the acquired indentation data (Y. P. Zheng and Mak 1999; Goh et al. 2005; Y. Zheng and Mak 1999; Mak, Liu, and Lee 1994). The advantage of this approach is that the evaluation of the material properties is done for the tissues under compression, while it could be hard to fully control the boundary conditions. Moreover, inverse methods associated to such indentation measurements usually need to elaborate assumptions about the layered structure of the tissues and the potential interaction between layers.

The second group focused on the *aspiration devices* (Aoki et al. 1997; Kappert et al. 2021; Luboz et al. 2012). After a negative pressure is applied in cup made of a chamber with a cylindrical aperture, the tissue put in contact with the cup is aspired into the chamber. Then an inverse calculation allows the estimation of the apparent Young's modulus based on the applied pressure and the height or the volume of the aspired tissue. The downside of the method is that the evaluation of the tissue properties is mainly performed under tension, while the behaviour of the biological tissues could differ for compression and tension.

Finally, the third group uses the *Shear Wave Elastography* (SWE) for estimating tissue shear modulus. Arda et al. were assessing the stiffness values of liver on healthy volunteers with SWE (Arda et al. 2013). Dubois et al. have proposed a protocol for a non-invasive muscle stiffness assessment with SWE of the muscles of the lower limb (Dubois et al. 2015). It was concluded that SWE provides a reliable information about the relative stiffness of the tissues. However, the absolute values provided by the SWE device are highly dependent on the tissue's fiber orientation, on the tissue viscous behaviour and on the orientation of the US probe during the acquisition (Haen et al. 2017; Vergari et al. 2014).

In addition, a recent article by Scott et al. (Scott et al. 2020) suggested the importance of the effect body position could have on the estimated material properties. In that study, seated, quadruped and prone positions were used to collect data on several regions of human thigh. Results of the study showed that data collected in prone position lead to identification of significantly stiffer material properties than the data collected in other body positions (Scott et al. 2020).

#### *1.2.1.3 Contacts, boundary conditions and loads*

A summary on the contacts and constraints in FE models of the literature is provided in Table 4. In the corresponding articles, where different types of soft tissues were modelled separately and information about their interactions was provided, a tied (no-slip) contact type was assumed in the lack of experimental data. The same is also valid for the interface between bones and soft tissue, except for one article: Al-Dirini et al. assumed a frictional contact with a friction coefficient of 0.3 (Al-Dirini et al. 2016). At the interface between the external support and the skin/soft tissue, a frictional contact was considered with friction coefficients being from 0 to 1 (C. W.J. Oomens et al. 2003), with the most common value of 0.4 (Dabnichki, Crocombe, and Hughes 1994; E. Linder-Ganz and Gefen 2004; Sopher et al. 2010; Al-Dirini et al. 2016; Levy and Gefen 2017; Macron et al. 2018; Zeevi et al. 2018; Levy, Kopplin, and Gefen 2013).

As a boundary condition representing the change from non-weight-bearing position to weight-bearing, a vertical displacement was most often applied to the surface of the modelled bony structure. When the pressure/force was applied to the skin, the bone was fixed. In some cases, a partial body weight was applied to the bone structure. As for the exterior surface of the soft tissues, in most cases (twelve articles) a contact with a supporting surface was established. In several studies, pressure patterns recorded by external sensor mats were applied to the skin surface (Bucki et al. 2012; Luboz et al. 2014b; 2018a; Fougeron et al. 2022).

#### *1.2.1.4 Damage indicator*

FE modelling provides the internal stress-strain field as a response to the external loading. Different parameters were used to relate the mechanical response to tissue damage. Von Mises stress corresponds to the deformation energy accumulated in the material and was used as one of the tissue damage indicators in many studies (Todd, B.; Thacker 1994; C. W.J. Oomens et al. 2003; Lin et al. 2004; E. Linder-Ganz and Gefen 2004; Verver et al. 2004; Makhsous et al. 2007; Eran Linder-Ganz et al. 2007; 2008; Wagnac, Aubin, and Dansereau 2008; Sopher et al. 2010; Bucki et al. 2012; Luboz et al. 2014b; Al-Dirini et al. 2016). Maximum shear strains could be measured directly on MRI and used as a parameter of interest in considerable amount of studies (C. W.J. Oomens et al. 2003; Eran Linder-Ganz et al. 2008; Vogl et al. 2010; Al-Dirini et al. 2016; Moerman et al. 2017; Luboz et al. 2018b; Macron et al. 2018). Ceelen et al. performed a series of experiments with indentation of the tibialis anterior muscle in rats (Ceelen, Stekelenburg, Loerakker, et al. 2008; Ceelen, Stekelenburg, Mulders, et al. 2008). The corresponding FE models demonstrated that when the maximum shear strain threshold of 0.75 in at least one slice was exceeded, the direct deformation damage was measurable using T2-weighted MRI (A. Stekelenburg et al. 2006). However, it was specified that this threshold is not an absolute value but an indication of the threshold existence. It was assumed that a similar process but with different strain threshold values could be observed in humans as well. The relationship between the maximum shear strain and damage was concluded to have an ability of representing the intrinsic muscle properties (Ceelen, Stekelenburg, Mulders, et al. 2008). Another parameter, strain energy density, was used as a damage indicator by Oomens et al. and Sopher et al. and Levy et al. (Sopher et al. 2010; Cees W.J. Oomens et al. 2015; Levy and Gefen 2017).

.

# Chapter I conclusion and the outline of the thesis

Over the past 20 years, research has sought to explain soft tissue injury risk factors in terms of soft tissue strain localization as a potential tool to inform on the risk of deep tissue injuries. However, the results obtained with FE modelling still need to be validated experimentally. Recent MRI investigations focusing on the deformation of the seated buttocks have observed little or no gluteus maximus muscle under the peak of the ischial tuberosity (Sharon Eve Sonenblum et al. 2013; 2015; Call et al. 2017; Sharon E Sonenblum et al. 2018).

These findings suggest that FE models depicting considerable muscle coverage are not consistent with actual anatomy. More importantly, none of the FE models have been validated in terms of strain localization (quantity of interest according to the series of experiments performed at the Eindhoven University of Technology). For the prediction of both superficial and deep tissue injuries, such validation evidences must be obtained prior to any clinical evaluation and rely on the capacity to assess experimental data in the clinical environment. Furthermore, given the large inter-individual and intra-individual loading and anatomic variability, the development of appropriate measurement methods to obtain reliable model input data including accurate description of the material properties, geometrical data, loading characteristics, and boundary and interface interaction conditions is a key challenge.

Personalized numerical modelling could be used as a tool contributing towards the development of the individualized PU prevention protocols. While MRI is considered to be one of the most reliable imaging modalities for collecting soft tissues' geometrical data, it is not necessarily accessible in the clinical environment for prevention purposes. B-mode Ultrasound previously showed promising results in relation with PU (Akins et al. 2016b; Swaine et al. 2018), besides being available in the bedside care, and being time and cost-effective procedure.

However, limitations of the 2D US modality also should be considered. In a recent study, Doridam et al. (Doridam et al. 2018) investigated the feasibility of using B-mode US imaging for the quantification of internal soft-tissue strains of buttock tissues in two perpendicular planes (sagittal and frontal) during sitting. In both planes the authors observed an important displacement of the tissues with their protocol indicating that the displacement field is 3D. As a result, tracking muscle features using 2D image registration techniques in each plane would introduce biases. This is a major limitation for the use of 2D US imaging as practical and clinically relevant alternative to MRI-based assessment of soft tissue motion under mechanical loading.

In addition, according to the literature, maximum shear strain could be related with tissue damage, therefore it will used as one of the main parameters representing tissue state in the following chapters.

Therefore, the main objective of my PhD project was defined as a study of the feasibility of using 2D ultrasound-based FE model for the person-specific sacral PU risk evaluation from the mechanical perspective as an alternative to 3D MRI-based model. To reach this objective, the following outline of the thesis was planned.

The first step was the design of an MRI-compatible experimental setup allowing to load the sacral soft tissues in compression and to experimentally characterize the soft tissue response under increasing loading using both US and MR imaging techniques. This required to accurately control the load amount and direction. In addition, since for US acquisition the

probe was planned be used as an indenter, an MRI-compatible copy of the US probe has to be used for the MRI part.

The second step was to investigate the capacity of a 3D model of the soft tissues of the sacral region to simulate the mechanical response under compression loading. The geometrical model was developed based on the MR data acquisition acquired in the undeformed configuration. A procedure was proposed for the subject-specific estimation of the elastic properties of skin and adipose tissue, data acquired based on the VLASTIC device. To evaluate the reliability of the model, mechanical result of the simulation is compared with the experimental data. This section introduces the Digital Volume Correlation (DVC) technique based on 3D-image non-rigid registration used for model validation.

Then, based on the rationale that US imaging is a promising candidate to substitute MR imaging, a 2D FE model of the sacrum was developed to simulate the mechanical response under compression loading. The proposed methodology was evaluated by comparing the response provided by the proposed 2D FE model to the one predicted by the MRI-based 3D FE model.

Finally, building upon the experimental data collected, the discrepancy between tissue motion assessed using a 2D imaging modality versus tissue motion assessed using a (reference) 3D imaging modality (Magnetic Resonance Imaging) was characterized to inform on the out-of-plane tissue motion under the compressive loading.

# CHAPTER II. Acquisition of the experimental geometry and material data

Building a personalized FE model requires to have subject-specific information about the geometry, the loading/boundary conditions and the constitutive parameters. The current chapter focuses on the experimental data acquisition and includes the work carried out to develop experimental methods to characterize the input data.

The first section synthetizes the morphological characteristics of the volunteer who agreed to participate to our study.

The second section describes the combined US and MRI experiment designed to collect the geometrical data of the sacral tissues. An MRI-compatible setup was designed for this study. It allows for a controlled mechanical loading of the tissues using the same shape of the indenter for both US and MRI acquisitions. The uncertainty of the load was estimated. Different load cases were defined and tested. The associated US and MR images are provided in the results section.

The last section of the current chapter focuses on the experimental evaluation of the elastic properties of the skin and adipose tissues of the participant. Experimental data was collected with a modified version of the VLASTIC device previously developed in (Kappert et al. 2021). This modified version, recently used for breast tissue by Briot et al. (Briot et al. 2022), estimates *in vivo* the linearized Young's moduli for a bi-layer tissue (defined here by skin and adipose tissue). The skin thickness was measured on the B-mode US image and used for the estimation of the linearized Young's moduli for this bi-layer tissue.

## *2.1 Participant*

One healthy male volunteer (34 y.o., 1.75 m and BMI 27.8 kg/m²) was enrolled in the study after informed consent and local ethics committee agreement (MAP-VS protocol N°ID RCB 2012-A00340-43).

## *2.2 Geometrical data acquisition*

### *2.2.1 MR-compatible custom-made indentation setup*

A custom-made MR-compatible setup was designed and assembled with the objective of applying a controlled external compressive force with only one vertical component (i.e. with no shearing component) on the sacrum vertebra. This force was applied to the external surface of the sacral skin via a US probe during the US acquisitions and via a 3D printed replica of this US probe for the MRI acquisitions.

The setup (the reader is referred to Figure 8 for a sketch and to Figure 9 for pictures of this setup) was built from a rigid plastic tube structure holding an indenter. For the US imaging experiment, an SL10-2 linear probe transducer developed by (Aixplorer, SuperSonic Imagine, France) was used as the indenter. For the MR imaging, a 3D printed replica of this probe was used as an indenter, built from a Raise3D Pro2 printer with a Premium PLA Filament of diameter 1.75 mm (Figure 9c). The connection between the indenter and the tube structure allowed setting and fixing its orientation. To track the orientation of the US plane during the MRI experiment, a cylindrical reflective marker (Figure 9e) was glued on the side of the indenter oriented towards the head of the participant.

The second sacral vertebra (S2) was loaded with the indenter by adding dead weights (plexiglass plates shown in Figure 8 as J and K) to the structure. The maximum load applied by the setup was determined in accordance to the literature. In the study of (Sheerin and de Frein 2007), the authors reported that pressures measured at the sacral region could reach values as high as 154 mmHg when the head was immobilized and spider strapping was used on an unpadded spinal board. Multiplied by the surface area of the 10-2 linear probe transducer used in this study (410 mm2), this results in a force of approximately 9 N. A preliminary test was then performed to evaluate the maximum load the subject could tolerate. Based on this test, a maximum load of 12 N was set for the experiment. This load was applied in 4 loading steps of 200 g or 400 g each resulting in various loads in the range 0-1200 [g] (Table 5).

A schematic representation of the proposed setup with additional details is provided in Figure 8.

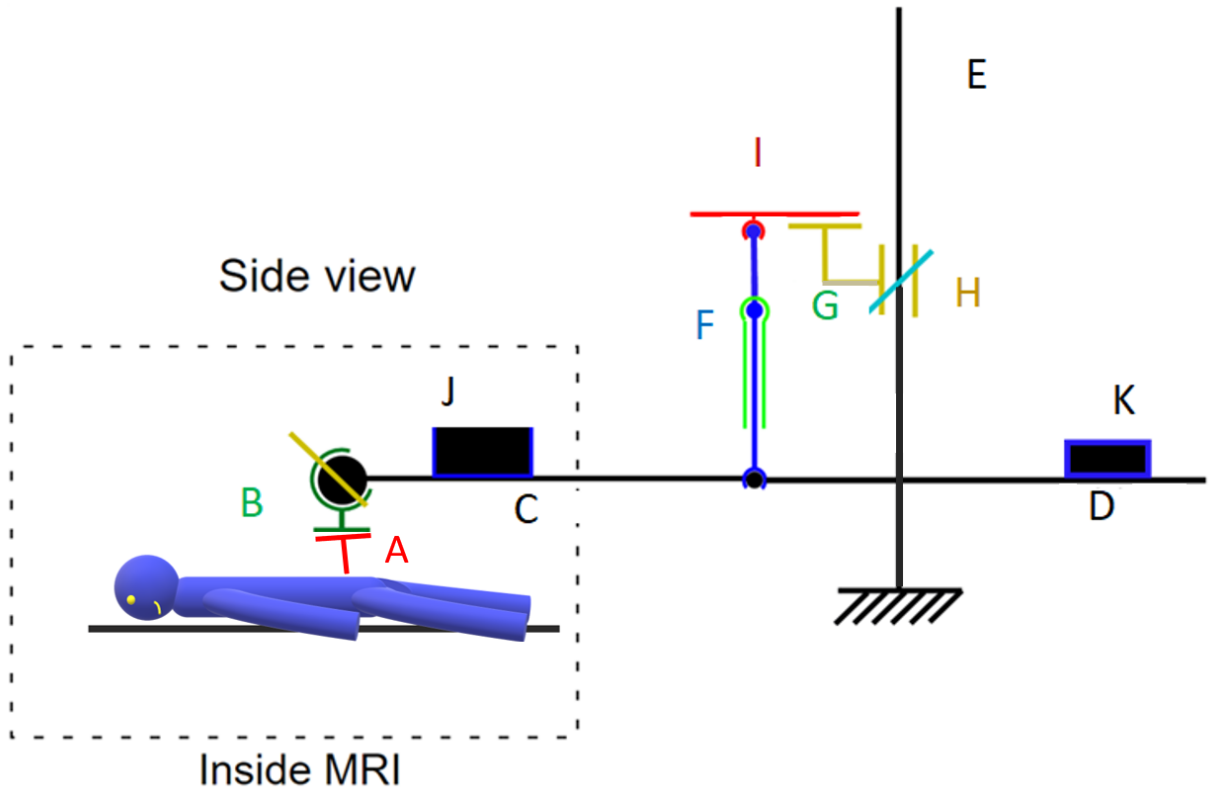


Figure 8: The contact area A indenter/body located at the region of the sacrum with the participant being in a prone position. Clamp B holds the indenter, allowing the adjustment of its orientation to keep it perpendicular to sacrum skin surface. It was positioned close to the left end of the system of rigid tubes (C and D) which were supported by the MR-compatible stand E, also made from rigid tubes. Tube system C was built long enough to allow the positioning of the supported indenter inside the MR scanner. To keep the vertical load translation from the setup to the body, the horizontality check of the system of tubes close to the indenter was performed. For the same purpose, the verticality check of two wires F holding the tube system C was performed using the glass tubes G attached to them. The supporting plates H, where the wire support I was positioned, allowed the vertical adjustment on the stand as a way to control the horizontality of the tube system. The loading mass J, adjusted for each load case, was positioned close to the indenter to stabilize the load. The

counterweight K was positioned on the far end from the indenter to reduce the setup self-weight for the loading step 4.

### *2.2.2 Data acquisition*

Seven sets of US acquisitions were performed in five loaded configurations (L1-L5), each set was obtained in decreasing order of loads from 1.2 kg to 200 g by steps of 200 g or 400 g. 3D MRI acquisitions were performed at the IRMaGe research platform (Univ. Grenoble Alpes) in 5 configurations: one unloaded and 4 loaded (L0-L4) in decreasing order of loads from 1.2 kg to 400 g by steps of 200 g or 400 g (Figure 9 b, d). A summary of the loads applied is given in Table 5 below.

Prior to the experiment, the uncertainties of the loads applied with the dead weights were assessed by repeating 4 times the previously defined loading scenario and measuring the load with a scale (B3C Sérénite 9260(A), uncertainty of 0.1 g). The results are reported as mean +/- 1 SD in Table 5.

The participant was instructed to lie in a prone position in a 3 Tesla Achieva 3.0T dStream Philips scanner (Figure 9 b). No mattress was used during the MRI acquisitions to allow enough space for the loading part of the setup. A soft material was put below the thoracic cage and abdomen so the skin above the first sacral vertebrae was visually horizontal.

For each load case, an MRI volume was acquired. A 3D proton density sequence was used with the following parameters: 399.5x399.5x119.5 $mm^3$ field of view and isotropic voxel size of 0.5x0.5x0.5 $mm^3$. Two surface body coils were placed on either side of the pelvis in the medio-lateral direction (red arrows on Figure 9 b) to increase the signal-to-noise ratio. The acquisition duration time was approximately 10 minutes per MRI scan. Due to limited time allowed in the MRI scanner, approximately 5 minutes were left between acquisitions in order to change the load. Participant was asked to not change body position between the acquisitions. To account for breathing, a gating technique was used.

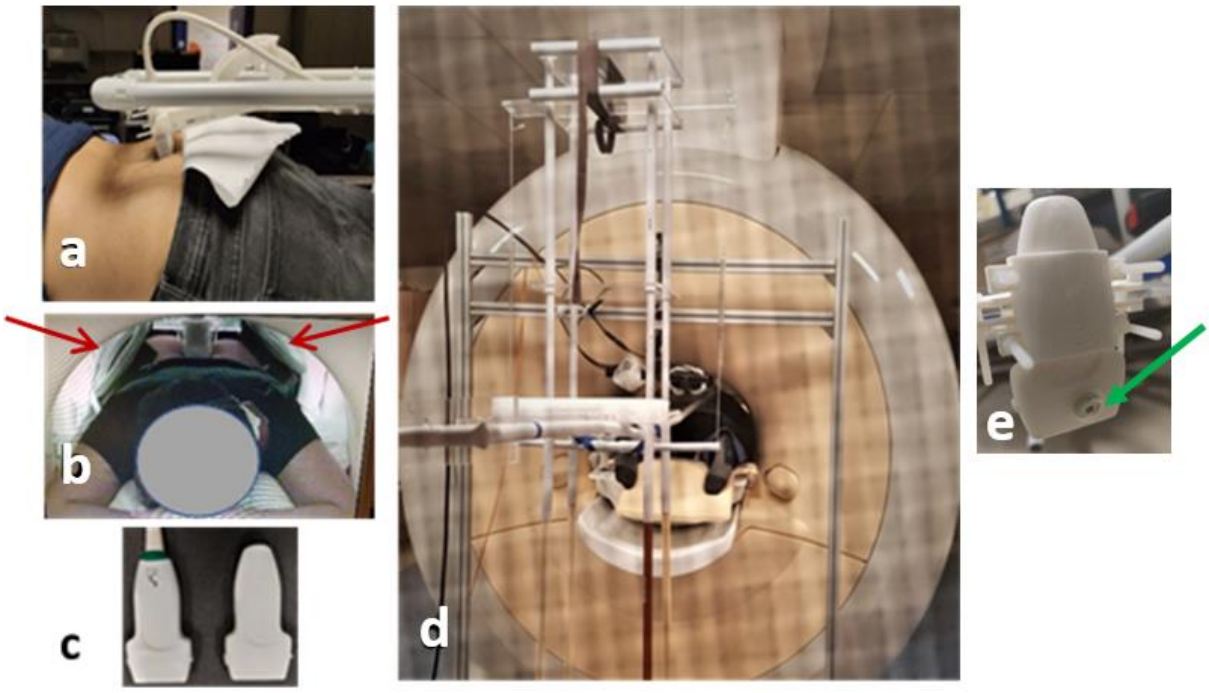

Figure 9: a) Ultrasound acquisition with the a SL10-2 linear probe transducer acting as an indenter. b) Participant lying in the MR scanner with two surface body coils (red arrows) placed on either side of the pelvis; c) Real US probe (left) and associated 3D-printed replica (right); d) Rear side of the MR scanner showing the rest of the setup and the participant lying in the scanner; e) Green arrow showing the cylindrical reflective marker attached to the 3D-printed indenter.

### *2.2.3 Acquired data*

#### *2.2.3.1 Loading uncertainty*

The results of the load reproducibility evaluation performed for five out of six load cases (L1-L5) are given in Table 5 below. Load case 0 corresponds to no load applied, therefore it was excluded from the reproducibility test.

Table 5 Load case reproducibility evaluation

| Load case | Mean, [g] | Standard deviation (SD), [g] | Mean, [N] |
|---|---|---|---|
| L0 | 0 | - | 0 |
| L1 | 1216 | 2 | 11.9 |
| L2 | 812 | 2 | 8 |
| L3 | 626 | 2 | 6.1 |
| L4 | 439 | 2 | 4.3 |
| L5 | 252 | 2 | 2.5 |

#### *2.2.3.2 Data collection results*

US images for the corresponding load cases are shown on Figure 10.

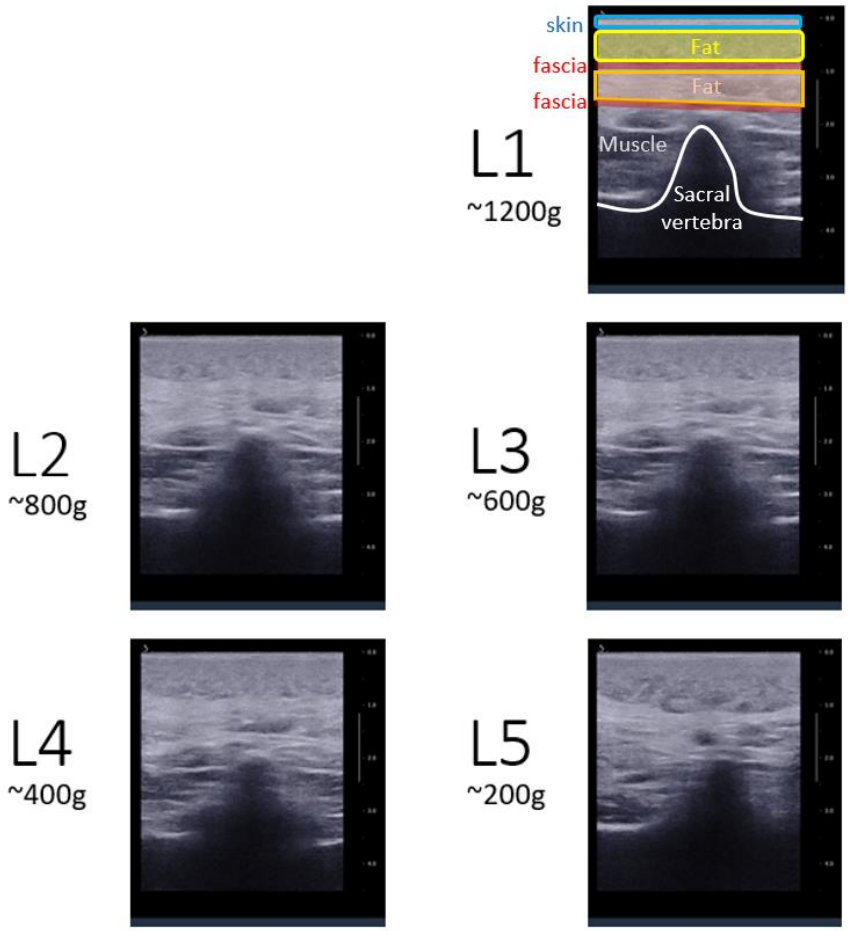


Figure 10: Ultrasound images of five load cases (L1, L2, L3, L4 and L5)

The MR images of the four loaded and one unloaded configuration (L1 - L4 and L0) were analyzed. A single transverse slice of the MR volume of each configuration in the plane containing the indentation mark left by the 3D-printed indenter is given in Figure 11 below.

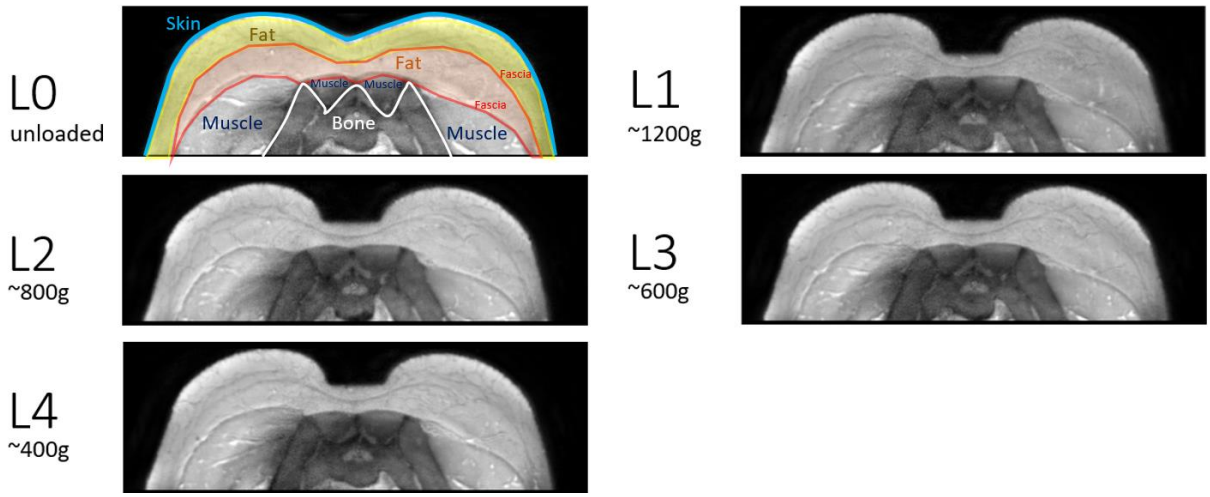


Figure 11: Transverse slices of the five load cases (L0, L1, L2, L3, L4) at the region of indentation.

## *2.3 Material parameters acquisition*

The objective of this section was to build upon new and unique opportunities offered by the Volume-based Light Aspiration device for *in vivo* Soft TIssue Characterization (VLASTIC (Kappert et al. 2021)) for the identification of the passive material properties of some sacral soft tissues (skin and fat). These values are intended to be used as input data for modelling these soft tissues in a FE model of the sacral region. This work has been performed as part of a broader work aiming at comparing the skin and adipose tissue stiffness (assumption of linear elastic constitutive behaviour) assessed experimentally *in vivo* using the VLASTIC against those estimated using Shear Wave Elastography. For a detailed report on that study, the reader is referred to **APPENDIX 1**. A shortened version, limited to the results obtained with VLASTIC acquisition on the participant, will be presented in this section.

### *2.3.1 VLASTIC setup*

A scheme of the aspiration device is shown in Figure 12. The principle is the following: A 3D printed semi-spherical cup with a circular aperture is positioned on the skin surface and a negative pressure is cyclically applied to the skin and the underlying adipose tissues. A programmable syringe pump (pump 11 elite, Harvard Apparatus, Holliston USA) is used to remove the air volume from the system at a controlled rate. From the pressure/volume curves, both Young moduli of the skin and the adipose tissue are estimated thanks to a FE inverse analysis (Elahi, Connesson, and Payan 2018). Experiment is limited to small strains and acquisitions are performed with nine different cup diameters of 4, 6, 8, 10, 12.5, 15, 20, 25, and 30 mm.

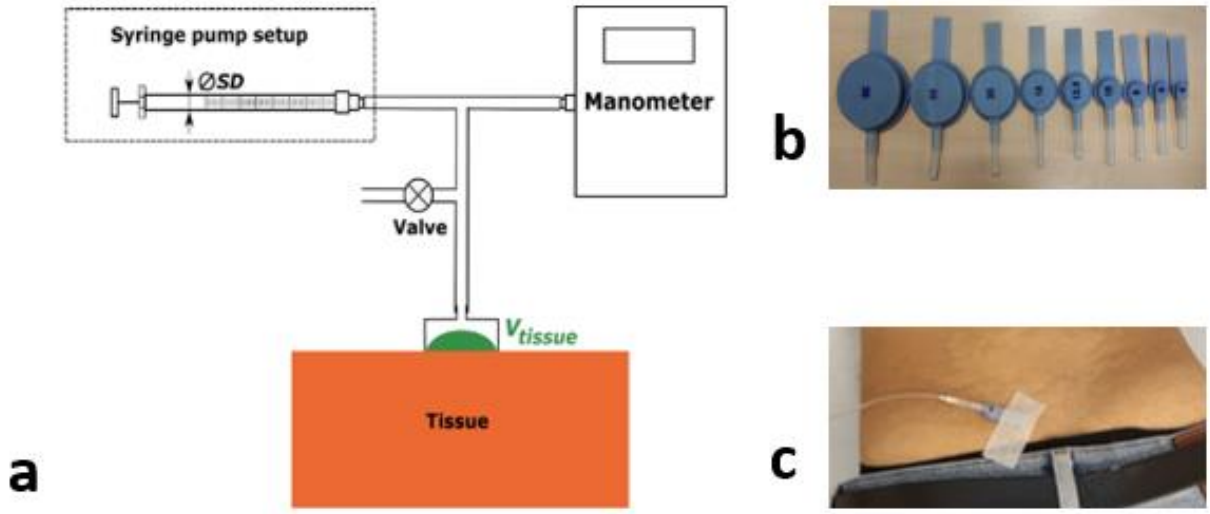


Figure 12: a) Scheme of the aspiration setup adapted from (Kappert et al. 2021). b) Nine cups of different diameters were used c) Cup positioned on the sacral region of the participant.

### *2.3.2 Data acquisition*

The participant was instructed to lie prone in a comfortable position. The cup was positioned on the upper left side from the medial sacral crest (Figure 12, c) on the relatively flat surface. The corresponding region of interest (ROI) was marked for further acquisitions. US gel was put on the edge of the cup to insure contact with the skin and to prevent pressure air leakage. Four cyclic pressurization/depressurization were applied for each acquisition. Nine acquisitions with each of the cups were collected. Measurements were repeated three times to

evaluate the uncertainties. Between each acquisition, the cup was taken off the skin, the excess of the gel was removed and the cup was repositioned once again at the same location.

An additional image of undeformed tissues in B-mode was taken using the 18 MHz linear probe of the Aixplorer system (Supersonic Imagine, Aix-en-Provence, France) for the assessment of skin thickness. For this purpose, a thick layer of US gel was put on the ROI to allow the measurements of the unloaded tissues; it was assumed here that no pressure was applied by the US probe. The probe was held manually and positioned perpendicular to the spine at approximately 90 degrees to the skin surface.

### *2.3.3 Acquired data*

In total, 36 pressure-volume experimental curves (4 cycles x 9 cup size) were acquired with the aspiration device.

Additionally, the skin thickness is measured directly on the B-mode US images of the undeformed tissues resulting in 2.9 mm. Figure 13 shows the measurement of the skin thickness (the red line) on the US image.

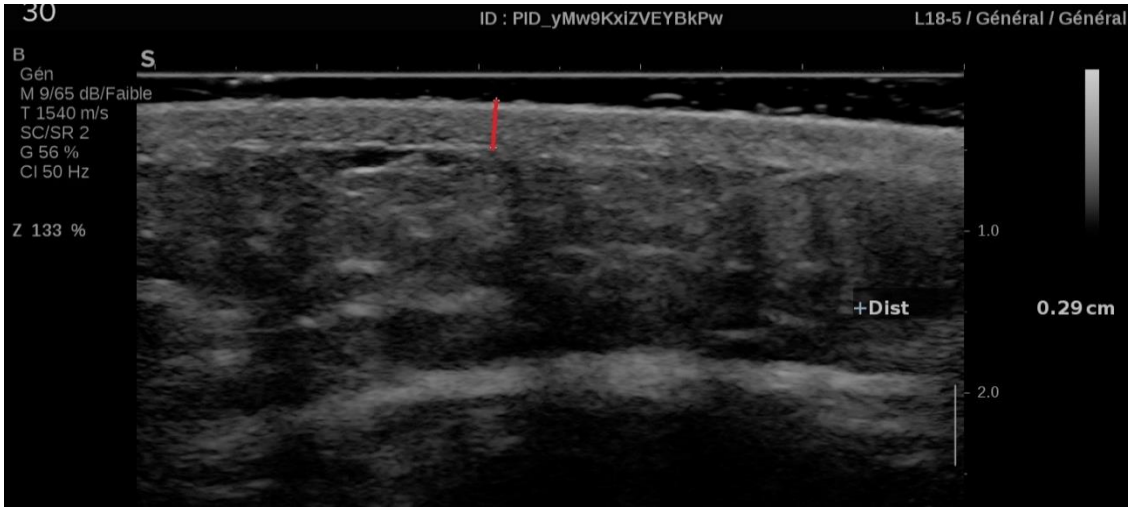


Figure 13: B-mode US image of the soft tissues at the sacral region with the measured skin thickness (in red)

# Chapter II conclusion

This chapter focused on the detailed description of the experimental protocol proposed in this PhD as well as data that were correspondingly collected. Subject-specific information about the geometry, the loading/boundary conditions and the constitutive parameters of the participant were therefore collected and will feed the 2D and 3D models (**chapters IV** and **III** respectively).

First, a custom-made MRI-compatible experimental setup allowing controlled loading of the sacral soft tissues in both US and MRI settings was presented. Two sets of data were collected with this setup: US images in five loaded configurations and MR images in, respectively, four loaded and one unloaded configuration. In both settings, the loads were applied in a descending order from the highest load to the lowest one. The unloaded MRI configuration was collected prior to the loaded ones. Posteriorly, data analysis has shown an important effect of the soft tissues' viscoelasticity on the acquisition results, with tissues requiring a long time to return to their initial shapes. Therefore, as a perspective work, it would probably be beneficial to repeat the data collection in the increasing order of the load, from the lowest to the highest load.

With respect to the literature focusing on pressure ulcer prevention, this work constitutes, to the best of our knowledge, the first attempt to collect imaging data under controlled loading conditions in the sacral region, and for different loading configurations. This is an important contribution because FE models developed in the literature are rarely evaluated against experimental data. The data collected in this chapter also opens the way to investigate the relevance of 2D US-based measurements for pressure ulcer risk assessment.

# CHAPTER III. Sacral PU risk assessment based on 3D FE model

To assess the mechanical state of internal soft tissues under external mechanical loading, FEA is commonly used and, as shown in the literature review presented in **chapter I**, MRI is often considered as a gold standard imaging modality for acquiring personalized 3D data.

The current chapter focuses on the development and the evaluation of a 3D model of the soft tissues of the sacral region based on the experimental data acquired in **chapter II**, to simulate the mechanical response under compression loading.

The first section presents the modelling assumptions and methodology proposed for preparing FE model. First, the preparation of the geometrical model is presented. The assumption made for the composition of the tissues of interest and their segmentation is presented. Second, the choice of material properties assumed for soft tissues is presented. We chose to adapt the constitutive laws of such tissues from various articles containing experimental data. An optimization method based on curve fitting was used on skin, adipose and muscle experimental data to identify the material parameters, assuming a Yeoh constitutive law. To propose subject-specific estimations of the elastic properties of skin and adipose tissue, data acquired with the VLASTIC device were used to adapt the previously fitted Yeoh material models. Third, the implementation of the boundary conditions and external loading is presented. Finally, a mesh sensitivity test was performed for one mechanical parameter.

Section two lists post-processing steps and introduces parameters of interest. As emphasized before, an important step of FE modelling is model evaluation. To evaluate the reliability of the model, mechanical result of the simulation is compared with the experimental data. This section introduces the Digital Volume Correlation (DVC) technique based on 3D-image non-rigid registration used for model validation.

Section three of current chapter lists results obtained with image registration for each of the four load cases putting in correspondence undeformed MR image and deformed one for each load case. Finally, a comparison is provided between the displacement and shear strain fields obtained with image registration and the ones that are yielded from ANSYS simulations.

## *3.1 Preparation of the 3D FE Model*

### *3.1.1 Personalized geometrical model*

The MR image recorded previously in the undeformed configuration (without any load applied by our experimental setup) was used for the 3D model. Manual segmentation of fat, fascia, muscles and bone tissues were performed with Amira 2019.1 software. The region of interest (ROI) for 3D modelling in relation to a full medical image is shown in (Figure 14, a). The corresponding segmented volume containing two layers of adipose tissue (separated by a fascia) and muscles is shown in (Figure 14, b). Skin and fasciae are represented as shell elements based on the surfaces delimiting the segmented tissues. Two layers of fascia were modeled: the superficial fascia separating the two layers of adipose tissues and the deep fascia located between adipose tissue and muscle.

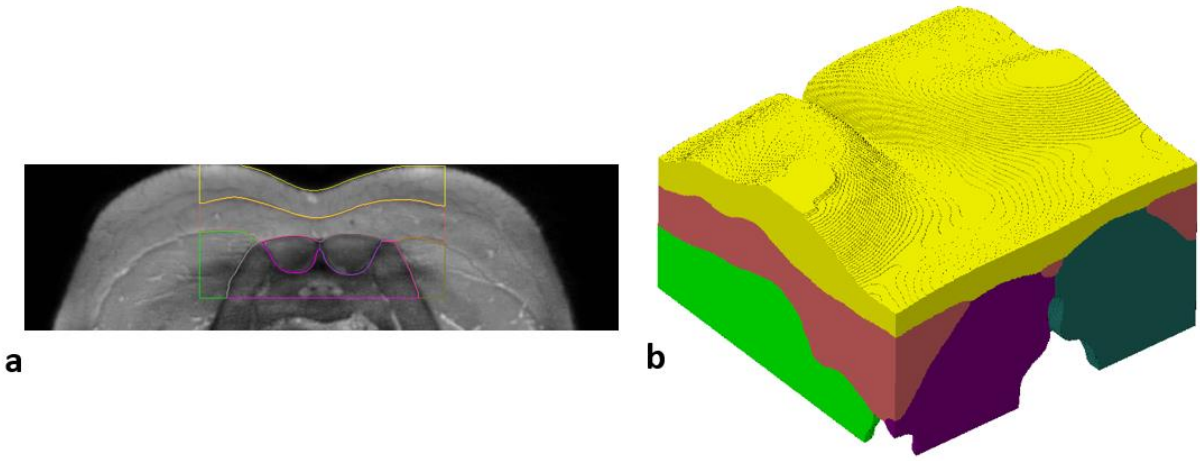


Figure 14: Segmented MR image. a) Transverse slice showing segmented volumes: superficial and deep adipose layers; right and left gluteus maximus muscles; right and left erector spinae muscles; contour of the bones. b) Volume of the segmented tissues shown in 3D

### *3.1.2 Constitutive modelling and calibration*

A hyperelastic Yeoh constitutive law was previously used in the literature (Fougeron et al. 2022) to represent soft tissues; therefore, it is chosen for skin, adipose tissue, fascia and muscle. This law assumes a strain-energy function $W$ given by the following analytical expression ( 1 ):

$$W = C_{10}(\overline{I_1} - 3) + C_{20}(\overline{I_1} - 3)^2 + C_{30}(\overline{I_1} - 3)^3 + \frac{1}{d_1}(J-1)^2 + \frac{1}{d_2}(J-1)^4 + \frac{1}{d_3}(J-1)^6 \quad (1)$$

where $\overline{I_1}$ is the first invariant of the left Cauchy-Green deformation tensor, $C_i$ are material parameters, $J$ is the determinant of the deformation gradient $\underline{\underline{F}}$, while $d_i$ are material parameters related to compressibility. These $d_i$ parameters are assumed to be equal and related to the Poisson ratio $\nu$ (Mott, Dorgan, and Roland 2008) ( 2 ):

$$\mathrm{d_1} = \mathrm{d_2} = \mathrm{d_3} = \frac{3 * (1 - 2 * \nu)}{2\mathrm{C_{10}} * (1 + \nu)} \quad (2)$$

To represent the near-incompressible behaviour of soft tissues, Poisson ratio is chosen to be 0.49: based on the literature review from **chapter I** this is indeed the value most commonly chosen in previous models (in 9 out of 25 reviewed articles related to FE models of the buttock region, for details please refer to Table 3).

As presented in subsection 3.1.2.1, as a first approximation, generic values for the $C_i$ material parameters representing skin, adipose tissue, fascia and muscle were computed using an optimized curve fitting procedure based on tension and compression experimental tests published in the literature (Ní Annaidh et al. 2012; Miller-Young, Duncan, and Baroud 2002; Gras et al. 2012; Astruc et al. 2018). In a second step (subsection 3.1.2.2), subject-specific tuning of the material parameter based on VLASTIC data is proposed.

### *3.1.2.1 Generic material parameters estimated from data reported in the literature*

#### *a) Skin*

Annaidh and colleagues provided data from the uniaxial tensile test performed on the skin sample harvested from the region of the sacrum (Annaidh et al. 2012). The corresponding stretch/stress curve (Figure 15, blue circle points) was used to fit the Yeoh constitutive parameters (Figure 15, blue line; (Fougeron et al. 2022)). A fitting is obtained with two coefficients only, namely C10=0.3 MPa and C20=1.9 MPa. Subject-specific tuning of the obtained for skin material model by updating C10 parameter according to VLASTIC aspiration measurements is detailed in the next section 3.1.2.2 (Figure 15, red line).

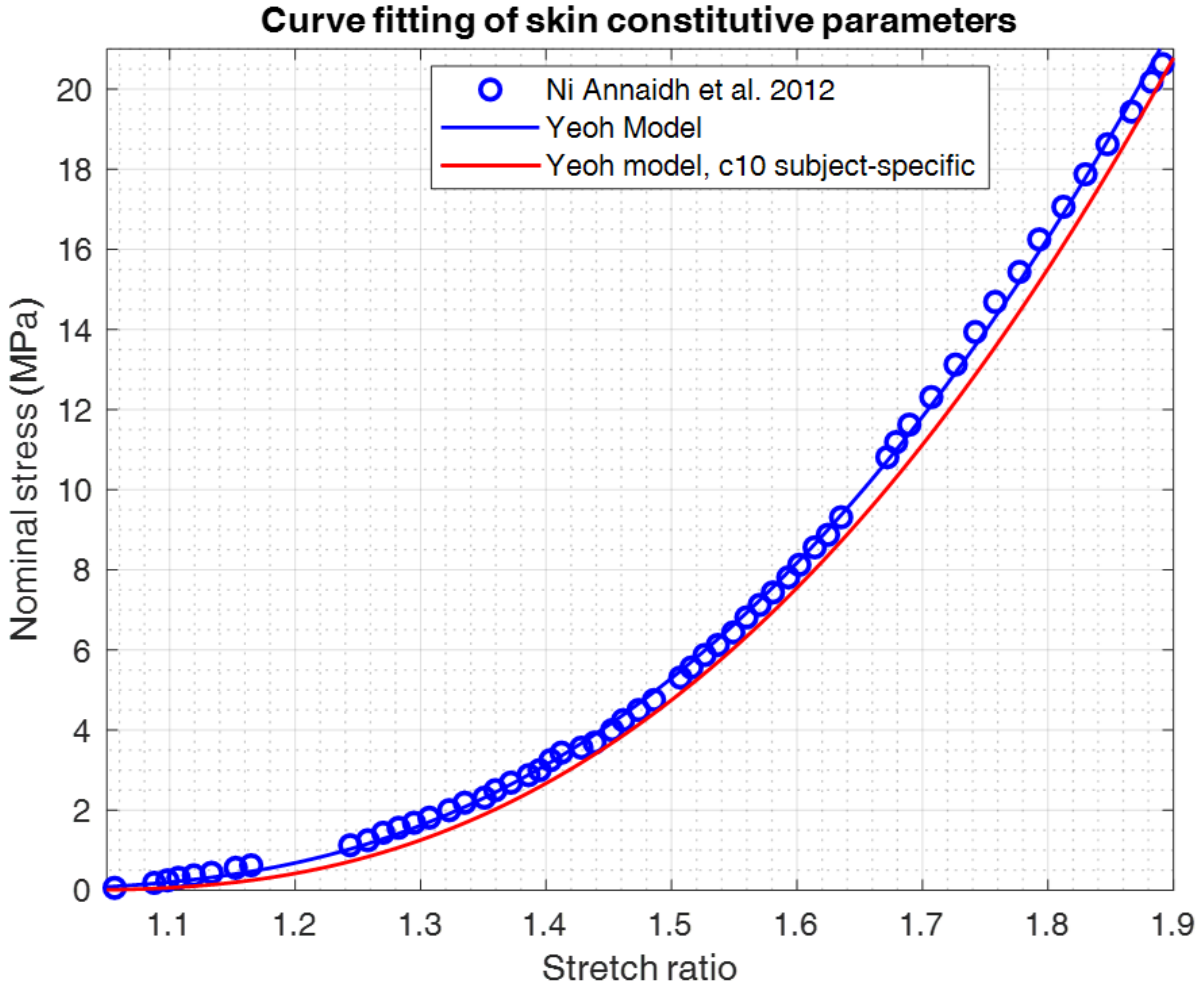


Figure 15: Skin stretch/stress experimental data after uniaxial tension (blue circles) fitted by a Yeoh constitutive model (blue curve). The red curve corresponds to the subject-specific update of the $C_{10}$ parameter after VLASTIC aspiration measurements.

***b) Adipose tissue***

Miller-Young and colleagues provided the data from unconfined compression tests performed on adipose tissue sample harvested from the heel fat pad (Miller-Young, Duncan, and Baroud 2002). The corresponding stretch/stress curve (Figure 16, blue circle points) was used to fit the Yeoh constitutive parameters (Figure 16, blue line). As for the skin, a fitting is obtained with two coefficients only, namely C10=0.7 kPa and C20=0.3 kPa. Subject-specific tuning of the obtained for adipose tissue material model by updating C10 parameter according to VLASTIC aspiration measurements is detailed in the next section 3.1.2.2 (Figure 16, red line).

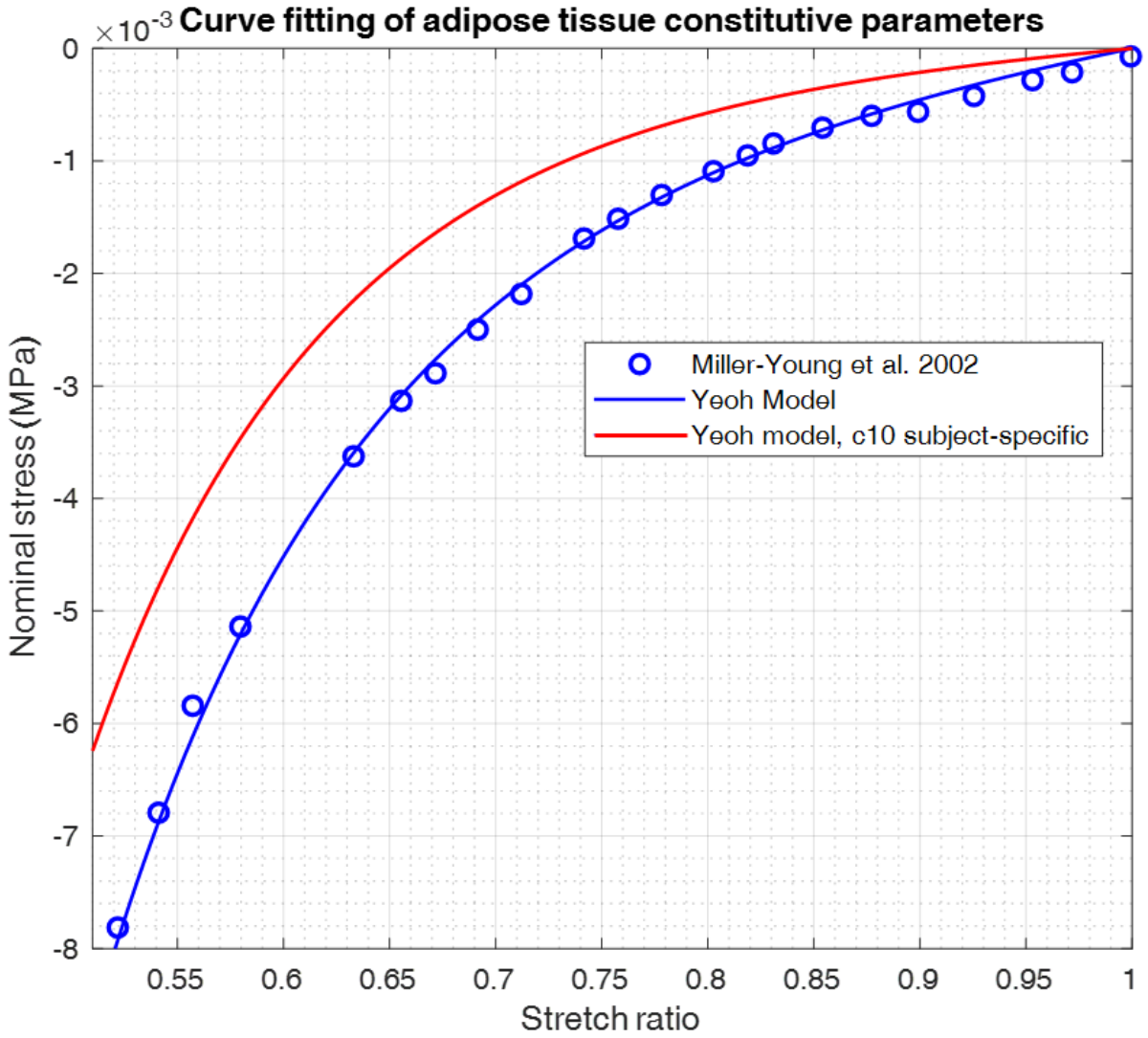


Figure 16: Adipose tissue stretch/stress experimental data after compression (blue circles) fitted by a Yeoh constitutive model (blue curve). The red curve corresponds to the subject-specific update of the $C_{10}$ parameter after VLASTIC aspiration measurements.

***c) Muscle***

Gras and colleagues performed uniaxial tensile test on a harvested sternocleidomastoideus muscle (Gras et al. 2012). The corresponding stretch/stress curve (Figure 17, blue circle points) was used to fit the Yeoh constitutive parameters (Figure 17, blue line). In that case, three coefficients are required to fit the curve, namely $C_{10}$=5e-3 MPa, $C_{20}$=6.9e-2 MPa and $C_{30}$=1.97 MPa.

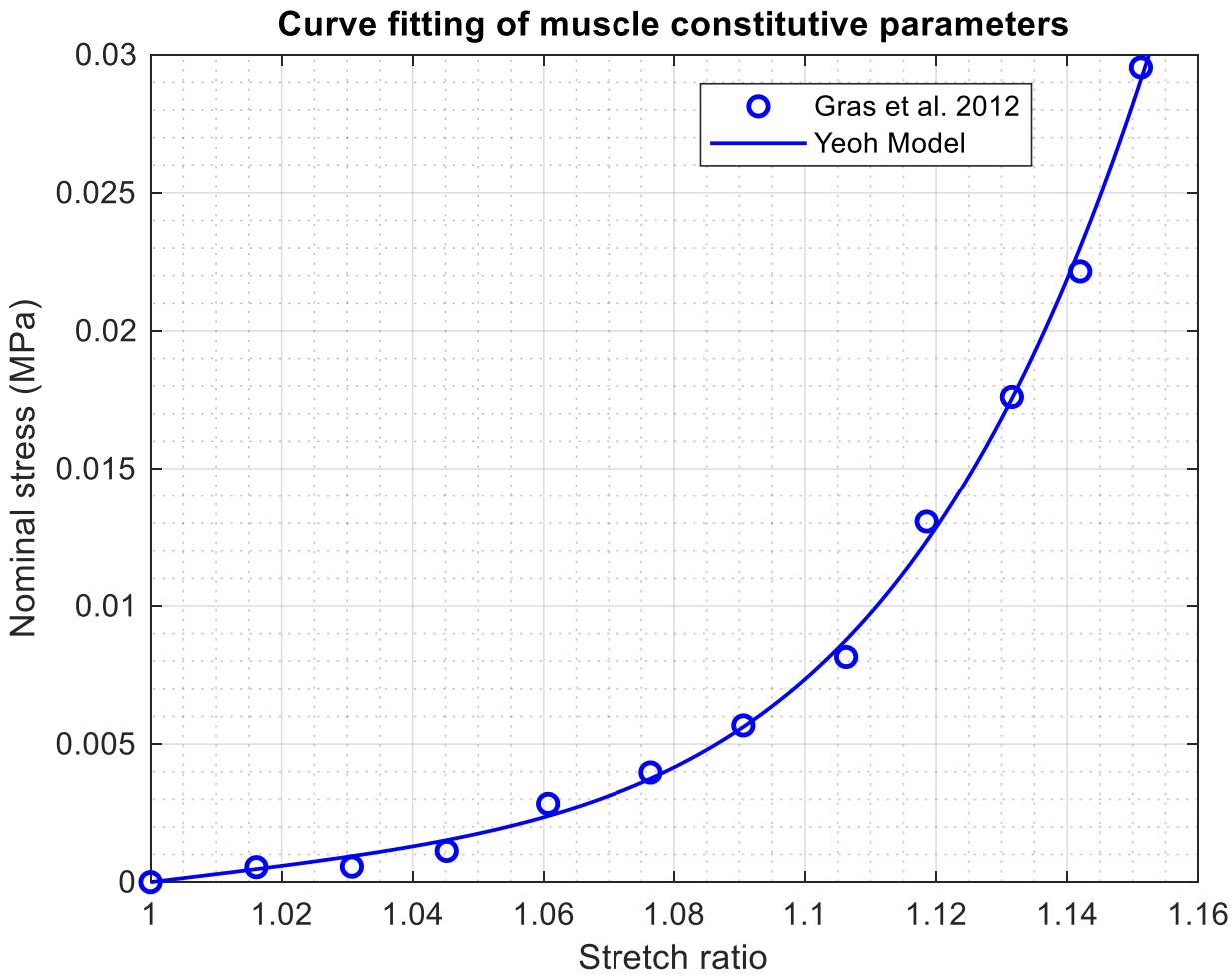


Figure 17: Curve fitting of muscle constitutive parameters presenting experimental data and fitted Yeoh model.

***d) Fascia***

Fascia constitutive parameters ($C_{10}$=0.1 MPa, $C_{20}$=0.18 MPa) are assumed from the experimental data that was collected and fitted by Astruc and colleagues (Astruc et al. 2018), from uniaxial tensile tests performed on the longitudinal sample harvested from posterior rectus sheath in the abdominal wall.

### *3.1.2.2 Subject-specific tuning of the material parameter based on VLASTIC data*

To the best of our knowledge, there is no valid methodology for the *in vivo* characterization of the non-linear hyperelastic behaviour of human soft tissues. However, the VLASTIC device can be used to estimate the linear part of the stretch/stress curves, at small strains levels. Moreover, as proposed in Briot et al. (Briot et al. 2022) for breast tissue, both skin and fat

stiffness can be estimated from local aspiration if a bi-layer structure is assumed for skin and adipose tissue. Equivalent Young moduli of both layers are therefore estimated based on repeating low intensity aspiration tests using cups of various diameters. An inverse procedure based on a bi-layer FE model representing the aspiration test was employed to estimate the equivalent Young moduli. The optimization cost function is defined as a least square of the offset between the numerical and experimental results. Thickness of the top layer (skin) of the FE model is imposed based on the pre-measured values from the US B-mode images. Equivalent Young moduli of the skin and the adipose tissue (respectively $E_s$ and $E_F$) identified from the 36 pressure-volume experimental curves (4 cycles x 9 cup size) are provided in Table 6 for three successive acquisitions (with the imposed pre-measured skin thickness of 2.9 mm). Ratios of the moduli $E_s/E_F$ for each acquisition are provided in the last column of Table 6. The average skin Young modulus is 37.7 kPa while for the adipose tissue average value is 1.8 kPa. The average ratio between skin and adipose values is 20.6.

Table 6: Resultant Young's moduli evaluated with the aspiration device for the skin and adipose tissues and the ratio between them. Imposed skin thickness measured with US

| Acquisition | Young's modulus, skin [kPa] | Young's modulus, adipose tissue [kPa] | Ratio |
|---|---|---|---|
| 1 | 35.1 | 1.9 | 18.5 |
| 2 | 40.7 | 1.8 | 22.6 |
| 3 | 37.2 | 1.8 | 20.7 |
| Mean | 37.7 | 1.8 | 20.6 |

In the case where the material can be assumed to be quasi-incompressible, which is mostly the case here since human soft tissue are mainly composed of water (see the 0.49 value chosen for the Poisson ratio), a direct relationship can be provided between the equivalent Young modulus and the first material parameter $C_{10}$ ( 3 ):

$$c_{10} = \frac{E}{6} \qquad (3)$$

The generic $C_{10}$ constitutive parameters of skin and adipose tissue as estimated above from the curve fitting process respectively conducted on the experimental data of Ni Annaidh et al. (Ní Annaidh et al. 2012) and Miller-Young et al. (Miller-Young, Duncan, and Baroud 2002), were therefore changed to the values provided by the *in vivo* aspiration measure, in line with ( 3 ), namely $C_{10Skin}$=37.7/6=6.3 kPa and $C_{10Fat}$=1.8/6=0.3 kPa. The corresponding changes have a consequence on the stretch/stress curve for skin an adipose tissue. The subject-specific new curves are drawn in red in Figure 15 and Figure 16 respectively.

Table 7 synthetizes all the values for the constitutive parameters that are finally implemented in our subject-specific FE model. Skin, adipose tissue and fascia are represented by 2$^{nd}$ order Yeoh model, therefore, four parameters are listed, while muscle tissue is represented by 3$^{rd}$ order Yeoh model, therefore, six parameters are shown in Table 7.

Table 7: Soft tissues material parameters implemented in the FE model

| | $c_{10}$, [MPa] | $c_{20}$, [MPa] | $c_{30}$, [MPa] | $d_1$, [$MPa^{-1}$] | $d_2$, [$MPa^{-1}$] | $d_3$, [$MPa^{-1}$] |
|---|---|---|---|---|---|---|
| Skin | 6.3e-3 | 1.9 | - | 3.2 | 3.2 | - |
| Adipose tissue | 0.3e-3 | 0.3e-3 | - | 66.16 | 66.16 | - |
| Fascia | 0.1 | 0.18 | - | 0.2 | 0.2 | - |
| Muscle | 5e-3 | 6.9e-2 | 1.97 | 4.03 | 4.03 | 4.03 |

#### *3.1.2.3 Material parameters of the indenter*

To simulate the indentation forces exerted on the sacrum, the indenter is modeled with a linear elastic model assuming a Young modulus of 200 GPa and a Poisson ratio of 0.3 (for simplification purpose, stainless steel grade 405 UNS S40500 material properties are used to model the indenter).

### *3.1.3 External mechanical loading*

The vertical load of 11.9 N, 8 N, 6.1 N and 4.3 N was imposed through the indenter by adding dead-weights to the experimental setup.

### *3.1.4 FE discretization and contact modelling*

The FE mesh was created with Hypermesh software, from the 3D surfaces extracted after the segmentation of the MR volume, and imported into ANSYS Mechanical APDL. Linear tetrahedral SOLID185 elements are used for adipose tissue and muscles, while skin and fasciae are approximated by shell elements SHELL181 with thickness of 2.9 mm and 0.5 mm respectively. Bending is restricted for the shell elements leaving only the membrane properties for element stiffness.

The surface of the sacral bone in contact with muscles and adipose tissues is fixed for all DOFs. Contact nodes between two types of soft tissues (for example between muscle and fat) are merged to avoid any complex sliding contacts between two tissue layers. A contact pair with frictionless standard behaviour of the contact surface and with finite sliding is defined between the indenter and the skin.

One node on the top of the indenter was chosen as a pilot node (Figure 18 presents the boundary conditions applied to the indenter and to the sacral bone) for load application. A quasi-static analysis was run with two load steps, with displacement and load being applied to a pilot node: $1^{st}$ - displacement until the contact, $2^{nd}$ - load of 11.9 N for the model of Load case 1 (L1); 8 N for the model of Load case 2 (L2); 6.1 N for the model of Load case 3 (L3) and 4.3 N for the model of Load case 4 (L4); see Table 5, **chapter II**.

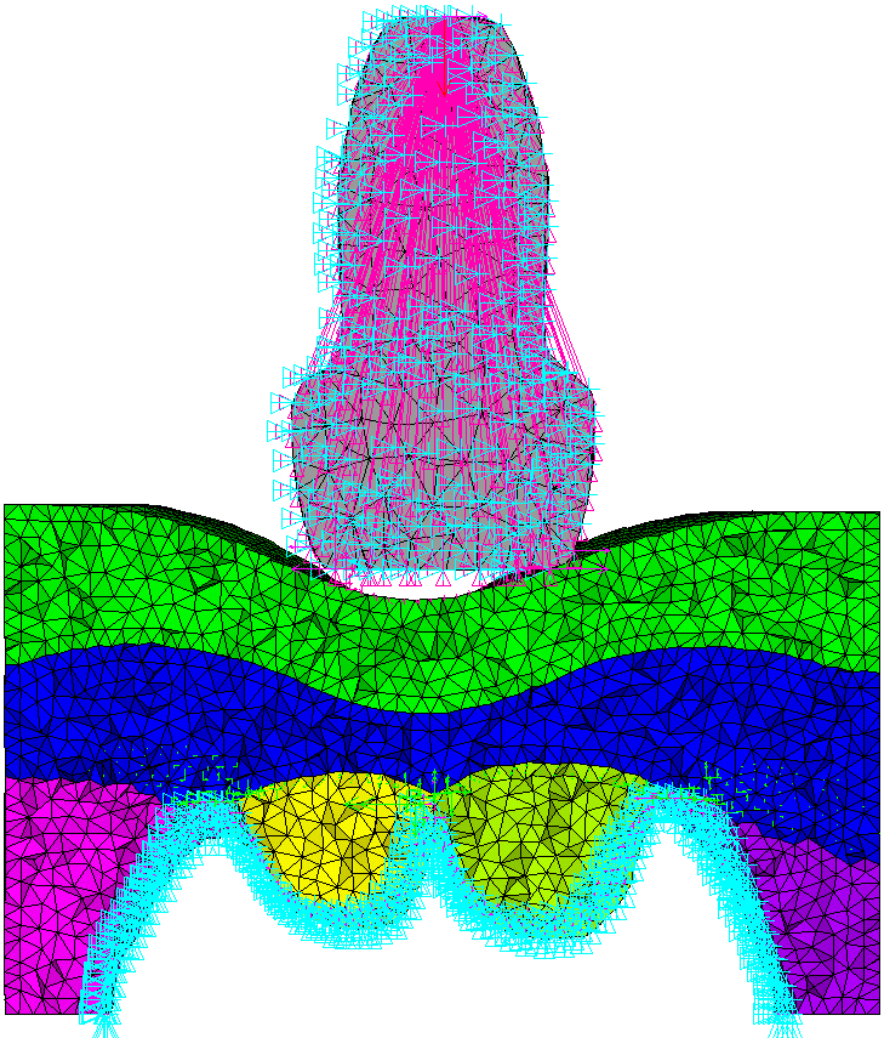

Figure 18: Boundary conditions shown on a transverse cut through the FE model

### *3.1.5 Mesh sensitivity*

To study mesh convergence, a sensitivity analysis using five models with different mesh sizes was conducted. Table 8 and Figure 19 provide the vertical displacements of the indenter when subjected to a 11.9 N load, for each of the five models; the displacement value was assessed as an absolute maximum value in the same slice for each model passing through the centre of indentation mark. As can be observed on Figure 19, a convergence is observed when the number of nodes increases.

Table 8: Synthesis of tested mesh sizes

| | | 3D tetra elements | | 2D shell elements | | |
|---|---|---|---|---|---|---|
| Model | Element size, [mm] | Number of nodes | Number of elements | Number of nodes | Number of elements | Max $D_z$, [mm] |
| M1 | 6 | 11164 | 43953 | 3988 | 7463 | 14.2 |
| M2 | 5 | 17777 | 73744 | 5761 | 10913 | 14.9 |
| M3 | 4 | 31320 | 138612 | 8814 | 16871 | 15.4 |
| M4 | 3 | 66464 | 315619 | 15610 | 30210 | 16.2 |
| M5 | 1.5 | 435424 | 2345687 | 61889 | 121757 | 17.4 |

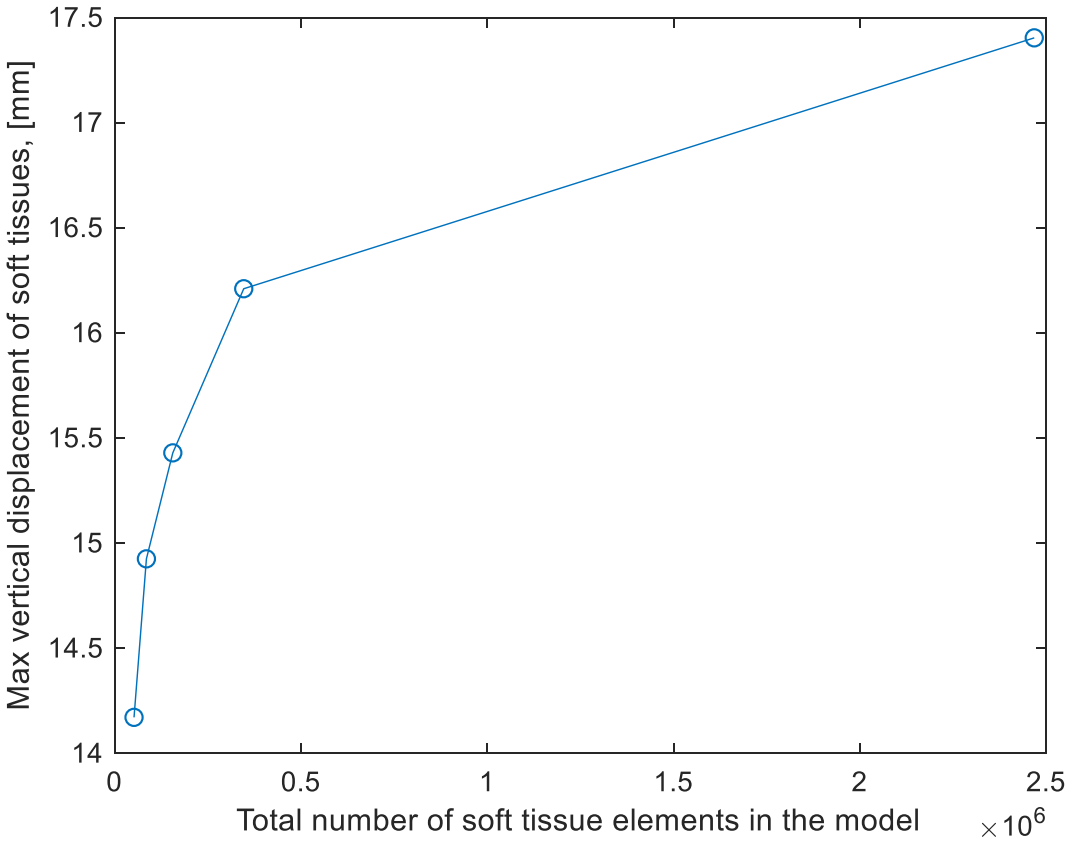


Figure 19: Maximal vertical displacement of the indenter [mm] vs total number of elements. Value was assessed as an absolute maximum in the same slice taken through the center of indentation mark.

Model M5 with the finest mesh took approximately 2 days to compute, while relative change between vertical displacement obtained with M4 and with M5 is 7% with the relative change in the total number of elements representing soft tissues being 614%. Therefore, it was decided to use M4 mesh for future FE simulations. Figure 20 shows a transverse cross-section in the central region of the indentation for the model with the selected mesh size.

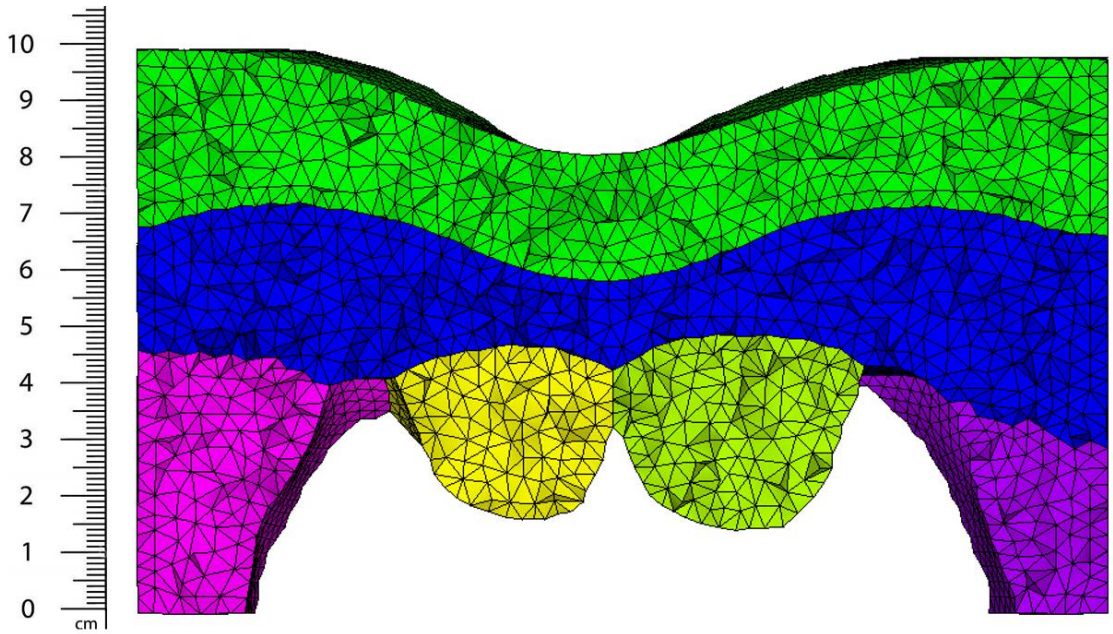


Figure 20: Transverse cut through the meshed model with the selected mesh size M4

## *3.2 Post processing and model evaluation*

### *3.2.1 ANSYS simulation post-processing*

The vertical displacement of soft tissues (displacement distribution in the direction of Z axis) was first observed since it allows to have a global assessment of the model, to see if assumptions related to the selected material parameters resulted in an indentation similar to the one observed on MR images. A second interesting output of the FE simulation is the maximum shear strain ( 4 ) that was previously associated with tissue damage (Ceelen, Stekelenburg, Loerakker, et al. 2008; Ceelen, Stekelenburg, Mulders, et al. 2008).

$$\varepsilon_{shear} = \frac{1}{2}\max(|\varepsilon_1 - \varepsilon_2|, |\varepsilon_2 - \varepsilon_3|, |\varepsilon_3 - \varepsilon_1|) \quad (4)$$

However, in terms of ANSYS simulation, elastic strain intensity is equated to maximal shear strain and defined as the largest of the absolute values $\varepsilon_1$-$\varepsilon_2$, $\varepsilon_2$-$\varepsilon_3$, $\varepsilon_3$-$\varepsilon_1$, where $\varepsilon_1$, $\varepsilon_2$ and $\varepsilon_3$ are the principal Hencky (logarithmic) strains ( 5 ). This results in the value twice bigger than the classic definition of the maximum shear strain.

$$\varepsilon_{shear\_ansys} = \max(|\varepsilon_1 - \varepsilon_2|, |\varepsilon_2 - \varepsilon_3|, |\varepsilon_3 - \varepsilon_1|) \quad (5)$$

For the remainder of the manuscript, all the values and results will be shown in terms of ANSYS definition of the maximal shear strain for the sake of simplicity.

### *3.2.2 Plane of interest*

All figures below in this 3rd chapter are plotted on the deformed shape of the model. Only soft tissues from the selected ROI are featured on a vertical transverse plane passing through the

center of indentation region. Figure 21 presents the location of the plane of interest (shown in red) on sagittal and frontal slices of the MR image.

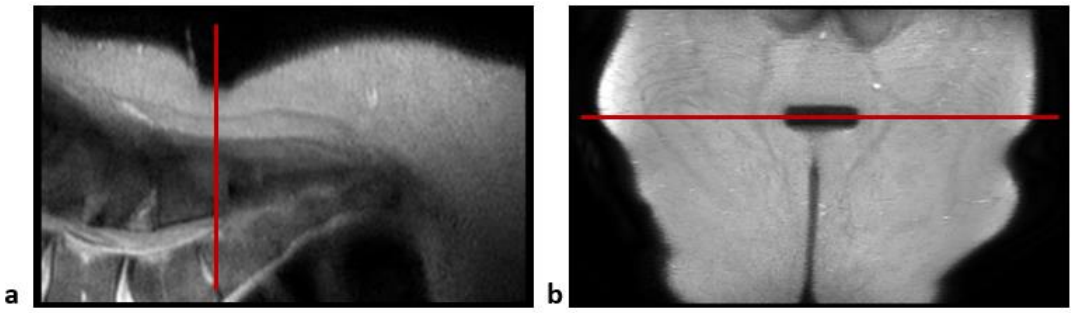


Figure 21: Red line marks the plane of interest on two MRI slices a) Sagittal slice; b) Frontal slice of the MR image

### *3.2.3 Image registration procedure*

Many attempts have been made to use Digital Volume Correlation (DVC) for *ex vivo* assessment of tissue motion in the intervertebral discs (Tavana et al. 2020), in rodent lungs (Arora et al. 2021) and *in vivo* in human lower leg muscles (Yaman et al. 2013) and in the heel (Trebbi et al. 2021). More recently, Trebbi, Mukhina et al. (Trebbi et al. 2022) suggest that DVC could be used as a validation technique for the results of FE simulation based on MR medical images. Such a DVC technique allows to estimate the tissue internal displacements and associated strains that can be compared to the same entities predicted by the FE model. The full text of that paper is provided in **APPENDIX 2**.

To extract 3D displacement fields associated with the different loading configurations, the algorithm based on the open source Elastix library (Klein et al. 2010) was used. The registration was performed between the *fixed* MRI volume (undeformed configuration, i.e. load case 0) and each *moving* MRI volume (loaded configurations, i.e. load cases 1-4).

Voxels of the fixed image were spatially mapped to the voxels of the moving image using a 2-step procedure. First, a rigid body transformation was defined by assuming that the MRI volume is a rigid body. The parameters of the transformation were computed as those that minimized the distance between the bones in the fixed image and each moving image based on a manually defined mask (image segmentation) to indicate the bony region assumed non-deformable. Second, B-spline non-rigid transformations were calculated between the aligned moving image and the fixed image. The coefficients of the B-spline transformations were optimized in each cube of a 3D grid that sampled the MR volume (size of the grid: 12 mm). For such optimization, Advanced Normalized Correlation metric was chosen as the similarity measurement since both the fixed and the moving images were collected using the same modality.

### *3.2.4 From displacement to strain field*

Displacement fields were extracted from both DVC and results of ANSYS simulations for each load case. Shear strain field was derived from displacement field based on following formulas:

The right Cauchy-Green deformation tensor ( 6 ) was derived from deformation gradient $\underline{\underline{F}}$:

$$\underline{\underline{C}} = \underline{\underline{F}}^T \underline{\underline{F}}$$

( 6 )

Then, the principal Logarithmic Hencky strain was calculated as ( 7 ):

$$\varepsilon_{principal} = \frac{1}{2} \ln \underline{\underline{C}}$$

( 7 )

And shear strain according to ANSYS terms of maximum shear strain (doudle of classic definition of maximum Hencky shear strain) was derived as follows ( 8 ):

$$\varepsilon_{shear} = \max(|\varepsilon_1 - \varepsilon_2|, |\varepsilon_2 - \varepsilon_3|, |\varepsilon_3 - \varepsilon_1|)$$

( 8 )

## *3.3 Results*

### *3.3.1 Measurements from DVC*

Figure 22 presents the result of the DVC for load cases L1-L4 for vertical displacement field $D_z$ and shear strain. Displacement and strain fields are plotted with the same scale for comparison purpose.

When the load decreased from configuration L1 to L2, highest values of the $D_z$ reduced from 17 mm to 13.2 mm. When the load further decreased to configuration L3, $D_z$ reduced to 12.2 mm. For the last load configuration L4, a vertical tissue displacement of 10 mm was observed.

As concerns Hencky shear strain distribution, the highest values were achieved in the tissues located directly under the indentation. Maximum shear strain values decreased from 2.1 for load configuration L1 to 1.4 for load configuration L2, stayed almost equal to 1.4 for load configuration L3 and decreased to 1.1 for load configuration L4.

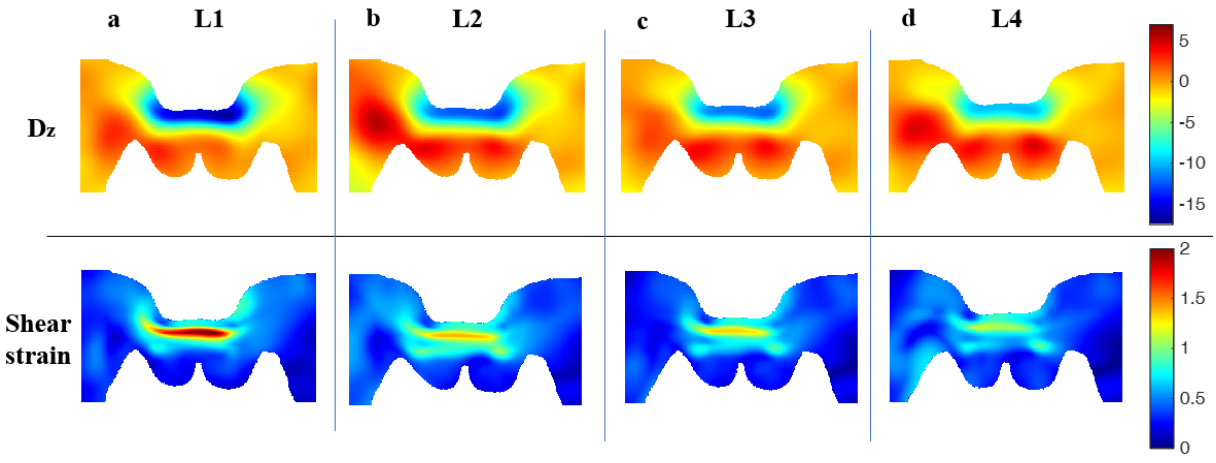


Figure 22: Results of DVC for $D_z$ and double Hencky shear strain. a) Load case 1 b) Load case 2 c) Load casse 3 d) Load case 4

### *3.3.2 Comparisons with ANSYS results*

Results of ANSYS simulations and DVC for each load case (L1-L4) are presented for comparisons in Figure 23-Figure 26. For a sake of comparison, the colour bar limits of each DVC measurement are set to be the same as they are in the corresponding ANSYS simulation.

The displacement distributions are observed to have similar patterns for DVC and ANSYS simulations, which is a first interesting result of our FE modeling. The highest value of ANSYS vertical displacement is 16.2 mm for configuration L4 (vs 17 mm for DVC). It decreased to 13.8 mm for configuration L3 (vs 13.2 mm for DVC), 12.4 mm for configuration L2 (vs 12.2 mm for DVC) and 10.7 mm for load configuration L4 (vs 10 mm for DVC).

As concerns Hencky shear strains, similar distributions are observed for DVC and ANSYS simulation, the highest values being located in the adipose tissue layer, directly beneath the indentation mark. For all load cases, it is interesting to note that maximum shear strain values are underestimated by the FE model. Maximum shear strain beneath the indentation is 1.2 for load configuration L1 (vs 2.1 for DVC). It decreased to 1 for L2 (vs 1.4 for DVC). For configuration L3, the value 0.9 is observed (vs 1.4 for DVC) and it decreased to 0.8 for L4 (vs 1.1 for DVC).

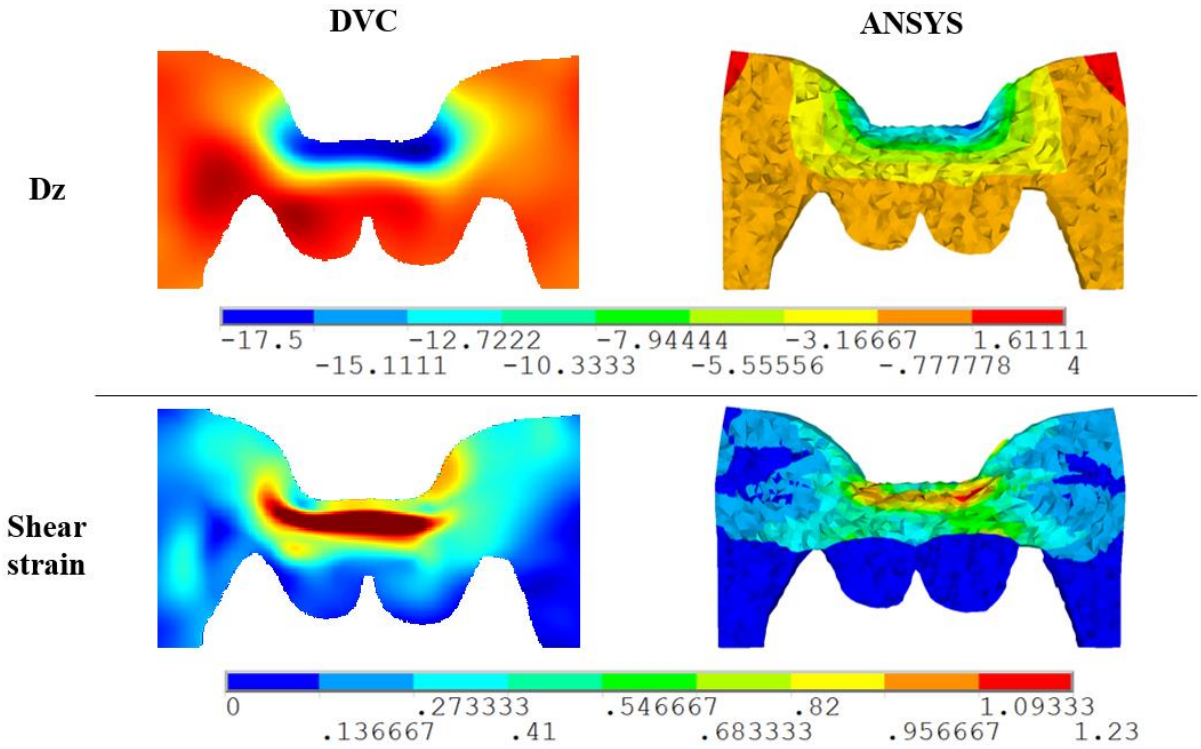


Figure 23: DVC vs ANSYS for evaluation of Dz and double Hencky shear strain, Load case 1 (~1200 g)

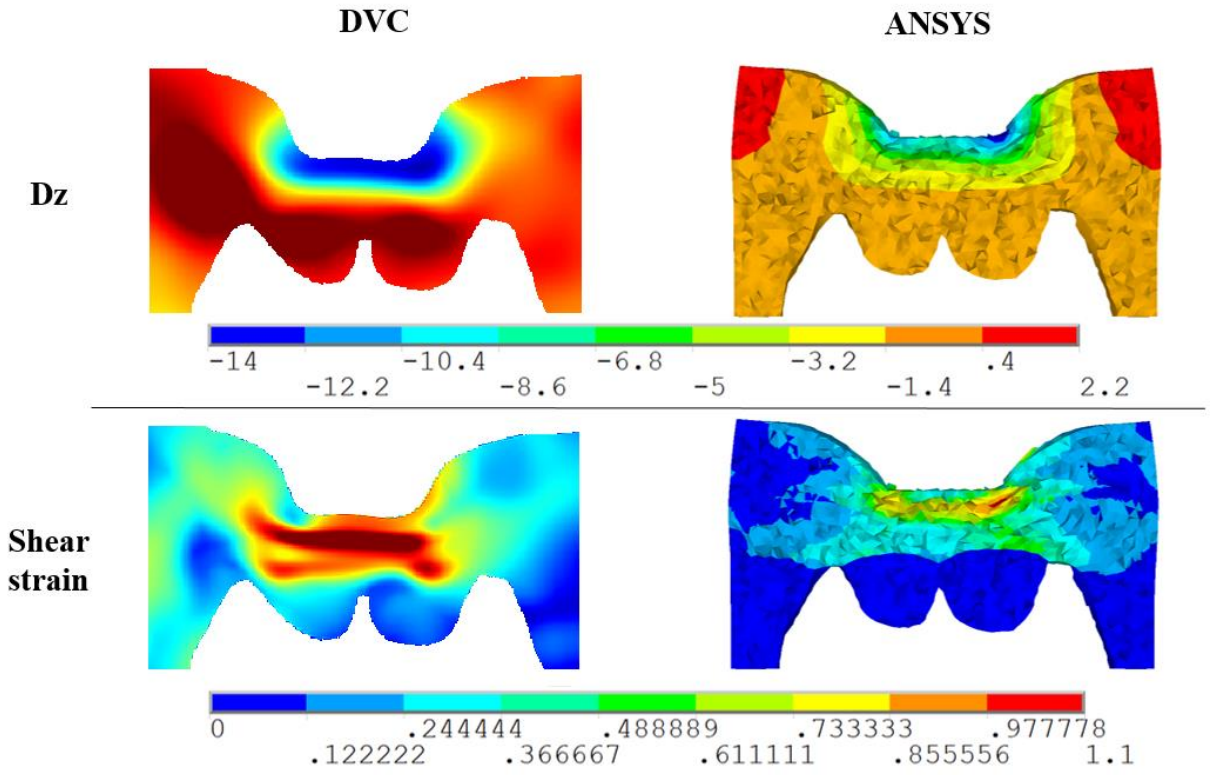


Figure 24: DVC vs ANSYS for evaluation of Dz and double Hencky shear strain, Load case 2 (~800 g)

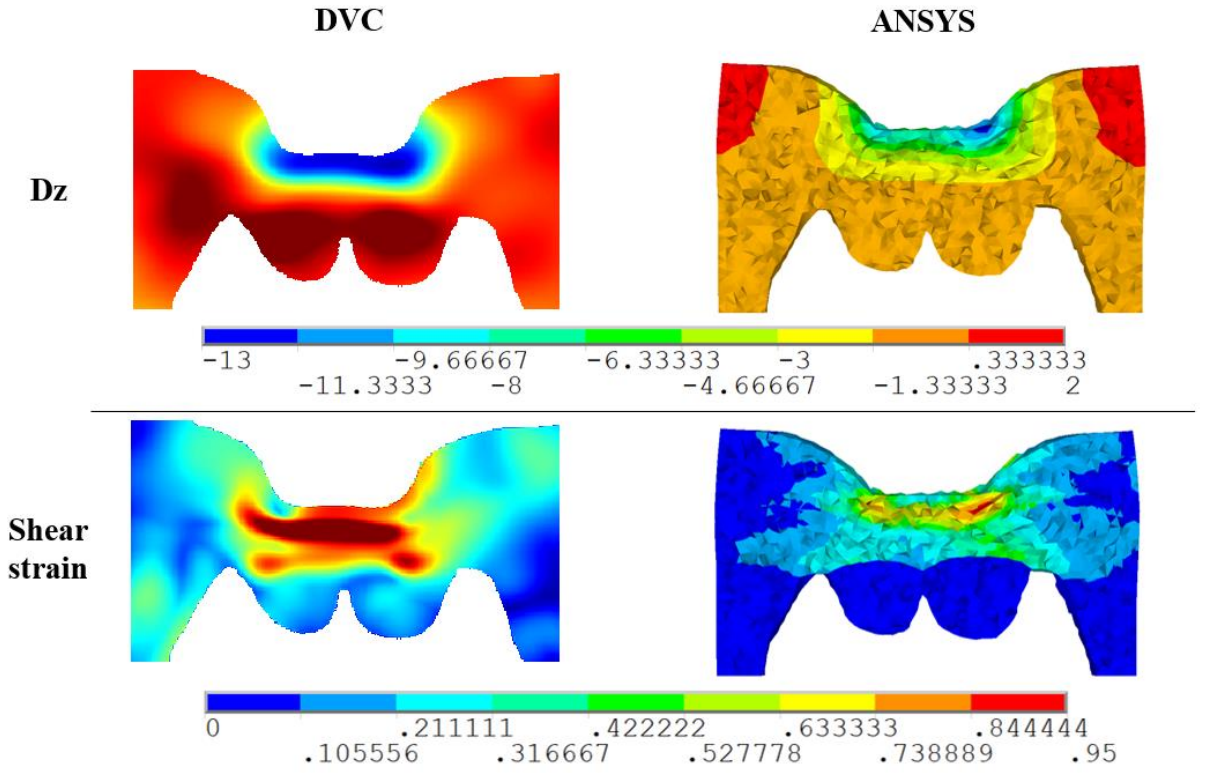


Figure 25: DVC vs ANSYS for evaluation of Dz and double Hencky shear strain, Load case 3 (~600 g)

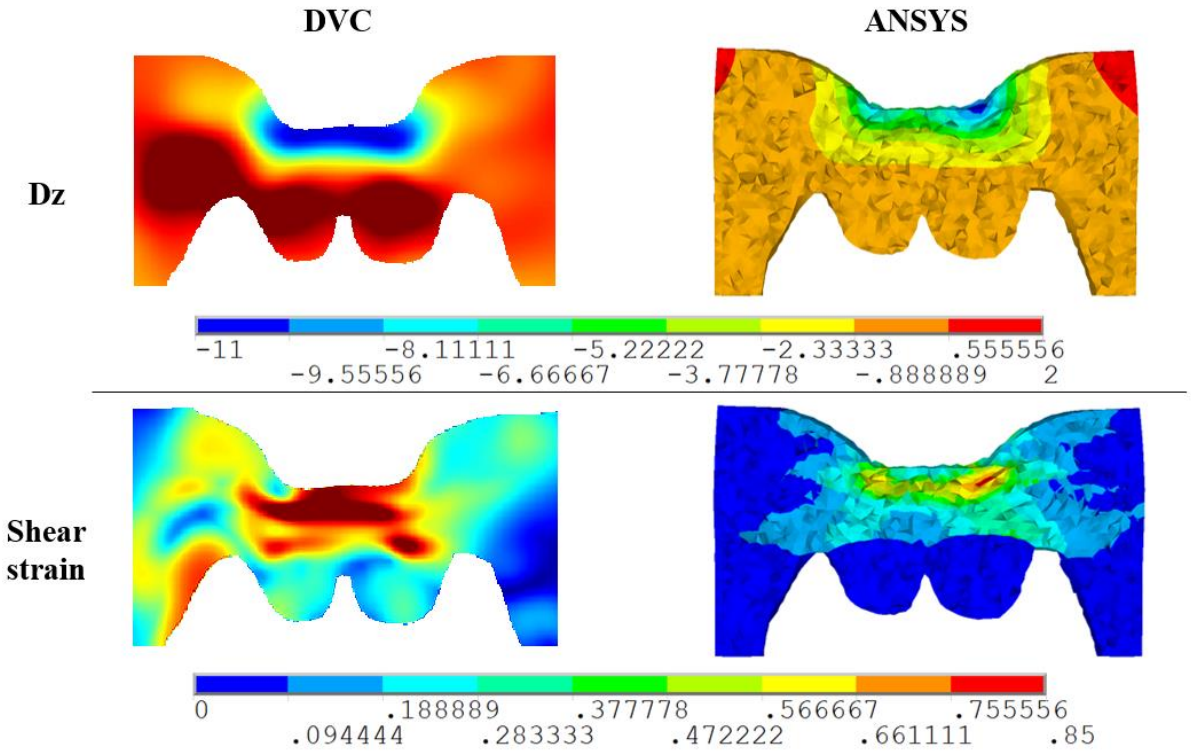


Figure 26: DVC vs ANSYS for evaluation of Dz and double Hencky shear strain, Load case 4 (~400 g)

# Chapter III conclusion

This chapter focused on describing all stages of the subject-specific 3D FE model creation. First, the geometrical data was segmented from MR medical images collected in **chapter II**. Next, constitutive laws were defined for each soft tissue (skin, adipose tissue, fascia and muscle) based on the curve fitting of a Yeoh material on the experimental data previously collected in the literature. Material models for skin and adipose tissue were then updated with a subject-specific value for the $C_{10}$ coefficient of the Yeoh constitutive law. This new value was derived from the Young moduli experimentally identified *in vivo* with the VLASTIC device (for the details of the experiment the reader is referred to **chapter II**). Model boundary conditions and four different load configurations (L1-L4) were described. Then, a mesh sensitivity study is performed to define mesh size.

The post-processing section of this chapter focused on two quantities of interest: the maximum vertical displacement of soft tissues and the maximum shear strain. Displacement was studied as an initial evaluation of the model while shear strain was observed in details as this parameter was previously associated with a risk of tissue injury (Ceelen, Stekelenburg, Loerakker, et al. 2008).

Digital Volume Correlation based on image registration was introduced as a possible tool for model validation. Such a measurement could indeed be used to identify the displacement fields between the undeformed configuration (L0) and each of the deformed configuration (L1-L4) is described.

Comparison of DVC tissue displacements with results provided by the FE model showed that maximum values as well as the displacement distribution field are estimated quite accurately for all load cases, with a relative change being less than 5% for load configurations L1-L3 and 7% for load configuration L4. This is a first level of validation that is quite interesting since the FE model is controlled in force (with loads values measured by our MR-compatible device) rather than in displacement. Getting such small differences between measurements and simulations is therefore quite encouraging in this framework.

As concerns shear strains, a similar distribution pattern was observed in ANSYS and DVC, with in both cases regions of the highest values located beneath the indentation mark. However, high differences were observed for the absolute maximum values of shear strains between both cases, going up to 43% for load configuration L1. There are several reasons that could be causing that. First, the positioning of the indenter in the model could have introduced inaccuracies since it is done manually. Then, we could still question the accuracy of the DVC. This technique previously showed good results in application to other body regions. However, it is very dependent on the initial image quality and due to experiment restrictions described in the conclusion of **chapter II,** image quality is quite reduced in our case. In particular, getting Hencky strain values larger than 2 is highly questionable: see for example the study of Napadow et al. (Napadow et al. 1999) who have measured a maximum Green Lagrange strain of 2 on tongue tissues (assumed as highly deformed) which corresponds to a Hencky strain of 0.8, much smaller than the value 2 obtained with our images. On the other hand, 3D FE simulation resulted in the maximum shear strains corresponding to 1.2 maximum shear Green-Lagrange strain in classic formulation. This value is higher than 0.75 tissue damage limit reported by Ceelen et al. (Ceelen, Stekelenburg, Loerakker, et al. 2008) for the same parameter.

This part of the study had some limitations in the definition of the FE model. First of all, the segmentation of the geometrical data is performed manually, which could have added inaccuracies in the model. Fasciae are presented as a layer with assumed thickness of 0.5 mm, while in reality it is a network of connected tissues.

Another limitation is the choice of the subject-specific material properties. The experimental data is limited to the identification of skin and adipose tissues Young moduli, while $C_{20}$ parameters for both of these tissues are used from the literature. Due to insufficient experimental material data in the literature of sacrum, sacral muscles constitutive laws are based on uniaxial tension data collected on a muscle from the human neck, fascia from experiments on the abdominal wall and adipose tissue from a compression test done on the heel fat pad. This approximation has for sure a consequence since biological tissues located in the different areas of the human body adapt to the experienced loads and, therefore, could get different material properties according to their location. Another parameter chosen to represent the incompressibility of the material is Poisson ratio. Such a parameter can have strong consequences as concerns the results of the simulations. As it was shown in the literature review of previous FE models **(chapter I)**, the choice for Poisson ratio varies between studies. It is important to note that even a small change of Poisson ratio from 0.49 to 0.495 results in d (incompressibility parameter) being twice less, with results of the simulation that can be highly affected (in the tested example the difference was 14% for vertical displacement).

# CHAPTER IV. Using US-based FEA for the assessment of the risk of sacral PU: Is a 2D-based model reliable enough for the estimation of the displacement field?

The estimation of the internal soft tissue strains in at-risk clinical situations using MR-based 3D FEA is currently hindered by costly acquisition, reconstruction and computation times. Ultrasound (US) imaging is a promising candidate for the clinical assessment of both morphological and material parameters. In a previous collaborative study detailed in **APPENDIX 3** to which I participated, we investigated the feasibility of assessing clinically relevant geometrical parameters using US-based imaging for the direct estimation of geometrical and material parameters in the sacral region. A bedside B-mode US and SWE protocol was designed for the evaluation of bone geometry, tissue morphology and mechanical characteristics over the sacrum. Reliability and reproducibility of this protocol were tested on a healthy young adults group (N=19). The protocol was then applied on a group of healthy older people (N=11) to assess for clinical feasibility. The study highlighted the need for further refinement of the protocol to improve reliability.

Based on the rationale that US 2D imaging is a promising candidate to substitute MR 3D imaging, we propose, in this chapter, a 2D FE model of the sacrum to simulate the mechanical response under compression loading. The proposed methodology is evaluated by comparing the response provided by the proposed 2D FE model to the one predicted by the MRI-based 3D FE model previously developed in **chapter III**.

The first section of this chapter introduces input data and modelling assumptions for the geometry, material properties and boundary conditions. The second section presents 2D simulation results for each of the four load cases studied in **chapter III.** Two kind of results will be studied in particular here: the distribution of the vertical tissue displacement and the distribution of the shear strain defined as an elastic strain intensity. These results will then be compared with the simulations provided by the 3D model.

## *4.1 Preparation of the 3D FE Model*

### *4.1.1 Personalized geometrical model*

The US data acquired with the SL10-2 linear probe transducer (Aixplorer, SuperSonic Imagine, France) in the undeformed configuration in **chapter II** was limited in terms of field of view of US imaging and didn't allow to visualize the whole soft tissue thickness. It was therefore decided to discard this 2D US image. To circumvent the problem and to propose a way to collect 2D data to build the 2D FE model, a transverse slice of the unloaded MR 3D image passing through the center of the indentation was used as an initial undeformed state.

The procedure proposed to define the region of interest for the construction of the FE geometrical model from the MR image is summarized in Figure 27 below. First, a 2D transverse MRI slice in the undeformed configuration was selected at the center of the indentation mark. In Figure 27(a), the slice for the unloaded (L0, 0 N) and fully loaded (L1, 11.9 N) configurations are superposed. Second, an area of interest corresponding to a field of view of the US probe was selected and plotted for L0 and overlapping L1 in Figure 27(b). Figure 27(c) shows only the unloaded image used as a basis for segmentation. Points delimiting skin, adipose tissue, fascia, muscle and bone were selected with MATLAB. An ANSYS geometric input file was written automatically by the MATLAB script with the

selected points being connected by B-spline. To represent an indenter, a rectangle was modeled with a fillet of 2 mm.

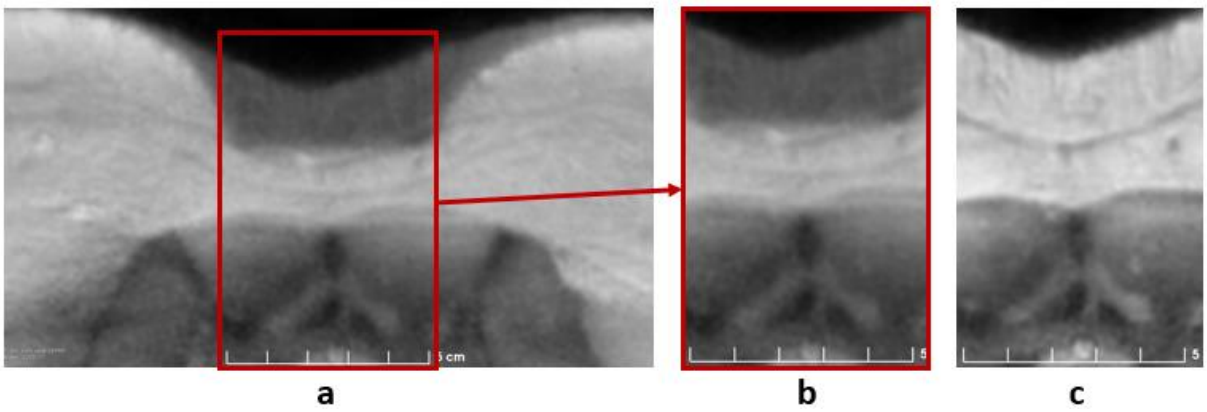


Figure 27: a) Transverse slice of the MR image chosen at the center of indentation mark: overlapping images of L0 (unloaded) and L1 loading configurations b) Selected region of interest: overlapping images of L0 and L1 c) Unloaded configuration L0 only.

The segmented area containing skin, two layers of adipose tissue, two sets of fascia and muscles is shown in Figure 28. From that segmentation, a 2D FE model was generated and extended by 5 cm to both directions to diminish edge effect from the results of the simulation (Figure 28(b)).

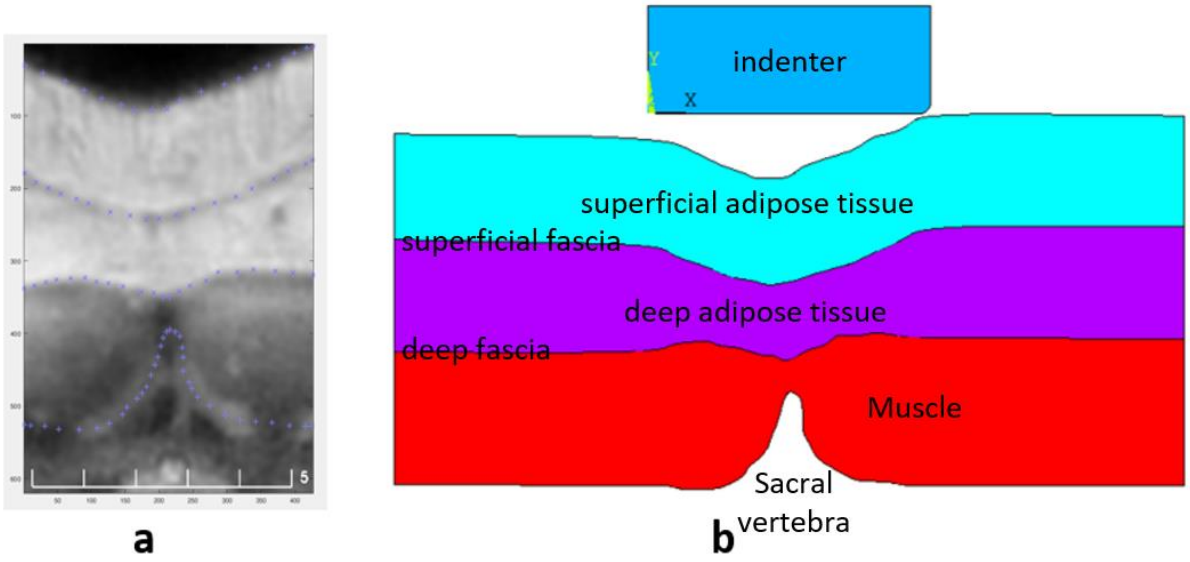


Figure 28: a) Segmentation process in MATLAB b) Regions of the corresponfing 2D FE model, from top to bottom: probe modeled as an indenter, superficial adipose tissue, deep adipose tissue and muscle layer

### *4.1.2 Constitutive modelling and calibration*

Two scenarios were tested with this 2D FE model: (1) using the results of the calibration procedure proposed in **chapter III** assuming a Yeoh hyperelastic constitutive law that was previously used in the literature to model soft tissues (Fougeron et al. 2022) and based on VLASTIC data collected in **chapter II,** (2) calibrating an Ogden hyperelastic constitutive model based on a custom made load sensor attached to the ultrasound probe as proposed in

(Fougeron et al. 2020). For more details regarding the second approach, the reader is referred to the abstract published as part of the conference proceedings in **APPENDIX 4**. Since the objective of the current chapter is to compare 2D and 3D FE models, only the results of the first approach will be presented further in the text.

### *4.1.3 External mechanical loading*

The vertical loads imposed to the 2D model via the indenter were the ones recorded during the MR experiment, namely 11.9 N, 8 N, 6.1 N and 4.3 N.

### *4.1.4. FE discretization and contact modelling*

ANSYS PLANE 182 elements with plane strain assumption and using a mixed U-P formulation were chosen to represent the adipose and muscle tissues. To model skin and fasciae, LINK 11 elements were chosen as a 2D equivalent of the membrane-like SHELL 181 element used in the 3D model. For comparison purposes, the same element size (3 mm) as those defined for the 3D model were imposed for the soft tissues. As a result, the FE mesh consisted of 1194 PLANE 182 and 160 LINK 11 elements. At the bottom of the 2D model (figure 29), the nodes in contact with the edges of the sacral bone were assumed fixed for all degrees of freedom. As a first approximation, all tissues were tied together to avoid the definition of internal contacts (like the ones occurring between fascia and adipose or muscular tissues). The US probe was fixed on both sides in the X direction and was able to move in the Y direction only. A contact pair was defined between this probe and the skin layer.

A quasi-static analysis was run with two steps: first, an initial displacement of the probe to come into contact with the skin and second, the force being evenly distributed between the nodes located on the top of the probe. A load of 11.9 N was applied for the model of Load case I (L1); 8 N for the model of Load case II (L2); 6.1 N for the model of Load case III (L3) and 4.3 N for the model of Load case IV (L4). Figure 29 shows boundary and loads conditions on the 2D meshed model.

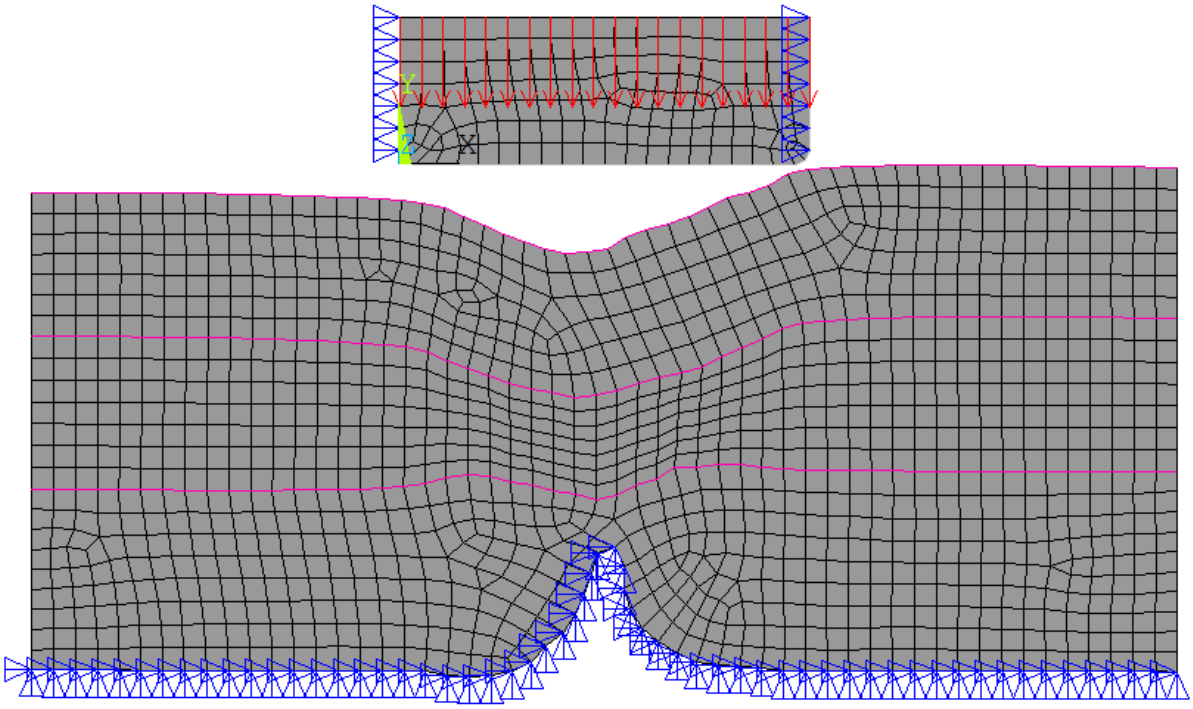

Figure 29: Boundary conditions plotted on a meshed model (PLANE elements in grey, LINK elements in magenta). The edges of the bone were fixed for all degrees of freedom (in blue); US probe was fixed on the sides (in blue) in X direction and the force was applied to the top surface of the probe (red arrows).

#### *4.1.5. Post processing*

One of the limitations of the FE simulations is the risk to generate artificial strain concentrations due to mesh size or geometrical non-regularity. To overcome this risk, it was decided to analyze a local maximum value of the relevant region of the elements inside the soft tissues instead of the absolute maximum value.

## *4.2 Comparison of the results with the ones provided by the 3D model*

Figure 30-Figure 33 show the comparisons between the results of the 2D model (left column) and 3D model (right column) for vertical displacements and shear strains fields for load cases L1-L4 correspondingly. As said earlier, only the results of the 2D model with the personalized Yeoh constitutive law proposed in **chapter III** are provided for comparison with results of the 3D model.

Displacement fields obtained with 2D and 3D models have similar patterns. However, for all four load cases, the vertical displacements of soft tissues were overestimated by the 2D model with a relative error being 30%: load case L1 (21 mm for 2D model vs 16.2 mm for 3D model); load case L2 (17.9 mm vs 13.8 mm); load case L3 (16 mm vs 12.4 mm) and load case L4 (13.9 mm vs 10.7 mm).

Local shear strain concentrations were observed in the 2D model in the superficial and deep layers of adipose tissue. Higher maximum shear strain values were observed in the 2D model as compared to the 3D one. However, the maximum shear strain values in the 2D model occur locally, at the corner region of the contact with the probe. To avoid focusing on such local maximum value, a maximum value of the relevant area of the elements inside the soft tissues

was analyzed. For load configuration L1 value was 1.2 (vs 1.2 for 3D model), decreasing to 1.1 for load case L2 (vs 1 for 3D model); for load case L3 it was 1 (vs 0.9 for 3D model) and for Load case L4 it was 0.9 (vs 0.8 for 3D model).

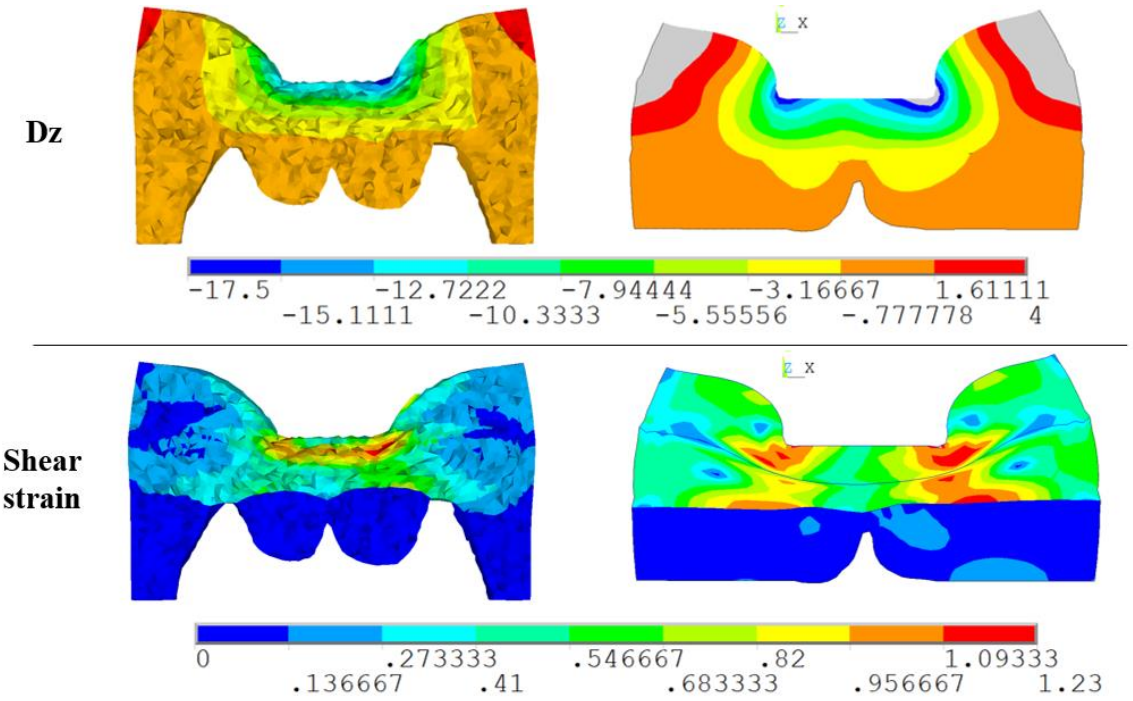


Figure 30: Vertical displacement (top row) and shear strain (bottom row) for 2D model (right) and 3D model (left), Load case I (~1200 g)

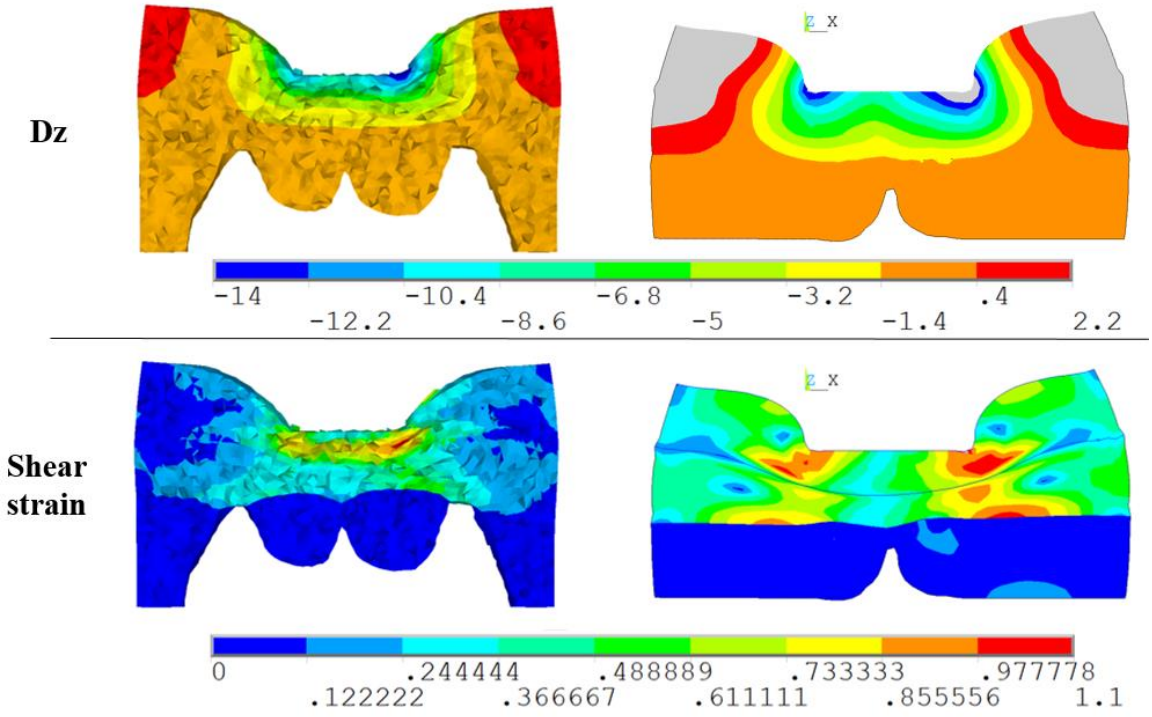


Figure 31: Vertical displacement (top row) and shear strain (bottom row) for 2D model (right) and 3D model (left), Load case II (~800 g)

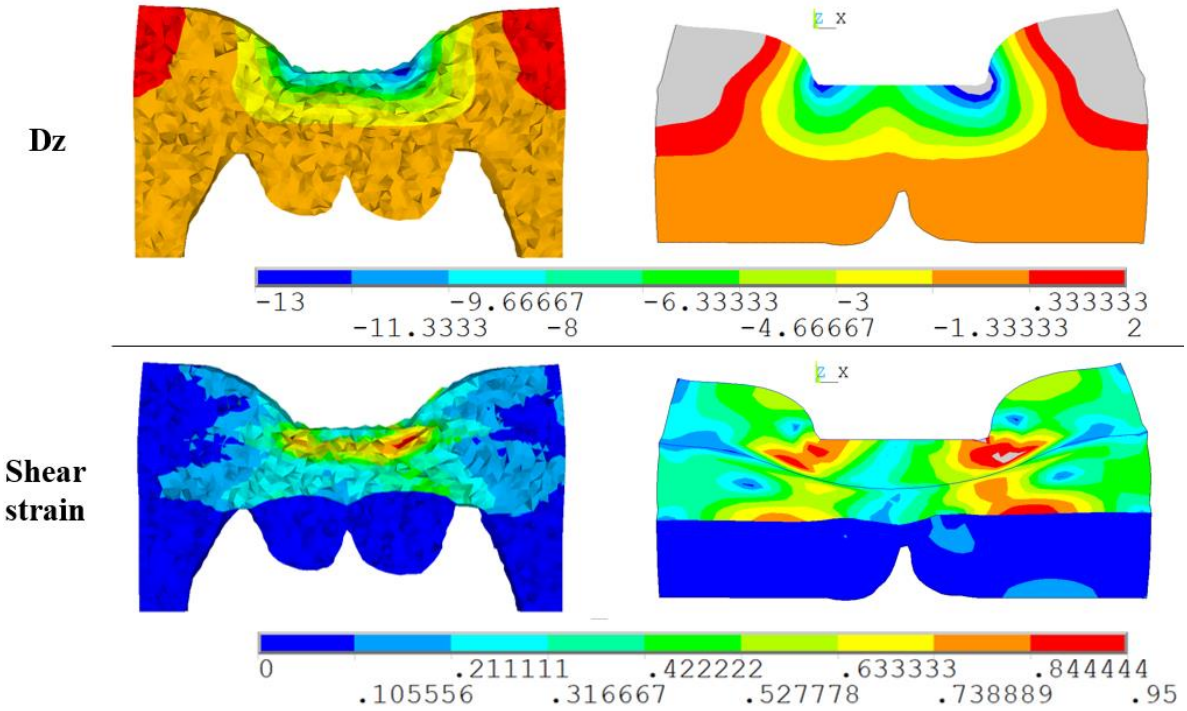


Figure 32: Vertical displacement (top row) and shear strain (bottom row) for 2D model (right) and 3D model (left), Load case III (~600 g)

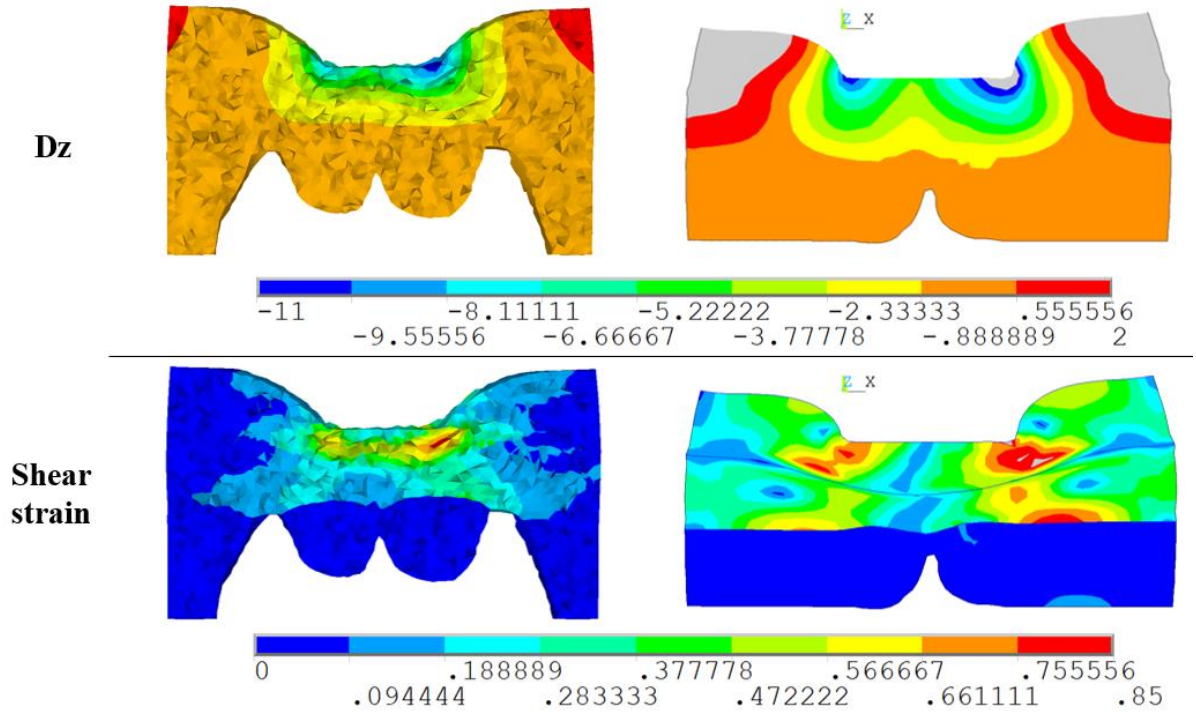


Figure 33: Vertical displacement (top row) and shear strain (bottom row) for 2D model (right) and 3D model (left), Load case IV (~400 g)

# Chapter IV conclusion

Assuming the 2D US images will get a better quality than the one we were able to record here (with a full visualization of the whole soft tissue thickness), B-mode US still remains a promising candidate to substitute MR imaging. It should indeed allow to obtain a subject-specific anatomical data, while being much more accessible and less costly than MRI. Nevertheless, the main limitation of B-mode US is the 2D modality, which does not account for the out-of-plane tissue motion (non-negligible assumption). **Chapter V** will propose an experimental characterization of sacral soft tissue motion, to estimate the discrepancy between tissue motion assessed using a 2D imaging modality (echography) versus tissue motion assessed using a (reference) 3D imaging modality (Magnetic Resonance Imaging), in order to inform on the relevance of 2D US-based measurements for pressure ulcer risk assessment.

This chapter focused on the development and the evaluation of a methodology for building 2D US-based FE model of the sacrum for simulating the mechanical response under controlled compressive loading. Due to the limited field of view of US imaging, the whole soft tissue thickness in the unloaded configuration could not be properly assessed. As a result, a 2D transverse slice of the MR volume was used for defining the geometry of the 2D FE model. A side study on the possible clinically relevant direct sacral PU risk assessment with US based on the geometrical parameters that are fed into FE model was described in **APPENDIX 3**.

Results show that the 2D FE model overestimates the mechanical response by up to 13% of relative difference between the maximum shear strain values obtained with 3D MRI-based model and 2D US-based model. Possible explanations beside 2D modality are 1/ the assumptions on the boundary conditions on the lateral displacement of the soft tissues (the extension by 5 cm on both sides in the 2D model to diminish edge effects that is probably not sufficient) and 2/ the plane strain assumption. These will be further investigated in perspective work. The model sensitivity check to the extension size on both sides (5 cm in this case) was not performed and will also be a part of the perspective work. The maximum values of shear strains were observed in the superficial adipose layer and skin in both models. To investigate the impact of the 2D modality, the portion of the tissue motion directed out of the 2D plane to the one observed in-plane will be characterized in **chapter V**.

# CHAPTER V. Impact of out-of-plane soft tissue motion under compressive loading

Because of the significant challenges associated with the *in situ* measurement of both loading and tissue motion using medical imaging in clinical routine, the objective of this chapter was to exploit the experimental data collected in **chapter II** to characterize sacral soft tissue motion under a controlled mechanical loading to experimentally estimate the discrepancy between tissue motion assessed using a 2D imaging modality (echography) versus tissue motion assessed using a (reference) 3D imaging modality (Magnetic Resonance Imaging) to inform on the relevance of 2D US-based measurements for pressure ulcer risk assessment.

First section of the chapter summarizes the procedure proposed for the data post-processing of the experimental data. It starts with obtaining displacement fields for all load cases from the analysis of collected MR images using DVC technique described in **chapter III**. The construction of the US plane (the slice that was expected to be obtained if simultaneous US acquisition had been possible) and the assessment of the uncertainty of plane's definition are then detailed. Region of interest was specified, and the parameters used to describe the out-of-place tissue motion (the ratio R of the norm of the out-of-plane displacement component to the norm of the in-plane component and the norm ratio N of the norm of out-of-plane component to maximum in-plane component) are also described. The second section presents the salient results obtained in terms of in-plane and out-of-plane tissue motion for all load cases.

The work presented in this chapter has been recently peer reviewed and published in the Journal of Tissue Viability (DOI: 10.1016/j.jtv.2022.09.007).

## *5.1 Data Analysis*

Based on the displacement fields computed by DVC, a post processing was performed to estimate the out-of-plane tissue motion. In-plane directions correspond to a plane of view of the US probe, in our case, a transverse slice through the center of indentation. US image is very dependent on the inclination of the probe; therefore, a verticality check of the US image plane was performed to insure the reproducibility of the indenter position.

### *5.1.1 Construction of the US plane from the reflective marker*

The ultrasound image plane (referred to afterwards as "US plane") was constructed as follows: First, two points A and B were manually selected on the posterior side of the reflective marker (Figure 34 b) on a sagittal slice of the MR volume and used as construction points to define a temporary unit vector $\underline{v'_1}$. The reflective marker was glued to the indenter surface inclined by 12.1° with respect to the middle transverse plane of the indenter (Figure 34 a). A corrected $\underline{v_1}$ was therefore defined corresponding to a rotation of the vector $\underline{v'_1}$ so that it lies in the plane parallel to the transverse plane of the indenter. Then, four points C, D, G and H were selected on the superior and inferior sides of the indentation mark on a frontal slice of the MR volume where the mark was visible as illustrated in Figure 34 c below. They were used to define a temporary unit vector $\underline{v'_2}$ passing through the midpoints of the line segments connecting C and D and G and H respectively (Figure 34 c). Third, a unit vector $\underline{v_3}$ perpendicular to the plane containing the vectors $\underline{v_1}$ and $\underline{v'_2}$ was defined as the result of the

cross product ($\underline{v_1}\, x\, \underline{v'_2}$). A new vector $\underline{v_2}$ perpendicular to both $v_1$ and $v_3$ was then defined as ($\underline{v_3}\, x\, \underline{v_1}$).

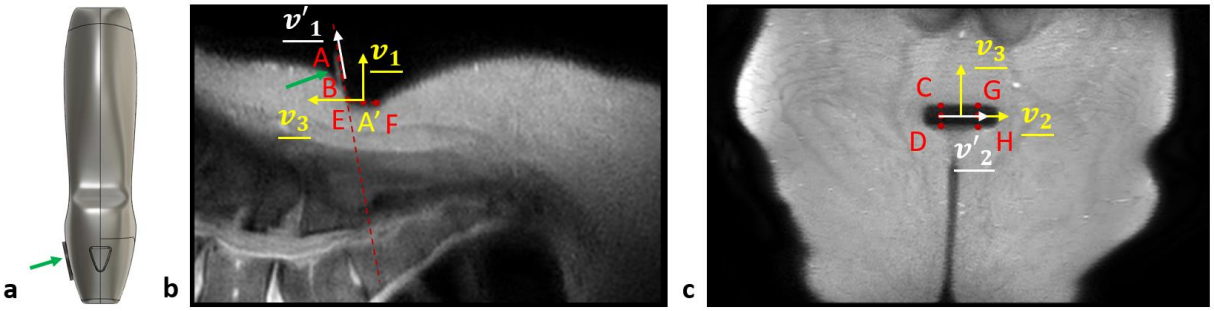


Figure 34: a) Sagittal view of the 3D printed indenter, green arrow points at the reflective marker; b) Sagittal slice, the red dotted line is aligned with the reflective marker; c) Frontal slice of the MR image.

The US plane was assumed to pass through the middle of the thickness of the piezoelectric transducers. The thickness of the indenter is estimated by selecting 2 points E and F in the same sagittal slice of the MR volume previously defined (Figure 34 b). The origin of the US coordinate system (US CSYS) was established at the mid-point A' of the line segment joining E and F. Finally, the homogeneous matrix $\underline{\underline{H}}$ of the US CSYS was defined as follows ( 9 ):

$$\underline{\underline{H}} = \begin{bmatrix} v_{1x} & v_{2x} & v_{3x} & A'_x \\ v_{1y} & v_{2y} & v_{3y} & A'_y \\ v_{1z} & v_{2z} & v_{3z} & A'_z \\ 0 & 0 & 0 & 1 \end{bmatrix} \quad (9)$$

### *5.1.2 In-plane and Out-of-plane displacements quantification*

To characterize the in-plane and out-of-plane displacements, the displacement field resulting from the 3D Image registration procedure defined in **chapter III** was separated into Y-Z (in-plane) and X (out-of-plane) directions in the loading coordinate system (MRI CSYS).

Two parameters were identified as follows ( 10 ) to quantify the out-of-plane displacements: First, for each voxel located in-plane, the ratio R of the norm of the out-of-plane $\|D_X\|$ component to the norm of the in-plane component $\|D_{YZ}\|$ was computed. Second, the norm ratio N of the norm of out-of-plane component $\|D_X\|$ to maximum in-plane component $\max(\|D_{YZ}\|)$ throughout the whole image was defined.

$$R = \frac{abs(D_X)}{\sqrt{{D_Y}^2 + {D_Z}^2}} \qquad N = \frac{abs(D_X)}{\max\left(\sqrt{{D_Y}^2 + {D_Z}^2}\right)} \quad (10)$$

### *5.1.3 Regions of interest*

Two regions of interest were defined. The first one, called ROI1, was defined in the vicinity of the indentation for the visualization of the displacement field in the soft tissues located above the bony prominence around the indentation zone as depicted in Figure 35 a.

The second, called ROI2, was defined for the evaluation of the out-of-plane displacement according to the definition of ratio R and norm ratio N. ROI2 was defined based on the data of load case 1 by selecting the region with the norm ratio values N higher than 0.3. This ROI2 was kept the same for the other load cases as well. An example of ROI1 and ROI2 is given in Figure 35.


Figure 35: Two regions of interest. a) Both ROI1 and ROI2 are shown on a transversal MRI slice; b) ROI1 (top) and ROI2 (bottom); c) the norm ratio N for the load case 1 plotted for ROI1 (top) and ROI2 (bottom).

### *5.1.4 Assessment of the uncertainty associated with US plane definition.*

To assess the uncertainty associated with the definition of the US CSYS, the points A, B, C, D, E, F, G, H were selected 10 times and the associated US CSYS were recalculated. The orientation matrix of the relative angular position of each US CSYS to that of the global MRI CSYS was then calculated. The decomposition of the rotation matrix was done using the YXZ rotation sequences of Cardan angles (MRI CSYS is shown in Figure 36). The rotation of the indenter from the vertical axis was assessed as the angle around the Y axis.

## *5.2 Results*

### *5.2.1 Uncertainty in quantification of US image plane definition.*

The mean difference in the relative angular position of each US CSYS to the vertical direction of the global MRI CSYS is 4.4° (range: [3.0°, 5.8°], standard deviation ± 1.2°).

### *5.2.2 Displacement fields*

#### *5.2.2.1 In- and out-of-plane displacements quantification*

The in-plane and the out-of-plane displacements distributions in the ROI1 decomposed in MRI CSYS are shown in Figure 36 for each load case. The same limits were set for all displacement fields. The MRI CSYS was defined with Y and Z being the in-plane directions and X being the out-of-plane direction (Figure 36: first and second rows for in-plane and last row for out-of-plane correspondingly). A quiver diagram was also drawn to illustrate the combined in-plane displacement distribution in the tissues.

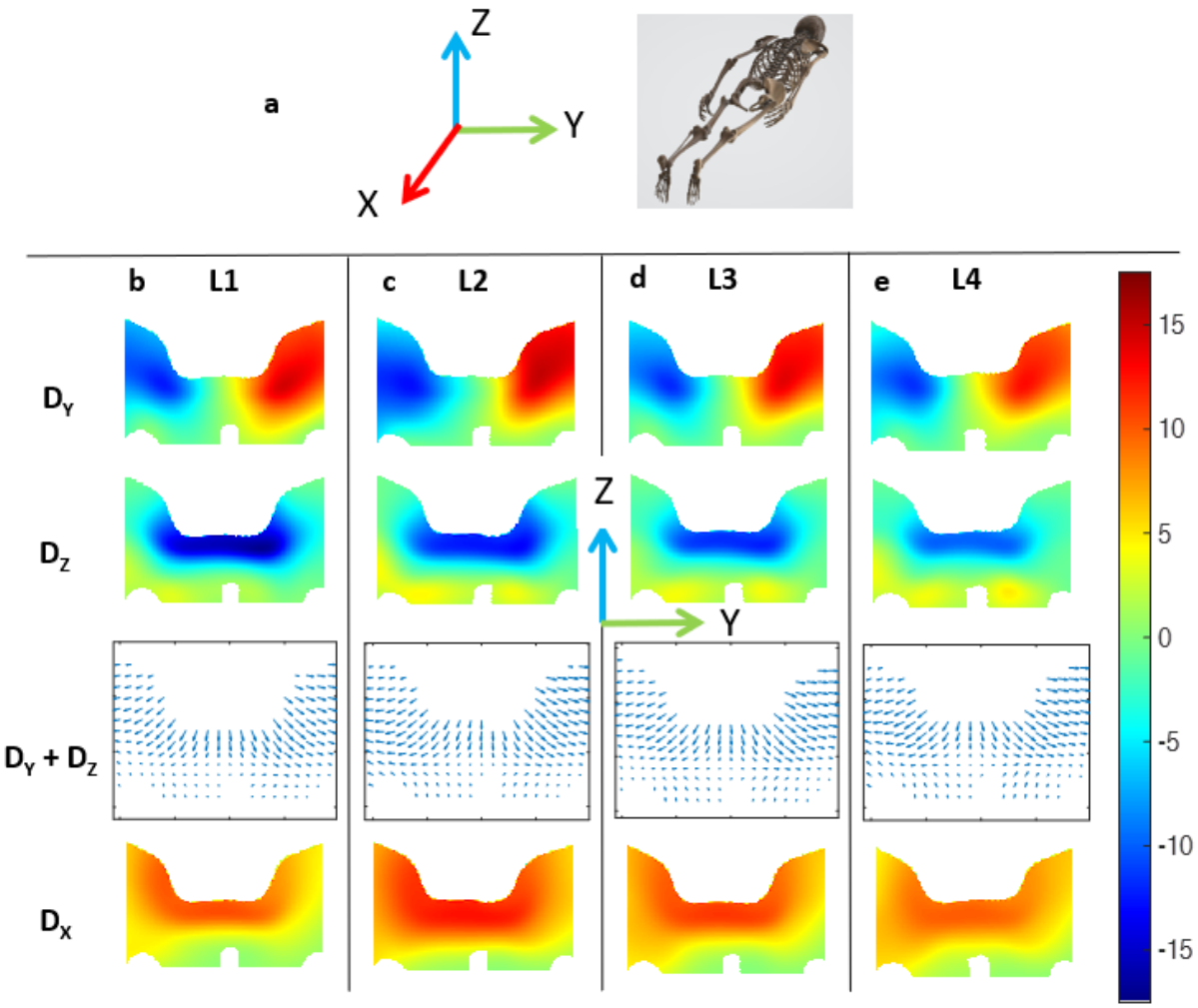


Figure 36: a) MRI CSYS; b) In-plane Y displacements in the top row; the Z in plane displacements in the second row; the quiver showing the combined in-plane displacements distribution in the third row, and in the last row the out-of-plane X displacements plotted in [mm]; ROI1, L1 (~1200 g) c) L2 (~800 g) d) L3 (~600 g) e) L4 (~400 g).

Table 9 summarized the displacement values for each of the four load cases. When the load was decreased from configuration L1 (~1200 g) to configuration L2 (~800 g), the tissue displacements estimated using DVC in the ROI1 decreased in the Z direction and, on the contrary increased in both the Y and X directions.

When the load was decreased from configuration L2 (800 g) to configuration L3 (600 g), as well as from configuration L3 (600 g) to configuration L4 (400 g), the tissue displacements estimated using DVC decreased in all 3 directions.

Table 9: Summary of the maximum displacement values in each of the directions for the four load cases

| Load case | Max Dx, [mm] | Max Dy, [mm] | Max Dz, [mm] |
|---|---|---|---|
| L1 | 12.4 | 14.6 | 17 |
| L2 | 14 | 16.1 | 13.2 |
| L3 | 12.3 | 15.8 | 12.2 |
| L4 | 10.7 | 13.7 | 10 |

### *5.2.2.2 Parameters of interest to quantify the out-of-plane displacement*

The first two rows of Figure 37 present the norm distribution N in MRI CSYS on each load case L1 - L4 in the ROI1 and ROI2. The ratio R parameter is shown in the ROI2 in the last row. The ratio values increased after the decrease in the load from L1 (~1200 g) to L2 (~800 g). For all load cases, more than half of the voxels have the ratios of the out-of-plane displacement values higher than 0.6. For load cases L2 - L4 the values equal to or higher than 1 were observed in a quarter of the voxels of ROI2.

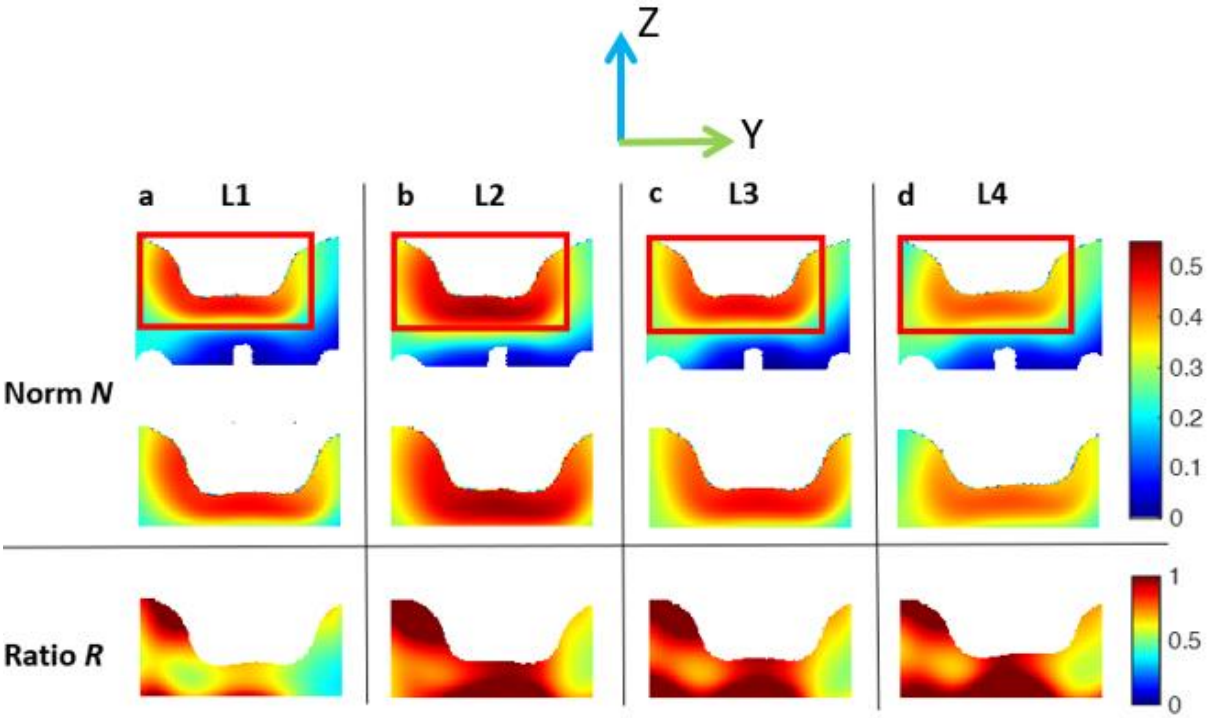


Figure 37: Norm N and ratio R of the out-of-plane displacement, ROI2: a) L1 (~1200 g); b) L2 (~800 g); c) L3 (~600 g); d) L4 (~400 g).

# Chapter V conclusion

The objective of this chapter was to characterize the sacral soft tissue out-of-plane displacements using a custom-made MRI-compatible setup under a realistic US transducer loading. This is an important question because the experimental assessment of the internal tissue deformations could reveal the individual PU injury risk. However, the assessment with accessible, low cost, and real-time techniques such as 2D B-mode US could be biased by possible out-of-plane motion.

Preliminary results obtained on N=1 healthy volunteer confirm that, for the selected region of interest and chosen loads, the tissue out-of-plane movement is important. The verticality of the US CSYS was also checked: the mean (±SD) value of the angle of interest was 4.4° (±1.2°).

Results showed that the ratios between the out-of-plane and in-plane displacements were higher than 0.6 for more than half of the voxels in the ROI2 for all load cases and higher than 1 for L2-L4 for a quarter of the voxels. The inverse correlation between the ratio parameter and the load could be explained by the expulsion of the fluid from the tissues under high deformations. The area of the high norm of the out-of-plane displacement values (more than 0.3 for L1) is theorized to be limited by the possible shielding effect of the fascia layer located in the adipose tissues.

The variation in the behaviour of the soft tissues in response to the reduction in the load from L1 to L2 was observed in different directions. The displacement in the direction of the loading decreased with the decrease in the load, while in two other directions, the values for L2 were higher than the ones for L1. One possible explanation could be the residual deformation left in the tissues.

Several limitations have been identified as a perspective work such as the lack of clinically relevant loading and the inclusion of only one healthy subject. The conclusions of this preliminary study should therefore be considered specific to this application and further work aiming at generalizing these results needs to be performed. However, the results suggest that the 2D US should be used with caution for the evaluation of tissue motion under compression.

# General Conclusion

PU is a condition often affecting people with reduced mobility: elderly, people with disability and those who have to undertake heavy surgeries. When pressure injury occurs, it may have an important effect on the psychological state and Quality of Life of the affected individual. In addition, it has been reported in the literature that the management of PU represents an important financial burden to a health-care system. Preventive PU handling would thus be beneficial to all concerned actors.

**Chapter I** focused on a comprehensive literature review of the previous research related to PU etiology and the development of tools to help decision-making based on these findings. First, the most common body locations for pressure injury, associated tissue composition and organization, and injury stages have been introduced. Current prevention techniques implemented in clinical routine include various risk assessment scales, the use of specific supporting systems like mattresses and cushions, visual skin assessment and frequent repositioning. In many clinical settings, medical professionals use different combinations of these techniques to provide a personalized care. However, an objective parameter that could be used as a predictor for pressure injury development would be beneficial: time and resources of healthcare professionals could then be on those presenting the most risks. To investigate PU etiology, numerous experiments have been conducted starting from the cellular level (Breuls et al. 2003; C. V. C. Bouten et al. 2001) to animal experiments (Ceelen, Stekelenburg, Loerakker, et al. 2008; Loerakker et al. 2011) and human studies. At least two main mechanisms of PU onset have been identified: ischemia/reperfusion injury under moderate sustained loading (Loerakker et al. 2011) and direct cell damage under high intensity loading (Gefen et al. 2008). To address the risk related to external mechanical loading, several numerical models have been developed to attempt to link the risk of pressure injury with the high strains observed in soft tissues. In an ideal world (beside the fact that PU would not exist), 3D imaging modalities like MRI or CT scan would allow to get a thorough information on the soft tissue geometry for building patient-specific FE model. These medical imaging means are unfortunately not easily accessible for prevention purpose. On the other hand, 2D B-mode US imaging is available in most clinical routine imaging technique but provides data with different features.

A gap in the literature has been identified, which supported the objective of this PhD project: the development and evaluation of a 2D US-derived FE model as a substitute for a 3D MRI-derived FE model for personalized PU risk assessment.

As a first step towards this objective, an MRI-compatible experimental setup was conceived allowing both US and MRI geometry data collection with a controlled loading. The thorough description of this setup and acquisition steps were provided in **chapter II**. A 3D printed copy of the US probe was used as a surrogate for indentation for an MRI acquisition. Compressive loads were applied through the indenter with pre-measured weights in four load steps. In the case of the MRI acquisition, a fully unloaded and four loaded configurations were collected, by progressively decreasing the load (note that the unloaded configuration was imaged prior to imaging the volunteer in the different loaded configurations). However, after post-processing, it became apparent that due to the viscoelastic properties of soft tissues and limited amount of time between the acquisitions it would be more beneficial to collect the data by progressively increasing loads. This could be a perspective for this work.

Given the inter-individual variability of tissue mechanical properties, a personalized assessment of the constitutive parameters *in vivo* is paramount in order to feed models that can

accurately predict the finite-strain behavior of biological soft tissues. In the second half of **chapter II** we focused on the identification of the elastic properties of the skin and adipose tissues based on pressure-volume experimental data collected with an aspiration device at the sacral region. The main limitation of this section is that the experimental work was limited to a single healthy volunteer. Given the large inter- and intra-individual anatomical variability and tissue mechanical properties, further investigations are required to consolidate the conclusions that will be obtained in this PhD work.

The next step was the development of the sacrum 3D FE model, which was described in **chapter III**. An MRI scan in the unloaded configuration collected during the first experiment from **chapter II** was used as a basis for model geometry. Material properties were chosen based on the approximation of the experimental data from the literature by a non-linear hyperelastic Yeoh material model for skin, adipose tissue, fascia and muscle. Generic material models for skin and adipose tissue were personalized using the Young's moduli estimated by the inverse calculations on the pressure-volume curves (second experiment from **chapter II)**. Mesh sensitivity analysis, chosen mesh size and boundary conditions were introduced in the chapter. DVC technique was introduced as a possible tool for evaluating the FE model (Trebbi et al. 2022).

In the second half of **chapter III**, the results of the 3D FE simulation were compared with the results of DVC, showing that maximum values and displacement distribution fields were approximated by the FE simulation quite accurately for each of the tested load cases with a relative change being less than 7%. On the other hand, much higher absolute maximum values (up to 43% difference) of the shear strains were predicted by the results of DVC compared to the ones observed with 3D FE model. This raises questions not only about the accuracy of the FE model, but also of the feasibility of using the DVC technique itself for our application: for one of the load cases, the strains estimated by DVC were higher than the ones reported in the literature for a highly deformable tissue (i.e. the tongue in Napadow et al. 1999). A possible reason behind this could be a lower quality of the initial images. Other limitations of the modeling included the manual segmentation of the medical image and the choice of the material properties. Specifically, judging from the simulation results, a sharp change between the elastic properties from adipose tissue to muscle enabled that the muscle tissues stayed mostly undeformed, whereas the results of the DVC did not show such a sharp change in behavior between tissues. 3D FE simulation for the load case with highest load resulted in a 1.2 maximum Green-Lagrange shear strain. This value is higher than the 0.75 value identified by Ceelen et al. (Ceelen, Stekelenburg, Loerakker, et al. 2008) as an injury limit. Thankfully, in our case, the highest load was applied only for 10 minutes and high strain values were observed in a thin tissue layer only.

In the second part of the manuscript, we explored the capacity of an US-derived 2D FE model to simulate the mechanical response of sacral soft tissues under compression loading. The development of the methodology and evaluation against the response predicted by the MRI-based 3D FE model were described in **chapter IV**. One of the limitations was the following: due to US restrictions described in that chapter, a transversal slice of an unloaded MRI image had to be used for tissue segmentation and 2D FE analysis. Load and boundary conditions, material properties and mesh type and size were chosen in line with the ones previously defined in **chapter III**. Comparison between the results predicted by 2D and 3D FE simulations showed that for all four load cases the 2D model overestimated the maximum vertical displacement by up to 30%. The local strain concentrations due to numerical non-linearities were excluded. Resulting shear strains were overestimated by the 2D model by up to 13% in relation to the 3D model. Several possible explanations of that behavior of the 2D

model were identified and discussed: (1) the extension of the geometry and fixed boundary conditions to the sides of the model and (2) the hypothesis of a plane-strain formulation. The perspective work will include the data collection with a US probe allowing to visualize tissues in the unloaded configuration. Possible ways to tackle this challenge could include (1) testing different available US probes and (2) aiming at only the partial data collection on the geometry of the sacral vertebra (instead of the full length) allowing to reduce the tissue thickness for visualization.

The last **chapter V** of the manuscript aimed at addressing one of the limitations identified in **chapter IV**: how much information on soft tissue motion is omitted when the 3D modality is reduced to a 2D modality? For this purpose, the MRI data acquired in **chapter II** was processed to separate the tissue motion into the components acting in plane that could be observed by the 2D US and the ones in the out-of-plane direction. Preliminary results obtained for one healthy individual indicated that the ratios between the out-of-plane and in-plane displacements were higher than 0.6 for more than half of the voxels in the selected region of interest. Additional work should be performed to confirm this observation on more subjects, but the preliminary results suggest that the 2D modality should be used with caution for the evaluation of soft tissue motion in the sacral region. An alternative would be to explore the possibility of using 3D US.

One of the limitations of the loading scenario explored throughout this work was the fact that the artificial loading was performed on the sacrum region while the participant was lying in the prone position, which does not correspond to the clinically relevant situation. As a step towards modelling the clinically relevant loading, a preliminary work was performed on collection of the pressure maps for two subjects in recumbent and sitting positions. Details of this work are provided in **APPENDIX 5**. Our work highlighted the difficulty of exposing the sacral vertebra to the load in some of the healthy volunteers due to the developed muscles and sufficient thickness of soft tissues in the region, while the most at-risk population often suffers from the reduced mobility and, therefore do not have the same tissue organization as healthy individuals.

In practice, surface loads at the skin/support interface have components in both normal (i.e. pressure) and tangential (i.e. shear) directions. Both have been reported to be detrimental to the soft tissues and cause soft tissue breakdown (Ming Zhang and Roberts 1993). In this PhD work, the mechanical response of sacral soft tissue under external pressure was investigated. Yet, the contribution of shear forces to soft tissue health in the sacral region should not be understated, particularly considering that shear stresses are unavoidable in many hospital bed protocols. A perspective work is to extent the current work to account for the impact of shear forces on the risk of pressure ulcer in the sacral region.

To conclude, this project aimed at evaluating the reliability of using a 2D US-based FE model as an alternative to 3D MRI-based FE model for the assessment of the subject-specific risk of PU development. This objective was met, highlighting future directions of the research towards the exploration of 3D US modality, further personalization of the constitutive models representing the soft tissues and subjecting the FE model to the clinically relevant loading.

# References


Agache, P. G., C. Monneur, J. L. Leveque, and J. De Rigal. 1980. “Mechanical Properties and Young’s Modulus of Human Skin in Vivo.” *Archives of Dermatological Research* 269 (3): 221–32. https://doi.org/10.1007/BF00406415.

Akins, Jonathan S., Jaxon J. Vallely, Patricia E. Karg, Kara Kopplin, Amit Gefen, Prerna Poojary-Mazzotta, and David M. Brienza. 2016a. “Feasibility of Freehand Ultrasound to Measure Anatomical Features Associated with Deep Tissue Injury Risk.” *Medical Engineering and Physics* 38 (9): 839–44. https://doi.org/10.1016/j.medengphy.2016.04.026.

———. 2016b. “Feasibility of Freehand Ultrasound to Measure Anatomical Features Associated with Deep Tissue Injury Risk.” *Medical Engineering and Physics* 38 (9): 839–44. https://doi.org/10.1016/j.medengphy.2016.04.026.

Al-Dirini, Rami M A, Matthew P Reed, Jingwen Hu, and Dominic Thewlis. 2016. “Development and Validation of a High Anatomical Fidelity FE Model for the Buttock and Thigh of a Seated Individual.” *Annals of Biomedical Engineering* 44 (9): 2805–16. https://doi.org/10.1007/s10439-016-1560-3.

Alipour, M., K. Mithraratne, R. D. Herbert, and J. Fernandez. 2018. “A Finite Element Muscle Building Block Derived from 3D Ultrasound: Application to the Human Gastrocnemius.” *Computer Methods in Biomechanics and Biomedical Engineering: Imaging and Visualization* 1163: 1–8. https://doi.org/10.1080/21681163.2018.1488222.

Ankrom, Michael A., Richard G. Bennett, Stephen Sprigle, Diane Langemo, Joyce M. Black, Dan R. Berlowitz, and Courtney H. Lyder. 2005. “Pressure-Related Deep Tissue Injury under Intact Skin and the Current Pressure Ulcer Staging Systems.” *Advances in Skin & Wound Care* 18 (1): 35–42. https://doi.org/10.1097/00129334-200501000-00016.

Annaidh, Aisling Ni, Karine Bruyère, Michel Destrade, Michael D. Gilchrist, Corrado Maurini, Melanie Otténio, and Giuseppe Saccomandi. 2012. “Automated Estimation of Collagen Fibre Dispersion in the Dermis and Its Contribution to the Anisotropic Behaviour of Skin.” *Annals of Biomedical Engineering* 40 (8): 1666–78. https://doi.org/10.1007/s10439-012-0542-3.

Aoki, Takahira, Toshiro Ohashi, Takeo Matsumoto, and Masaaki Sato. 1997. “The Pipette Aspiration Applied to the Local Stiffness Measurement of Soft Tissues.” *Annals of Biomedical Engineering*. https://doi.org/10.1007/BF02684197.

Arda, Kemal, Nazan Ciledag, Bilgi Kadri Arabis, Elif Aktas, and Kenan Köse. 2013. “Quantitative Assessment of the Elasticity Values of Liver with Shear Wave Ultrasonographic Elastography.” *Indian J Med Res*, no. 137: 911–15.

Arora, Hari, Ria L. Mitchell, Richard Johnston, Marinos Manolesos, David Howells, Joseph M. Sherwood, Andrew J. Bodey, and Kaz Wanelik. 2021. “Correlating Local Volumetric Tissue Strains with Global Lung Mechanics Measurements.” *Materials* 14 (2): 1–17. https://doi.org/10.3390/ma14020439.

Astruc, Laure, Maurice De Meulaere, Jean François Witz, Vit Nováček, Frédéric Turquier,

Thierry Hoc, and Mathias Brieu. 2018. “Characterization of the Anisotropic Mechanical Behavior of Human Abdominal Wall Connective Tissues.” *Journal of the Mechanical Behavior of Biomedical Materials* 82 (December 2017): 45–50. https://doi.org/10.1016/j.jmbbm.2018.03.012.

Bader, D. L., and C. A. Gant. 1988. “Changes in Transcutaneous Oxygen Tension as a Result of Prolonged Pressures at the Sacrum.” *Clinical Physics and Physiological Measurement* 9 (1): 33–40. https://doi.org/10.1088/0143-0815/9/1/002.

Barrois, B., C. Labalette, P. Rousseau, A. Corbin, D. Colin, F. Allaert, and J. L. Saumet. 2008. “A National Prevalence Study of Pressure Ulcers in French Hospital Inpatients.” *Journal of Wound Care* 17 (9). https://doi.org/10.12968/jowc.2008.17.9.30934.

Barrois, Brigitte, Denis Colin, and François André Allaert. 2018. “Prevalence, Characteristics and Risk Factors of Pressure Ulcers in Public and Private Hospitals Care Units and Nursing Homes in France.” *Hospital Practice (1995)* 46 (1): 30–36. https://doi.org/10.1080/21548331.2018.1418139.

Bauer, Karen, Kathryn Rock, Munier Nazzal, Olivia Jones, and Weikai Qu. 2016. “Pressure Ulcers in the United States’ Inpatient Population From 2008 to 2012: Results of a Retrospective Nationwide Study.” *Ostomy Wound Management* 62 (11): 30–38.

Beeckman, Dimitri, Lisette Schoonhoven, Jacqui Fletcher, Kátia Furtado, Lena Gunningberg, Hilde Heyman, Christina Lindholm, Louis Paquay, José Verdú, and Tom Defloor. 2007. “EPUAP Classification System for Pressure Ulcers: European Reliability Study.” *Journal of Advanced Nursing* 60 (6): 682–91. https://doi.org/10.1111/j.1365-2648.2007.04474.x.

Bell, Muyinatu A.Lediju, Shalki Kumar, Lily Kuo, H. Tutkun Sen, Iulian Iordachita, and Peter Kazanzides. 2016. “Toward Standardized Acoustic Radiation Force (ARF)-Based Ultrasound Elasticity Measurements with Robotic Force Control.” *IEEE Transactions on Biomedical Engineering* 63 (7): 1517–24. https://doi.org/10.1109/TBME.2015.2497245.

Bhattacharya, Surajit, and R. Mishra. 2015. “Pressure Ulcers: Current Understanding and Newer Modalities of Treatment.” *Indian Journal of Plastic Surgery* 48 (1): 4–16. https://doi.org/10.4103/0970-0358.155260.

Black, Joyce M. 2005. “Moving toward Consensus on Deep Tissue Injury and Pressure Ulcer Staging.” *Advances in Skin & Wound Care* 18 (8). https://doi.org/10.1097/00129334-200510000-00008.

Böl, Markus, Rahul Iyer, Johannes Dittmann, Mayra Garcés-Schröder, and Andreas Dietzel. 2019. “Investigating the Passive Mechanical Behaviour of Skeletal Muscle Fibres: Micromechanical Experiments and Bayesian Hierarchical Modelling.” *Acta Biomaterialia* 92: 277–89. https://doi.org/10.1016/j.actbio.2019.05.015.

Bouten, C. V.C., M. M. Knight, D. A. Lee, and D. L. Bader. 2001. “Compressive Deformation and Damage of Muscle Cell Subpopulations in a Model System.” *Annals of Biomedical Engineering* 29 (2): 153–63. https://doi.org/10.1114/1.1349698.

Bouten, Carlijn V., Cees W. Oomens, Frank P. Baaijens, and Daniel L. Bader. 2003. “The

Etiology of Pressure Ulcers: Skin Deep or Muscle Bound?" *Archives of Physical Medicine and Rehabilitation* 84 (4): 616–19. https://doi.org/10.1053/apmr.2003.50038.

Breuls, R. G.M., C. V.C. Bouten, C. W.J. Oomens, D. L. Bader, and F. P.T. Baaijens. 2003. "Compression Induced Cell Damage in Engineered Muscle Tissue: An in Vitro Model to Study Pressure Ulcer Aetiology." *Annals of Biomedical Engineering* 31 (11): 1357–64. https://doi.org/10.1114/1.1624602.

Briot, N., G. Chagnon, N. Connesson, and Y. Payan. 2022. "In Vivo Measurement of Breast Tissues Stiffness Using a Light Aspiration Device." *Clinical Biomechanics* 99 (October): 105743. https://doi.org/10.1016/J.CLINBIOMECH.2022.105743.

Bronneberg, D. 2007. *Biochemical Markers for Early Detection of Superficial Pressure Ulcers*. https://doi.org/10.6100/IR629192.

Bucki, M., V. Luboz, C. Lobos, N. Vuillerme, F. Cannard, B. Diot, and Y. Payan. 2012. "Patient-Specific Finite Element Model of the Buttocks for Pressure Ulcer Prevention--Linear versus Non-Linear Modelling." *Computer Methods in Biomechanics and Biomedical Engineering* 15 Suppl 1 (September): 38–40. https://doi.org/10.1080/10255842.2012.713681.

Call, Evan, Thomas Hetzel, Chad McLean, Joshua N. Burton, and Craig Oberg. 2017. "Off Loading Wheelchair Cushion Provides Best Case Reduction in Tissue Deformation as Indicated by MRI." *Journal of Tissue Viability* 26 (3): 172–79. https://doi.org/10.1016/j.jtv.2017.05.002.

Ceelen, K. K., A. Stekelenburg, S. Loerakker, G. J. Strijkers, D. L. Bader, K. Nicolay, F. P.T. Baaijens, and C. W.J. Oomens. 2008. "Compression-Induced Damage and Internal Tissue Strains Are Related." *Journal of Biomechanics* 41 (16): 3399–3404. https://doi.org/10.1016/j.jbiomech.2008.09.016.

Ceelen, K. K., A. Stekelenburg, J. L.J. Mulders, G. J. Strijkers, F. P.T. Baaijens, K. Nicolay, and C. W.J. Oomens. 2008. "Validation of a Numerical Model of Skeletal Muscle Compression with MR Tagging: A Contribution to Pressure Ulcer Research." *Journal of Biomechanical Engineering* 130 (6): 1–8. https://doi.org/10.1115/1.2987877.

Chen, Sheng, Justin Scott, Tamara Reid Bush, and Sara Roccabianca. 2020. "Inverse Finite Element Characterization of the Human Thigh Soft Tissue in the Seated Position." *Biomechanics and Modeling in Mechanobiology* 19 (1): 305–16. https://doi.org/10.1007/s10237-019-01212-7.

Choe, Sung Sik, Jin Young Huh, In Jae Hwang, Jong In Kim, and Jae Bum Kim. 2016. "Adipose Tissue Remodeling: Its Role in Energy Metabolism and Metabolic Disorders." *Frontiers in Endocrinology* 7 (APR): 1–16. https://doi.org/10.3389/fendo.2016.00030.

Clark, M., L. B. Rowland, H. A. Wood, and R. A. Crow. 1989. "Measurement of Soft Tissue Thickness over the Sacrum of Elderly Hospital Patients Using B-Mode Ultrasound." *Journal of Biomedical Engineering* 11 (3): 200–202. https://doi.org/10.1016/0141-5425(89)90141-6.

Coleman, Susanne, Claudia Gorecki, E. Andrea Nelson, S. José Closs, Tom Defloor, Ruud

Halfens, Amanda Farrin, Julia Brown, Lisette Schoonhoven, and Jane Nixon. 2013. “Patient Risk Factors for Pressure Ulcer Development: Systematic Review.” *International Journal of Nursing Studies* 50 (7): 974–1003. https://doi.org/10.1016/j.ijnurstu.2012.11.019.

Dabnichki, P. A., A. D. Crocombe, and S. C. Hughes. 1994. “Deformation and Stress Analysis of Supported Buttock Contact.” *Proceedings of the Institution of Mechanical Engineers, Part H: Journal of Engineering in Medicine* 208 (1): 9–17. https://doi.org/10.1177/095441199420800102.

Dąbrowska, A. K., F. Spano, S. Derler, C. Adlhart, N. D. Spencer, and R. M. Rossi. 2018. “The Relationship between Skin Function, Barrier Properties, and Body-Dependent Factors.” *Skin Research and Technology* 24 (2): 165–74. https://doi.org/10.1111/srt.12424.

Dealey, Carol, J Posnett, and A Walker. 2012. “The Cost of Pressure Ulcers in the United Kingdom.” *Journal of Wound Care* 21 (June): 261–66.

Defloor, Tom, and Lisette Schoonhoven. 2004. “Inter-Rater Reliability of the EPUAP Pressure Ulcer Classification System Using Photographs.” *Journal of Clinical Nursing* 13 (8): 952–59. https://doi.org/10.1111/j.1365-2702.2004.00974.x.

Demarré, Liesbet, Aurélie Van Lancker, Ann Van Hecke, Sofie Verhaeghe, Maria Grypdonck, Juul Lemey, Lieven Annemans, and Dimitri Beeckman. 2015. “The Cost of Prevention and Treatment of Pressure Ulcers: A Systematic Review.” *International Journal of Nursing Studies* 52 (11): 1754–74. https://doi.org/10.1016/j.ijnurstu.2015.06.006.

Diridollou, S., F. Patat, F. Gens, L. Vaillant, D. Black, J. M. Lagarde, Y. Gall, and M. Berson. 2000. “In Vivo Model of the Mechanical Properties of the Human Skin under Suction.” *Skin Research and Technology* 6 (4): 214–21. https://doi.org/10.1034/j.1600-0846.2000.006004214.x.

Doridam, J., A. Macron, C. Vergari, A. Verney, P. Y. Rohan, and H. Pillet. 2018. “Feasibility of Sub-Dermal Soft Tissue Deformation Assessment Using B-Mode Ultrasound for Pressure Ulcer Prevention.” *Journal of Tissue Viability* 27 (4): 238–43. https://doi.org/10.1016/j.jtv.2018.08.002.

Downie, Fiona, Heidi Guy, Pauline Gilroy, Dawn Royall, and Sarah Davies. 2013. “Are 95% of Hospital-Acquired Pressure Ulcers Avoidable?” 9 (3).

Dubois, Guillaume, Walid Kheireddine, Claudio Vergari, Dominique Bonneau, Patricia Thoreux, Philippe Rouch, Mickael Tanter, Jean Luc Gennisson, and Wafa Skalli. 2015. “Reliable Protocol for Shear Wave Elastography of Lower Limb Muscles at Rest and During Passive Stretching.” *Ultrasound in Medicine and Biology* 41 (9): 2284–91. https://doi.org/10.1016/j.ultrasmedbio.2015.04.020.

Elahi, Seyed Ali, Nathanael Connesson, and Yohan Payan. 2018. “DISPOSABLE SYSTEM for IN-VIVO MECHANICAL CHARACTERIZATION of SOFT TISSUES BASED on VOLUME MEASUREMENT.” *Journal of Mechanics in Medicine and Biology* 18 (4): 1–17. https://doi.org/10.1142/S0219519418500379.

Essex, Holly N., Michael Clark, Joyce Sims, Ann Warriner, and Nicky Cullum. 2009. "Health-Related Quality of Life in Hospital Inpatients with Pressure Ulceration: Assessment Using Generic Health-Related Quality of Life Measures." *Wound Repair and Regeneration* 17 (6): 797–805. https://doi.org/10.1111/j.1524-475X.2009.00544.x.

Fougeron, Nolwenn, Nathanaël Connesson, Grégory Chagnon, Thierry Alonso, Laurent Pasquinet, Manuelle Bahuon, Eugénie Guillin, Antoine Perrier, and Yohan Payan. 2022. "New Pressure Ulcers Dressings to Alleviate Human Soft Tissues: A Finite Element Study." *Journal of Tissue Viability*, no. December 2021. https://doi.org/10.1016/j.jtv.2022.05.007.

Fougeron, Nolwenn, Pierre-Yves Rohan, Diane Haering, Jean-Loïc Rose, Xavier Bonnet, and Hélène Pillet. 2020. "Combining Freehand Ultrasound-Based Indentation and Inverse Finite Element Modelling for the Identification of Hyperelastic Material Properties of Thigh Soft Tissues." *Journal of Biomechanical Engineering*, no. c: 1–22. https://doi.org/10.1115/1.4046444.

Galhardo, Carlucio, Leila Blanes, Yara Juliano, and Lydia Masako Ferreira. 2010. "Health-Related Quality of Life and Depression in Older Patients With Pressure Ulcers." *Wounds* 22 (1): 20–26.

Garber, Susan L., Diana H. Rintala, Karen A. Hart, and Marcus J. Fuhrer. 2000. "Pressure Ulcer Risk in Spinal Cord Injury: Predictors of Ulcer Status over 3 Years." *Archives of Physical Medicine and Rehabilitation* 81 (4): 465–71. https://doi.org/10.1053/mr.2000.3889.

Gawlitta, Debby, Wei Li, Cees W.J. Oomens, Frank P.T. Baaijens, Dan L. Bader, and Carlijn V.C. Bouten. 2007. "The Relative Contributions of Compression and Hypoxia to Development of Muscle Tissue Damage: An in Vitro Study." *Annals of Biomedical Engineering* 35 (2): 273–84. https://doi.org/10.1007/s10439-006-9222-5.

Gefen, Amit, Bastiaan van Nierop, Dan L. Bader, and Cees W. Oomens. 2008. "Strain-Time Cell-Death Threshold for Skeletal Muscle in a Tissue-Engineered Model System for Deep Tissue Injury." *Journal of Biomechanics* 41 (9): 2003–12. https://doi.org/10.1016/j.jbiomech.2008.03.039.

Gefen, Amit, and Daphne Weihs. 2016. "Cytoskeleton and Plasma-Membrane Damage Resulting from Exposure to Sustained Deformations: A Review of the Mechanobiology of Chronic Wounds." *Medical Engineering and Physics* 38 (9): 828–33. https://doi.org/10.1016/j.medengphy.2016.05.014.

Goh, J.C.H, P.V.S. Lee, S.L. Toh, and C.K. Ooi. 2005. "Development of an Integrated CAD-FEA Process for below-Knee Prosthetic Sockets." *Clinical Biomechanics*, no. 20: 623–29.

Gras, Laure Lise, David Mitton, Philippe Viot, and Sébastien Laporte. 2012. "Hyper-Elastic Properties of the Human Sternocleidomastoideus Muscle in Tension." *Journal of the Mechanical Behavior of Biomedical Materials* 15: 131–40. https://doi.org/10.1016/j.jmbbm.2012.06.013.

Gray, Robert J., David Voegeli, and Dan L. Bader. 2016. "Features of Lymphatic Dysfunction

in Compressed Skin Tissues - Implications in Pressure Ulcer Aetiology." *Journal of Tissue Viability* 25 (1): 26–31. https://doi.org/10.1016/j.jtv.2015.12.005.

Haen, T. X., A. Roux, M. Soubeyrand, and S. Laporte. 2017. "Shear Waves Elastography for Assessment of Human Achilles Tendon's Biomechanical Properties: An Experimental Study." *Journal of the Mechanical Behavior of Biomedical Materials* 69: 178–84. https://doi.org/10.1016/j.jmbbm.2017.01.007.

Harris, K., P. M. Walker, D. A.G. Mickle, R. Harding, R. Gatley, G. J. Wilson, B. Kuzon, N. McKee, and A. D. Romaschin. 1986. "Metabolic Response of Skeletal Muscle to Ischemia." *American Journal of Physiology - Heart and Circulatory Physiology* 250 (2). https://doi.org/10.1152/ajpheart.1986.250.2.h213.

Hendriks, F. M., D. Brokken, J. T.W.M. van Eemeren, C. W.J. Oomens, F. P.T. Baaijens, and J. B.A.M. Horsten. 2003. "A Numerical-Experimental Method to Characterize the Non-Linear Mechanical Behavior of Human Skin." *Skin Research and Technology* 9 (3): 274–83. https://doi.org/10.1034/j.1600-0846.2003.00019.x.

Houten, Elijah E.W. Van, Marvin M. Doyley, Francis E. Kennedy, John B. Weaver, and Keith D. Paulsen. 2003. "Initial in Vivo Experience with Steady-State Subzone-Based MR Elastography of the Human Breast." *Journal of Magnetic Resonance Imaging* 17 (1): 72–85. https://doi.org/10.1002/jmri.10232.

Houwing, R., M. Overgoor, M. Kon, G. Jansen, B. S. van Asbeck, and J. R. Haalboom. 2000. *Pressure-Induced Skin Lesions in Pigs: Reperfusion Injury and the Effects of Vitamin E. Journal of Wound Care*. Vol. 9. https://doi.org/10.12968/jowc.2000.9.1.25939.

Jiang, Li-ping, Qian Tu, Yanyan Wang, and En Zhang. 2011. "Ischemia-Reperfusion Injury-Induced Histological Changes Affecting Early Stage Pressure Ulcer Development in a Rat Model." *Ostomy Wound Management* 55 (August): 52–56.

Kappert, K. D.R., N. Connesson, S. A. Elahi, S. Boonstra, A. J.M. Balm, F. van der Heijden, and Y. Payan. 2021. "In-Vivo Tongue Stiffness Measured by Aspiration: Resting vs General Anesthesia." *Journal of Biomechanics* 114 (December): 110147. https://doi.org/10.1016/j.jbiomech.2020.110147.

Klein, Stefan, Marius Staring, Keelin Murphy, Max A. Viergever, and Josien P.W. Pluim. 2010. "Elastix: A Toolbox for Intensity-Based Medical Image Registration." *IEEE Transactions on Medical Imaging* 29 (1): 196–205. https://doi.org/10.1109/TMI.2009.2035616.

Koppenhaver, Shane, Emily Gaffney, Amber Oates, Laura Eberle, Brian Young, Jeffrey Hebert, Laurel Proulx, and Minoru Shinohara. 2020. "Lumbar Muscle Stiffness Is Different in Individuals with Low Back Pain than Asymptomatic Controls and Is Associated with Pain and Disability, but Not Common Physical Examination Findings." *Musculoskeletal Science and Practice* 45 (November): 102078. https://doi.org/10.1016/j.msksp.2019.102078.

Krause, James S., and Lynne Broderick. 2004. "Patterns of Recurrent Pressure Ulcers after Spinal Cord Injury: Identification of Risk and Protective Factors 5 or More Years after Onset." *Archives of Physical Medicine and Rehabilitation* 85 (8): 1257–64.

https://doi.org/10.1016/j.apmr.2003.08.108.

Lawton, Sarah. 2019. “Skin 1: The Structure and Functions of the Skin.” *Clinical Practice Systems of Life Skin* 115 (12): 1–2. http://www.hse.gov.uk/skin/professional/causes/structure.htm.

Levy, Ayelet, and Amit Gefen. 2017. “Assessment of the Biomechanical Effects of Prophylactic Sacral Dressings on Tissue Loads: A Computational Modeling Analysis.” *Ostomy Wound Management* 63 (10): 48–55. https://doi.org/10.25270/owm.10.4855.

Levy, Ayelet, Kara Kopplin, and Amit Gefen. 2013. “Simulations of Skin and Subcutaneous Tissue Loading in the Buttocks While Regaining Weight-Bearing after a Push-up in Wheelchair Users.” *Journal of the Mechanical Behavior of Biomedical Materials* 28: 436–47. https://doi.org/10.1016/j.jmbbm.2013.04.015.

Lin, F., B. Moran, J. Bankard, R. Hendrix, and M. Makhsous. 2004. “A Subject-Specific FEM Model for Evaluating Buttock Tissue Response under Sitting Load.” *Annual International Conference of the IEEE Engineering in Medicine and Biology - Proceedings* 26 VII (C): 5088–91.

Linder-Ganz, E., and A. Gefen. 2004. “Mechanical Compression-Induced Pressure Sores in Rat Hindlimb: Muscle Stiffness, Histology, and Computational Models.” *Journal of Applied Physiology* 96 (6): 2034–49. https://doi.org/10.1152/japplphysiol.00888.2003.

Linder-Ganz, Eran, Santiego Engelberg, Mickey Scheinowitz, and Amit Gefen. 2006. “Pressure-Time Cell Death Threshold for Albino Rat Skeletal Muscles as Related to Pressure Sore Biomechanics.” *Journal of Biomechanics* 39 (14): 2725–32. https://doi.org/10.1016/j.jbiomech.2005.08.010.

Linder-Ganz, Eran, Noga Shabshin, Yacov Itzchak, and Amit Gefen. 2007. “Assessment of Mechanical Conditions in Sub-Dermal Tissues during Sitting: A Combined Experimental-MRI and Finite Element Approach.” *Journal of Biomechanics* 40 (7): 1443–54. https://doi.org/10.1016/j.jbiomech.2006.06.020.

Linder-Ganz, Eran, Noga Shabshin, Yacov Itzchak, Ziva Yizhar, Itzhak Siev-Ner, and Amit Gefen. 2008. “Strains and Stresses in Sub-Dermal Tissues of the Buttocks Are Greater in Paraplegics than in Healthy during Sitting.” *Journal of Biomechanics* 41 (3): 567–80. https://doi.org/10.1016/j.jbiomech.2007.10.011.

Linder-Ganz, Eran, Gilad Yarnitzky, Ziva Yizhar, Itzhak Siev-Ner, and Amit Gefen. 2009. “Real-Time Finite Element Monitoring of Sub-Dermal Tissue Stresses in Individuals with Spinal Cord Injury: Toward Prevention of Pressure Ulcers.” *Annals of Biomedical Engineering* 37 (2): 387–400. https://doi.org/10.1007/s10439-008-9607-8.

Loerakker, S., E. Manders, G. J. Strijkers, K. Nicolay, F. P.T. Baaijens, D. L. Bader, and C. W.J. Oomens. 2011. “The Effects of Deformation, Ischemia, and Reperfusion on the Development of Muscle Damage during Prolonged Loading.” *Journal of Applied Physiology* 111 (4): 1168–77. https://doi.org/10.1152/japplphysiol.00389.2011.

Loerakker, S., L. R. Solis, D. L. Bader, F. P.T. Baaijens, V. K. Mushahwar, and C. W.J. Oomens. 2013. “How Does Muscle Stiffness Affect the Internal Deformations within the

Soft Tissue Layers of the Buttocks under Constant Loading?" *Computer Methods in Biomechanics and Biomedical Engineering* 16 (5): 520–29. https://doi.org/10.1080/10255842.2011.627682.

Luboz, Vincent, Mathieu Bailet, Christelle Boichon Grivot, Michel Rochette, Bruno Diot, Marek Bucki, and Yohan Payan. 2018a. "Personalized Modeling for Real-Time Pressure Ulcer Prevention in Sitting Posture." *Journal of Tissue Viability* 27 (1): 54–58. https://doi.org/10.1016/j.jtv.2017.06.002.

———. 2018b. "Personalized Modeling for Real-Time Pressure Ulcer Prevention in Sitting Posture." *Journal of Tissue Viability* 27 (1): 54–58. https://doi.org/10.1016/j.jtv.2017.06.002.

Luboz, Vincent, Marion Petrizelli, Marek Bucki, Bruno Diot, Nicolas Vuillerme, and Yohan Payan. 2014a. "Biomechanical Modeling to Prevent Ischial Pressure Ulcers." *Journal of Biomechanics* 47 (10): 2231–36. https://doi.org/10.1016/j.jbiomech.2014.05.004.

———. 2014b. "Biomechanical Modeling to Prevent Ischial Pressure Ulcers." *Journal of Biomechanics* 47 (10): 2231–36. https://doi.org/10.1016/j.jbiomech.2014.05.004.

Luboz, Vincent, Emmanuel Promayon, Grégory Chagnon, Thierry Alonso, Denis Favier, Christine Barthod, and Yohan Payan. 2012. "Validation of a Light Aspiration Device for In Vivo Soft Tissue Characterization (LASTIC)." *Studies in Mechanobiology, Tissue Engineering and Biomaterials* 11: 243–56. https://doi.org/10.1007/8415_2012_123.

Macron, Aurélien, Hélène Pillet, Jennifer Doridam, Isabelle Rivals, Mohammad Javad Sadeghinia, Alexandre Verney, and Pierre Yves Rohan. 2020. "Is a Simplified Finite Element Model of the Gluteus Region Able to Capture the Mechanical Response of the Internal Soft Tissues under Compression?" *Clinical Biomechanics* 71: 92–100. https://doi.org/10.1016/j.clinbiomech.2019.10.005.

Macron, Aurélien, Hélène Pillet, Jennifer Doridam, Alexandre Verney, and Pierre Yves Rohan. 2018. "Development and Evaluation of a New Methodology for the Fast Generation of Patient-Specific Finite Element Models of the Buttock for Sitting-Acquired Deep Tissue Injury Prevention." *Journal of Biomechanics* 79: 173–80. https://doi.org/10.1016/j.jbiomech.2018.08.001.

Magny, Emmanuelle, Helene Vallet, Judith Cohen-Bittan, Mathieu Raux, Antony Meziere, Marc Verny, Bruno Riou, Frédéric Khiami, and Jacques Boddaert. 2017. "Pressure Ulcers Are Associated with 6-Month Mortality in Elderly Patients with Hip Fracture Managed in Orthogeriatric Care Pathway." *Archives of Osteoporosis* 12 (1). https://doi.org/10.1007/s11657-017-0365-9.

Mak, A. F.T., G. H.W. Liu, and S. Y. Lee. 1994. "Biomechanical Assessment of Below-Knee Residual Limb Tissue." *Journal of Rehabilitation Research and Development*.

Makhsous, Mohsen, Dohyung Lim, Ronald Hendrix, James Bankard, William Z. Rymer, and Fang Lin. 2007. "Finite Element Analysis for Evaluation of Pressure Ulcer on the Buttock: Development and Validation." *IEEE Transactions on Neural Systems and Rehabilitation Engineering* 15 (4): 517–25. https://doi.org/10.1109/TNSRE.2007.906967.

Miller-Young, Janice E., Neil A. Duncan, and Gamal Baroud. 2002. “Material Properties of the Human Calcaneal Fat Pad in Compression: Experiment and Theory.” *Journal of Biomechanics* 35 (12): 1523–31. https://doi.org/10.1016/S0021-9290(02)00090-8.

Ming Zhang, and V. C. Roberts. 1993. “The Effect of Shear Forces Externally Applied to Skin Surface on Underlying Tissues.” *Journal of Biomedical Engineering* 15 (6): 451–56. https://doi.org/10.1016/0141-5425(93)90057-6.

Moerman, Kevin M., Andre M.J. Sprengers, Aart J. Nederveen, and Ciaran K. Simms. 2013. “A Novel MRI Compatible Soft Tissue Indentor and Fibre Bragg Grating Force Sensor.” *Medical Engineering and Physics* 35 (4): 486–99. https://doi.org/10.1016/j.medengphy.2012.06.014.

Moerman, Kevin M., Marc van Vijven, Leandro R. Solis, Eline E. van Haaften, Arjan C.Y. Loenen, Vivian K. Mushahwar, and Cees W.J. Oomens. 2017. “On the Importance of 3D, Geometrically Accurate, and Subject-Specific Finite Element Analysis for Evaluation of in-Vivo Soft Tissue Loads.” *Computer Methods in Biomechanics and Biomedical Engineering* 20 (5): 483–91. https://doi.org/10.1080/10255842.2016.1250259.

Mott, P. H., J. R. Dorgan, and C. M. Roland. 2008. “The Bulk Modulus and Poisson’s Ratio of ‘Incompressible’ Materials.” *Journal of Sound and Vibration* 312 (4–5): 572–75. https://doi.org/10.1016/j.jsv.2008.01.026.

Napadow, Vitaly J., Qun Chen, Van J. Wedeen, and Richard J. Gilbert. 1999. “Intramural Mechanics of the Human Tongue in Association with Physiological Deformations.” *Journal of Biomechanics* 32 (1): 1–12. https://doi.org/10.1016/S0021-9290(98)00109-2.

Ní Annaidh, Aisling, Karine Bruyère, Michel Destrade, Michael D. Gilchrist, and Mélanie Otténio. 2012. “Characterization of the Anisotropic Mechanical Properties of Excised Human Skin.” *Journal of the Mechanical Behavior of Biomedical Materials* 5 (1): 139–48. https://doi.org/10.1016/j.jmbbm.2011.08.016.

Olszewski, Waldemar L. 2003. “Pathophysiological Aspects of Lymphedema” 1 (3): 235–43.

Oomens, C. W.J., O. F.J.T. Bressers, E. M.H. Bosboom, C. V.C. Bouten, and D. L. Bader. 2003. “Can Loaded Interface Characteristics Influence Strain Distributions in Muscle Adjacent to Bony Prominences?” *Computer Methods in Biomechanics and Biomedical Engineering* 6 (3): 171–80. https://doi.org/10.1080/1025584031000121034.

Oomens, C. W.J., W. Zenhorst, M. Broek, B. Hemmes, M. Poeze, P. R.G. Brink, and D. L. Bader. 2013. “A Numerical Study to Analyse the Risk for Pressure Ulcer Development on a Spine Board.” *Clinical Biomechanics* 28 (7): 736–42. https://doi.org/10.1016/j.clinbiomech.2013.07.005.

Oomens, Cees W.J., Daniel L. Bader, Sandra Loerakker, and Frank Baaijens. 2015. “Pressure Induced Deep Tissue Injury Explained.” *Annals of Biomedical Engineering* 43 (2): 297–305. https://doi.org/10.1007/s10439-014-1202-6.

Pailler-Mattei, C., S. Bec, and H. Zahouani. 2008. “In Vivo Measurements of the Elastic Mechanical Properties of Human Skin by Indentation Tests.” *Medical Engineering and*

*Physics* 30 (5): 599–606. https://doi.org/10.1016/j.medengphy.2007.06.011.

Pathak, A. P., M. B. Silver-Thorn, C. A. Thierfelder, and T. E. Prieto. 1998. "A Rate-Controlled Indentor for in Vivo Analysis of Residual Limb Tissues." *IEEE Transactions on Rehabilitation Engineering* 6 (1): 12–20. https://doi.org/10.1109/86.662616.

Peeters, E. A.G., C. W.J. Oomens, C. V.C. Bouten, D. L. Bader, and F. P.T. Baaijens. 2005. "Mechanical and Failure Properties of Single Attached Cells under Compression." *Journal of Biomechanics* 38 (8): 1685–93. https://doi.org/10.1016/j.jbiomech.2004.07.018.

Peirce, Shayn M., Thomas C. Skalak, and George T. Rodeheaver. 2000. "Ischemia-Reperfusion Injury in Chronic Pressure Ulcer Formation: A Skin Model in the Rat." *Wound Repair and Regeneration* 8 (1): 68–76. https://doi.org/10.1046/j.1524-475X.2000.00068.x.

Polliack, Adrian, Richard Taylor, and Dan Bader. 1997. "Sweat Analysis Following Pressure Ischaemia in a Group of Debilitated Subjects." *Journal of Rehabilitation Research and Development* 34 (3): 303–8.

Reddy, Narender P., George Van B. Cochran, and Thomas A. Krouskop. 1981. "Interstitial Fluid Flow as a Factor in Decubitus Ulcer Formation." *Journal of Biomechanics* 14 (12): 879–81. https://doi.org/10.1016/0021-9290(81)90015-4.

Redelings, Matthew D., Nolan E. Lee, and Frank Sorvillo. 2005. "Pressure Ulcers: More Lethal than We Thought?" *Advances in Skin & Wound Care* 18 (7): 367–72. https://doi.org/10.1097/00129334-200509000-00010.

Sadler, Zachary, Justin Scott, Joshua Drost, Sheng Chen, Sara Roccabianca, and Tamara Reid Bush. 2018. "Initial Estimation of the in Vivo Material Properties of the Seated Human Buttocks and Thighs." *International Journal of Non-Linear Mechanics* 107: 77–85. https://doi.org/10.1016/j.ijnonlinmec.2018.09.007.

Šateková, Lenka, Katarína Žiaková, and Renáta Zeleníková. 2017. "Predictive Validity of the Braden Scale, Norton Scale, and Waterlow Scale in the Czech Republic." *International Journal of Nursing Practice* 23 (1): 1–10. https://doi.org/10.1111/ijn.12499.

Scott, Justin, Sheng Chen, Sara Roccabianca, and Tamara Reid Bush. 2020. "The Effects of Body Position on the Material Properties of Soft Tissue in the Human Thigh." *Journal of the Mechanical Behavior of Biomedical Materials* 110 (November 2019): 103964. https://doi.org/10.1016/j.jmbbm.2020.103964.

Sheerin, Fintan, and Ruairi de Frein. 2007. "The Occipital and Sacral Pressures Experienced by Healthy Volunteers Under Spinal Immobilization: A Trial of Three Surfaces." *Journal of Emergency Nursing* 33 (5): 447–50. https://doi.org/10.1016/j.jen.2006.11.004.

Soetens, J. F.J., P. R. Worsley, D. L. Bader, and C. W.J. Oomens. 2019. "Investigating the Influence of Intermittent and Continuous Mechanical Loading on Skin through Non-Invasive Sampling of IL-1α." *Journal of Tissue Viability* 28 (1): 1–6. https://doi.org/10.1016/j.jtv.2018.12.003.

Soetens, J. F.J., P. R. Worsley, J. M. Herniman, G. J. Langley, D. L. Bader, and C. W.J. Oomens. 2019. *The Expression of Anaerobic Metabolites in Sweat and Sebum from Human Skin Subjected to Intermittent and Continuous Mechanical Loading*. *Journal of Tissue Viability*. Tissue Viability Society. https://doi.org/10.1016/j.jtv.2019.10.001.

Sommer, Gerhard, Maximilian Eder, Laszlo Kovacs, Heramb Pathak, Lars Bonitz, Christoph Mueller, Peter Regitnig, and Gerhard A. Holzapfel. 2013. "Multiaxial Mechanical Properties and Constitutive Modeling of Human Adipose Tissue: A Basis for Preoperative Simulations in Plastic and Reconstructive Surgery." *Acta Biomaterialia* 9 (11): 9036–48. https://doi.org/10.1016/j.actbio.2013.06.011.

Sonenblum, Sharon E, Jason Ma, Stephen H Sprigle, Thomas R Hetzel, and John McKay Cathcart. 2018. "Measuring the Impact of Cushion Design on Buttocks Tissue Deformation: An MRI Approach." *Journal of Tissue Viability* 27 (3): 162–72. https://doi.org/10.1016/j.jtv.2018.04.001.

Sonenblum, Sharon Eve, Stephen H. Sprigle, John Mc Kay Cathcart, and Robert John Winder. 2013. "3-Dimensional Buttocks Response to Sitting: A Case Report." *Journal of Tissue Viability* 22 (1): 12–18. https://doi.org/10.1016/j.jtv.2012.11.001.

———. 2015. "3D Anatomy and Deformation of the Seated Buttocks." *Journal of Tissue Viability* 24 (2): 51–61. https://doi.org/10.1016/j.jtv.2015.03.003.

Sopher, Ran, Jane Nixon, Claudia Gorecki, and Amit Gefen. 2010. "Exposure to Internal Muscle Tissue Loads under the Ischial Tuberosities during Sitting Is Elevated at Abnormally High or Low Body Mass Indices." *Journal of Biomechanics* 43 (2): 280–86. https://doi.org/10.1016/j.jbiomech.2009.08.021.

Sree, Vivek D., Manuel K. Rausch, and Adrian B. Tepole. 2019. "Linking Microvascular Collapse to Tissue Hypoxia in a Multiscale Model of Pressure Ulcer Initiation." *Biomechanics and Modeling in Mechanobiology*, no. 0123456789. https://doi.org/10.1007/s10237-019-01187-5.

Stecco, Carla, Veronica Macchi, Andrea Porzionato, Fabrice Duparc, and Raffaele De Caro. 2011. "The Fascia: The Forgotten Structure." *Italian Journal of Anatomy and Embryology* 116 (3): 127–38.

Stekelenburg, A., C. W.J. Oomens, G. J. Strijkers, L. De Graaf, D. L. Bader, and K. Nicolay. 2006. "A New MR-Compatible Loading Device to Study in Vivo Muscle Damage Development in Rats Due to Compressive Loading." *Medical Engineering and Physics* 28 (4): 331–38. https://doi.org/10.1016/j.medengphy.2005.07.005.

Stekelenburg, Anke, Gustav J. Strijkers, Henry Parusel, Dan L. Bader, Klaas Nicolay, and Cees W. Oomens. 2007. "Role of Ischemia and Deformation in the Onset of Compression-Induced Deep Tissue Injury: MRI-Based Studies in a Rat Model." *Journal of Applied Physiology* 102 (5): 2002–11. https://doi.org/10.1152/japplphysiol.01115.2006.

Swaine, Jillian M., Andrew Moe, William Breidahl, Daniel L. Bader, Cees W.J. Oomens, Leanne Lester, Edmond O'Loughlin, Nick Santamaria, and Michael C. Stacey. 2018. "Adaptation of a MR Imaging Protocol into a Real-Time Clinical Biometric Ultrasound

Protocol for Persons with Spinal Cord Injury at Risk for Deep Tissue Injury: A Reliability Study." *Journal of Tissue Viability* 27 (1): 32–41. https://doi.org/10.1016/j.jtv.2017.07.004.

Tabibiazar, Raymond, Lauren Cheung, Jennifer Han, Jeffrey Swanson, Andreas Beilhack, Andrew An, Soheil S. Dadras, et al. 2006. "Inflammatory Manifestations of Experimental Lymphatic Insufficiency." *PLoS Medicine* 3 (7): 1114–39. https://doi.org/10.1371/journal.pmed.0030254.

Tavana, S., J. N. Clark, J. Prior, N. Baxan, S. D. Masouros, N. Newell, and U. Hansen. 2020. "Quantifying Deformations and Strains in Human Intervertebral Discs Using Digital Volume Correlation Combined with MRI (DVC-MRI)." *Journal of Biomechanics* 102: 109604. https://doi.org/10.1016/j.jbiomech.2020.109604.

Tayyib, Nahla, and Fiona Coyer. 2016. "Effectiveness of Pressure Ulcer Prevention Strategies for Adult Patients in Intensive Care Units: A Systematic Review Protocol." *JBI Database of Systematic Reviews and Implementation Reports* 14 (3): 35–44. https://doi.org/10.11124/JBISRIR-2016-2400.

Todd, B.; Thacker, J. 1994. "Three-Dimensional Computer Model of the Human Buttocks, in Vivo." *Journal of Rehabilitation Research and Development* 31 (2): 111–19.

Traa, Willeke A., Mark C. van Turnhout, Jules L. Nelissen, Gustav J. Strijkers, Dan L. Bader, and Cees W.J. Oomens. 2019. "There Is an Individual Tolerance to Mechanical Loading in Compression Induced Deep Tissue Injury." *Clinical Biomechanics* 63: 153–60. https://doi.org/10.1016/j.clinbiomech.2019.02.015.

Trebbi, Alessio, Ekaterina Mukhina, Pierre-Yves Rohan, Nathanaël Connesson, Mathieu Bailet, Antoine Perrier, and Yohan Payan. 2022. "Medical Engineering and Physics MR-Based Quantitative Measurement of Human Soft Tissue Internal Strains for Pressure Ulcer Prevention." *Medical Engineering and Physics* 108 (June): 1–10. https://doi.org/10.1016/j.medengphy.2022.103888.

Trebbi, Alessio, Antoine Perrier, Mathieu Bailet, and Yohan Payan. 2021. "MR-Compatible Loading Device for Assessment of Heel Pad Internal Tissue Displacements under Shearing Load." *Medical Engineering and Physics* 98 (November): 125–32. https://doi.org/10.1016/j.medengphy.2021.11.006.

Turner, Mark D., Belinda Nedjai, Tara Hurst, and Daniel J. Pennington. 2014. "Cytokines and Chemokines: At the Crossroads of Cell Signalling and Inflammatory Disease." *Biochimica et Biophysica Acta - Molecular Cell Research* 1843 (11): 2563–82. https://doi.org/10.1016/j.bbamcr.2014.05.014.

Upton, Dominic, and Felicity South. 2011. "The Psychological Consequences of Wounds - A Vicious Circle That Should Not Be Overlooked." *Wounds UK* 7 (4): 136–38.

Vanderwee, Katrien, Michael Clark, Carol Dealey, Lena Gunningberg, and Tom Defloor. 2007. "Pressure Ulcer Prevalence in Europe: A Pilot Study." *Journal of Evaluation in Clinical Practice* 13 (2): 227–35. https://doi.org/10.1111/j.1365-2753.2006.00684.x.

Verdú-Soriano, José, Miriam Berenguer-Pérez, and José A. Quesada. 2021. "Trends in

Mortality Due to Pressure Ulcers in Spain, over the Period 1999–2016." *Journal of Tissue Viability* 30 (2): 147–54. https://doi.org/10.1016/j.jtv.2021.03.007.

Vergari, Claudio, Philippe Rouch, Guillaume Dubois, Dominique Bonneau, Jean Dubousset, Mickael Tanter, Jean Luc Gennisson, and Wafa Skalli. 2014. "Intervertebral Disc Characterization by Shear Wave Elastography: An in Vitro Preliminary Study." *Proceedings of the Institution of Mechanical Engineers, Part H: Journal of Engineering in Medicine* 228 (6): 607–15. https://doi.org/10.1177/0954411914540279.

Verver, M. M., J. van Hoof, C. W.J. Oomens, J. S.H.M. Wismans, and F. P.T. Baaijens. 2004. "A Finite Element Model of the Human Buttocks for Prediction of Seat Pressure Distributions." *Computer Methods in Biomechanics and Biomedical Engineering* 7 (4): 193–203. https://doi.org/10.1080/10255840410001727832.

Vogl, Thomas J., Christophe Then, Nagy N.N. Naguib, Nour Eldin A. Nour-Eldin, Maya Larson, Stefan Zangos, and Gerhard Silber. 2010. "Mechanical Soft Tissue Property Validation in Tissue Engineering Using Magnetic Resonance Imaging. Experimental Research." *Academic Radiology* 17 (12): 1486–91. https://doi.org/10.1016/j.acra.2010.08.010.

Wagnac, Éric L., Carl Éric Aubin, and Jean Dansereau. 2008. "A New Method to Generate a Patient-Specific Finite Element Model of the Human Buttocks." *IEEE Transactions on Biomedical Engineering* 55 (2): 774–83. https://doi.org/10.1109/TBME.2007.912640.

Woodhouse, Marjolein, Peter R. Worsley, David Voegeli, Lisette Schoonhoven, and Dan L. Bader. 2015. "The Physiological Response of Soft Tissue to Periodic Repositioning as a Strategy for Pressure Ulcer Prevention." *Clinical Biomechanics* 30 (2): 166–74. https://doi.org/10.1016/j.clinbiomech.2014.12.004.

Worsley, Peter R., Hanneke Crielaard, Cees W.J. Oomens, and Dan L. Bader. 2020. "An Evaluation of Dermal Microcirculatory Occlusion under Repeated Mechanical Loads: Implication of Lymphatic Impairment in Pressure Ulcers." *Microcirculation*. https://doi.org/10.1111/micc.12645.

Yaman, Alper, Cengizhan Ozturk, Peter A. Huijing, and Can A. Yucesoy. 2013. "Magnetic Resonance Imaging Assessment of Mechanical Interactions between Human Lower Leg Muscles in Vivo." *Journal of Biomechanical Engineering* 135 (9). https://doi.org/10.1115/1.4024573.

Zahouani, Hassan, C. Pailler-Mattei, B. Sohm, R. Vargiolu, V. Cenizo, and R. Debret. 2009. "Characterization of the Mechanical Properties of a Dermal Equivalent Compared with Human Skin in Vivo by Indentation and Static Friction Tests." *Skin Research and Technology* 15 (1): 68–76. https://doi.org/10.1111/j.1600-0846.2008.00329.x.

Zampell, Jamie C., Seth Aschen, Evan S. Weitman, Alan Yan, Sonia Elhadad, Marina De Brot, and Babak J. Mehrara. 2012. "Regulation of Adipogenesis by Lymphatic Fluid Stasis: Part I. Adipogenesis, Fibrosis, and Inflammation." *Plastic and Reconstructive Surgery* 129 (4): 825–34. https://doi.org/10.1097/PRS.0b013e3182450b2d.

Zeevi, Tal, Ayelet Levy, Neima Brauner, and Amit Gefen. 2018. "Effects of Ambient Conditions on the Risk of Pressure Injuries in Bedridden Patients—Multi-Physics

Modelling of Microclimate." *International Wound Journal* 15 (3): 402–16. https://doi.org/10.1111/iwj.12877.

Zheng, Y., and A. F.T. Mak. 1999. "Effective Elastic Properties for Lower Limb Soft Tissues from Manual Indentation Experiment." *IEEE Transactions on Rehabilitation Engineering* 7 (3): 257–67. https://doi.org/10.1109/86.788463.

Zheng, Y. P., and A. F.T. Mak. 1999. "Extraction of Quasi-Linear Viscoelastic Parameters for Lower Limb Soft Tissues from Manual Indentation Experiment." *Journal of Biomechanical Engineering* 121 (3): 330–39. https://doi.org/10.1115/1.2798329.

# APPENDICIES

# APPENDIX 1

Ref. Ares(2021)8014192 - 30/12/2021

# H2020-MSCA-ITN-2018

# STINTS ETN
# Skin Tissue Integrity under Shear

# Project ID: 811965

**Starting date:** 1st January 2019 **Duration:** 4 years

| | |
|---|---|
| **Deliverable Number** | D1.6 |
| **Deliverable Title** | Estimation of Skin Elasticity for Various Subjects |
| **Work Package Number** | WP1 |
| **Due Date (Annex 1)** | 31st December 2020 |
| **Submission Date** | 30th December 2021 |
| **Deliverable Lead Beneficiary** | Université Grenoble Alpes (UGA) |
| **Authors** | Ekaterina Mukhina (UGA), Yohan Payan (UGA), Nathanaël Connesson (UGA) and Pierre-Yves Rohan (AMP) |
| **Nature** | Report |

**Project funded by the European Union within the Horizon 2020 programme (2014-2020)**

**Dissemination Level**

| | | |
|---|---|---|
| PU | Public | |
| CO | Confidential, only for members of the consortium (including the Commission Services) | **X** |

| | |
|---|---|
| **Executive Summary** | This report describes the estimation of the skin and adipose tissue stiffnesses for two subjects by two different methods: with an aspiration device and with shear wave elastography. |


# Estimation of Skin Elasticity for Various Subjects

The global aim of the ESR9 project was set to examine the possibility of using ultrasound-based Finite Element (FE) models for the evaluation of the mechanical response of soft tissues in clinically relevant situations as a representative of the subject-specific risk of PU development in the pelvic region. Yet, the use of FE models in a framework compatible with clinical constraints is hindered by, amongst others, heavy and time-consuming assessment of material properties. The objective of this deliverable was to build upon new and unique opportunities offered by both the Volume-based Light Aspiration device for *in vivo* Soft TIssue Characterization (VLASTIC [1]) and Shear Wave Elastography for the identification of the passive material properties of soft tissues of the sacral region. As a perspective, these values could be used as input data for modelling the soft tissues in a FE model of the sacral region to predict contact interactions between a body part and a medical device in case of both passive and active uses.

## 1. Introduction

Sustained internal tissue loads (mechanical strains and stresses) which develop during immobile weight-bearing postures such as while in bed or in a chair have been identified as a fundamental cause for the onset and progression of pressure ulcers (PUs), particularly of the deep tissue injury (DTI) type [2], [3]. FE modelling has been proposed and efficiently employed to simulate tissue loads in the buttocks - the main weight-bearing anatomical structure during sitting. It has been shown that the soft tissue response to the mechanical deformations is highly dependent on the constitutive parameters assumed for the model, especially, for adipose and muscle tissues [4]–[6]. The personalisation of material properties is a highly challenging bottleneck for the whole community.

As a matter of fact, most of the studies in the literature use non-personalised constitutive parameters identified from *ex vivo* tests performed on either animal or human soft tissues [7]–[10]. This method allows a controlled testing environment. However, it does not allow to consider subject-specific properties which could vary a lot and, at the same time, could have an important effect on the tissue susceptibility to loading.

As an alternative, several groups have proposed to use inverse methods to identify subject-specific *in vivo* constitutive parameters based on medical images [11]. Inverse methods theory provides an interesting solution for that kind of problem. This theory is based on optimization techniques that allow adjusting the material parameters so that the calculated response matches the measured one in a particular norm. The calculated response can be obtained from a numerical method such as the FE analysis. Subject-specificity allows a more accurate knowledge of the material's behaviour and thus has an important advantage in comparison with the previous method. However, there are still some downsides, including high experimental errors, both due to measurement (difficulty to control boundary conditions, post processing of the images) and modelling assumptions (contact modelling, sliding, choice of the organization and composition of the soft tissues). In addition, 3D medical imaging, like CT or MRI, is not easily accessible in the bedside routine even in the clinical environment.

There have been several groups of easily attainable alternative testing systems proposed in the literature to assess *in vivo* subject-specific constitutive parameters. A brief review was performed for three groups of these systems.

The first group of systems is based on the principle of indentation; the reaction of the soft tissues to the quasi-static compression is assessed via the analysis of the force-displacement data [12]–[17]. The use of the Hertz contact model is one of the widely utilized approaches of extracting the stiffness parameters from the acquired indentation data [14], [18]–[20]. The advantage of this approach is that the evaluation of the material properties is done for the tissues under compression, while it could be hard to fully control the boundary conditions. Moreover, inverse methods associated to such indentation measurements usually need to elaborate assumptions about the layered structure of the tissues and the potential interaction between layers.

The second group focused on the aspiration devices [1], [21], [22]. After the negative pressure is applied, the tissue is aspired into a cup or chamber. Then the inverse calculation allows the estimation of the apparent Young's modulus based on the applied pressure and the height or the volume of the aspired tissue. The downside of the method is that the evaluation of the tissue properties is performed under tension, while the behaviour of the biological tissues could differ for compression and tension.

And the third group uses Shear Wave Elastography (SWE) for the evaluation of the shear modulus of the tissues. Arda et al. have assessed the stiffness values of the liver on healthy volunteers with SWE, by estimation of the shear modulus [23]. Dubois et al. have proposed a SWE protocol for non-invasive stiffness assessment of the muscles of the lower limb [24]. It was concluded that the SWE evaluation provides reliable information about the relative stiffness of the tissues, however, the absolute values are highly dependent on the tissue's fibre orientation, on the tissue viscous behaviour, and on the orientation of the US probe during the acquisition [25], [26].

To the best of our knowledge, the constitutive parameters of the sacral soft tissues have not been assessed experimentally *in vivo* before. Therefore, the objective of the current study was to quantify the stiffness parameters of the sacral soft tissues combining two techniques: the aspiration device and US shear wave elastography. The aim being to facilitate the assessment of the constitutive parameters at the bedside.

## 2. Materials and methods

### 2.1 Participants

Before inclusion, the participants were informed of the purpose of the study. They gave their consent to the experimental procedure as required by the Helsinki declaration (1964). All the methods were carried out in accordance with relevant guidelines and regulations.

Two healthy volunteers, male and female (Table 1), participated in the acquisitions.

Table 1 Morphological information for both subjects.

| Subject | Sex | Age (y.o.) | Weight (kg) | Height (m) | BMI (kg/m²) |
|---|---|---|---|---|---|
| 1 | male | 34 | 85 | 1.75 | 27.8 |
| 2 | female | 30 | 64 | 1.75 | 20.9 |

## 2.2 Setups and measurement devices

Two measurement devices were used in the present study: a custom-built modified version of the aspiration device (Volume-based Light Aspiration device for *in vivo* Soft TIssue Characterization (VLASTIC) [1]) and an Aixplorer SWE ultrasound device (Supersonic Imagine, Aix-en-Provence, France), with a 50 mm 18 MHz linear probe.

The custom-made aspiration device is shown in Figure 1. It consists of a manometer and two tubes connected by a valve, leading to syringes. A 3D printed semi-spherical cup is positioned on the skin; the pump is switched on applying the negative pressure to the skin and underlining tissues through the first tube and to the reference tube (closed at one end). The pressure in both tubes is measured by the manometer, while the aspired volume is measured with the syringe. The aspiration device was limited only to the small strains and acquisitions were performed with nine different cup diameters of 4, 6, 8, 10, 12.5, 15, 20, 25, and 30 mm.

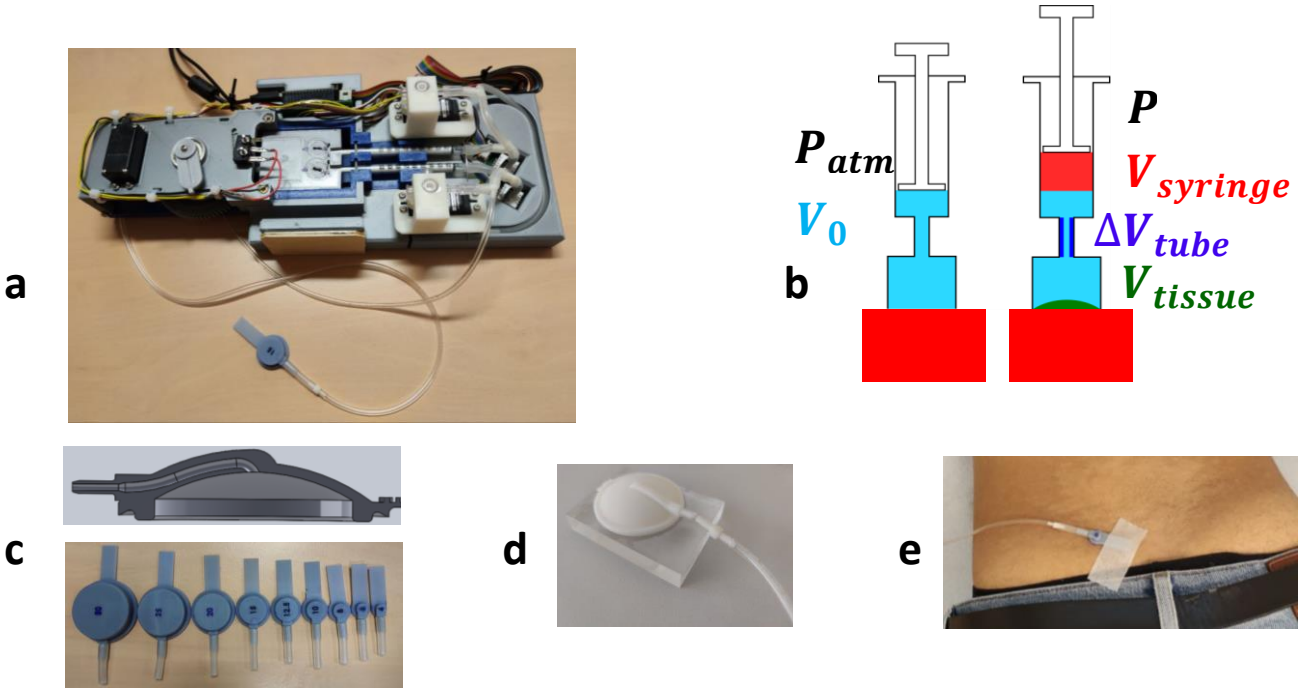


Figure 1 The aspiration device. a) Device assembly b) Functional scheme c) Inner design of the cup and cups of different diameters d) Calibration process e) Acquisition process.

## 2.3 Measurement protocols

### 2.3.1 Volume-based Light Aspiration device for *in vivo* Soft TIssue Characterization (VLASTIC)

Prior to the data collection, calibration of the system was performed on a non-deformable material in line with the previous study [1] to assess the response of the system itself: the compression of the system components and the air.

For the acquisitions on the participants, the cup was positioned on the upper left side from the medial sacral crest on the relatively flat surface; the region was marked for the further acquisitions. Ultrasonic gel was put on the edge of the cup to ensure contact with the skin and to prevent pressure air leakage. Four pressurization/depressurization cycles were applied for each acquisition.

For both subjects, nine acquisitions with each of the cups of diameter 4, 6, 8, 10, 12.5, 15, 20, 25 and 30 mm respectively were collected. The measurements were repeated three times to evaluate the uncertainties. Between each acquisition, the cup was taken off the skin, excess gel was removed from the skin and the cup was repositioned once again at the same location.

### 2.3.2 SWE

A thick layer of ultrasound gel was put on the area of interest to allow the measurements of the unloaded tissues. The ultrasound probe was positioned perpendicular to the spine at approximately 90 degrees to the skin surface. Three series of 8 continuous images were recorded with the ultrasound device set to “general mode”, “low” spatial smoothing and 3-image temporal smoothing for each subject for the Region of Interest (ROI) including the skin and underlining adipose tissues.

At the end of the acquisition, an additional image of the undeformed tissues in B-mode was taken to measure the thickness of the skin.

## 2.4 Post-processing

Data were processed in Matlab 2019a (The MathWorks Inc., Natick, MA).

### 2.4.1 Aspiration data

A bi-layer structure of the soft tissues was assumed, with a non-linear elastic Neo-Hookean model chosen to represent the skin and the underlying fat tissues. The stiffening behaviour of the tissues was not considered in the current study, for more information on this please refer to the [1].

An inverse FE-based procedure was employed to identify the constitutive parameters. The optimisation cost function was defined as a least square of the offset between the numerical and experimental results. Two separate optimisations were performed. For the first one, thickness of the top layer (skin) of the Finite Element model was imposed based on the pre-measured values from the US B-mode images. For the second one, thickness of the top layer (skin) was considered as one of the optimised parameters.

Linearized Young’s moduli of the skin and the adipose tissue (respectively $E_S$ and $E_F$) were identified from the 36 pressure-volume experimental curves (4 cycles x 9 cup sizes; namely 4, 6, 8, 10, 12.5, 15, 20, 25 and 30 mm).

### 2.4.2 SWE data

Images were extracted from the SWE videos and processed using previously written code [26]. Briefly, an operator defined a rectangular ROI of the elastographic image in the first frame of the series excluding the borders of the elastographic chart to avoid border effects. The depth and size of the ROI were adapted to tissue size, in order to maximize the ROI. The ROI was then semi-automatically tracked in the following images; the shear modulus was space-averaged in each frame ROI, and a time-average was then calculated from all frames to obtain a single value for the series, then the four series were averaged again to obtain a single value for the skin and the hypodermis.

# 3. Results

## 3.1 Skin thickness

The skin thickness was measured directly on the B-mode US images of the undeformed tissues in the same region where the aspiration and SWE acquisitions were performed. Figure 2 shows the measurement of the skin thickness (the red line) on the US image for subject 1, and Table 2 has a summary of the values obtained for both subjects.

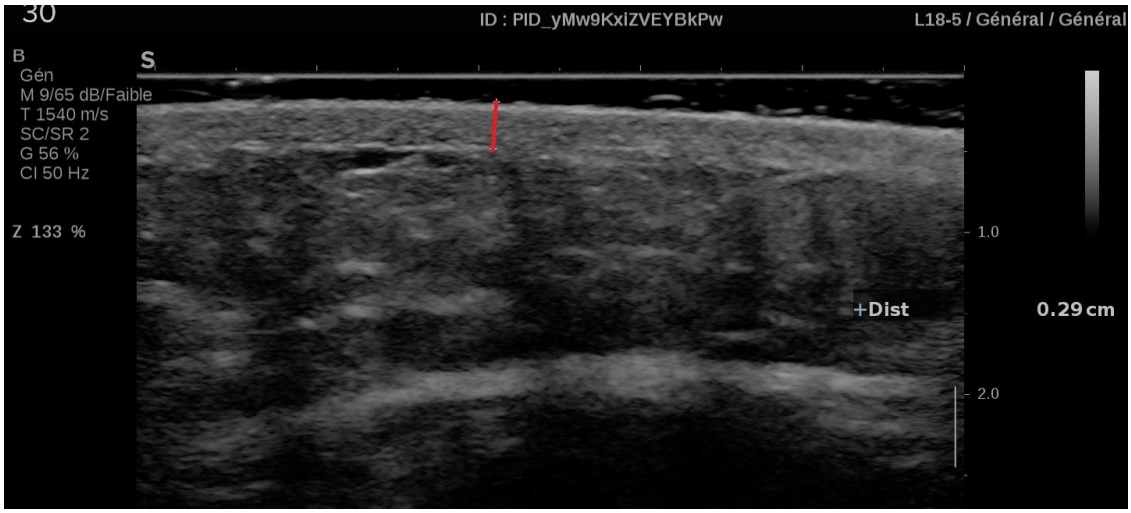


Figure 2 B-mode US image of the soft tissues at the sacral region with measured skin thickness, subject 1.

Table 2 Skin thicknesses for both subjects.

| Subject | Skin thickness (mm) |
|---|---|
| 1 | 2.9 |
| 2 | 3.0 |

## 3.2 Aspiration

Figure 3 and Figure 4 present the constitutive tissue stiffness (dP/dS, where P is the aspiration pressure in the system and S is the aspired volume) for subjects 1 and 2 respectively as a function of the cup diameter. The resultant Young's moduli estimated for both layers are also provided for the two optimisation configurations defined above: (1) when the skin thickness was imposed with the value measured on the B-mode US images and (2) when the skin thickness was one of the optimised parameters. On the graphs, the black line indicates the value for the top layer and the red line indicates the value for the bottom layer.

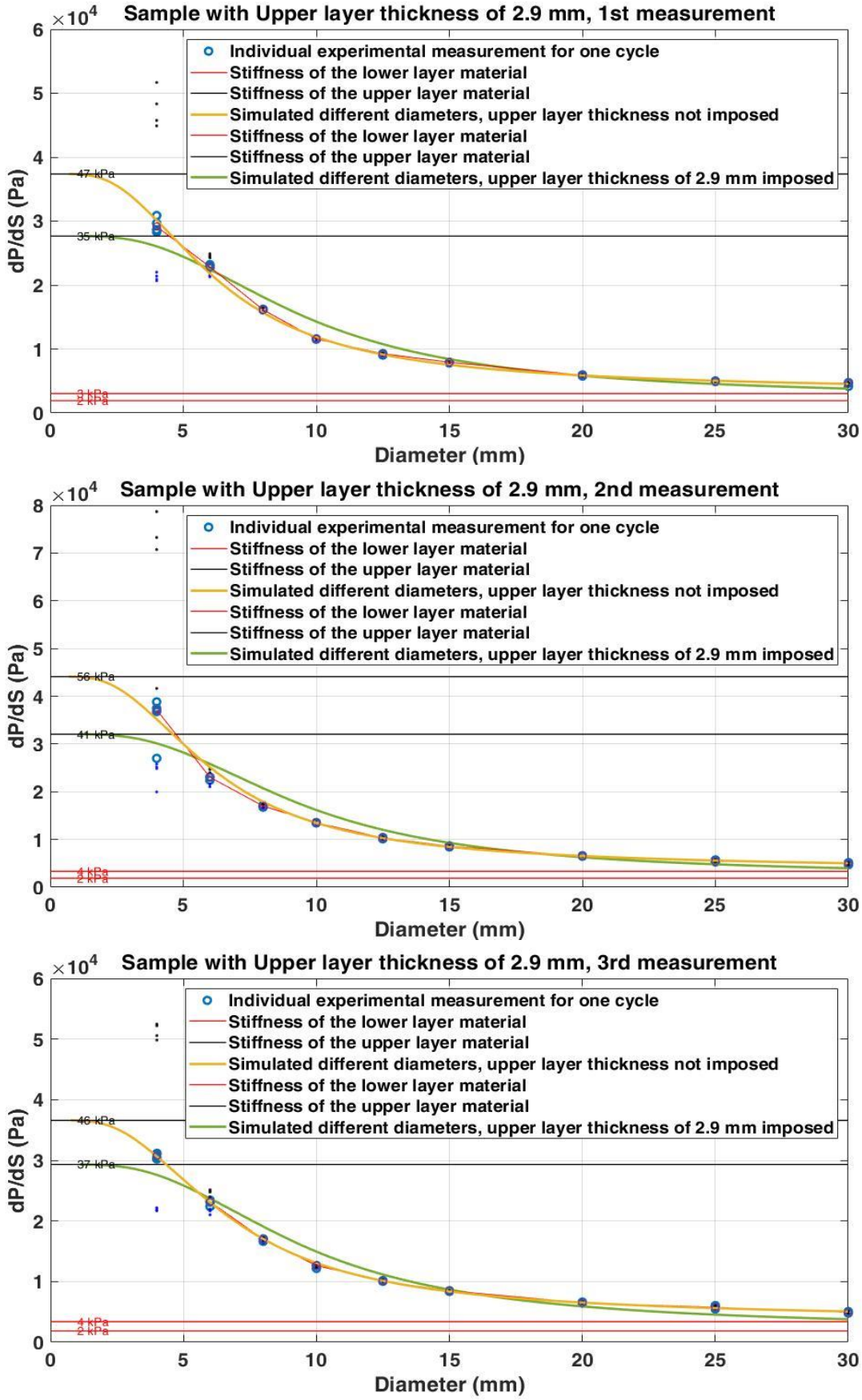


Figure 3 Estimated stiffness of the skin and the adipose tissues for fitting optimisation with and without imposing the skin thickness. Three measurements for subject 1.

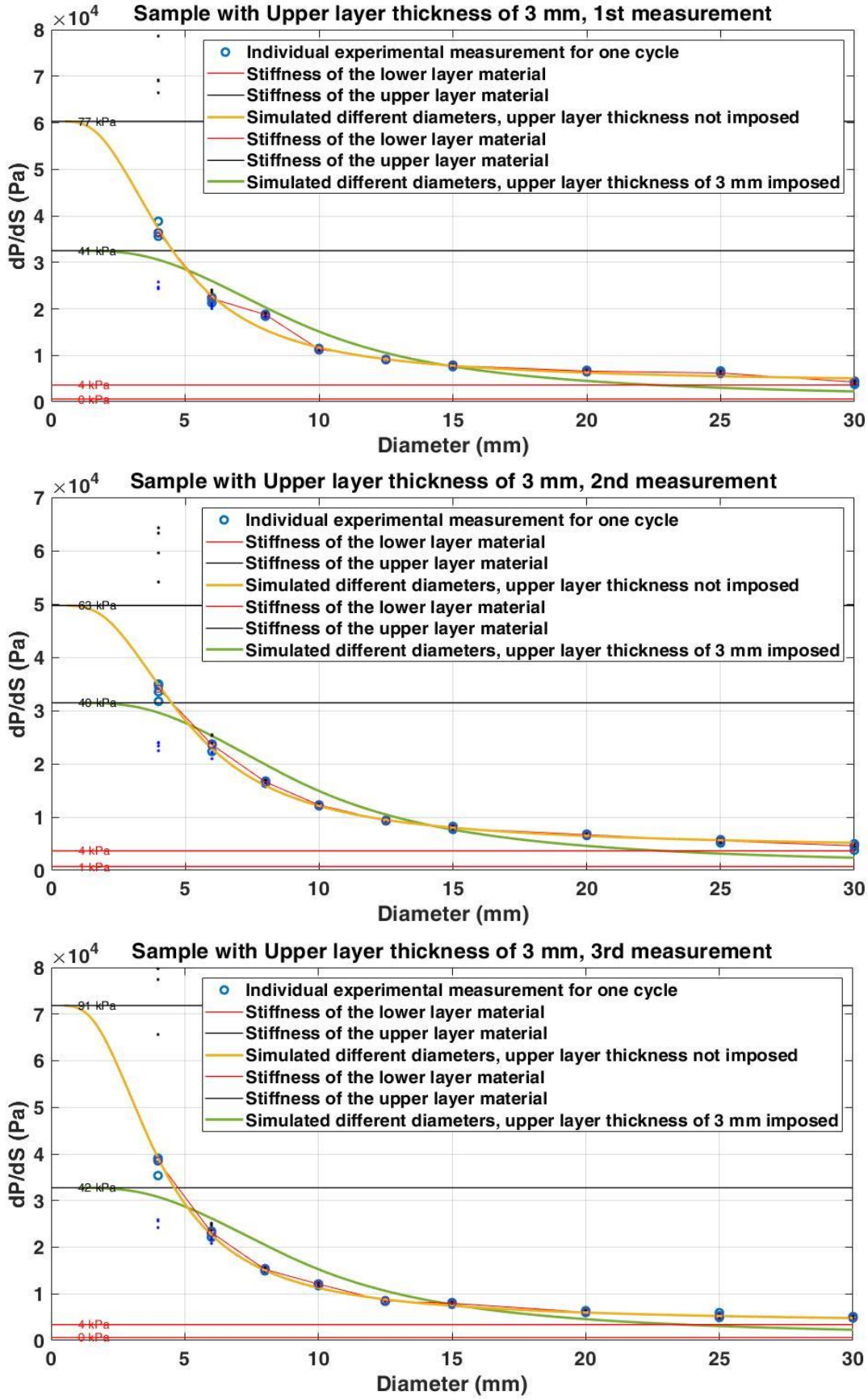


Figure 4 Estimated stiffness of the skin and the adipose tissues for fitting optimisation with and without imposing the skin thickness. Three measurements for subject 2.

Table 3 lists the Young's moduli for each of the three acquisitions for both subjects estimated by the optimisation algorithm with imposed skin thickness. The average skin Young's moduli were 37.7 kPa and 41 kPa for subjects 1 (male) and 2 (female) respectively. The corresponding average adipose tissue Young's moduli were 1.8 kPa and 0.5 kPa. The average ratio between skin and adipose values were 20.6 and 84.4 for the two subjects.

The variability of the skin Young's modulus was higher than the variability for the adipose tissue for the first subject in the contrast with the results of the second subject. In addition, the variation in the ratio value was higher for the second subject: 18 % vs 35 %.

Table 3 Resultant Young's moduli evaluated with the aspiration device for the skin and adipose tissues and the ratio between them. Imposed skin thickness measured with US.

| Subject | Acquisition | Young's modulus, skin (kPa) | Young's modulus, adipose tissue (kPa) | Ratio |
|---|---|---|---|---|
| 1 | 1 | 35.1 | 1.9 | 18.5 |
| | 2 | 40.7 | 1.8 | 22.6 |
| | 3 | 37.2 | 1.8 | 20.7 |
| 2 | 1 | 41.3 | 0.4 | 103.2 |
| | 2 | 40.0 | 0.6 | 66.7 |
| | 3 | 41.6 | 0.5 | 83.2 |

Table 4 lists the Young's moduli for each of the three acquisitions for both subjects estimated by the optimisation algorithm with skin thickness being one of the optimised parameters. The average skin Young's moduli were 49.9 kPa and 76.9 kPa for subjects 1 (male) and 2 (female) correspondingly. The corresponding average adipose tissue Young's moduli were 3.6 kPa and 4 kPa, and the average ratio between skin and adipose values were 13.8 and 19.2 for the two subjects.

The variability of the skin Young's modulus was higher than the variability for the adipose tissue for both subjects. In addition, the variation in the ratio value was higher for the second subject: 19 % vs 37 % correspondingly. The average skin thickness obtained by the optimisation algorithm was 1.9 mm vs 2.9 mm measured on the US image for the first subject and 1.4 mm vs 3 mm for the second subject.

Table 4 Resultant Young's moduli evaluated with the aspiration device for the skin and adipose tissues and the ratio between them. Skin thickness is one of the optimised parameters.

| Subject | Acquisition | Young's modulus, skin (kPa) | Young's modulus, adipose tissue (kPa) | Ratio | Skin thickness (mm) |
|---|---|---|---|---|---|
| 1 | 1 | 47.5 | 3.4 | 14 | 1.9 |
| | 2 | 56.1 | 3.7 | 15.2 | 1.8 |
| | 3 | 46.7 | 3.8 | 12.3 | 2 |
| 2 | 1 | 76.5 | 4.1 | 18.7 | 1.4 |
| | 2 | 62.9 | 4.2 | 15 | 1.5 |
| | 3 | 91.2 | 3.8 | 24 | 1.2 |

The Young's modulus for the adipose tissue estimated with the second optimization was 2–10 times higher than the one of the first with the imposed skin thickness.

## 3.3 SWE

The SWE for subject 1 is shown in Figure 5 below. It can be observed that the adipose layer consists of two regions with different elasticity: the upper region positioned closer to the skin with greater values and the lower region with smaller values. The summary of the SWE results is presented in Table 5.

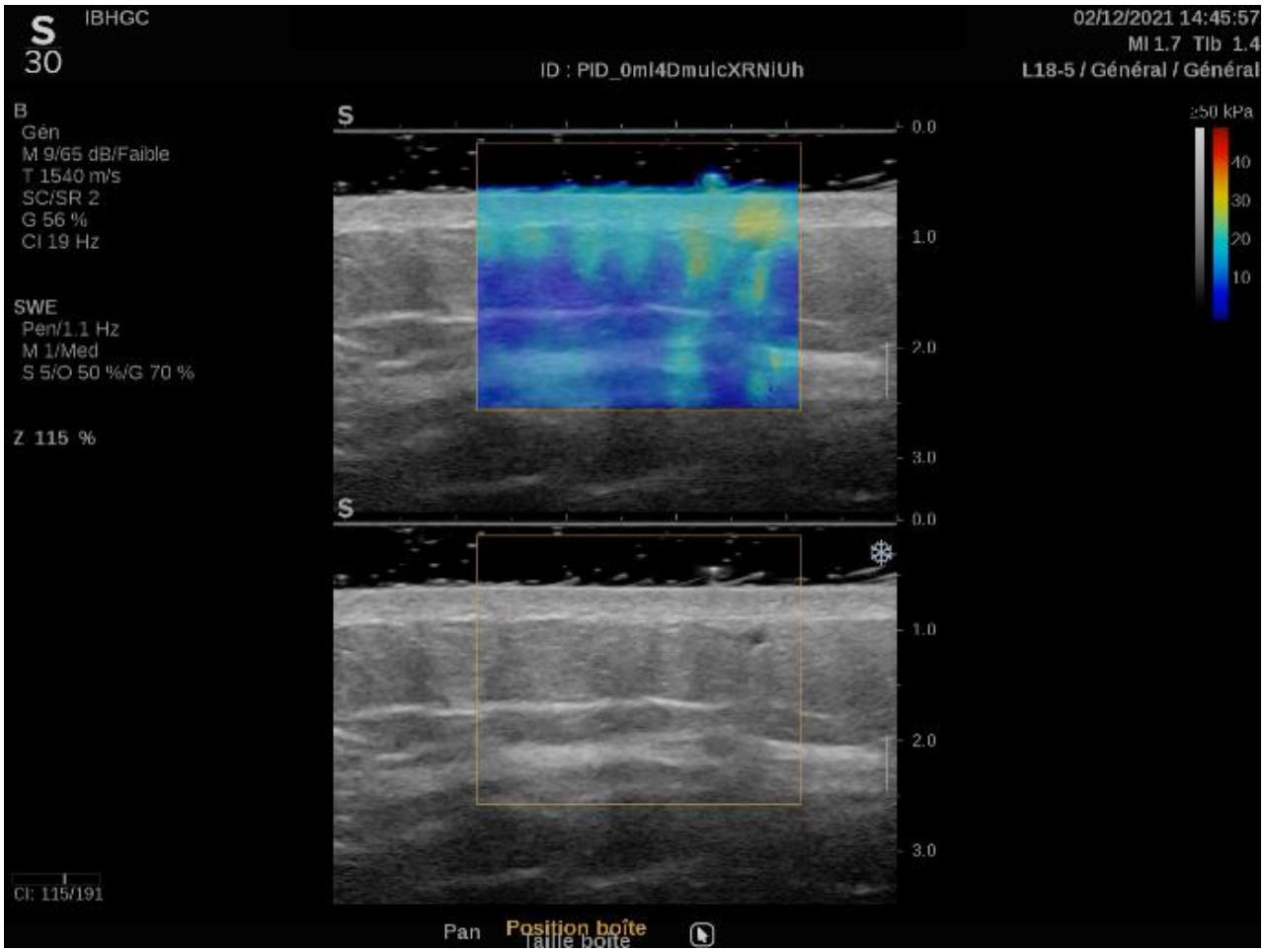


Figure 5 Example of the SWE image with the region of interest including the layer of gel, skin and adipose tissue.

Table 5 Resultant Young's moduli evaluated with the SWE for the skin and adipose tissues and the ratio between them.

| Subject | Young's modulus, skin (kPa) | Young's modulus, adipose tissue (kPa) | Ratio |
|---|---|---|---|
| 1 | 17.5 | 10.2 | 1.7 |
| 2 | 14.4 | 10.6 | 1.4 |

## 4. Discussion

Personalisation of the material properties for the numerical models is essential for making clinically relevant simulations and to eventually allow the assessment of the PU risk.

Different methods for the constitutive parameters' personalisation have been proposed in the literature: *ex vivo* tests, inverse identification based on the medical images in loaded/unloaded configurations and *in vivo* tests (indentation-based, aspiration-based or SWE). Each of these methods has its own advantages and disadvantages. The objective of this work was to estimate the stiffness parameters of the sacral soft tissues *in vivo*. It was decided to evaluate the elastic moduli values using two techniques: the aspiration device and the SWE.

Stiffness parameters obtained in literature studies vary a lot; a short review of the values provided for the skin and for the adipose tissues is provided below.

Ní Annaidh et al. performed tensile tests on the excised skin from the lumbar area of the back, the mean elastic modulus was estimated to be 83.3 ± 34.9 MPa [7]. While Pailler-Mattei et al. derived the elastic parameters from the *in vivo* indentation test, resulting in the Young's modulus of the dermis to be 35 kPa for the forearm region [9]. Bunegin and Moore performed suction tests on the skin of the thigh estimating the shear modulus to be 43 ± 7 kPa [27]. In another indentation test by Bader and Bowker, the shear modulus of the forearm and thigh skin was estimated to be 0.5 ± 0.15 kPa [28]. Torsion tests by Agache et al. estimated the Young's modulus of skin to be between 0.42 MPa and 0.8 MPa [29].

Hendriks at al. performed suction tests on forearm hypodermis resulting in a shear modulus of 0.04 kPa [30]. In the indentation test conducted by Pailler-Mattei et al. on the forearm, shear modulus of the hypodermis was calculated to be 2 kPa [9]. Adipose breast tissue was evaluated with the MR elastography by Van Houten et al., the shear modulus was in the range between 0.16 and 8.3 kPa [31]. Biaxial tensile and triaxial shear tests were performed by Sommer et al. on abdomen hypodermis tissue resulting in shear modulus values of 0.4 ± 0.2 kPa [32].

Young's modulus values obtained in the current study with the aspiration device are consistent with these in previous literature. However, a short review above shows the high variability of the stiffness values assessed by different studies.

Comparison between the two cases of optimization of the aspiration measurements showed that when the skin thickness is not imposed on the model, but allowed to be optimised as well, the resulting curve fits the experimental data much better (yellow vs green curve in Figure 3 and Figure 4). This result suggests that the visual uniformity of the skin layer on the US B-mode image could possibly not account for material properties variation.

The SWE values for the ratio between the Young's modulus for the skin and adipose tissues, however, are not consistent with literature values. One possible explanation for this discrepancy lies in the fact that the relationship between shear wave speed and mechanical properties (stiffness) has been reported to be affected by the thickness of the structure being imaged. Several authors have outlined in the literature, that, when the tissue thickness and the shear wavelength are within the same order of magnitude, guided wave propagation along the tissue is observed as the shear wave reflects off its boundaries (the reader is referred to [33] for the specific case of tendon tissue and to [34] for layered soft tissues). Depending on the tissue stiffness (shear wave propagation speed is proportional to the square root of tissue elasticity), the measured shear wave speed is generally underestimated for the tissue with thickness smaller than 1 cm. With the thickness of the skin being smaller than 5 mm in the present study, it is very likely that the skin mechanical properties estimated by the SWE were highly affected. Further

investigations are planned to evaluate the use of the shear wave propagation in layered soft tissues for the estimation of their intrinsic mechanical properties.

Several assumptions were tested in this work. First one was related to the aspiration device: the apparent Young's modulus is dependent on the cup size used. This is consistent with the results presented in Figure 3 and Figure 4, lower values of the cup diameter result principally in the aspiration of only the top layer and in the assessment of the skin stiffness, while for the larger cup diameters the ratio between the aspired bottom layer and the top layer becomes much higher, resulting in the assessment mainly of the adipose tissue.

Another assumption was related to the resultant ratio between the skin and the adipose tissue stiffnesses. It was assumed that the ratios derived from the aspiration measurements and by SWE would be similar. However, ratio values obtained by the SWE were almost 10 times lower for the subject 1 and more than 15 lower for the subject 2.

There are some limitations to the method used to derive the stiffness values from the aspiration acquisitions: both materials (skin and adipose tissues) are considered to be homogeneous isotropic and linearly elastic (only the initial slope of the curve was assessed). When it comes to the results of SWE the Young's modulus is not measured directly, it is derived from the measured wave velocity under some assumptions. In addition, the shear wave propagation is highly dependent on the US probe positioning, tissue fibre direction and pre-strain [25], [26], [35].

To our knowledge, the skin and adipose stiffness parameters derived from the aspiration and the SWE measurements were not previously compared in the literature on the same subjects at a sacral area. Results of this study suggest the importance of using with caution the stiffness values directly obtained with SWE and preferably make some additional measurements for the personalization of the FE models.

## References


[1] K. D. R. Kappert *et al.*, "In-vivo tongue stiffness measured by aspiration: Resting vs general anesthesia," *J. Biomech.*, vol. 114, no. December, p. 110147, 2021.

[2] A. Stekelenburg, G. J. Strijkers, H. Parusel, D. L. Bader, K. Nicolay, and C. W. Oomens, "Role of ischemia and deformation in the onset of compression-induced deep tissue injury: MRI-based studies in a rat model," *J. Appl. Physiol.*, vol. 102, no. 5, pp. 2002–2011, 2007.

[3] K. K. Ceelen *et al.*, "Validation of a numerical model of skeletal muscle compression with MR tagging: A contribution to pressure ulcer research," *J. Biomech. Eng.*, vol. 130, no. 6, pp. 1–8, 2008.

[4] C. W. J. Oomens, O. F. J. T. Bressers, E. M. H. Bosboom, C. V. C. Bouten, and D. L. Bader, "Can loaded interface characteristics influence strain distributions in muscle adjacent to bony prominences?," *Comput. Methods Biomech. Biomed. Engin.*, vol. 6, no. 3, pp. 171–180, 2003.

[5] V. Luboz, M. Petrizelli, M. Bucki, B. Diot, N. Vuillerme, and Y. Payan, "Biomechanical modeling to prevent ischial pressure ulcers," *J. Biomech.*, vol. 47, no. 10, pp. 2231–2236, 2014.

[6] A. Macron *et al.*, "Is a simplified Finite Element model of the gluteus region able to capture the mechanical response of the internal soft tissues under compression?," *Clin. Biomech.*, vol. 71, pp. 92–100, 2020.

[7] A. Ní Annaidh, K. Bruyère, M. Destrade, M. D. Gilchrist, and M. Otténio, "Characterization of the anisotropic mechanical properties of excised human skin," *J. Mech. Behav. Biomed. Mater.*, vol. 5, no. 1, pp. 139–148, 2012.

[8] F. Khatyr, C. Imberdis, P. Vescovo, D. Varchon, and J. Lagarde, "Model of the viscoelastic behaviour of skin in vivo and study of anisotropy," pp. 96–103, 2004.

[9] C. Pailler-Mattei, S. Bec, and H. Zahouani, "In vivo measurements of the elastic mechanical properties of human skin by indentation tests," *Med. Eng. Phys.*, vol. 30, no. 5, pp. 599–606, 2008.

[10] H. Zahouani, C. Pailler-Mattei, B. Sohm, R. Vargiolu, V. Cenizo, and R. Debret, "Characterization of the mechanical properties of a dermal equivalent compared with human skin in vivo by indentation and static friction tests," *Ski. Res. Technol.*, vol. 15, no. 1, pp. 68–76, 2009.

[11] H.-V. Tran, F. Charleux, A. Ehrlacher, and M. C. Ho Ba Tho, "Propriétés mécaniques multi-couches de la peau humaine in vivo Modèle numérique anatomique," *Colloq. Natl. En Calc. Des Struct.*, vol. 2005, no. 2, p. 2014, 2005.

[12] Z. Sadler, J. Scott, J. Drost, S. Chen, S. Roccabianca, and T. R. Bush, "Initial estimation of the in vivo material properties of the seated human buttocks and thighs," *Int. J. Non. Linear. Mech.*, vol. 107, pp. 77–85, 2018.

[13] A. P. Pathak, M. B. Silver-Thorn, C. A. Thierfelder, and T. E. Prieto, "A rate-controlled indentor for in vivo analysis of residual limb tissues," *IEEE Trans. Rehabil. Eng.*, vol. 6, no. 1, pp. 12–20, 1998.

[14] Y. P. Zheng and A. F. T. Mak, "Extraction of quasi-linear viscoelastic parameters for lower limb soft tissues from manual indentation experiment," *J. Biomech. Eng.*, vol. 121, no. 3, pp. 330–339, 1999.

[15] K. M. Moerman, A. M. J. Sprengers, A. J. Nederveen, and C. K. Simms, “A novel MRI compatible soft tissue indentor and fibre Bragg grating force sensor,” *Med. Eng. Phys.*, vol. 35, no. 4, pp. 486–499, 2013.

[16] M. A. L. Bell, S. Kumar, L. Kuo, H. T. Sen, I. Iordachita, and P. Kazanzides, “Toward Standardized Acoustic Radiation Force (ARF)-Based Ultrasound Elasticity Measurements with Robotic Force Control,” *IEEE Trans. Biomed. Eng.*, vol. 63, no. 7, pp. 1517–1524, 2016.

[17] N. Fougeron, P.-Y. Rohan, D. Haering, J.-L. Rose, X. Bonnet, and H. Pillet, “Combining Freehand Ultrasound-Based Indentation and Inverse Finite Element Modelling for the Identification of Hyperelastic Material Properties of Thigh Soft Tissues,” *J. Biomech. Eng.*, no. c, pp. 1–22, 2020.

[18] J. C. . Goh, P. V. S. Lee, S. L. Toh, and C. K. Ooi, “Development of an integrated CAD-FEA process for below-knee prosthetic sockets,” *Clin. Biomech.*, no. 20, pp. 623–629, 2005.

[19] Y. Zheng and A. F. T. Mak, “Effective elastic properties for lower limb soft tissues from manual indentation experiment,” *IEEE Trans. Rehabil. Eng.*, vol. 7, no. 3, pp. 257–267, 1999.

[20] A. F. T. Mak, G. H. W. Liu, and S. Y. Lee, “Biomechanical assessment of below-knee residual limb tissue,” *Journal of Rehabilitation Research and Development*, vol. 31, no. 3. pp. 188–198, 1994.

[21] T. Aoki, T. Ohashi, T. Matsumoto, and M. Sato, “The pipette aspiration applied to the local stiffness measurement of soft tissues,” *Annals of Biomedical Engineering*, vol. 25, no. 3. pp. 581–587, 1997.

[22] V. Luboz *et al.*, “Validation of a Light Aspiration Device for In Vivo Soft Tissue Characterization (LASTIC),” *Stud. Mechanobiol. Tissue Eng. Biomater.*, vol. 11, pp. 243–256, 2012.

[23] K. Arda, N. Ciledag, B. K. Arabis, E. Aktas, and K. Köse, “Quantitative assessment of the elasticity values of liver with shear wave ultrasonographic elastography,” *Indian J Med Res*, no. 137, pp. 911–915, 2013.

[24] G. Dubois *et al.*, “Reliable Protocol for Shear Wave Elastography of Lower Limb Muscles at Rest and During Passive Stretching,” *Ultrasound Med. Biol.*, vol. 41, no. 9, pp. 2284–2291, 2015.

[25] T. X. Haen, A. Roux, M. Soubeyrand, and S. Laporte, “Shear waves elastography for assessment of human Achilles tendon’s biomechanical properties: an experimental study,” *J. Mech. Behav. Biomed. Mater.*, vol. 69, pp. 178–184, 2017.

[26] C. Vergari *et al.*, “Intervertebral disc characterization by shear wave elastography: An in vitro preliminary study,” *Proc. Inst. Mech. Eng. Part H J. Eng. Med.*, vol. 228, no. 6, pp. 607–615, 2014.

[27] L. Bunegin and J. B. Moore, “Simultaneous spectrophotometric and mechanical property characterization of skin,” *Photonic Ther. Diagnostics II*, vol. 6078, no. February 2006, p. 607807, 2006.

[28] D. L. Bader and P. Bowker, “Mechanical characteristics of skin and underlying tissues in vivo,” *Biomaterials*, vol. 4, no. 4, pp. 305–308, 1983.

[29] P. G. Agache, C. Monneur, J. L. Leveque, and J. De Rigal, “Mechanical properties and Young’s modulus of human skin in vivo,” *Arch. Dermatol. Res.*, vol. 269, no. 3, pp. 221–232, 1980.

[30] F. M. Hendriks, D. Brokken, J. T. W. M. van Eemeren, C. W. J. Oomens, F. P. T. Baaijens, and J. B. A. M. Horsten, “A numerical-experimental method to characterize the non-linear mechanical behavior of human skin,” *Ski. Res. Technol.*, vol. 9, no. 3, pp. 274–283, 2003.

[31] E. E. W. Van Houten, M. M. Doyley, F. E. Kennedy, J. B. Weaver, and K. D. Paulsen, “Initial in vivo experience with steady-state subzone-based MR elastography of the human breast,” *J. Magn. Reson. Imaging*, vol. 17, no. 1, pp. 72–85, 2003.

[32] G. Sommer *et al.*, “Multiaxial mechanical properties and constitutive modeling of human adipose tissue: A basis for preoperative simulations in plastic and reconstructive surgery,” *Acta Biomater.*, vol. 9, no. 11, pp. 9036–9048, 2013.

[33] J. Brum, M. Bernal, J. L. Gennisson, and M. Tanter, “In vivo evaluation of the elastic anisotropy of the human Achilles tendon using shear wave dispersion analysis,” *Phys. Med. Biol.*, vol. 59, no. 3, pp. 505–523, 2014.

[34] T. M. Nguyen, M. Couade, J. Bercoff, and M. Tanter, “Assessment of viscous and elastic properties of sub-wavelength layered soft tissues using shear wave spectroscopy: Theoretical framework and in vitro experimental validation,” *IEEE Trans. Ultrason. Ferroelectr. Freq. Control*, vol. 58, no. 11, pp. 2305–2315, 2011.

[35] J.-L. Gennisson, S. Catheline, S. Chaffaï, and M. Fink, “Transient elastography in anisotropic medium: Application to the measurement of slow and fast shear wave speeds in muscles,” *J. Acoust. Soc. Am.*, vol. 114, no. 1, pp. 536–541, 2003.

# APPENDIX 2

Medical Engineering and Physics 108 (2022) 103888

Contents lists available at ScienceDirect

Medical Engineering and Physics

journal homepage: www.elsevier.com/locate/medengphy

# MR-based quantitative measurement of human soft tissue internal strains for pressure ulcer prevention

Alessio Trebbi [*,a], Ekaterina Mukhina [a], Pierre-Yves Rohan [b], Nathanaël Connesson [a], Mathieu Bailet [c], Antoine Perrier [d], Yohan Payan [a]

[a] Univ. Grenoble Alpes, CNRS, TIMC, 38000 Grenoble, France
[b] Institut de Biomécanique Humaine Georges Charpak, Arts et Métiers ParisTech, 151 bd de l'Hôpital, 75013. Paris, France
[c] TwInsight, 38000 Grenoble, France
[d] Univ. Grenoble Alpes, CNRS, TIMC, 38000 Grenoble, France, Groupe hospitalier Diaconesses–Croix Saint-Simon, 75020 Paris, France, TwInsight, 38000 Grenoble, France

ARTICLE INFO

*Keywords:*
DVC
FEM
Heel
Sacrum

ABSTRACT

Pressure ulcers are a severe disease affecting patients that are bedridden or in a wheelchair bound for long periods of time. These wounds can develop in the deep layers of the skin of specific parts of the body, mostly on heels or sacrum, making them hard to detect in their early stages.

Strain levels have been identified as a direct danger indicator for triggering pressure ulcers. Prevention could be possible with the implementation of subject-specific Finite Element (FE) models. However, generation and validation of such FE models is a complex task, and the current implemented techniques offer only a partial solution of the entire problem considering only external displacements and pressures, or cadaveric samples.

In this paper, we propose an *in vivo* solution based on the 3D non-rigid registration between two Magnetic Resonance (MR) images, one in an unloaded configuration and the other deformed by means of a plate or an indenter. From the results of the image registration, the displacement field and subsequent strain maps for the soft tissues were computed. An extensive study, considering different cases (on heel pad and sacrum regions) was performed to evaluate the reproducibility and accuracy of the results obtained with this methodology.

The implemented technique can give insight for several applications. It adds a useful tool for better understanding the propagation of deformations in the heel soft tissues that could generate pressure ulcers. This methodology can be used to obtain data on the material properties of the soft tissues to define constitutive laws for FE simulations and finally it offers a promising technique for validating FE models.

## 1. Introduction

Pressure ulcers are serious injuries generated by prolonged mechanical loadings applied on soft tissues. Most of the pressure ulcers occur on the heel and on the sacrum as these locations are loaded when patients are bedridden or wheelchair bound for long periods of time [1-3]. Ulceration requires high amounts of resources from the nursing cares and time to be healed and therefore represents a serious problem to the individual and the health care system [4]. In the worst cases, these complications lead to amputations and death. Depending on the type of external mechanical load, anatomy and tissue integrity, pressure ulcers can start superficially or deep within the soft tissues. Superficial wounds are formed on the skin surface and progress downwards, making them easy to identify in the early stages with solutions that can be promptly adopted to stop their progression. On the other hand, deep tissue injuries arise in muscle or fat layers around bony prominences and are often caused by high strains of the biological tissues. A value of 0.65 for the Green Lagrange (GL) maximal shear strain was provided by Ceelen et al. as a threshold that should not be exceeded to avoid any pressure ulcer [5]. This last case represents a major threat due to the impossibility to quickly identify the ulcer formation and promptly take action [6]. For this purpose, techniques to monitor the level of strain in the deep layers

* Corresponding author.
*E-mail addresses:* Alessio.Trebbi@univ-grenoble-alpes.fr (A. Trebbi), ekaterina.mukhina@univ-grenoble-alpes.fr (E. Mukhina), Pierre-Yves.ROHAN@ensam.eu (P.-Y. Rohan), nathanael.connesson@univ-grenoble-alpes.fr (N. Connesson), mathieu.bailet@twinsight-medical.com (M. Bailet), Yohan.Payan@univ-grenoble-alpes.fr (Y. Payan).

https://doi.org/10.1016/j.medengphy.2022.103888
Received 1 June 2022; Received in revised form 27 August 2022; Accepted 1 September 2022
Available online 5 September 2022
1350-4533/© 2022 IPEM. Published by Elsevier Ltd. All rights reserved.

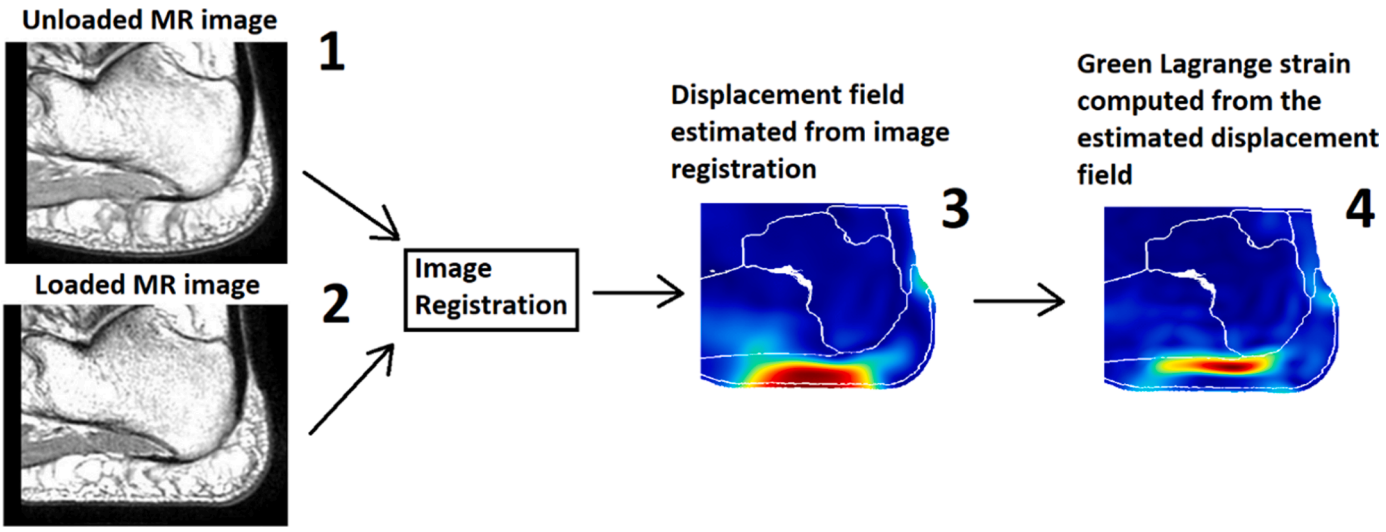


**Fig. 1.** Scheme of quantitative measurement of soft tissue internal strains obtained from image registration. Image 1: unloaded configuration. Image 2: Loaded configuration. The image registration estimates the displacement field (Image 3) that transforms the unloaded image into the loaded configuration. The strain field can then be derived from the displacement field (Image 4).

of the skin and underlying soft tissues are currently extensively investigated in the literature [7].

A common methodology to estimate internal tissue strains relies on FE modeling, with simulations that reproduce the body part morphology, tissue biomechanical parameters and the type of loading [8-10]. However, validation of FE simulations of the mechanical response of *in vivo* biological tissues to external mechanical loads has always been problematic. Keenan et al. report that none of the current heel models have been properly validated against independent experimental measurements and that further work is needed to develop models that are well validated to draw reliable clinical conclusions [8]. Regarding the buttock region, Savonnet et al. reached a similar conclusion stating that only few models were validated with experimental observations [9]. Because direct validation of internal mechanical strains is a challenging problem, many research works proposed to evaluate FE models of the foot in terms of their capacity to predict interface plantar pressure by comparing the contact pressure predicted by the FE model with the measurements from pressure mattresses [11]. Yet, as observed in Macron et al. [12] on data from 13 healthy volunteers, interface pressure distributions do not correlate with internal strains and one cannot be used to predict the other. This issue was partially addressed by Linder-Granz et al. [13] for a buttock FE model in a study where the authors compared contours of the computational domain in the deformed configuration predicted by the simulations to the ground truth segmented contours obtained from MR images. This comparison, however, considers only the external shape and not the quantity of interest, which is the local internal tissue displacement and associated tissue strains.

In an original contribution, Stekelenburg et al. [14] proposed to use MR tagging and phase contrast sequences on a rat leg model under indentation to assess local tissue displacements and compute the associated tissue strains. The main restriction of this approach is that the indenter (used inside the MR machine to deform the tissue) has to be applied rapidly and repetitively as the tagging grid fades within 1 s because of MR relaxation. This requirement can be complex to overcome with an MR compatible device. Moreover, this constraint does not allow for conventional control systems for the application of loads such as gravity, hydrostatic pressure or compression springs [15] [16] [17]. Additionally, with dynamic loads applied, the viscoelastic properties of the biological tissues could have an impact on the mechanical response, thus increasing the complexity to estimate the tissues passive mechanical properties from the experimental measurements.

Digital Volume Correlation (DVC) is an emerging non-invasive technique that allows to characterize experimentally material mechanical response to external loadings by tracking the displacement of natural patterns. From the displacement field, local strains can be computed. Combined with 3D MR images, DVC can, for example, be used to estimate human tissue internal strains [18]. From two MR datasets, one collected in an arbitrary undeformed configuration and another in a deformed configuration, the non-linear transformations that will align the MR volume at rest to the deformed one can be computed using a procedure call Image Registration. To illustrate the process, a graphical summary of the procedure is proposed based on data collected by the authors on the foot (Fig. 1). DVC has previously been used in for *in vivo* strain estimation in human intervertebral discs, brain and leg muscles under external mechanical loading [19–21].

Our group has recently developed an MR-compatible device for applying controlled shearing and normal loads to the human heel pad [16]. With such a device, 3D MR volumes of the heel pad soft tissue can be imaged under various loads applied on the foot sole. This paper aims at describing the methodology proposed by our group to implement DVC on human soft tissues and at estimating the internal strains from the DVC-derived 3D displacement field. The long-term objective is to validate a FE model, in terms of its capacity to predict the localization and the intensity of the strain field in the soft tissues.

## 2. Materials and methods

### *2.1. Materials: heel and sacrum MR datasets previously collected on one healthy volunteer*

The MRI datasets used in this study have been collected in a previous study [17]. For the sake of clarity, the main details regarding the experimental setup, protocol and participant are summarized in the following paragraph. For more details, the reader is referred to the associated publication.

A healthy volunteer (male, 40 years old) gave his informed consent to participate in the experimental part of a pilot study approved by an ethical committee (MammoBio MAP-VS pilot study N°ID RCB 2012-A00340–43, IRMaGe platform, Univ. Grenoble Alpes).

For the heel MR image datasets, the volunteer was placed in a supine position with his right foot locked in a MR compatible device designed to apply both a normal force (15 N) or a combined normal-and-shearing force (15 N normal + 45 N shearing) on the heel pad by means of an

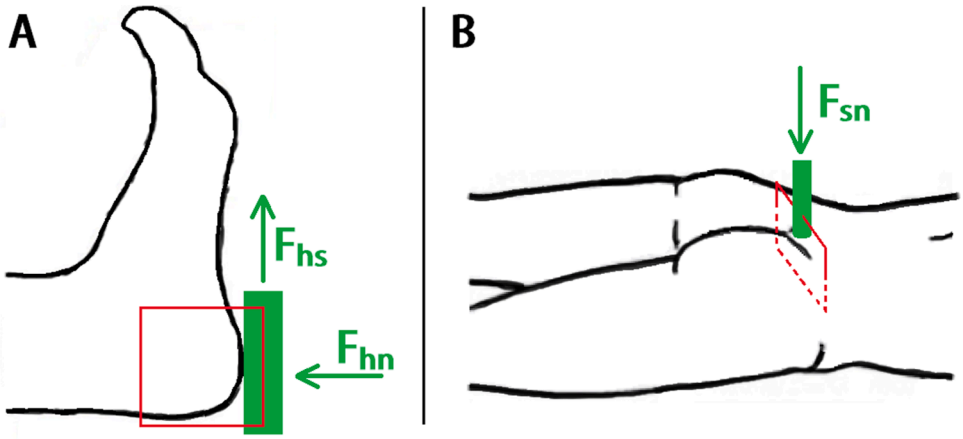


**Fig. 2.** (A) Scheme of the heel configurations during the MR acquisitions. The green rectangle represents the plate applying the loads. Direction of the loads is represented by the green arrows Fhn (Force heel normal) and Fhs (Force heel shear). The red rectangle shows the orientation of the MRI slice that will be shown in the rest of the paper. (B) Scheme for the sacrum configuration (Analogous to A). The green block represents the indenter with the respective Fsn (Force sacrum normal) applied. The indenter has the external shape of an ultrasound probe, 10–2 linear probe transducer developed by (Aixplorer, SuperSonic Imagine, France).

**Table 1**
List of MR acquisitions. The first name indicates the body location of the image. The unloaded configurations are indicated by the initial number 0 (01, 02). The loaded configurations are indicated by the integer positive numbers (1,2).

| Name | Description | Load |
|---|---|---|
| Heel 01 | Unloaded heel – Acquisition 1 | 0 N |
| Heel 02 | Unloaded heel – Acquisition 2 | 0 N |
| Heel 1 | Heel with normal load | 15 N normal |
| Heel 2 | Heel with normal and shearing load | 15 N normal and 45 N shear |
| Sacrum 01 | Unloaded Sacrum – Acquisition 1 | 0 N |
| Sacrum 02 | Unloaded Sacrum – Acquisition 2 | 0 N |
| Sacrum 1 | Sacrum with normal load | 12 N normal |

indenting platform. The setup is illustrated in Fig. 2A. A proton density MR sequence was used to collect 3D images composed of 512 × 428 × 512 voxels with voxel size of 0.3125 mm x 0.375 mm x 0.3125 mm (MRI system Achieva 3.0T dStream Philips Healthcare). Two acquisitions of the same unloaded configuration allowed to avoid having the same noise pattern between equivalent images in the subsequent image registration process in order to test the repeatability of strain calculation.

For the sacrum images, the subject was placed in the MR bed in a prone position. An indenter actuated by gravity applied a normal load (12 N) on the sacrum region. The 3D images were composed by 800 × 800 × 240 voxels with a dimension of 0.5 × 0.5 × 0.5 mm Fig. 2B. Likewise, two acquisitions were collected in the unloaded configuration to test the repeatability of strain calculation.

Four 3D MR images of the heel and three 3D MR images of the sacrum region were considered in this contribution and were referred to using a unique name as listed in Table 1.

A 2D snapshot of each MR volume (presented as the red rectangle in Fig. 2) is provided in Fig. 3.

### 2.2. Rigid registration

The four MR volumes of the heel and the three MR volumes of the sacrum were rigidly registered to align the calcaneus bone and the sacrum bone respectively using the publicly available registration package Elastix [22].

### 2.3. Digital volume correlation between the loaded and the unloaded MR images

The registration package Elastix [22] was then used to perform DVC. Two images are involved in this registration process: the reference image$I_0(x)$ (unloaded configuration: Heel/Sacrum 01/02, called “fixed image” in the Elastix library) and the deformed image,$I_Q(x)$ (loaded configuration: Heel 1 and 2 and Sacrum 1, called “moving image” in the Elastix library), where $x$ represents the position of a point in the images. The registration between these two images defines a non-rigid deformation field $u_Q(x)$, which describes how the reference unloaded image transforms into the deformed image. Applying the deformation field to the reference image creates a transformed-deformed image $I_0(x + u_Q(x))$

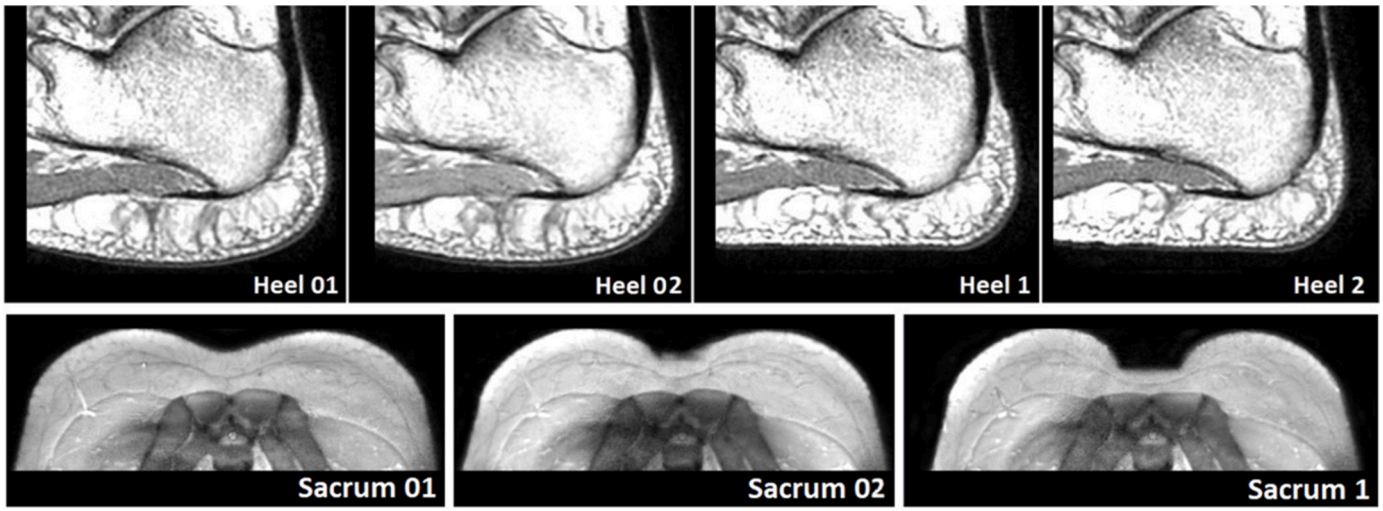


**Fig. 3.** Slices of the heel and the sacrum unloaded and loaded configurations described in Table 1. The respective region is indicated in Fig. 2 by the red rectangle.

**Table 2**
List of image registrations to evaluate the reproducibility of strain calculation from image registration. Each line represents an image registration composed by its fixed and moving image. The tests are grouped in three Cases: A) Heel with normal load, B) Heel with normal+shearing load, C) Sacrum with normal load. The resulting displacement fields and shearing strain field are respectively denoted with the letters D and S. The second letter in the field nomenclature reports the respective case of the registration. The numbers report the name of the fixed and moving images.

| Fixed image | Moving image | Case | Displacement field | Shear strain field |
|---|---|---|---|---|
| Heel 01 | Heel 1 | A | $DA_{011}$ | $SA_{011}$ |
| Heel 02 | Heel 1 | | $DA_{021}$ | $SA_{021}$ |
| Heel 01 | Heel 2 | B | $DB_{012}$ | $SB_{012}$ |
| Heel 02 | Heel 2 | | $DB_{022}$ | $SB_{022}$ |
| Sacrum 01 | Sacrum 1 | C | $DC_{011}$ | $SC_{011}$ |
| Sacrum 02 | Sacrum 1 | | $DC_{021}$ | $SC_{021}$ |

that aims to look identical to the deformed image.

The optimal deformation field was estimated by minimizing a cost function by means of an iterative optimization method (adaptive stochastic gradient descent) embedded in a hierarchical (multiresolution) scheme. The cost function relates to the similarity between the two images (*i.e.* the reference image and its transformation) using image features and was based on the Normalized Correlation Coefficient (NCC).

During the optimization step, the value of the cost function was evaluated at non-voxel positions, for which intensity interpolation with cubic B-Spline was used.

### 2.4. Computing mechanical strains from the DVC-derived displacement fields

From the displacement fields obtained by the registrations, strain maps were calculated as follows: The relation between the position $X$ of a material point in the undeformed configuration and its position $x$ in a deformed configuration $Q$ is described by the spatial displacement vector$u_Q(x)$ which consists of 3 components $u_{Qx}$,$u_{Qy}$,$u_{Qz}$:

$$u_Q(x) = \left[u_{Qx},\ u_{Qy},\ u_{Qz}\right]^T \tag{1}$$

From these, the deformation gradient $F$ can be computed:

$$F = I + \frac{\partial u}{\partial X} \tag{2}$$

And the right Cauchy-Green deformation tensor $C$ deduced:

$$C = F^T F \tag{3}$$

The Green Lagrange principal strains:

$$E_p = eig\left(\frac{1}{2}\ (C - I)\right) \tag{4}$$

The maximum GL shear strains are defined as:

$$E_s = \frac{1}{2} * \max(|E_1 - E_2|,\ |E_1 - E_3|,\ |E_2 - E_3|) \tag{5}$$

### 2.5. Uncertainty of the image registration procedure

To evaluate the uncertainty of the DVC we consider six evaluation Cases A to F. The first three cases are related to the repetition of the same strain measurement and to the analysis of the differences between the respective results (reproducibility of the registration). The last three cases focus on the ability of DVC to estimate a known a priory strain field (accuracy of the registration).

#### 2.5.1. Reproducibility

Reproducibility refers to the closeness of agreement between test results. In this section, we propose to evaluate the reproducibility of strain calculation through image registration. Two acquisitions of the unloaded configurations of the heel and sacrum (namely Heel 01 and Heel 02 and sacrum 01 and sacrum 02 respectively) were registered to the same moving image (Heel 1 and Sacrum 1 respectively). The corresponding strain maps are computed from the two estimated deformation fields. The reproducibility is then inspected by analyzing the differences between these two strain maps. Three cases, summarized in Table 2, are considered: heel under normal load (A), heel under normal+shearing load (B) and sacrum under normal load (C).

#### 2.5.2. Accuracy

Accuracy reflects how close a data is to a known or accepted value. In this section, we propose to evaluate the accuracy of our image registration procedure to identify a known *a priori* strain field. We focus specifically here on the images of the heel. Two different displacement fields are considered:

1 For the first case, an artificial displacement field $D_{FEM}$ is generated from a Finite Element (FE) simulation. A rectangular parallelepiped volume with the same size of the 3D MR images is first generated in ANSYS 19.2 APDL (ANSYS, Inc., Canonsburg, PA). This volume is then meshed with 8-nodes hexahedral elements and a linear elastic material model is implemented. The 3D mesh is composed of 24,389 hexahedral elements. The nodes on the sides of the parallelepiped are fixed in order to avoid any displacements outside of the defined

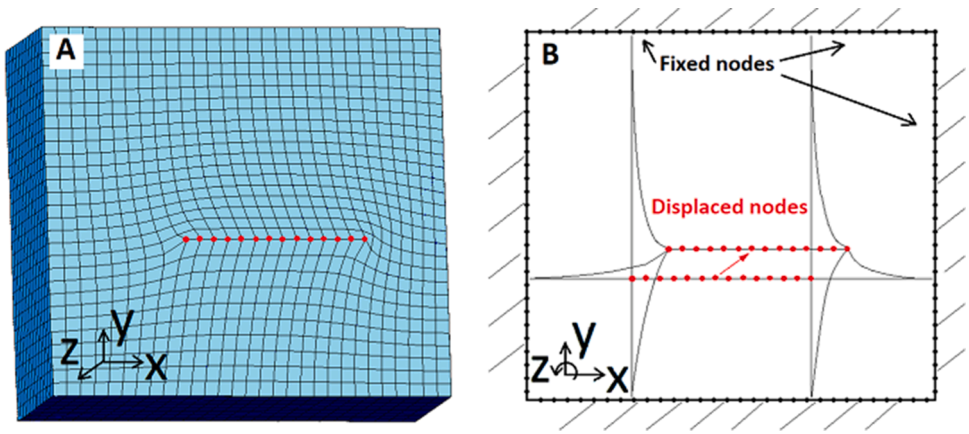


**Fig. 4.** Generation of an artificial displacement field from a FE simulation generated by Ansys. The size of the cube matches with the size of the MR images of the heel. A selection of nodes (red dots) on a plane orthogonal to the y axis was displaced as boundary conditions. (A) Section of the simulated cube along a plane orthogonal to the z axis. (B) Schematization of the boundary conditions imposed. The external nodes were fixed, and the selection of red nodes was displaced.

**Table 3**
List of transformations to create the artificial images to test the accuracy of strain calculation through image registration. The image column lists the images to be transformed. The displacement field column lists the transformation to be applied to generate the artificially deformed image.

| Image | Applied displacement field | Artificial image | Shear strain field |
|---|---|---|---|
| Heel 01 | $D_{FEM}$ | Heel FEM | $S_{FEM}$ |
| Heel 01 | $DA_{011}$ | Heel TRA | $SA_{011}$ |

volume. A set of 196 internal central nodes located on the same XZ plane are then submitted to a prescribed displacement boundary condition in a normal (Y) and in a tangent (X) direction (Fig. 4). The displacement field computed by ANSYS is then extracted for all the nodes of the parallelepiped and interpolated to fit the resolution of the MR images. The corresponding displacement field is applied to the unloaded image (Heel 01) to generate a new artificially loaded image of the heel, named Heel FEM (Table 3 and Fig. 5). It is worth noting that the objective of the FE method is mainly to produce a known *a priori* displacement filed. This displacement filed will be subsequently estimated through the image registration technique. The simulation itself, and the artificially generated image Heel FEM, do not have any real physical meaning. The main benefit of using such an FE solver is the possibility to get a ground-truth strain field that can be compared to values estimated from image registration.

2 For the second case, the previously computed displacement field $DA_{011}$ is applied to the unloaded image (Heel 01) to generate a new artificially loaded image of the heel, named Heel TRA (from the word transformed) (Table 3 and Fig. 5).

Image registration was then computed between Heel 02 and the two artificially deformed images Heel FEM and Heel TRA. Note here that having two acquisitions of the same unloaded configuration (Heel 01 and Heel 02) allowed to implement different noise patterns during the registration process in the fixed and moving image (Cases D and F of Table 4). On the other hand, to show the impact of having the same noise pattern between the fixed and the moving image the image Heel 01 was also considered for Case E (Table 4).

#### 2.5.3. Error quantification

The error estimation was performed analyzing the obtained strain fields with a Bland–Altman plot. This representation is a method of data plotting used in analyzing the agreement between two different set of data corresponding to the same measurement. The plotted graph shows the error distribution throughout the whole range of measured strain values.

## 3. Results

### 3.1. Strain measurements for heel under normal load (case A, Table 2)

The distribution of the DVC-derived displacement field in the heel domain under normal load is given in the sagittal slice containing the highest shear strains (Fig. 6A). The highest displacements are uniform in the area where the plate was in contact with the plantar skin of the heel. Fig. 6B shows the corresponding maximal GL shear strains computed from the displacement field. Shear strains are concentrated around the lower part of the calcaneus bone propagating towards the plantar fascia and the flexor digitorium brevis.

The agreement between $SA_{011}$ and $SA_{021}$ was described graphically with a Bland-Altman plot (Figure 7) with mean of differences, reported with corresponding 95% confidence interval (CI), and lower and upper limits of agreement, calculated as mean $\pm$ 2σ (where σ represents the standard deviation SD). Differences were assessed using a Wilcoxon-Signed-Rank Test (paired data) at the default 5% significance level.

### 3.2. Strain measurements for heel under normal+shearing load (case B, Table 2)

The application of the shearing load had a relevant impact on the soft tissue displacements. The plate moved the posterior and the plantar regions of the heel skin towards the forefoot. This caused the shear strains to propagate on a wider region of the fat pad and the muscle (Figure 8). A concentration of high levels of strains is found in the fat pad under the flexor digitorium brevis.

Figure 9 shows the correlation between the strain measurements of the heel under normal+shearing loads (Case B of Table 2). Errors of 0.1 are observed across most of the strain intensities even for the highest strains (around 0.5). These errors tend to narrow down for the peak values. The SD shows that 95% of voxels have a strain error lower than 0.04. In general, this shearing configuration (Case B) shows errors with a double intensity and twice the propagation with respect to the normal

**Table 4**
Following cases A, B and C mentioned in Table 2, cases D, E and F relate to the estimation of the accuracy of strain calculation through image registration. The shear strain fields SD and SE will be compared with $S_{FEM}$. The shear strain fields SF will be compared with $SA_{011}$.

| Fixed | Moving | Case | Displacement field | Shear strain field |
|---|---|---|---|---|
| Heel 02 | Heel FEM | D | DD | SD |
| Heel 01 | Heel FEM | E | DE | SE |
| Heel 02 | Heel TRA | F | DF | SF |

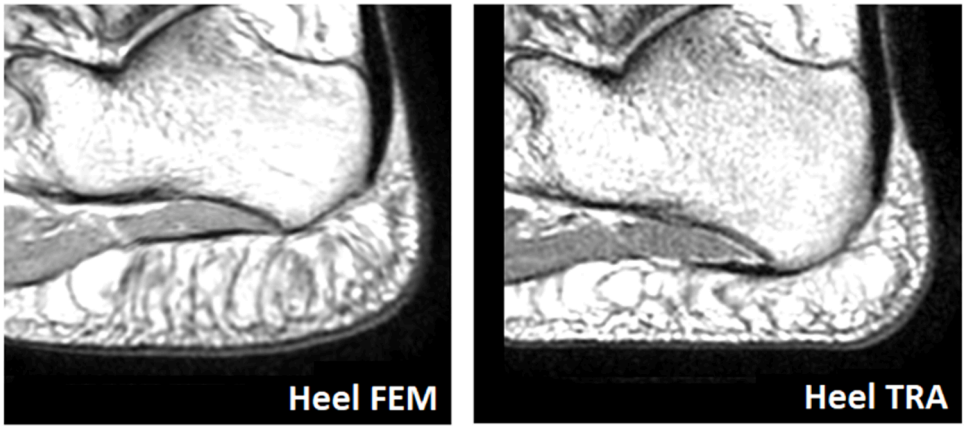


**Fig. 5.** Artificial images obtained once the displacement fields $D_{FEM}$ and $DA_{011}$ are applied to the unloaded image Heel 01.

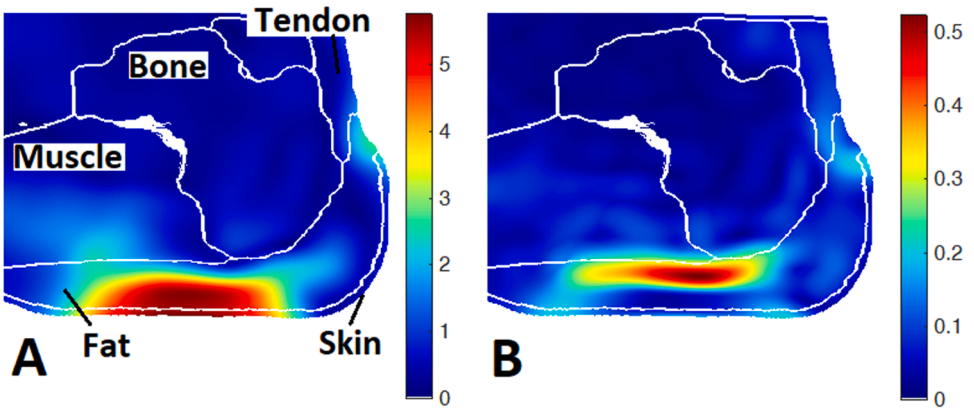


**Fig. 6.** Case A. Biological tissues are delimited by white lines. A slice from the MR volume is shown from the sagittal plane corresponding to the location of the highest shear strain. (A) Visual representation of $DA_{011}$. Modulus of displacement field [mm] for heel under normal load. (B) Visual representation of $SA_{011}$. Max GL shear strain field for heel under normal load (0.5 corresponds to 50% of deformation).

load configuration (Case A).

### 3.3. Strain measurements for sacrum under normal load (case C, Table 2)

For the sacrum loading configuration (Figure 10), the highest levels of displacements are found around the edges of the indenter. Shear strains are concentrated on the soft tissues around the contact area between the indenter and the skin. Adipose tissue and skin are subject to the highest levels of strains.

Figure 11 presents the Bland-Altman plot between the shear strain measurements produced by an indenter on the sacrum region (Case C of Table 2). In this case, the errors are considerably higher than what was observed for the heel application. Errors of 0.3 are spread throughout the image and the SD describes an error distribution where 95% of the voxels have an error that is lower than 0.15.

### 3.4. Estimation of strain field generated by the Fe model (case D, Table 4)

Figure 12 shows the results of image registration in the estimation of the artificial displacement field generated by Ansys (Fig. 4). Magnitudes of displacements were selected in order to generate strains comparable with Cases A and B.

Fig. 13 presents the correlation between the strain field calculated by Ansys and the corresponding measurements obtained by image registration (Case D of Table 4). The error distribution is comparable to Case A. For the regions with the highest levels of strains, the measurements slightly underestimate the strains since the points distribution shows an inclination that is higher than the red line. This artifact could be a result of the transformation step described in Table 3. In this process, some details of the original displacement field could have been lost in the image reconstruction after the application of the displacement to the respective voxels.

### 3.5. Deformation field from ANSYS – same noise pattern (case E, Table 4)

This case is running the registration between two images with the same noise pattern, undeformed (Heel 01), and artificially deformed (Heel FEM). Using the same image helps considerably the algorithms of the image registration process since the noise pattern present in the unloaded image matches the one of the unloaded image. This allows to easily identify the respective deformation matching the voxels with their equivalent copy in the respective deformed image. Results in terms of error distribution are as expected very precise showing a relevant strain field estimation (Figure 14). This reflects the described facilitations in terms of using an image and its deformed version in the registration process.

### 3.6. Deformation field from Elastix (case F, Table 4)

Case F is analogous to Case D with the main difference that the considered displacement field is not generated by Ansys but is taken from the image registration computed in Case A. The error distribution in terms of maximal error and SD is comparable to Case A (Figure 15). For the regions with the highest levels of strains, as detected also in case D, the measurements slightly underestimate the strains. In this case, the deformed image is also the result of an image transformation reported in Table 3.

## 4. Discussion

In this study, a method to estimate 3D internal tissue strains in the heel and sacrum regions based on DVC-derived displacement fields was developed in the context of pressure ulcers etiology. The methodology to implement DVC between two MR exams of human soft tissues (one at rest and the other one deformed) and to estimate the internal strains from the DVC 3D displacement field was first described. The implemented methodology requires a MR compatible device to apply loading on the skin surface during the acquisition of MR images. The obtained acquisitions were then used as input for 3D image registration. Images were first aligned based on the fixed body part (like bones) and then the non-rigid transformation was calculated. This transformation consists of a displacement field mapping every voxel between its initial position in the unloaded image and its final position in the loaded image. The GL shear strains are then computed from this displacement field. This methodology was implemented to analyze strain propagation in body regions that are critical in terms of pressure ulcer development: heel and sacrum.

For the results related to the heel pad, the calculated strain maps show as expected shear and compressive strain concentrations around the bony prominences of the calcaneus. This is coherent with the study of Luboz et al. which highlighted that strains generated around the calcaneus head strongly depended on the shape of this calcaneus bone [23]. Strains values in the deep tissues of the human heel were considerably higher than those in superficial tissue layers (Fig. 6B). This is consistent with previous findings listing the strain concentration in deep tissues as a key aspect in the etiology of ulceration [24]. The strains were concentrated in the fat pad region and propagating towards the interface with the muscular region. Oomens et al. identified skeletal muscle and fat as the two main biological tissues where pressure ulcers could develop [25]. The application of a shearing load pushing the first layer of skin towards the forefoot generated significantly higher shearing

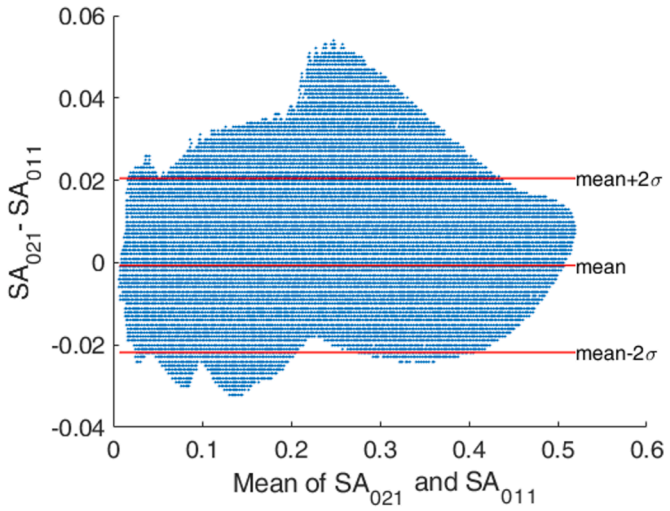


**Fig. 7.** Bland-Altman plot referring to the strain estimation computed from Case A: heel under normal load. The upper and lower red line correspond the 95% confidence interval, meaning that 95% of the values have an error lower than 0.02 strain. The most relevant part of the plot is the region with the highest values of the strains 0.4–0.5 as these can represent the threat for tissue damage.

loads in the anterior region of the fat pad compared with the configuration with only normal plantar pressure. Shear loadings can therefore impact significantly wider regions with higher levels of shear strains compared with normal loads of comparable intensity. This confirms what Ceelen et al. stated, namely (1) that shearing loads are more dangerous to treat than normal loadings, in terms of shear strain concentrations, and (2) that they must be taken into consideration for an effective pressure ulcer prevention [5].

For the results related to the sacrum, the calculated displacement and strain maps have values that are significantly higher than the results from the heel. The application of a load by means of an indentation device with a small contact area is probably more likely to generate higher shear strains right on the contact surface between the skin and the indenter [5].

The second objective of this article was to evaluate in a general way the reproducibility and the accuracy of strain calculation through image registration. Respectively, two main methodologies were presented: one related to the repetition of the same strain measurement from an equivalent set of images, and the other one to the calculation of a known *a priory* displacement field.

Concerning reproducibility as how much two equivalent measurement match, Fig. 7,10,12 are considered. Comparing the strain error distribution between image registrations of the heel related to Case A and Case B, we found that errors are twice higher and more distributed in the case where the shearing load is applied. This suggests that strain measurement from image registration is affected by the type of deformation applied on the soft tissues. A possible explanation for this effect can be related to the fact that a normal load displaces the skin in a normal direction generating a clear displacement of the edge between the portion of image representing the biological tissues and the dark background (see Fig. 3 Heel 01 and Heel 1). On the other hand, a shear load displaces the skin only in a tangent direction to the surface of the skin without generating any clear movement of the edge between the skin and the background (see Fig. 3 Heel 1 and Heel 2).

The image registration related to the sacrum has a much wider strain error distribution and values compared to the examples of the heel. This implies that strain measurement from image registration strongly depends on the image characteristics. To explain the reasons behind this we can try to analyze how image registration works. The first steps in the algorithms of image registration are feature detection and feature matching [26]. Salient and distinctive objects as edges are considered as features. The accuracy of image registration therefore directly depends on the quality of the acquired images to define clearly these edges [27]. The main parameters that characterize the quality of digital images are related to resolution and noise [28]. Noise is generated by the statistical fluctuation of the value from voxel to voxel. A common measurement of noise is the standard deviation, a measure of how spread out the values of the pixels are. The lower the standard deviation, the higher the

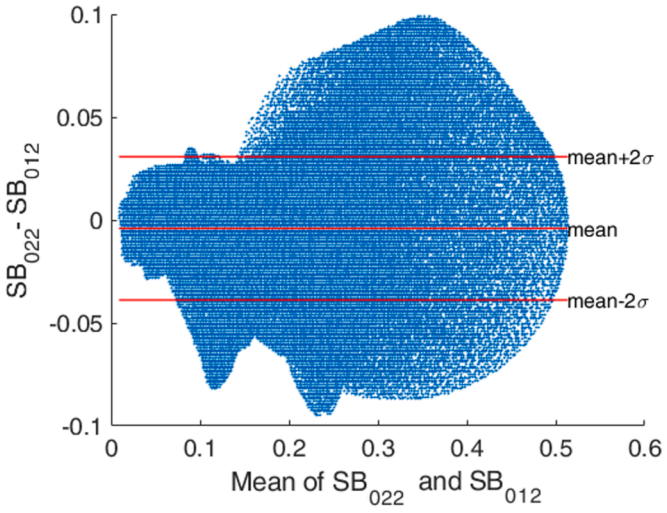


**Fig. 9.** .Bland-Altman plot referring to the strain estimation computed from Case B: heel under normal+shearing load. Error magnitude is around twice higher than the configuration with normal load only (Fig. 7).

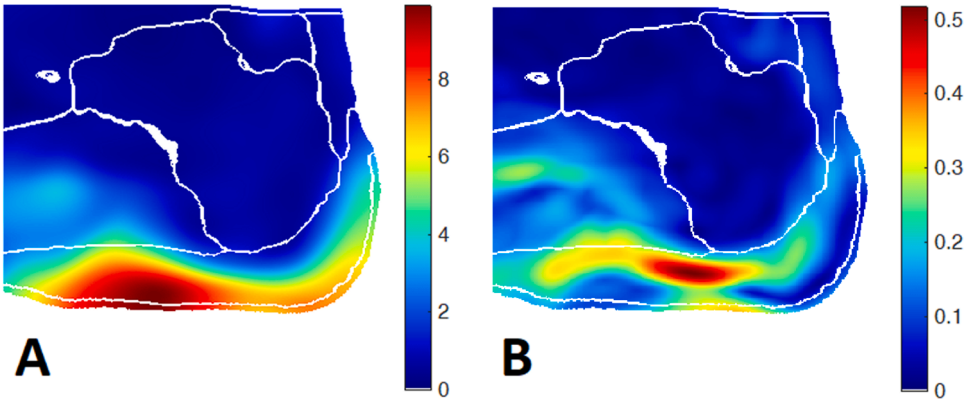


**Fig. 8.** (A) Modulus (in mm) of displacement field for heel under shearing load $DB_{012}$. (B) Max GL shear strain field for heel under shearing load $SB_{012}$.

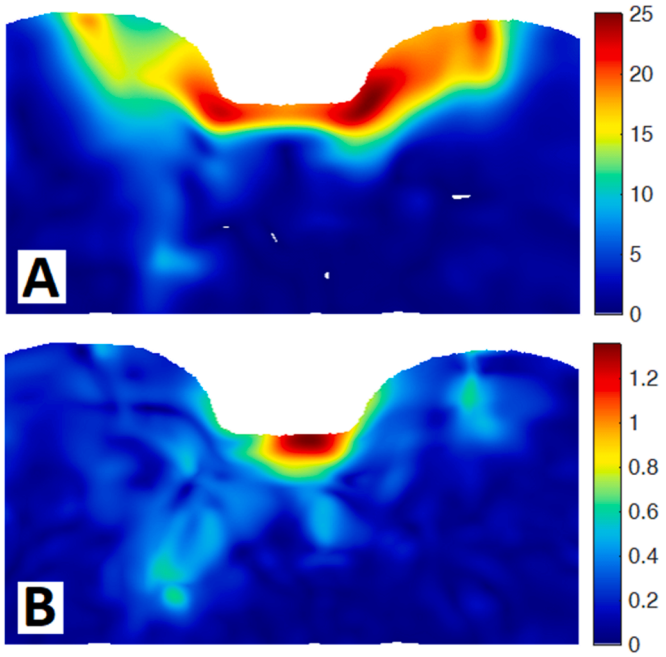


**Fig. 10.** (A) Modulus (in mm) of displacement field for sacrum under normal load $DC_{011}$. (B) Max GL shear strain field for sacrum under normal load $SC_{011}$.

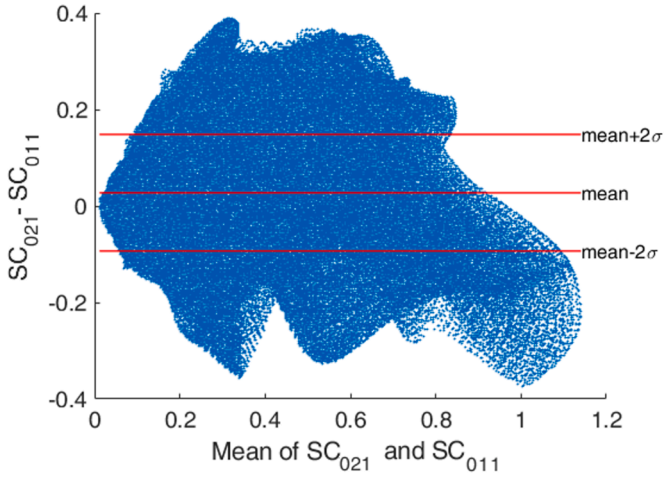


**Fig. 11.** Bland-Altman plot referring to the strain estimation computed from Case C: sacrum under normal load. Errors are considerably higher than the previous configurations of the heel.

accuracy of the average voxel value [29]. Spatial resolution is the ability of the imaging system to detect small objects that are close to each other [30]. The size of the voxels defines the maximum spatial resolution. However, image resolution is also influenced by other parameters such as blur factors. The most common blur factor is motion blur: when motion occurs during acquisition, the boundaries of patient structures will move from their initial position, making the boundaries blurred in the image. The motion can in general be reduced by fixing the body part with heavy MR-compatible pillows or casts [16]. These solutions, however, are ineffective when motions are generated by physiological movements such as breathing, peristalsis or heart beats. The line spread function (LSF) can be used to evaluate and quantify spatial resolution [31,32]. From this parameter, it was calculated that in the more crucial region of the images, the MR image of the heel had a quality parameter related to the spatial resolution that was 4.5 time higher than the one calculated for the sacrum images. It is possible therefore that this aspect played a crucial role in the strain estimation through image registration, thus decreasing significantly its reproducibility.

Concerning accuracy as how close a measurement is to a known or accepted value, Cases D and F were considered. These cases report errors of shearing strains around 0.02. This value can be compared to the level of strains that is considered to be sufficient to generate significant tissue damage. According to Ceelen et al., this value is around 0.65 for the shearing strain [5].

An interesting aspect is related to Case E, which uses the same image Heel 01 and its transformed version (Heel TRA) for the estimation of the displacement field. In this case, the strain errors are much less distributed (with a 95% confidence value below 0.007 error). This is due to the fact that any variability due to noise, or other artifacts, present in both images will have an impact on the strain estimation. This implies that for images with appropriate quality levels, this methodology can reach high accuracy.

The diversity of results obtained between the heel and sacrum applications implies that crucial further research is therefore required in finding the relation between specific image quality parameters and the respective error distribution in the strain calculation. This would permit in fact to select the image acquisition protocols in order to obtain the type of images to minimize errors in the registration process.

An advantage of the proposed methodology to calculate strains is that no additional tool to perform the error estimation is required. Considering Case E, the error estimation can be performed just with an additional image transformation (Table 3) and the respective image registration.

It is clear that the accuracy of the results is strongly related to the image registration process and to the selected parameters to perform it. By tuning the respective parameters of the registration process, it is possible to identify smaller deformations or to select the amount of volume compression and expansion. An optimization for the selection of the ideal parameters of the registration for the related application will be considered in the future steps to improve the accuracy of this methodology.

It must be considered that this work was based on specific mechanical configurations of a single subject meaning that results obtained are to be considered specific to this application. Fat and muscle biomechanical properties can change significantly as a consequence of diseases (for example, diabetes) and chronic immobilizations [33,34]. This inter-subject variability may introduce significant variations in the strain calculations making imperative to analyze each subject specifically.

## 5. Conclusion

The results obtained from the practical application on the heel and sacrum, in terms of location and magnitude of strains, are in line with the literature. This technique of calculating strains offers broad new possibilities to analyze the impact of external loads on the internal state of the soft tissues. The standard technique of FE is a very complex and time-consuming task involving segmentations, meshing and selections of proper constitutive laws. The possibility of strain calculation through image registration can provide results in terms of strain propagation in a significantly faster framework and offer the possibility for comparison and validation with results obtained from FE simulations. The present study proposed to quantify subdermal tissue strain distributions on the heel and sacrum from image registrations based on MR-acquisitions. This data is crucial for understanding the etiology of pressure ulcers that occur in the deep tissues of the heel pad.

The pilot study described here indicates that the crucial steps for computing strains from image registration are feasible to be implemented in a wider study. Further research will include analysis on more subjects and with different loading configurations, together with the adaptation of this methodology to different parts of the body to gain insight into the relative mechanical soft tissue properties.

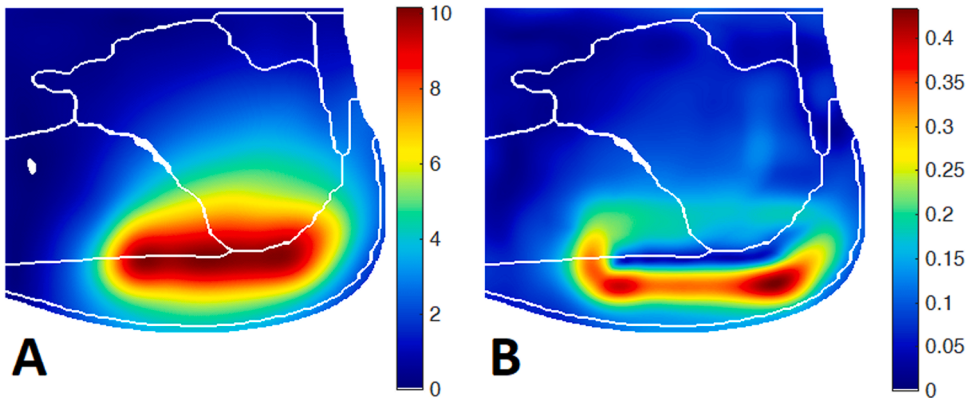


**Fig. 12.** (A) Estimation of the displacement field (mm) generated by Ansys DD. (B) Estimation of GL max shear strain generated by Ansys SD.

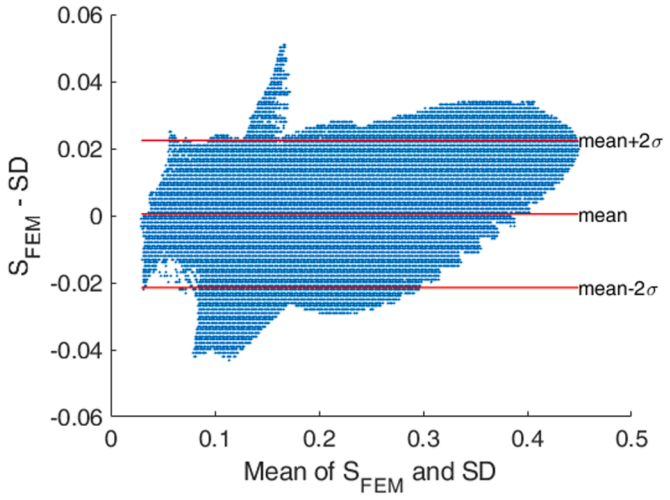


**Fig. 13.** Bland-Altman plot referring to the strain estimation computed from Case D: Displacement field generated by Ansys. The intensity of errors is around 0.02, which is comparable with case A (Fig. 7).

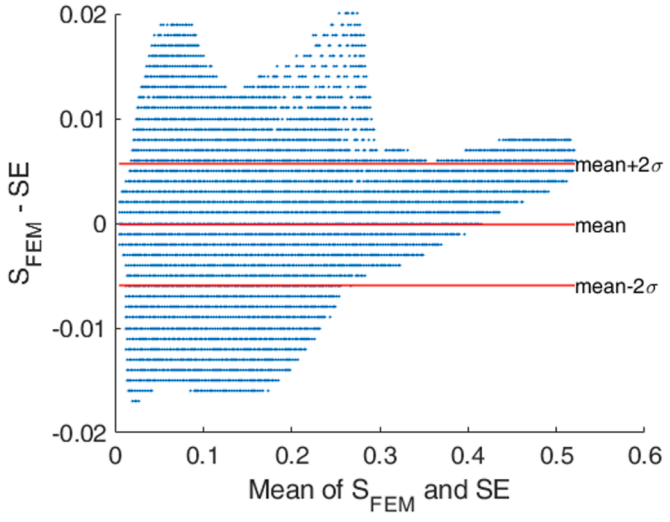


**Fig. 14.** Bland-Altman plot referring to the strain estimation computed from Case E: Displacement field generated by Ansys. Errors are lower than the other considered cases. This is due to the same noise pattern between the fixed and moving image in the registration procedure.

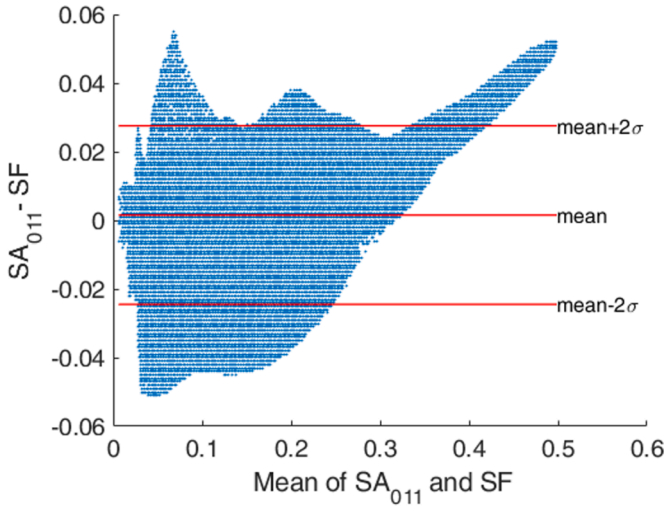


**Fig. 15.** Bland-Altman plot referring to the strain estimation computed from Case F: Displacement field generated by Elastix in Case A. The intensity of errors is around 0.02 comparable with Case A and D (resp. Fig. 7 and Fig. 14). This shows that, in the analyzed cases, similar images (Heel 01, 02, 1) generate errors of comparable magnitude (0.02).

## Ethical approval

A volunteer (male, 40 years old) agreed to participate in an experiment part of a pilot study approved by an ethical committee (MammoBio MAP-VS pilot study). He gave his informed consent to the experimental procedure as required by the Helsinki declaration (1964) and the local Ethics Committee.

## Declaration of Competing Interest

None.

## Acknowledgments

This research has received funding from the European Union's Horizon 2020 research and innovation program under the Marie Skłodowska-Curie Grant Agreement No. 811965; project STINTS (Skin Tissue Integrity under Shear). IRMaGe MRI facility was partly funded by the French program "Investissement d'Avenir" run by the "Agence Nationale pour la Recherche"; grant "Infrastructure d'avenir en Biologie Sante" - ANR-11-INSB-0006.

## References


[1] Barczak CA, Barnett RI, Childs EJ, Bosley LM. Fourth national pressure ulcer prevalence survey. Adv Wound Care 1997;10:18–26.

[2] Dugaret E, Videau MN, Faure I, Gabinski C. Bourdel-Marchasson I, Salles N. Prevalence and incidence rates of pressure ulcers in an Emergency Department. Int Wound J 2014;11:386–91. https://doi.org/10.1111/J.1742-481X.2012.01103.X.

[3] Vanderwee K, Clark M, Dealey C, Gunningberg L, Defloor T. Pressure ulcer prevalence in Europe: a pilot study. J Eval Clin Pract 2007. https://doi.org/10.1111/j.1365-2753.2006.00684.x.

[4] Thompson D. A critical review of the literature on pressure ulcer aetiology. Http://DxDoiOrg/1012968/Jowc200514226735 2013;14:87–90. https://doi.org/10.12968/JOWC.2005.14.2.26735.

[5] Ceelen KK, Stekelenburg A, Loerakker S, Strijkers GJ, Bader DL, Nicolay K, et al. Compression-induced damage and internal tissue strains are related. J Biomech 2008;41:3399–404. https://doi.org/10.1016/J.JBIOMECH.2008.09.016.

[6] Gefen A. The biomechanics of heel ulcers. J Tissue Viability 2010. https://doi.org/10.1016/j.jtv.2010.06.003.

[7] Fougeron N, Connesson N, Chagnon G, Alonso T, Pasquinet L, Bahuon M, et al. New pressure ulcers dressings to alleviate human soft tissues: a finite element study. J Tissue Viability 2022;31:506–13. https://doi.org/10.1016/J.JTV.2022.05.007.

[8] Keenan BE, Evans SL, Oomens CWJ. A review of foot finite element modelling for pressure ulcer prevention in bedrest: current perspectives and future recommendations. J Tissue Viability 2021. https://doi.org/10.1016/J.JTV.2021.06.004.

[9] Savonnet L., Wang X., Duprey S. Finite element models of the thigh-buttock complex for assessing static sitting discomfort and pressure sore risk: a literature review. Https://Doi-OrgSid2nomade-1GrenetFr/101080/10255842201814661172018;21:379–88. https://doi.org/10.1080/10255842.2018.1466117.

[10] Rma A.-.D., Affiliations P.G. A Comprehensive Literature Review of the Pelvis and the Lower Extremity FE Human Models under Quasi-static Conditions 2012. https://doi.org/10.3233/WOR-2012-1039-4218.

[11] Perrier A., Luboz V., Bucki M., Cannard F., Vuillerme N., Payan Y. Biomechanical Modeling of the Foot. Biomech. Living Organs Hyperelastic Const. Laws Finite Elem. Model., 2017. https://doi.org/10.1016/B978-0-12-804009-6.00025-0.

[12] Macron A, Pillet H, Doridam J, Rivals I, Sadeghinia MJ, Verney A, et al. Is a simplified Finite Element model of the gluteus region able to capture the mechanical response of the internal soft tissues under compression? Clin Biomech 2020;71:92–100. https://doi.org/10.1016/J.CLINBIOMECH.2019.10.005.

[13] Linder-Ganz E, Shabshin N, Itzchak Y, Gefen A. Assessment of mechanical conditions in sub-dermal tissues during sitting: a combined experimental-MRI and finite element approach. J Biomech 2007. https://doi.org/10.1016/j.jbiomech.2006.06.020.

[14] Stekelenburg A, Strijkers GJ, Parusel H, Bader DL, Nicolay K, Oomens CW. Role of ischemia and deformation in the onset of compression-induced deep tissue injury: MRI-based studies in a rat model. J Appl Physiol 2007. https://doi.org/10.1152/japplphysiol.01115.2006.

[15] Chatzistergos PE, Naemi R, Chockalingam N. An MRI compatible loading device for the reconstruction of clinically relevant plantar pressure distributions and loading scenarios of the forefoot. Med Eng Phys 2014. https://doi.org/10.1016/j.medengphy.2014.06.006.

[16] Petre M, Erdemir A, Cavanagh PR. An MRI-compatible foot-loading device for assessment of internal tissue deformation. J Biomech 2008. https://doi.org/10.1016/j.jbiomech.2007.09.018.

[17] Trebbi A, Perrier A, Bailet M, Payan Y. MR-compatible loading device for assessment of heel pad internal tissue displacements under shearing load. Med Eng Phys 2021;98:125–32. https://doi.org/10.1016/J.MEDENGPHY.2021.11.006.

[18] Tavana S, Clark JN, Prior J, Baxan N, Masouros SD, Newell N, et al. Quantifying deformations and strains in human intervertebral discs using Digital Volume Correlation combined with MRI (DVC-MRI). J Biomech 2020;102:109604. https://doi.org/10.1016/J.JBIOMECH.2020.109604.

[19] Yoder JH, Peloquin JM, Song G, Tustison NJ, Moon SM, Wright AC, et al. Internal three-dimensional strains in human intervertebral discs under axial compression quantified noninvasively by magnetic resonance imaging and image registration. J Biomech Eng 2014;136. https://doi.org/10.1115/1.4028250/371076.

[20] Schulz G, Crooijmans HJA, Germann M, Scheffler K, Müller-Gerbl M, Müller B. Three-dimensional strain fields in human brain resulting from formalin fixation. J Neurosci Methods 2011;202:17–27. https://doi.org/10.1016/J.JNEUMETH.2011.08.031.

[21] Yaman A, Ozturk C, Huijing PA, Yucesoy CA. Magnetic resonance imaging assessment of mechanical interactions between human lower leg muscles *in vivo*. J Biomech Eng 2013;135. https://doi.org/10.1115/1.4024573/370990.

[22] Klein S, Staring M, Murphy K, Viergever MA, Pluim JPW. Elastix: a toolbox for intensity-based medical image registration. IEEE Trans Med Imaging 2010. https://doi.org/10.1109/TMI.2009.2035616.

[23] Luboz V, Perrier A, Bucki M, Diot B, Cannard F, Vuillerme N, et al. Influence of the Calcaneus Shape on the Risk of Posterior Heel Ulcer Using 3D Patient-Specific Biomechanical Modeling. Ann Biomed Eng 2015. https://doi.org/10.1007/s10439-014-1182-6.

[24] Stekelenburg A, Gawlitta D, Bader DL, Oomens CW. Deep Tissue Injury: how Deep is Our Understanding? Arch Phys Med Rehabil 2008;89:1410–3. https://doi.org/10.1016/J.APMR.2008.01.012.

[25] Oomens CWJ, Bader DL, Loerakker S, Baaijens F. Pressure Induced Deep Tissue Injury Explained. Ann Biomed Eng 2015. https://doi.org/10.1007/s10439-014-1202-6.

[26] Oliveira F.P.M., Tavares J.M.R.S. Medical image registration: a review. Https://Doi-OrgSid2nomade-1GrenetFr/101080/102558422012670855 2013;17:73–93. https://doi.org/10.1080/10255842.2012.670855.

[27] Nederveen AJ, Avril S, Speelman L. MRI strain imaging of the carotid artery: present limitations and future challenges. J Biomech 2014;47:824–33. https://doi.org/10.1016/J.JBIOMECH.2014.01.014.

[28] Goldman LW. Principles of CT: radiation Dose and Image Quality. J Nucl Med Technol 2007;35:213–25. https://doi.org/10.2967/JNMT.106.037846.

[29] Alsleem H, Davidson R. Quality parameters and assessment methods of digital radiography images. Radiographer 2012;59:46–55. https://doi.org/10.1002/J.2051-3909.2012.TB00174.X.

[30] Williams MB, Krupinski EA, Strauss KJ, Breeden WK, Rzeszotarski MS, Applegate K, et al. Digital Radiography Image Quality: image Acquisition. J Am Coll Radiol 2007;4:371–88. https://doi.org/10.1016/J.JACR.2007.02.002.

[31] Samei E, Ranger NT, Dobbins JT, Chen Y. Intercomparison of methods for image quality characterization. I. Modulation transfer functiona). Med Phys 2006;33:1454–65. https://doi.org/10.1118/1.2188816.

[32] Nugent P.W., Shaw J.A., Kehoe M.R., Smith C.W., Moon T.S., Swanson R.C. Measuring the modulation transfer function of an imaging spectrometer with rooflines of opportunity. Https://Doi-OrgSid2nomade-1GrenetFr/101117/13497051 2010;49:103201. https://doi.org/10.1117/1.3497051.

[33] Fontanella CG, Nalesso F, Carniel EL, Natali AN. Biomechanical behavior of plantar fat pad in healthy and degenerative foot conditions. Med Biol Eng Comput 2016. https://doi.org/10.1007/s11517-015-1356-x.

[34] Talmadge RJ, Roy RR, Caiozzo VJ. Reggie Edgerton V. Mechanical properties of rat soleus after long-term spinal cord transection. J Appl Physiol 2002. https://doi.org/10.1152/japplphysiol.00053.2002.

# APPENDIX 3

Journal of Tissue Viability xxx (xxxx) xxx

Contents lists available at ScienceDirect

Journal of Tissue Viability

journal homepage: www.elsevier.com/locate/jtv

# Reliability of B-mode ultrasound and shear wave elastography in evaluating sacral bone and soft tissue characteristics in young adults with clinical feasibility in elderly

Maher Abou Karam, M.D. [a,*], Ekaterina Mukhina [b], Nils Daras [a], Isabelle Rivals, PhD [c,d], Hélène Pillet, PhD [a], Wafa Skalli, PhD [a], Nathanaël Connesson, PhD [b], Yohan Payan, PhD [b], Pierre-Yves Rohan, PhD [a]

[a] Institut de Biomécanique Humaine Georges Charpak, Arts et Métiers Institute of Technology, 151 bd de l'Hôpital, 75013, Paris, France
[b] Univ. Grenoble Alpes, CNRS, Grenoble INP, TIMC-IMAG, Grenoble, France
[c] Sorbonne Université, INSERM, UMRS1158, Neurophysiologie Respiratoire Expérimentale et Clinique, Paris, France
[d] Equipe de Statistique Appliquée, ESPCI Paris, PSL Research University, Paris, France

ARTICLE INFO

*Keywords:*
Pressure ulcer
Sacrum
Medial sacral crest
Elderly
Ultrasound
Shear wave elastography
Elasticity
Reliability

ABSTRACT

*Background:* Physiologic aging is associated with loss of mobility, sarcopenia, skin atrophy and loss of elasticity. These factors contribute, in the elderly, to the occurrence of a pressure ulcer (PU). Brightness mode ultrasound (US) and shear wave elastography (SWE) have been proposed as a patient-specific, bedside, and predictive tool for PU. However, reliability and clinical feasibility in application to the sacral region have not been clearly established.

*Method:* The current study aimed to propose a simple bedside protocol combining US and SWE. The protocol was first tested on a group of 19 healthy young subjects by two operators. The measurements were repeated three times. Eight parameters were evaluated at the medial sacral crest. Intraclass Correlation Coefficient (ICC) was used for reliability assessment and the modified Bland Altman plot analysis for agreement assessment. The protocol was then evaluated for clinical feasibility on a healthy older group of 11 subjects with a mean age of 65 ± 2.4 yrs.

*Findings:* ICC showed poor to good reliability except for skin SWE and hypodermis thickness with an ICC (reported as: mean (95%CI)) of 0.78 (0.50–0.91) and 0.98 (0.95–0.99) respectively. No significant differences were observed between the young and older group except for the muscle Shear Wave Speed (SWS) (respectively 2.11 ± 0.27 m/s vs 1.70 ± 0.17 m/s).

*Interpretation:* This is the first protocol combining US and SWE that can be proposed on a large scale in nursing homes. Reliability, however, was unsatisfactory for most parameters despite efforts to standardize the protocol and measurement definitions. Further studies are needed to improve reliability.

## 1. Introduction

Tissue morphology, mechanical properties, physiology, and repair properties can all change over time as a result of aging, lifestyle, chronic injury, or disease. Over a bony prominence, these changes - associated with a mechanical load - can lead to a localized injury known as a "pressure ulcer" [1].

The prevalence of this lesion ranges between 9% [2] and 15% [3] in long term care or hospitalized patients, and is most frequently observed over the sacrum or the heel. Two thirds of PU are observed in patients above 70 years of age [4]. The occurrence of PU is associated with significant increase in hospital costs, length of stay and, most importantly, an increased risk of death [5–7].

While numerous and efficient therapies have been developed, prevention remains the center of interest of all healthcare professionals and thus of researchers [4]. However, current practices in PU prevention are far from satisfactory with more than 85% lack in documented repositioning care plan. This is majorly due to the lack of staff and time [2]. PU prevention protocols are based on risk assessment tools or scales (Norton

* Corresponding author.
*E-mail address:* maher.abou_karam@ensam.eu (M. Abou Karam).

https://doi.org/10.1016/j.jtv.2022.02.003
Received 22 October 2021; Received in revised form 6 February 2022; Accepted 8 February 2022
Available online 16 February 2022
0965-206X/© 2022 Tissue Viability Society. Published by Elsevier Ltd. All rights reserved.

Please cite this article as: Maher Abou Karam, *Journal of Tissue Viability*, https://doi.org/10.1016/j.jtv.2022.02.003

**List of abbreviations**

| | |
|---|---|
| B-mode | Brightness mode |
| CI | confidence interval |
| CT | Computed tomography |
| FE | Finite element |
| HT | Hypodermis thickness |
| hSWE | hypodermis shear wave elastography |
| HE | Medial sacral crest height |
| ICC | intraclass correlation coefficient |
| IT | ischial tuberosity |
| MRI | Magnetic resonance imaging |
| MSC | Medial sacral crest |
| mSWE | muscle shear wave elastography |
| OA | Medial sacral crest opening angle |
| PSIS | Posterior superior iliac spine |
| PU | Pressure ulcer |
| ROC | Medial sacral crest radius of curvature |
| ST | Skin thickness |
| SWE | Shear wave elastography |
| sSWE | Skin shear wave elastography |
| US | ultrasound |

scale, Braden scale …) [8]. The impact of these tools on the incidence of PU remains uncertain and fail to meet the needs of all patients in different clinical settings [7].

The process of aging is associated with physiological changes including sarcopenia, osteoporosis, progressive increase in blood glucose and skin atrophy [9]. The decrease in muscular power has a high impact on the performance of daily activities even in healthy older persons leading to increased immobility [10]. In consequence, the elderly are considered at risk of developing PU and therefore, a target group for preventive screening protocols. Several bedside technologies combined with assessment tools were investigated for early detection of PU, especially in long term care facilities. High frequency ultrasound (HFUS) was particularly studied, given its accessibility and capacity to detect preclinical superficial skin changes, mainly the presence of fluid/oedema at different levels of the skin [11]. However, a randomized controlled trial [12] failed to demonstrate that HFUS was an effective strategy for predicting the development of Category/Stage I PU s of the heel or sacrum compared with a focused physical assessment. Also, a systematic review [13] evaluated HFUS among other technologies. Despite giving meaningful and consistent results, it could not be recommended due to lack of reliability of protocols, being limited to detecting macroscopic level tissue damage, and its training requirements for image interpretation.

In terms of etiology/pathophysiology, studies based on both *in vitro* (cell models) and *in vivo* (animal models) approaches have demonstrated that at least two damage mechanisms, are involved in the development of PU: first, compression damage due to tissue ischemia/reperfusion initiated by local, moderate and persistent mechanical loads; secondly, direct deformation damage above a threshold level related to shear strain; even for a short period of time (during transfer from bed to a wheelchair for example) [14]. These results suggest the presence of a direct link between mechanical determinants and biological processes leading to tissue damaging and, in fine, necrosis.

Based on the rationale that elucidating the relationship between external loads and internal local stresses and strains within loaded soft tissues has the potential of improving the management and prevention of PUs, several Finite Element (FE) models of the buttocks have been proposed in the literature. Models are mostly based on the segmentation of MRI or CT scan sequences [15–18]. However, the use of MRI and CT scans is limited due to cost, accessibility, and time [19]. In this perspective, brightness mode (B-mode) ultrasound (US) imaging was proposed as an alternative to MRI or CT-scan. Feasibility, reproducibility, and its use for personalized FE models were investigated mainly over the ischial tuberosity [19–23].

Recent studies [19,24,25] proposed B-mode US for the evaluation of biomechanical risk of PU in a seated position by assessing, among other parameters, tissue thickness changes in different positions. On the other hand, ultrasound elastography, a relatively new method that shows structural changes in tissues following application of physical stress can be used in the examinations of musculoskeletal system [26]. Shear wave elastography (SWE) uses focused ultrasonic beams, to remotely generate mechanical vibration sources radiating low-frequency, shear waves inside tissues [27]. It allows a bedside evaluation of the local mechanical properties of soft biological tissues by assessing shear modulus [28–30]. Experiments demonstrated that ultrasound elastography is a promising technique for PU detection, especially at an early stage of the pathology, when the disease is still visually undetectable [28].

Previous studies investigating the combination of B-mode US and SWE elastography in the context of PU prevention focused on potential changes of tissue stiffness during prolonged loading [31] or tissue characteristics in different body postures [32].

The current study aimed to propose and test a bedside B-mode US and SWE protocol that can be used as a risk assessment tool for sacral PU in elderly. The protocol was designed for the evaluation of bone geometry, tissue morphology and mechanical characteristics over the sacrum. Reliability and reproducibility of our protocol were tested on a healthy young adults group. The protocol was then applied on a group of healthy older people to assess for clinical feasibility.

## 2. Materials and methods

1. Data Collection

The current study was approved by the ethics committee (Comité de protection des Personnes CPP NX06036) and each subject gave an informed consent. For the reproducibility analysis 19 young healthy subjects participated to the experiment, 8 women and 11 men (Age: 25.7 ± 3.8 yrs, Weight: 75.2 ± 16.4 kg, BMI: 24.5 ± 4.9 kg/m$^2$). For the elderly group 11 healthy subjects, 7 women and 4 men were recruited (Age: 65 ± 2.4 yrs, Weight: 72.5 ± 18.6 kg, BMI: 25.34 ± 5 kg/m$^2$). Exclusion criteria included: the presence of chronic or acute low back pain, history of lower spine surgery or sacral PU, and the presence of PU skin signs at the moment of the acquisition.

### 2.1. Ultrasound acquisition protocol

B-mode US images and shear wave elastography (SWE) videos were obtained using a commercial device (SupersonicMach30, SuperSonic Imagine, France). Two probes were used, the curvilinear (SuperCurved C6-1X) with low frequency (1–6 MHz allowing increased depth visualization) and large field of view, and the linear (SuperLinear L10-2) probe with a higher frequency (2–10 MHz allowing superficial layers visualization). The general mode and penetration optimization were chosen for all acquisitions.

A standardized - tissue and musculoskeletal US/SWE over the sacral region - protocol was developed and was first pilot tested on a sample of three healthy young volunteers, consequently, adjustments were made. The definitive protocol is described thoroughly in Appendix 1.

Acquisitions were taken in the lying prone position. After anatomic palpation of the two posterior superior iliac spines (PSIS), the curvilinear probe was first used in B-mode to recognize the anatomic region of interest: the MSC. An image was captured to assess bone anatomy and the skin was marked with a tape. Switching to the linear probe, the second image captured the skin and hypodermis at the level of the MSC. The third part, also using the linear probe at the marked skin level, was a series of three videos (of 10 s each) in SWE mode with a region of

interest (ROI) including both skin and hypodermis. For the fourth and last part, three SWE videos of the gluteus maximus muscle were taken lateral to the sacro-coccygeal region at the lower part of the sacrum. The images/videos using the linear probe were taken with minimal applied pressure, using a thick gel layer and making sure it was visible on the US image. A summary of the acquisition protocol and images are shown in Fig. 1.

### 2.2. Parameter estimation

To reduce acquisition time, processing and measurements for images/videos were done separately using a custom software written in Matlab (R2019a) (MathWorks, Inc, Natick MA). In total 8 parameters were measured using the images/videos captured during each acquisition. First, the bone anatomy image (Fig. 1a) was used to measure the MSC radius of curvature (ROC), opening angle (OA), and height (HE). Then, the second image (Fig. 1b) was used to measure the skin thickness (ST) and the hypodermis thickness (HT). For the SWE videos of the third (Fig. 1c) and fourth (Fig. 1d) part of the acquisition, images were extracted and processed using a separate written code [33]. The average value of the images of each video was calculated and then, the average of the three videos determined the shear wave velocity of one acquisition for: the skin (sSWE), the hypodermis (hSWE), and gluteus maximus muscle (mSWE). Details about the definitions and recommendations for these measurements are reported in Table 1.

## 3. Method evaluation

### 3.1. Sample size and reliability assessment

All the data were analyzed with the IBM SPSS for Windows (Version 27.0. Armonk, NY: IBM Corp).

The reliability study was conducted on the young, healthy group by two operators: a physician and an engineer. Both operators received extensive training consisting of two phases: first, measurements were repeated until reaching adequate reproducibility compared with an expert sonographer then, deviations were assessed, and possible problems were determined and corrected.

The operators were asked to repeat the protocol three times on each subject, i.e., captured three images for each of the bone geometry parameters and tissue morphology, and nine SWE videos for each tissue stiffness parameter.

The reliability of our protocol was assessed by calculating the intra class correlation coefficient (ICC) for within-operator and between-operator for the young subjects group [34]. The minimum sample size required for this test-retest reliability study was estimated based on the recommendations made in Bujang et al. [35]. With three observations per subject, a minimum sample size of 15 is required to detect an ICC value of 0.5 with power of 90% when taking a type I error risk of 5% (Table 1a of [35]).

Given that ultrasound acquisition is highly operator dependent, and that the processing/measurement of a given image/video (i.e. definitions of parameters) might also differ from one operator to another, we decided to quantify the variability first at processing level, and then at both processing and acquisition level. First, the two operators processed and measured one acquisition conducted by the physician on all subjects. Each operator repeated measurement of the same image/video three times, allowing an intra-image analysis [36]. For this analysis, the ICC model 3 (2-way mixed) was chosen for within-operator reliability, and ICC model 2 (2-way random) for between-operator reliability with absolute agreement type and single measure [37]. For between operator reliability, values of one of the three measurement, chosen randomly for each operator, was used. Then, each operator processed and measured their own acquisitions allowing an inter-image analysis [36]. The same model and type for within-operator ICC (2-way mixed and absolute agreement) were used with single measure, and for between-operator reliability also the ICC model 2 was used but with consistency agreement type and single measure since different images are compared. Also, for between operator reliability, values of one of the three measurements, chosen randomly for each operator, was used. This procedure was conducted for each parameter and the ICC with 95% confidence interval was reported. Values less than 0.5, between 0.5 and 0.75, between 0.75 and 0.9, and greater than 0.90 indicated poor, moderate, good, and excellent reliability, respectively [37].

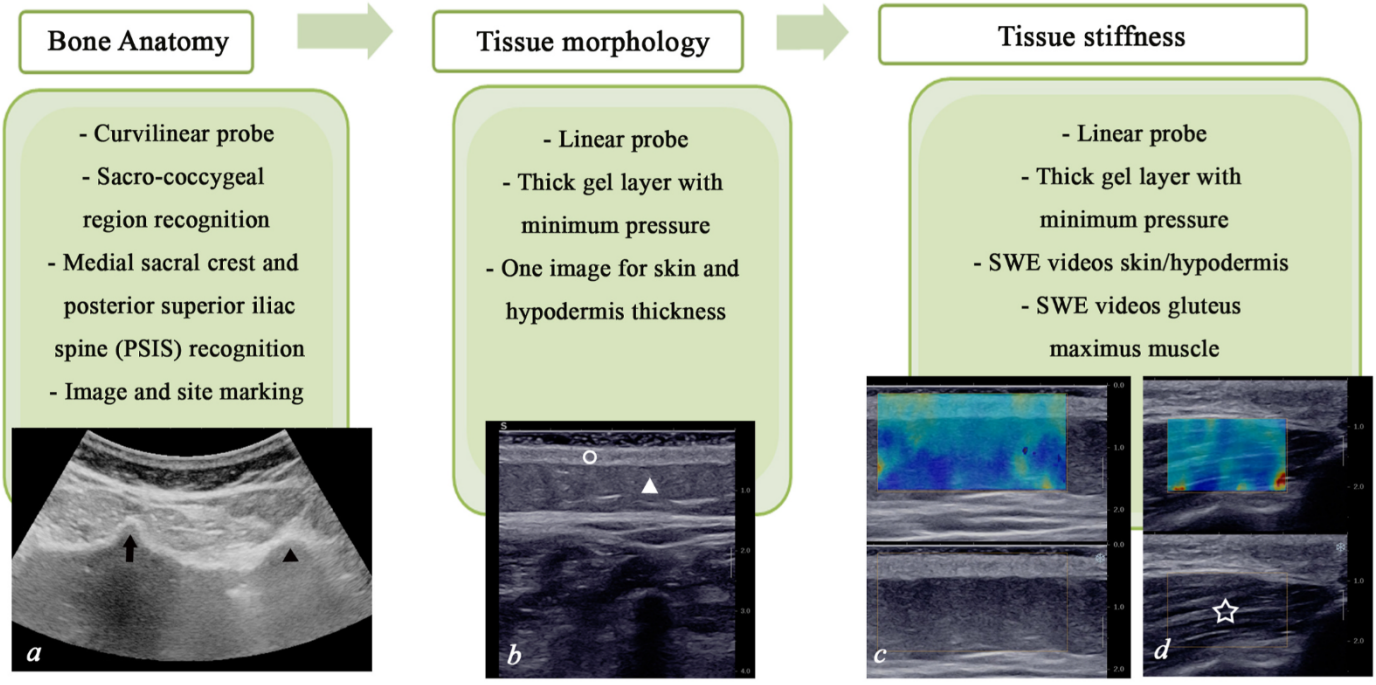


**Fig. 1.** US acquisition protocol of the sacral region in the transverse view. In B-mode: the medial sacral crest (arrow) at the level of the PSIS (black triangle) (a), skin (arrow) and adipose tissue (white triangle) over MSC (b); in SWE mode: the skin and adipose tissue (c), gluteus maximus muscle (star) (d).

**Table 1**
Description of parameter measurement post acquisition using a customized MATLAB algorithm.

| | PARAMETER NAME | DESCRIPTION | POST-PROCESSING |
|---|---|---|---|
| ***Bone anatomy (curvilinear probe - B-mode)*** | Radius of curvature (ROC) | 10 points distributed equally on both sides of the tip of MSC; the circle plotted was viewed to ensure it captures the shape of the tip [19] | 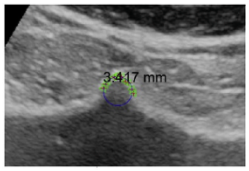  |
| | Opening angle (OA) | 3 points: one on the middle of the MSC tip and two bilateral points | 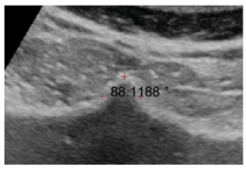  |
| | Height (HE) | 3 points: the geometry of the MSC could be compared to a triangle, the tip is the highest point of the triangle and two points for the base of the MSC; the distance from the upper point to the base is the HE |   |
| ***Tissue morphology (linear probe - B-mode)*** | Skin thickness (ST) | 2 points: the upper limit marked by the most superficial, homogenous, and continuous line of the epidermis; lower border marked by the transition between dermis and hypoechoic adipose tissue | 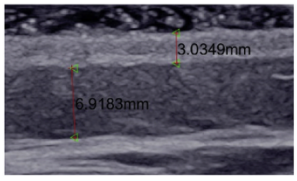  |
| | Hypodermis thickness (HT) | 2 points: thickest hypoechoic region under the skin; hyperechoic muscle fascia marks the lower border | |
| ***Tissue stiffness (linear probe – SWE mode)*** | SWE skin (sSWE) | Region of interest (ROI): largest, most homogenous SWE signal | 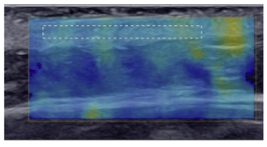 |
| | SWE hypodermis (hSWE) | | 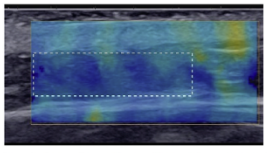 |
| | SWE gluteus muscle (mSWE) | | 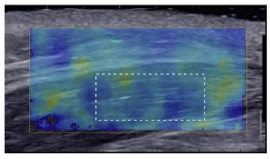 |

### 3.2. Agreement assessment

The modified Bland Altman plot analysis for continuous measures [38] was used as a measure of the level of agreement within and between operators for both the intra-image and inter-image analysis. In the absence of a gold standard, the value of each measurement was compared to the average of all measurements for one subject (bias line equal to zero). The difference between each observer and the overall mean for a subject is estimated. The 95% level of agreement with the mean is estimated as ±2 x Standard deviation (SD), where SD represents the square root of the variance of the differences.

### 3.3. Healthy young adults vs healthy elderly

The same protocol was conducted once (one acquisition and measured once) on the older group by one operator: the physician. For the young adults group data, the measurements of one of the three acquisitions collected by the physician were chosen randomly. Normality was checked with the Shapiro–Wilk test and the equality of variance was assessed with the Levene's test. If both normal distribution and equality of variance of the different groups could be assumed, data were reported per parameter and per group as mean ± 1 SD and groups (young versus old) were compared using the student t-test. In case the normality or equality of variance assumption was violated, groups were compared with the Wilcoxon test. For all the tests, the significance level was set at 0.05 *a priori*.

## 4. Results

### 4.1. Reliability assessment

Within operator and between operator ICC with the 95% confidence interval, for both the intra and inter-image analysis for all parameters, are reported in Table 2. First in the intra-image analysis, all ICC confidence interval values showed good to excellent reliability for within operator, except for the ROC, and the OA of the MSC for the physician with moderate to excellent reliability. For between operator ICC the following parameters: HE, hypodermis thickness, SWE skin, SWE

**Table 2**
Reliability assessment results with Intraclass correlation coefficient ICC for both intra-image and inter-image analysis for both operators: 1 the physician and 2 the engineer.

| Parameter | Operator | Intra-image analysis | | Inter-image analysis | |
|---|---|---|---|---|---|
| | | Within operator ICC (95% CI) | Between operator ICC (95% CI) | Within operator ICC (95% CI) | Between operator ICC (95% CI) |
| **Radius of curvature** | **1** | 0.86 (0.68–0.94) | 0.84 (0.64–0.94) | 0.90 (0.79–0.96) | 0.69 (0.34–0.87) |
| | **2** | 0.93 (0.84–0.97) | | 0.76 (0.53–0.90) | |
| **Opening angle** | **1** | 0.86 (0.66–0.94) | 0.81 (0.57–0.92) | 0.74 (0.53–0.89) | 0.58 (0.17–0.82) |
| | **2** | 0.96 (0.91–0.98) | | 0.73 (0.50–0.88) | |
| **Height** | **1** | 0.97 (0.93–0.99) | 0.97 (0.92–0.99) | 0.89 (0.78–0.96) | 0.74 (0.43–0.89) |
| | **2** | 0.98 (0.95–0.99) | | 0.69 (0.45–0.87) | |
| **Skin thickness** | **1** | 0.94 (0.87–0.97) | 0.88 (0.73–0.95) | 0.71 (0.49–0.87) | 0.53 (0.09–0.80) |
| | **2** | 0.95 (0.88–0.98) | | 0.59 (0.32–0.80) | |
| **Hypodermis thickness** | **1** | 0.99 (0.99–1.00) | 0.99 (0.99–1.00) | 0.98 (0.96–0.99) | 0.98 (0.95–0.99) |
| | **2** | 0.99 (0.99–1.00) | | 0.99 (0.98–1.00) | |
| **SWE skin** | **1** | 0.99 (0.99–1.00) | 0.99 (0.99–1.00) | 0.83 (0.67–0.93) | 0.78 (0.50–0.91) |
| | **2** | 0.99 (0.99–1.00) | | 0.85 (0.72–0.94) | |
| **SWE hypodermis** | **1** | 0.99 (0.98–1.00) | 0.98 (0.94–0.99) | 0.70 (0.46–0.86) | 0.65 (0.27–0.85) |
| | **2** | 0.98 (0.97–0.99) | | 0.80 (0.63–0.91) | |
| **SWE muscle** | **1** | 0.96 (0.88–0.99) | 0.93 (0.79–0.98) | 0.71 (0.41–0.90) | 0.41 (-0.22-0.80) |
| | **2** | 0.98 (0.96–1.00) | | 0.84 (0.63–0.95) | |

hypodermis, SWE muscle, showed good to excellent reliability. The ICC for the OA and the skin thickness showed moderate to excellent reliability. For the inter-image analysis, within operator ICC showed excellent reliability for the hypodermis thickness parameter for both operators. The physician (operator 1) showed good to excellent reliability for the ROC and HE. For the SWE skin parameter he showed moderate to excellent reliability; for the opening angle parameter moderate to good reliability; for the remaining parameters poor to good reliability. The engineer (operator 2) showed moderate to excellent reliability for the ROC, SWE skin, SWE hypodermis, and SWE muscle parameters. For the opening angle parameter, the engineer showed moderate to good reliability; for the HE, skin thickness poor to good reliability. The between operator ICC also showed excellent reliability for the hypodermis thickness. The ICC for SWE skin parameter showed moderate to excellent reliability. The ICC of the remaining parameters showed poor to good reliability.

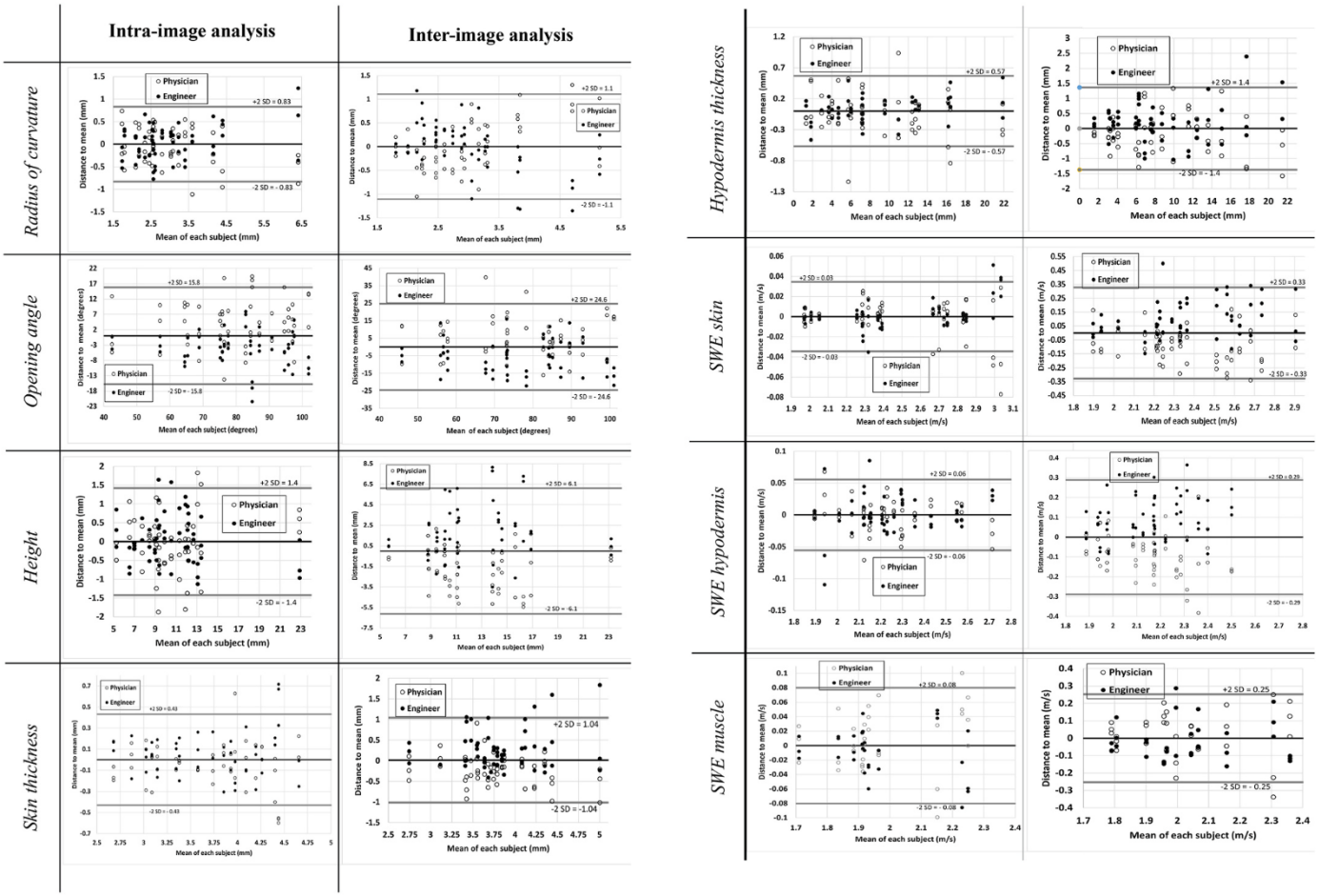


**Fig. 2.** Agreement plots with the mean of measurements for the intra-image and inter-image analyses for the 8 parameters.

### 4.2. Agreement assessment

The modified Bland Altman agreement plots for both the intra and inter image analysis are reported in Fig. 2. The 95% limits of agreement with the mean varied from the intra to the inter-image analysis as follows: for the ROC from ±0.83 mm to ±1.1 mm; for the opening angle from ±15.8° to ±24.8°; for the HE from ±1.4 mm to ±6.1 mm; for the skin thickness from ±0.43 mm to ±1.04 mm; for the hypodermis thickness from 0.57 mm to 1.4 mm; for the SWE skin from ±0.03 m/s to ±0.33 m/s; for the SWE hypodermis from ±0.06 m/s to ±0.29 m/s; and for the SWE muscle from ±0.08 m/s to ±0.25 m/s.

### 4.3. Healthy young adults VS healthy elderly

The results of means, normality tests and Student's t-test test are reported in Table 3. There was insufficient evidence to claim that the distributions were not normal or that the variances were not equal. Based on the results of the student t-test, we concluded that there is a statistically significant difference only for the mSWE (2.11 ± 0.27 m/s for the young adults group vs 1.70 ± 0.17 m/s for the elderly, p-value = 0.001). Because of the relatively small sample size, the sample means for each parameter were also compared using the Wilcoxon signed rank test. The conclusions were the same i.e., there is a statistically significant difference only for the mSWE.

Images reported in Fig. 3 show observations for the older group subjects that diverged from the group. The upper and lower limits for skin and hypodermis SWE were found in a 62-year-old male subject with a BMI of 39.1 kg/m$^2$ (Fig. 3b) and a 67-year-old male with a BMI of 27.4 kg/m$^2$ (Fig. 3a), respectively. A 62-year-old female elderly with a BMI of 22.3 kg/m$^2$ (Fig. 3c) showed a heterogeneous distribution of hypodermis thickness over the MSC.

## 5. Discussion

This study aimed to evaluate the use of B-mode US and SWE in the assessment of bone geometry, tissue morphology and tissue stiffness in the context of sacral PU prevention in elderly. A protocol was developed to evaluate the region over the MSC. It was tested for reliability on a group of 19 healthy young subjects by two operators: a physician and an engineer. Afterwards, the protocol was tested on a group of 11 healthy older people by the physician only. The parameters evaluated by our protocol were: the radius of curvature (ROC), opening angle (OA), and height (HE) of the MSC for the bone geometry; the skin thickness (ST), and hypodermis thickness (HT) for the tissue morphology; skin shear wave velocity (sSWE), hypodermis shear wave velocity (hSWE), and muscle shear wave velocity (mSWE) for tissue stiffness.

1. Reliability study

The intra-image analysis was first conducted to assess the operators understanding and reliability of measuring each parameter. Within-operator ICC was good to excellent for all parameters for the engineer. For the physician, most parameters showed good to excellent reliability except for the ROC (CI 0.68–0.94) and OA (CI 0.66–0.94), showing moderate to excellent reliability. This might be due to an unclear definition of these two parameters. While the ROC is measured by placing points on the tip of MSC, the position of the start and ending points are not always clear. Between operator ICC, for the intra-image analysis, showed good to excellent reliability for all parameters except ROC, OA, ST with moderate to excellent reliability. These results also highlight the difficulty in choosing the points for the ROC and OA. For the ST parameter, although the skin is a continuous layer over the hypodermis, both stratum corneum: the most superficial layer of the epidermis, and the reticular layer: the lower part of the dermis, are wavy layers and thus might affect ST measurement depending on the part of the image chosen to assess ST [39]. The inter-image analysis aimed to test whether operators are capable of successfully repeating an acquisition three times and reproducing the acquisition protocol. Because acquisitions measured were not the same, ICC results were expected to have lower values. The discussion will involve only the parameters that showed good to excellent reliability on the intra-image analysis. First the HE parameter, within operator reliability was good to excellent for the physician but low to good for the engineer. A possible explanation might be that the acquisitions were not taken at the same level over the MSC. Another explanation is the fact that, in terms of anatomy, the sacrum is the most variable portion of the spine. In fact, the MSC is formed by the fusion of the spinous processes of the first three to four sacral vertebrae, and therefore bone morphology might differ from a level to another [40]. In this perspective, an emphasis should be on taking the acquisition at the level of the two PSIS, since it is a fixed, palpable and US visible anatomic landmark (using the curvilinear probe). Also, the only study, that the authors found in the literature, that included US and SWE tissue evaluation of the sacral region reported neither the protocol of measurement nor the US anatomic landmark used during acquisition [31]. The authors think that this biased the results since the anatomy of the sacrum is complex and irregular [40,41].

For the shear wave velocity: within operator and between operator ICCs showed moderate to excellent reliability for the skin; low to good reliability for hypodermis and muscle for both within and between operator ICCs. Possible reasons include signal instability and inhomogeneity associated with tissue depth and operator's experience. Another reason might be tissue anisotropy, therefore tissue SWE signal depends on the orientation of the probe relative to the layer tested. Also, this affects much more muscular fibres since they're organised with a geometric alignment compared with the less structured adipose tissue or skin [42]. This explains the larger gap observed in the CI of between operator ICC for the mSWE (Table 2).

The agreement plots were drawn to assess clinical significance of difference between measurements even when a parameter showed good reliability [38]. In the absence of a gold standard imaging tool in our study the level of agreement necessary for confident usage remains uncertain. However, we hypothesized that the clinical difference between different groups is significantly higher than the uncertainty of the measurements. For the bone geometry parameters, previous studies focused on ischium morphology and its impact on internal soft tissue strain thus on the occurrence of PU using mainly FE models [23,43]. Our

**Table 3**
Mean of each parameter for the young adults group and healthy elderly, normality using Shapiro-wilk test and comparison using Student's t-test.

| Parameter | | Young adults | | Healthy elderly | | Student's t-test p-value |
|---|---|---|---|---|---|---|
| | | Mean ± SD | Shapiro Wilk test p-value | Mean ± SD | Shapiro Wilk test p-value | |
| Bone anatomy (MSC) | OA (°) | 80.32 ± 21.06 | 0.628 | 79.54 ± 19.19 | 0.509 | 0.920 |
| | HE (mm) | 10.39 ± 4.45 | 0.119 | 8.20 ± 2.94 | 0.293 | 0.159 |
| | ROC (mm) | 2.90 ± 1.21 | 0.191 | 2.19 ± 0.17 | 0.550 | 0.088 |
| Tissue morphology | ST (mm) | 3.61 ± 0.55 | 0.982 | 3.30 ± 0.53 | 0.215 | 0.147 |
| | HT (mm) | 8.67 ± 5.21 | 0.380 | 6.08 ± 3.56 | 0.457 | 0.156 |
| Tissue stiffness | sSWE (m/s) | 2.27 ± 0.28 | 0.087 | 2.22 ± 0.55 | 0.295 | 0.800 |
| | hSWE (m/s) | 2.06 ± 0.16 | 0.497 | 1.98 ± 0.33 | 0.437 | 0.465 |
| | mSWE (m/s) | 2.11 ± 0.27 | 0.128 | 1.70 ± 0.17 | 0.758 | 0.001 |

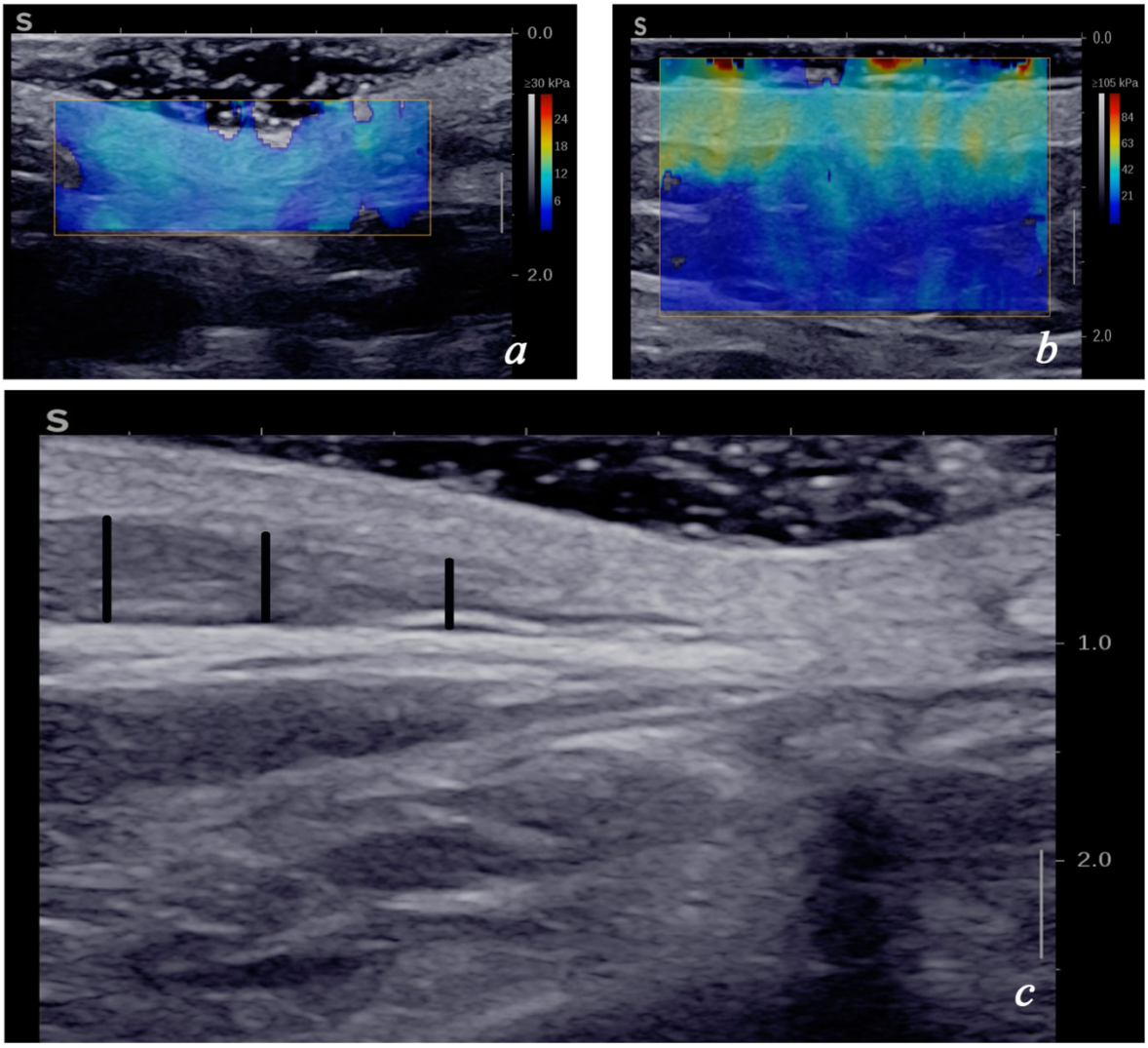


**Fig. 3.** Observations in the older group: lowest and highest skin/hypodermis SWE signal (a,b respectively), hypodermis heterogeneous thickness distribution over the MSC (double arrow) (c).

aim was to combine the three bone parameters: ROC, OA, and HE to differentiate a sharp tip from a flat tip [44]. For our knowledge, no research was conducted on the impact of the shape of the MSC on surrounding tissue deformation. In fact, reliability of bone morphology assessment using ultrasound is controversial: Akins et al. [19] found good between operator reliability for ischial tuberosity (IT) radius of curvature but they only reported the average ICC = 0.712, while Swaine et al. [20] found poor reliability for estimating inferior curvature of the IT in both its short and long axis. The methodology for our protocol combining an intra-image and-inter image analysis seemed promising but, with lack of reliability in the results and no clinical baseline for the MSC morphology, no interpretation could be given to the agreement plots reported in Fig. 2 for these parameters.

For tissue morphology parameters, skin thickness showed low reliability and a 95% CI of agreement with the mean of ±1.04 mm for the inter-image analysis. With a maximum skin thickness reported in the literature of 4 mm [39] this parameter needs further investigation before clinical use. A possible solution might be to tell operators to measure the ST directly over the MSC. In this perspective and since the linear probe is limited in depth and field of view, the first acquisition using the curvilinear probe is crucial for identifying and marking the level of the MSC, but also its exact position over the spine midline. In fact, previous studies investigating the inter-operator reliability of tissue thickness measurement over IT showed: excellent reliability for total thickness with an average ICC = 0.948, also without reporting the confidence interval [19]; moderate to excellent reliability (0.60–0.95) for skin and fat thickness [20]. To our knowledge, no study investigated the reliability of measuring tissue thickness using US over the sacrum. On the other hand, hypodermis thickness parameter showed excellent reliability and a 95% CI of agreement with the mean of ±1.4 mm for the inter-image analysis. Since hypodermis thickness is variable, and mainly related to body mass index [45] with a value exceeding sometimes 50 mm over lumbar spine [46], the clinical significance of this agreement seems plausible. However, the interpretation depends on another factor: the homogeneity of the distribution of the hypodermis over the sacrum. This is going to be discussed in the next section.

For tissue stiffness parameters, although reliability was not satisfactory for all three parameters: skin, hypodermis, and muscle; the 95% CI level of agreement with the mean of the inter-image analysis of ±0.33 m/s; ±0.29 m/s; ±0.25 m/s respectively, was minimal. In fact, previous studies investigating changes of shear wave velocity values in specific circumstances or disease showed: with prolonged loading in elderly, shear wave velocity of superficial region (mainly skin + hypodermis) over IT varied form 2.5 m/s to 3.3 m/s [31]; contracture strips of the gluteal muscle showed a shear wave velocity of 7.23 m/s vs 1.84 m/s for a healthy muscle at the same position [47]. Because the aim of

this evaluation is to point out subjects who significantly diverge from normal values, the SWE values for the three regions remain interesting to report. Nevertheless, interpretation should be taken with caution and further investigations are needed to increase reliability. Possible solutions might include operator's training, and taking SWE videos in the transverse and vertical directions, especially for muscle stiffness, since the properties parallel to the fibers are quite different from loading perpendicular to the fibers [48].

2. Young adults vs healthy elderly

The following discussion will highlight observations noted when comparing parameters of the young adults group and the healthy older people for the acquisitions conducted only by the physician. The interpretations cannot be generalized since reliability of measurements was not satisfactory.

For bone parameters, aging is associated with structural, geometric and bone volumetric density changes [49]. It is unclear how that might affect the external shape of the MSC; the similar median values in the boxplot, and the absence of statistical significance of differences between the means for the three parameters might suggest that there are no US changes observable. Therefore, the estimation of these parameters aims to evaluate the impact of bone geometry on tissue deformation independently from age difference.

For the tissue morphology parameters, the median values for both ST and HT were lower for the older group, but no statistical difference was noted between means. In fact, studies have shown that thinning of the skin, associated with age, is observed in subjects with more than 70 years [50] while our older age group had a mean age of 65 ± 2.4 yrs. Nevertheless, the mean ST of the young adults group 3.61 ± 0.55 mm was close to values previously reported for the skin over the sacrum like, for example, Yalcin et al. [51] found a mean of 3.2 ± 0.5 mm. Also studies comparing tissue thickness differences between SCI patients without *vs* with history of PU showed total thickness average of 15.3 mm *vs* 9.5 mm over the apex of IT [25]. Thus, the difference is quantifiable, but the challenge remains to determine a risk threshold value at high-risk patients. On the other hand, an observation, not reported in the literature to our knowledge, was noted for the hypodermis thickness distribution over the sacrum. One subject (Fig. 3c) clearly showed thinning of HT from the lateral to medial spine. Possible causes might be a spinal deformation causing a shift in the hypodermis layer while the skin, loosely bonded to subjacent organs, can slide over and maintain the same thickness [39]. This highlights the importance of measuring the HT directly over the tip of the MSC instead of the thickest region as mentioned in our protocol. In fact, HT is considered as an important parameter affecting internal soft tissue response to load [23] and thus, PU risk.

For the tissue stiffness parameters, median shear wave velocity for skin, hypodermis, and muscle was lower for the elderly group. Only for the muscle the difference showed statistical significance ($p = 0.001$). In fact, physiologic aging is associated with a loss of muscle mass starting at the age of 30 [10]. This might be caused by the infiltration of fat tissue and connective tissue into skeletal muscle [52]. Previous studies suggest that this is associated with an increase in muscle stiffness [53] and, with continuous compression, a further increase in muscle stiffness leading to injury [54]. While our results seem contradictory, since we noted a decrease in shear wave velocity between the young and the elderly group, the signal was collected closer to the proximal attachment of the gluteus maximus (lateral to the sacro-coccygeal region) rather than the muscle belly. Moreover, most studies, evaluating tissue stiffness and PU, focused on the variation of stiffness with loading [31,54,55]. The complexity and duration of the exam, especially for high-risk subjects, makes it impossible to evaluate a large number in a loading position. That is why we proposed in our study to evaluate tissue characteristics in an off-loading position and determine normal ranges within homogenous groups. While studies suggest that aging is associated with a decline in skin stiffness [9,56] making it more susceptible to PU, there is no specific threshold value proposed for increased risk. On the other hand, sustained pressure application was associated with an increase in tissue stiffness [31,57,58]. The two subjects presenting maximum and minimum skin/hypodermis baseline shear wave velocity in the elderly group (Fig. 3b; Fig. 3a) were overweight (BMI >25 kg/m$^2$). It is known that BMI values have an impact on the biomechanical behavior of tissues [59,60], further investigations are needed to evaluate changes in tissue elasticity associated with BMI changes. Also the mean values of sSWE and hSWE over the sacrum of the elderly group (2.22 ± 0.55 m/s and 1.98 ± 0.33 m/s respectively) are close to values reported in the literature (2.5 m/s and 1.8 m/s respectively) for a similar sample of nine healthy volunteers with a mean age of 70.1 ± 4.8 years [31].

3. Limits and perspectives

The lack of reliability of measures is the main limit of our study. This is mainly related to: difficulty in repeating acquisitions on the same anatomic level, definition of parameters, lack of signal stability, and ultrasound expertise. Also, the patient's prone position might be problematic for higher risk subjects. The sample size and the number of operators is also a limitation of this study. However, the protocol we developed is clinically feasible and can be easily proposed to evaluate patients at bedside. The relatively easy palpation of the anatomic landmark (PSIS) allows the exam to be conducted by any physician or nurse. The perspectives include a review of the protocol to increase reliability and an evaluation of higher risk elderly in nursing homes. Also, this protocol can quantify all layers' characteristics including bone, muscle, hypodermis, and skin using only US and SWE. This might serve in - patient specific - finite element modeling since quantifying tissue strain and stress distribution over a bony prominence is essential in determining an injury threshold [23,55,61].

## 6. Conclusion

In this study, we developed a protocol using US and SWE to assess bone and tissue characteristics over the sacrum in the context of PU prevention in elderly. It is the first protocol that combines assessment of all layers over bony prominences using only one imaging technique.

The protocol's reliability was evaluated on a sample of young adults and then tested on a group of healthy older subjects. We provided a thorough description of anatomic landmarks on palpation and US visualization to ensure reproducibility and real clinical application. However, reliability was not satisfactory and further improvements of the protocol are needed. The results comparing the young to healthy older age group suggested that changes related only to age might affect tissue thickness and elasticity more than bone morphology, but this cannot be generalized or quantified before increasing reliability and sample size. On the other hand, an observation in one of the subjects of the elderly group was not found in the literature: a heterogeneous distribution of the hypodermis thickness over the sacrum. In order to evaluate the use of this tool for PU risk assessment, it is essential to test it on a high-risk sample like elderly in nursing homes or long hospital stay.

Finally, our recommendations for the scientific community - when using US and SWE – are:

- anatomic palpation and US recognition using the curvilinear probe.
- report exact anatomic region and provide proof on the US image.
- when measuring thickness and SWE ensure that acquisition is taken pressure free directly over the bone prominence and not in the surrounding region.
- results cannot be generalized before testing for reliability.

## Declaration of competing interest

None.

## Acknowledgement

This project has received funding from the European Union's Horizon 2020 research and innovation program under the Marie Skłodowska-Curie grant agreement No. 811965.

## APPENDIX 1

### *Ultrasound and SWE protocol*

#### *Position and anatomic landmarks*

The volunteer is asked to lie down in the prone position with a cushion under the pubis to reduce lumbar lordosis. The examiner inspects the skin to identify any redness/swelling over the sacral region. Then, he palpates the posterior superior iliac spine (PSIS) and recognizes the continuation of intergluteal cleft representing the midline of the spine.

#### *Curvilinear probe*

The curvilinear probe allows a large field of view and better visualization of deep layers. After applying gel on the skin or the probe, the examiner scans the sacral region between the two PSIS in B-mode transverse view. The MSC appears as a reverse V-shaped hyperechoic contour (Fig. 1a). Sliding the probe lateral to the midline allows the recognition of the round shaped PSIS (Fig. 1a). An image is captured showing the MSC and PSIS. The region is marked over the skin with a marker or medical tape.

NB: if PSIS is not visible on US the use of sagittal view of the sacrum allows to recognize the anatomic site of the MSC. The examiner can align the site in the middle of the US image and then rotate the probe 90° to return to transverse view.

#### *Linear probe*

The linear probe is used to assess the superficial layers over the MSC. A thick layer of gel is applied directly on the midline of the marked level. The probe is then applied in the transverse B-mode view with minimum pressure. Artefacts from air bubbles appear as a linear hypoechoic signal perpendicular to skin layers. The examiner eliminates air bubbles using the probe or by adding and spreading the gel again. An image is captured showing the skin and adipose tissue, and the thick layer of gel over the skin (Fig. 1b).

The linear probe is also used in SWE mode at the same level with a thick gel layer and minimum pressure. The region of interest (ROI) covering the skin and adipose tissue is chosen, and the examiner waits for a homogeneous signal on the screen, increasing/decreasing elasticity range matching tissue stiffness. One measurement is three videos in SWE of 10 s each (or more if signal fluctuates). The last acquisition in SWE mode, for the gluteus maximus muscle, is taken lateral to the sacro-coccygeal region using the same procedure. The anatomic landmark is the sacral horns and sacro-coccygeal ligament described as the "frog sign". The muscle fibers are described as horizontal echoic lines under the skin and hypodermis (Fig. 1c).

## References

[1] NPIAP/EPUAP/PPPIA. Prevention and treatment of pressure ulcers/injuries: clinical practice guideline. The international guideline. Australia: Emily Haesler; 2019.
[2] Moore Z, Cowman S. Pressure ulcer prevalence and prevention practices in care of the older person in the Republic of Ireland. J Clin Nurs 2012;21(3–4):362–71. https://doi.org/10.1111/j.1365-2702.2011.03749.x.
[3] Børsting TE, Tvedt CR, Skogestad IJ, Granheim TI, Gay CL, Lerdal A. Prevalence of pressure ulcer and associated risk factors in middle- and older-aged medical inpatients in Norway. J Clin Nurs Feb. 2018;27(3–4):e535–43. https://doi.org/10.1111/jocn.14088.
[4] Agrawal K, Chauhan N. Pressure ulcers: back to the basics. Indian J Plast Surg 2012;45(2):244–54. https://doi.org/10.4103/0970-0358.101287.
[5] Allman RM, Goode PS, Burst N, Bartolucci AA, Thomas DR. Pressure ulcers, hospital complications, and disease severity: impact on hospital costs and length of stay. Adv Wound Care Feb. 1999;12(1):22–30.
[6] Situm M, Kolić M, Spoljar S. [QUALITY OF life and psychological aspects IN patients with chronic leg ulcer]. Acta Med Croat Mar. 2016;70(1):61–3.
[7] Moore ZE, Patton D. Risk assessment tools for the prevention of pressure ulcers. Cochrane Database Syst Rev Jan. 2019;2019(1). https://doi.org/10.1002/14651858.CD006471.pub4.
[8] Balzer K, Pohl C, Dassen T, Halfens R. The Norton, Waterlow, Braden, and Care Dependency Scales: comparing their validity when identifying patients' pressure sore risk. J Wound, Ostomy Cont Nurs Aug. 2007;34(4):389–98. https://doi.org/10.1097/01.WON.0000281655.78696.00.
[9] Boss GR, Seegmiller JE. Age-related physiological changes and their clinical significance. West J Med Dec. 1981;135(6):434–40.
[10] Harms CA, Cooper D, Tanaka H. Exercise physiology of normal development, sex differences, and aging. Compr Physiol Oct. 2011;1(4):1649–78. https://doi.org/10.1002/cphy.c100065.
[11] Oliveira AL, Moore Z, Connor TO, Patton D. Accuracy of ultrasound, thermography and subepidermal moisture in predicting pressure ulcers: a systematic review. J Wound Care May 2017;26(5):199–215. https://doi.org/10.12968/jowc.2017.26.5.199.
[12] Grubbs S, et al. The effect of high frequency ultrasound on the prevention of pressure ulcers in long-term care patients. Internet J Acad Physician Assistants Dec. 2008;7(1). Jul. 14, 2021. [Online]. Available: https://ispub.com/IJAPA/7/1/11804.
[13] Scafide KN, Narayan MC, Arundel L. Bedside technologies to enhance the early detection of pressure injuries: a systematic review. J Wound, Ostomy Cont Nurs Apr. 2020;47(2):128–36. https://doi.org/10.1097/WON.0000000000000626.
[14] Oomens Cw j, Broek M, Hemmes B, Bader Dl. How does lateral tilting affect the internal strains in the sacral region of bed ridden patients? — a contribution to pressure ulcer prevention. Clin BioMech Jun. 2016;35:7–13. https://doi.org/10.1016/j.clinbiomech.2016.03.009.
[15] Levy A, Kopplin K, Gefen A. An air-cell-based cushion for pressure ulcer protection remarkably reduces tissue stresses in the seated buttocks with respect to foams: finite element studies. J Tissue Viability Feb. 2014;23(1):13–23. https://doi.org/10.1016/j.jtv.2013.12.005.
[16] Al-Dirini RMA, Reed MP, Hu J, Thewlis D. Development and validation of a high anatomical fidelity FE model for the buttock and thigh of a seated individual. Ann Biomed Eng Sep. 2016;44(9):2805–16. https://doi.org/10.1007/s10439-016-1560-3.
[17] Luboz V, Petrizelli M, Bucki M, Diot B, Vuillerme N, Payan Y. Biomechanical modeling to prevent ischial pressure ulcers. J Biomech Jul. 2014;47(10):2231–6. https://doi.org/10.1016/j.jbiomech.2014.05.004.
[18] Linder-Ganz E, Shabshin N, Itzchak Y, Gefen A. Assessment of mechanical conditions in sub-dermal tissues during sitting: a combined experimental-MRI and finite element approach. J Biomech Jan. 2007;40(7):1443–54. https://doi.org/10.1016/j.jbiomech.2006.06.020.
[19] Akins JS, et al. Feasibility of freehand ultrasound to measure anatomical features associated with deep tissue injury risk. Med Eng Phys Sep. 2016;38(9):839–44. https://doi.org/10.1016/j.medengphy.2016.04.026.
[20] Swaine JM, et al. Adaptation of a MR imaging protocol into a real-time clinical biometric ultrasound protocol for persons with spinal cord injury at risk for deep tissue injury: a reliability study. J Tissue Viability Feb. 2018;27(1):32–41. https://doi.org/10.1016/j.jtv.2017.07.004.
[21] Macron A, Pillet H, Doridam J, Verney A, Rohan P-Y. Development and evaluation of a new methodology for the fast generation of patient-specific Finite Element models of the buttock for sitting-acquired deep tissue injury prevention. J Biomech Oct. 2018;79:173–80. https://doi.org/10.1016/j.jbiomech.2018.08.001.
[22] Doridam J, Macron A, Vergari C, Verney A, Rohan P-Y, Pillet H. Feasibility of sub-dermal soft tissue deformation assessment using B-mode ultrasound for pressure ulcer prevention. J Tissue Viability Nov. 2018;27(4):238–43. https://doi.org/10.1016/j.jtv.2018.08.002.
[23] Macron A, et al. Is a simplified Finite Element model of the gluteus region able to capture the mechanical response of the internal soft tissues under compression? Clin BioMech Jan. 2020;71:92–100. https://doi.org/10.1016/j.clinbiomech.2019.10.005.
[24] Gabison S, Hayes K, Campbell KE, Swaine JM, Craven BC. Ultrasound imaging of tissue overlying the ischial tuberosity: does patient position matter? J Tissue Viability Nov. 2019;28(4):179–85. https://doi.org/10.1016/j.jtv.2019.07.001.
[25] Sonenblum SE, Seol D, Sprigle SH, Cathcart JM. Seated buttocks anatomy and its impact on biomechanical risk. J Tissue Viability 2020. https://doi.org/10.1016/j.jtv.2020.01.004. Jan.
[26] Paluch Ł, Nawrocka-Laskus E, Wieczorek J, Mruk B, Frel M, Walecki J. Use of ultrasound elastography in the assessment of the musculoskeletal system. Pol J Radiol May 2016;81:240–6. https://doi.org/10.12659/PJR.896099.
[27] Bercoff J, Tanter M, Fink M. Supersonic shear imaging: a new technique for soft tissue elasticity mapping. IEEE Trans Ultrason Ferroelectrics Freq Control Apr. 2004;51(4):396–409. https://doi.org/10.1109/TUFFC.2004.1295425.
[28] Deprez J-F, Brusseau E, Fromageau J, Cloutier G, Basset O. On the potential of ultrasound elastography for pressure ulcer early detection. Med Phys 2011;38(4):1943–50. https://doi.org/10.1118/1.3560421.
[29] Dubois G, et al. Reliable protocol for shear wave elastography of lower limb muscles at rest and during passive stretching. Ultrasound Med Biol Sep. 2015;41(9):2284–91. https://doi.org/10.1016/j.ultrasmedbio.2015.04.020.

[30] Sigrist RMS, Liau J, Kaffas AE, Chammas MC, Willmann JK. Ultrasound elastography: review of techniques and clinical applications. Theranostics 2017;7(5):1303–29. https://doi.org/10.7150/thno.18650.
[31] Schäfer G, Dobos G, Lünnemann L, Blume-Peytavi U, Fischer T, Kottner J. Using ultrasound elastography to monitor human soft tissue behaviour during prolonged loading: a clinical explorative study. J Tissue Viability Nov. 2015;24(4):165–72. https://doi.org/10.1016/j.jtv.2015.06.001.
[32] Mansur R, Peko L, Shabshin N, Cherbinski L, Neeman Z, Gefen A. Ultrasound elastography reveals the relation between body posture and soft-tissue stiffness which is relevant to the etiology of sitting-acquired pressure ulcers. Physiol Meas Jan. 2021;41(12):124002. https://doi.org/10.1088/1361-6579/abc66d.
[33] Vergari C, et al. Intervertebral disc characterization by shear wave elastography: an in vitro preliminary study. Proc Inst Mech Eng H Jun. 2014;228(6):607–15. https://doi.org/10.1177/0954411914540279.
[34] Mcgraw K, Wong SP. Forming inferences about some intraclass correlation coefficients. Psychol Methods 1996;1:30–46. https://doi.org/10.1037/1082-989X.1.1.30. Mar.
[35] Bujang MA. A simplified guide to determination of sample size requirements for estimating the value of intraclass correlation coefficient: a review, vol. 12. Archives of Orofacial Sciences; Jun. 2017. p. 1–11.
[36] Hebert JJ, Koppenhaver SL, Parent EC, Fritz JM. A systematic review of the reliability of rehabilitative ultrasound imaging for the quantitative assessment of the abdominal and lumbar trunk muscles. Spine Nov. 2009;34(23):E848–56. https://doi.org/10.1097/BRS.0b013e3181ae625c.
[37] Koo TK, Li MY. A guideline of selecting and reporting intraclass correlation coefficients for reliability research. J Chiropr Med Jun. 2016;15(2):155–63. https://doi.org/10.1016/j.jcm.2016.02.012.
[38] Jones M, Dobson A, O'Brian S. A graphical method for assessing agreement with the mean between multiple observers using continuous measures. Int J Epidemiol Oct. 2011;40(5):1308–13. https://doi.org/10.1093/ije/dyr109.
[39] Skin, Mescher AL, editors. Junqueira's Basic Histology Text and Atlas, 16e, Book, Section vols. New York, NY: McGraw Hill; 2021 [Online]. Available:, accessmedicine.mhmedical.com/content.aspx?aid=1180414032, . [Accessed 17 May 2021].
[40] Cheng JS, Song JK. Anatomy of the sacrum. Neurosurg Focus Aug. 2003;15(2):1–4. https://doi.org/10.3171/foc.2003.15.2.3.
[41] Baron-Sarrabère M-P, Micheau A, Cyteval C. Sacrum, coccyx, articulations sacro-iliaques : technique radiologique et aspects normaux. Sep. 2016. https://doi.org/10.1016/S1879-8551(16)60680-2. https://www.em-premium.com/data/traites/rx/30-60680/.
[42] Serafin-Król M, Maliborski A. Diagnostic errors in musculoskeletal ultrasound imaging and how to avoid them. J Ultrason Sep. 2017;17(70):188–96. https://doi.org/10.15557/JoU.2017.0028.
[43] Gefen A. Risk factors for a pressure-related deep tissue injury: a theoretical model. Med Biol Eng Comput Jun. 2007;45(6):563–73. https://doi.org/10.1007/s11517-007-0187-9.
[44] Candadai RS, Reddy NP. Stress distribution in a physical buttock model: effect of simulated bone geometry. J Biomech Dec. 1992;25(12):1403–11. https://doi.org/10.1016/0021-9290(92)90054-5.
[45] Gibney MA, Arce CH, Byron KJ, Hirsch LJ. Skin and subcutaneous adipose layer thickness in adults with diabetes at sites used for insulin injections: implications for needle length recommendations. Curr Med Res Opin Jun. 2010;26(6):1519–30. https://doi.org/10.1185/03007995.2010.481203.
[46] Lee JJ, et al. Fat thickness as a risk factor for infection in lumbar spine surgery. Orthopedics Nov. 2016;39(6):e1124–8. https://doi.org/10.3928/01477447-20160819-05.
[47] Guo R, Xiang X, Qiu L. Shear-wave elastography assessment of gluteal muscle contracture. Medicine (Baltim) Nov. 2018;97:44. https://doi.org/10.1097/MD.0000000000013071.
[48] P. Escobar, S. Wittles, S. Asfour, and L. Latta, "Mechanical characteristics of muscle, skin and fat - elastic moduli for finite element modeling of limbs," p. 4.
[49] Riggs BL, et al. Population-based study of age and sex differences in bone volumetric density, size, geometry, and structure at different skeletal sites. J Bone Miner Res Dec. 2004;19(12):1945–54. https://doi.org/10.1359/jbmr.040916.
[50] Lasagni C, Seidenari S. Echographic assessment of age-dependent variations of skin thickness. Skin Res Technol 1995;1(2):81–5. https://doi.org/10.1111/j.1600-0846.1995.tb00022.x.
[51] Yalcin E, Akyuz M, Onder B, Unalan H, Degirmenci I. Skin thickness on bony prominences measured by ultrasonography in patients with spinal cord injury. J Spinal Cord Med May 2013;36(3):225–30. https://doi.org/10.1179/2045772312Y.0000000088.
[52] McCormick R, Vasilaki A. Age-related changes in skeletal muscle: changes to life-style as a therapy. Biogerontology 2018;19(6):519–36. https://doi.org/10.1007/s10522-018-9775-3.
[53] Rahemi H, Nigam N, Wakeling JM. The effect of intramuscular fat on skeletal muscle mechanics: implications for the elderly and obese. J R Soc Interface Aug. 2015;12(109):20150365. https://doi.org/10.1098/rsif.2015.0365.
[54] Gefen A, Gefen N, Linder-Ganz E, Margulies SS. In vivo muscle stiffening under bone compression promotes deep pressure sores. J Biomech Eng Jan. 2005;127(3):512–24. https://doi.org/10.1115/1.1894386.
[55] Linder-Ganz E, Shabshin N, Itzchak Y, Yizhar Z, Siev-Ner I, Gefen A. Strains and stresses in sub-dermal tissues of the buttocks are greater in paraplegics than in healthy during sitting. J Biomech 2008;41(3):567–80. https://doi.org/10.1016/j.jbiomech.2007.10.011.
[56] Luebberding S, Krueger N, Kerscher M. Mechanical properties of human skin in vivo: a comparative evaluation in 300 men and women. Skin Res Technol May 2014;20(2):127–35. https://doi.org/10.1111/srt.12094.
[57] Gefen A. The biomechanics of sitting-acquired pressure ulcers in patients with spinal cord injury or lesions. Int Wound J 2007;4(3):222–31. https://doi.org/10.1111/j.1742-481X.2007.00330.x.
[58] Shoham N, Gefen A. Deformations, mechanical strains and stresses across the different hierarchical scales in weight-bearing soft tissues. J Tissue Viability May 2012;21(2):39–46. https://doi.org/10.1016/j.jtv.2012.03.001.
[59] Sopher R, Nixon J, Gorecki C, Gefen A. Exposure to internal muscle tissue loads under the ischial tuberosities during sitting is elevated at abnormally high or low body mass indices. J Biomech Jan. 2010;43(2):280–6. https://doi.org/10.1016/j.jbiomech.2009.08.021.
[60] Elsner JJ, Gefen A. Is obesity a risk factor for deep tissue injury in patients with spinal cord injury? J Biomech Dec. 2008;41(16):3322–31. https://doi.org/10.1016/j.jbiomech.2008.09.036.
[61] Loerakker S, et al. The effects of deformation, ischemia, and reperfusion on the development of muscle damage during prolonged loading. J Appl Physiol Jul. 2011;111(4):1168–77. https://doi.org/10.1152/japplphysiol.00389.2011.

# APPENDIX 4

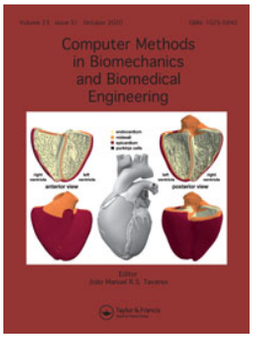

Taylor & Francis
Taylor & Francis Group

Computer Methods in Biomechanics and Biomedical Engineering

ISSN: 1025-5842 (Print) 1476-8259 (Online) Journal homepage: https://www.tandfonline.com/loi/gcmb20

# Calibration of the fat and muscle hyperelastic material parameters for the assessment of the internal tissue deformation in relation to pressure ulcer prevention

E. Mukhina, P.-Y. Rohan, N. Connesson & Y. Payan

**To cite this article:** E. Mukhina, P.-Y. Rohan, N. Connesson & Y. Payan (2020) Calibration of the fat and muscle hyperelastic material parameters for the assessment of the internal tissue deformation in relation to pressure ulcer prevention, Computer Methods in Biomechanics and Biomedical Engineering, 23:sup1, S197-S199, DOI: 10.1080/10255842.2020.1813426

**To link to this article:** https://doi.org/10.1080/10255842.2020.1813426

© 2020 The Author(s). Published by Informa UK Limited, trading as Taylor & Francis Group

Published online: 02 Nov 2020.

Submit your article to this journal

View related articles

View Crossmark data

Full Terms & Conditions of access and use can be found at
https://www.tandfonline.com/action/journalInformation?journalCode=gcmb20

COMPUTER METHODS IN BIOMECHANICS AND BIOMEDICAL ENGINEERING
2020, VOL. 23, NO. S1, S197–S199
https://doi.org/10.1080/10255842.2020.1813426

Taylor & Francis
Taylor & Francis Group

OPEN ACCESS Check for updates

# Calibration of the fat and muscle hyperelastic material parameters for the assessment of the internal tissue deformation in relation to pressure ulcer prevention

E. Mukhina[a,b], P.-Y. Rohan[b], N. Connesson[a] and Y. Payan[a]

[a]Univ. Grenoble Alpes, CNRS, Grenoble INP, TIMC-IMAG, Grenoble, France; [b]Institut de Biomécanique Humaine Georges Charpak, Paris, France

## 1. Introduction

Our group aims at proposing a protocol for evaluating the subject-specific risk for sacral pressure ulcer (PU). The idea is to model the way soft tissue will be deformed under the external pressure and to compute internal strains. It has been indeed showed that high strains can create deep tissue injuries (Ceelen et al. 2008). Because of the clinical constraints, we propose to use Ultrasound (US) to build the subject-specific biomechanical model of the sacral soft tissue as an alternative to 3D MR imaging (because of cost, time and accessibility). This paper focuses on the way such a subject-specific model will be designed and more specifically on the methodology we propose for estimating the constitutive parameters of the internal sacral soft tissue, namely the adipose tissue and the muscle. The values of these parameters have indeed a strong influence on the computed internal strains.

## 2. Methods

### 2.1. Experimental set up and the numerical model

One subject participated in the experiment (male, 33 y.o., BMI = 26.1 kg/m$^2$). Data for the subdermal tissue were acquired for the participant laying in the prone position. An ultrasound acquisition of the subdermal tissue in the region above the superior process of median sacral crest was performed using a commercial device (Aixplorer, SuperSonic Imagine, France) with a linear ultrasound (US) probe of 8 MHz central frequency (SuperLinear SL 15-4). Custom made load sensor was attached to the ultrasound probe (Fougeron et al. 2020). Several cycles of the indentation with the probe were performed and the one with the clearest video frames in the beginning and the end of the indentation cycle was chosen as a basis to build a 2D finite element (FE) model in Ansys 19.2 software. The model geometry was obtained by extracting the coordinates of the splines delimiting the skin, fat, muscle and bone via Matlab R2019a and by converting the units from pixels to millimeters. For this purpose, the first frame of the indentation cycle was used (Figure 1).

Several assumptions were made: since the model was built in 2D, the plane strain formulation was used; and the US probe was assumed to be in contact with the skin throughout 2 cm in width (relevant for the recalculation of the force applied by the probe from 3D to 2D). The load cycle was divided into 4 load steps for the consecutive comparison between the frames of the US data with the results of the numerical model.

All displacements were constrained on the lower wall of the 2D model, below the bone, and the bonded contact was used for the nodes of the different tissue types. The load was applied to the top of the US probe, with only Y direction displacement of the probe being allowed. The no-separation contact was used between the probe and the skin. And plane183 element type was used for the mesh.

### 2.2. Constitutive model

For the bone, the linear elastic material model was used with Young's modulus of 13.4 GPa, Poisson's ratio ($\nu$) of 0.3 based on the values reported in the literature (Rho et al. 1997). First-order Ogden hyperelastic material model was chosen to represent the soft tissues behavior. The values for the skin were fixed to 20 kPa for the shear modulus ($\mu 1$) and 5 for the exponent ($\alpha$) based on the values reported in the literature (Luboz et al. 2014). The same value of $\alpha = 5$ was set up for both muscle and adipose tissues. The calculation of d (incompressibility parameter) was based on the literature (Macron et al. 2018).

© 2020 The Author(s). Published by Informa UK Limited, trading as Taylor & Francis Group
This is an Open Access article distributed under the terms of the Creative Commons Attribution License (http://creativecommons.org/licenses/by/4.0/), which permits unrestricted use, distribution, and reproduction in any medium, provided the original work is properly cited.

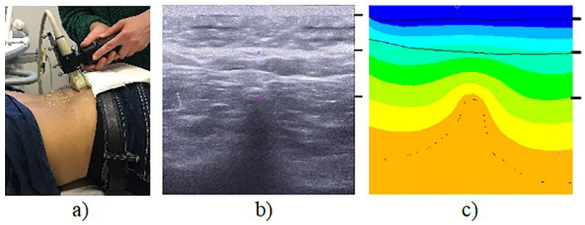


**Figure 1.** (a) Experimental set up. (b) Ultrasound data. (c) Example of simulation result. For (b) and (c): above 1st black right-side dash – skin; above 2nd – fat; below 2nd – muscle and bone; 3rd dash – top apex of the bone.

**Table 1.** Resultant shear modulus and Poisson's ratio parameters of the two cases of optimization for muscle (_m) and fat (_f) tissues.

| | μ1_m, kPa | μ1_f, kPa | $\nu$_m | $\nu$_f |
|---|---|---|---|---|
| Case1 | 4.52 | 9.64 | 0.499 | 0.499 |
| Case2 | 6.49 | 6.55 | 0.499 | 0.474 |

### 2.3. Calibration of the material properties

The Matlab algorithm using the least square method was utilized for the inverse evaluation of the soft tissues' (adipose tissue and muscle) material parameters. Two cases were compared: (1) optimization based on the variation in only the total thickness of soft tissues above the sacrum (2) optimization based on a combination of the two error vectors (for the variation in the total thickness and separately for the variation in muscle thickness). A sensitivity analysis of the shear moduli values to the change in values of exponents ($\alpha$) and Poisson's ratios ($\nu$) was performed: first, only the shear moduli values for both analyzed tissues were optimized, while $\alpha$ and $\nu$ were fixed. And after, this optimization was recalculated changing the fixed values of $\alpha$ and $\nu$ by 1%. Change in Poisson's ratios showed to have a noticeable effect (up to 30%) on the values of the μ1.

Therefore, four parameters were calculated in the end of optimization process: Poisson's ratios and shear moduli for adipose and muscle tissues.

## 3. Results and discussion

The values of the material properties of the analyzed soft tissues obtained after the optimization process are provided in Table 1.

Figure 2 shows the comparison between the change in the total and muscle thicknesses in the numerical model using the optimal μ1 and $\nu$ parameters from two optimizations and the values from the US images.

While the results of two optimizations were close for the total thickness of the soft tissues, they vary for the evaluation of the muscle thickness. This suggests

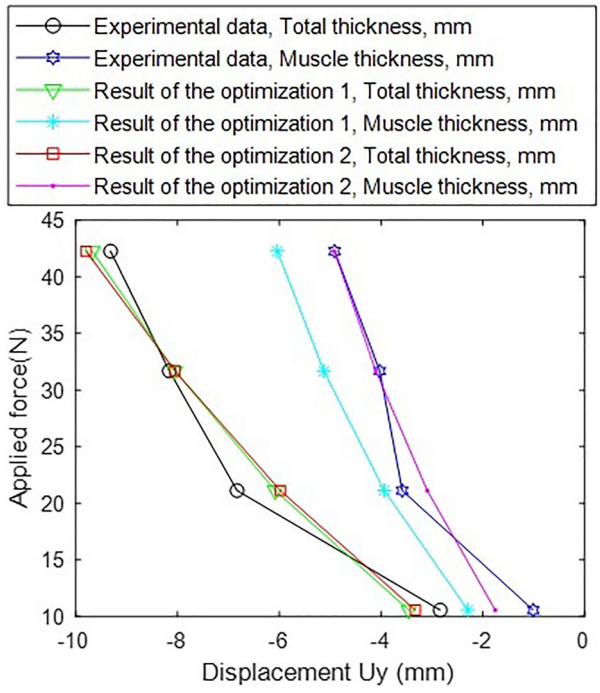


**Figure 2.** Comparison between the results of the optimizations and the experimental data.

that the minor improvement in one parameter (total thickness) could have a major effect on the separate tissue types if they are not considered during the optimization.

The proposed FE model also has some limitations: due to acquisitions being performed manually, slight change of the probe angle is allowed, which could have an effect on the tissue's geometry during the indentation cycle. Future work will include the development of the protocol to reduce this bias. Another limitation is the 2D modality of US, effects of that will be assessed in the following work.

## 4. Conclusions

Presented work shows the possibility of using the US data for the assessment of the soft tissues' material properties. This is clinically relevant, since US allows to obtain a subject-specific anatomical data, while being much more accessible and less costly than MRI. Results also imply the importance of using several parameters representing different types of soft tissues for the inverse optimization of the material properties.

## Acknowledgements

This project has received funding from the European Union's Horizon 2020 research and innovation programme

under the Marie Skłodowska-Curie grant agreement No. 811965.

## References

Ceelen KK, Stekelenburg A, Loerakker S, Strijkers GJ, Bader DL, Nicolay K, Baaijens FPT, Oomens CWJ. 2008. Compression-induced damage and internal tissue strains are related. J Biomech. 41(16):3399–3404.

Luboz V, Petrizelli M, Bucki M, Diot B, Vuillerme N, Payan Y. 2014. Biomechanical modeling to prevent ischial pressure ulcers. J Biomech. 47(10):2231–2236.

Rho JY, Tsui TY, Pharr GM. 1997. Elastic properties of human cortical and trabecular lamellar bone measured by nanoindentation. Biomaterials. 18(20):1325–1330.

Macron A, Pillet H, Doridam J, Verney A, Rohan PY. 2018. Development and evaluation of a new methodology for the fast generation of patient-specific finite element models of the buttock for sitting-acquired deep tissue injury prevention. J Biomech. 79:173–180.

Fougeron N, Rohan P-Y, Haering D, Rose J-L, Bonnet X, Pillet H. 2020. Combining freehand ultrasound-based indentation and inverse finite element modelling for the identification of hyperelastic material properties of thigh soft tissues. J Biomech Eng c. 142(9):22.

**KEYWORDS** Pressure ulcers; finite element; inverse method

ekaterina.mukhina@univ-grenoble-alpes.fr

# APPENDIX 5

Ref. Ares(2021)3116345 - 10/05/2021

# H2020-MSCA-ITN-2018

# STINTS ETN
# Skin Tissue Integrity under Shear

# Project ID: 811965

**Starting date:** 1st January 2019 **Duration:** 4 years

| | |
|---|---|
| **Deliverable Number** | D1.4 |
| **Deliverable Title** | Pressure Maps Collected on Supporting Surface such as a Cushion or a Shoe |
| **Work Package Number** | WP1 |
| **Due Date (Annex 1)** | 30th June 2020 |
| **Submission Date** | 10th May 2021 |
| **Deliverable Lead Beneficiary** | Université Grenoble Alpes (UGA) |
| **Authors** | Ekaterina Mukhina (UGA), Yohan Payan (UGA), Nathanaël Connesson (UGA) and Pierre-Yves Rohan (Arts et Métiers ParisTech) |
| **Nature** | Report |

**Project funded by the European Union within the Horizon 2020 programme (2014-2020)**

| **Dissemination Level** | | |
|---|---|---|
| PU | Public | |
| CO | Confidential, only for members of the consortium (including the Commission Services) | X |

| | |
|---|---|
| **Executive Summary** | Some of the most common body sites for Pressure Ulcer (PU) development are the sacrum, buttock and heel. The focus of ESR9's (EM) individual project is the PU risk for the sacrum/buttock region. Hence, this report describes studies in which pressure distribution maps were obtained for these sites. Maps were acquired in both recumbent and sitting postures. These studies are therefore relevant to both mattresses and seat cushions as supporting surfaces. |

# Pressure Maps Collected on Supporting Surface such as a Cushion or a Shoe

The overall aim of ESR9's (EM) individual research project is to examine the possibility of using ultrasound-based Finite Element models for the evaluation of the mechanical response of soft tissues in clinically relevant situations, as a representative of the subject-specific risk of PU development in the pelvic region. A literature review on the aetiology of Pressure Ulcers (PUs), the mechanical and biological responses to the loading, and the methods used for the evaluation of the mechanical state of the sub-dermal tissues has proved insightful. In particular, a series of animal experiments involving the indentation of the tibialis anterior muscle of Brown-Norway rats established that deformation-induced damage was apparent only when a given mechanical shear strain threshold was exceeded (1–3) and could be used to assess soft tissue injury risk.

## 1. Introduction

*Clinical motivation*

PU is a medical condition mainly affecting people with the reduced mobility and/or sensitivity. In the study performed by Garber et al., 31% of the participants with spinal cord injury reported the occurrence of the PU over one-year period (4). Over the lifetime, this number increases to 9 out of 10 patients (4–6). If not recognized and treated fast enough, PUs can have a high cost for society and for the overall well-being of the person affected (7). The cost of the PU prevention has been reported to be in the range of 3–88€ per day (depending on the different studies), while cost of treatment could reach 470€ per day in the most extreme cases (8).

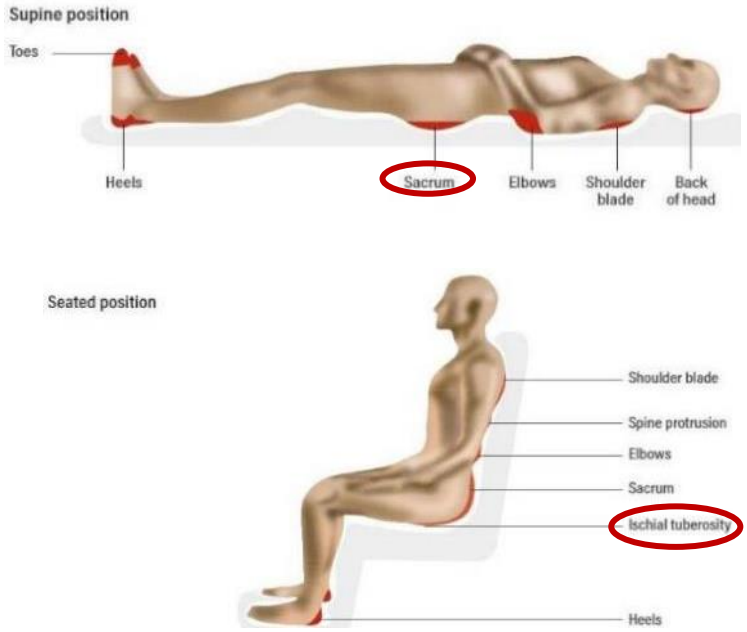


Figure 1 Common sites for PUs [adapted from (9)]

Common sites of the PU localization are the load bearing areas of the body (see Figure 1). Analysis of the PUs occurring in the inpatient population in USA showed that 47% of all observed PU were located on the lower back (combining lower back and sacral regions), 17% on the buttock and 14% on the heel. In this study we focused on the region of the pelvis, specifically, areas over the sacrum and ischial tuberosities. The sacral region is subjected to the higher loads in the recumbent position, while the ischial tuberosities are more exposed in the seated posture (10,11).

*Aetiology*

Several studies in the literature have consistently demonstrated that at least two mechanisms are involved in PU onset (1) mechanically induced capillary occlusion resulting in tissue ischemia (12,13) along with reperfusion injury (14,15) and (2) cell deformation which can lead to a loss of membrane integrity and ultimately affecting viability and remodelling capacity (5,12,16–18). Occlusion of circulation and lymphatic vessels leads to the change in metabolism, which can result in cell death over long period of time (hours). Direct cell deformation under high strains could lead to a damage after even 10 minutes (1,19). At the tissue level, a series of animal experiments involving indentation of the tibialis anterior muscle of Brown-Norway rats (2,3,12,17,20–23) established that deformation-induced damage was apparent only when a maximum Green-Lagrange shear strain threshold of 0.75 was exceeded (1–3), and that the damage area was correlated to the magnitude of the elastic strain energy applied (20). The ESR9 PhD project focuses on the evaluation of the **mechanical response of soft tissues as a representative of the subject-specific risk** of PU.

*Experimental assessment of interface pressure*

**One key challenge for closing the experiment-model feedback loop (model validation) is the development of appropriate experimental measurement methods to obtain reliable model input and validation data including accurate description of the interface interactions**. Sensors have been developed to estimate the distribution of pressures for use in both research and clinical settings. Commercially-available pressure mapping systems that are routinely used in clinical routines provide real-time visual feedback of peak pressure values and position asymmetries, and are used to aid the decision making when considering PU prevention in the clinical setting. The results from pressure mapping studies have shown that the recorded values depend on the individual, their posture and the type of support surface (24–26). In contrast to pressure mapping, very few studies focus on monitoring shear forces at the individual-support surface interface. This is mainly due to the technical challenges inherent in developing compliant, thin and flexible sensors that can distinguish between signals associated with normal forces with forces acting parallel to the skin surface. Laszczak et al. (27) have described this type of sensor system for the measurement of the interface pressure and shear between the limb residual and the socket for the lower limb amputee. A pilot test for one subject showed very promising results, being the first sensor system of its kind allowing positioning directly inside the socket without any alterations.

*Objective*

Sacral and buttock regions, accounting for the large part of the developing PUs, are subjected to the highest loads in the recumbent and sitting postures (values of 5–15 kPa were reported for mattresses and 8–22 kPa for seat cushions (28–30)). The objective of this work was to collect experimental interface pressure measurements in these postures for further use during Finite Element modelling to perform an **experiment-model feedback loop; vital for model refinement and adjustment.**

## 2. Materials and Methods

Two different systems measuring the pressure distribution were used in the study. Each of them was used to collect the pressure distribution data in one of the postures: sitting (Texisense pressure mapping system) or recumbent (Zebris pressure mapping system).

### 2.1. Participants

Two healthy male volunteers (Table 1) participated in the first part of the study for the acquisitions in the recumbent position.

Table 1 Morphological information for subjects participated in the first part of the study

| Subject | Sex | Age [y.o.] | Weight [kgf] | Height [m] | BMI [kg/m²] |
|---|---|---|---|---|---|
| 1 | male | 34 | 85 | 1.75 | 27.8 |
| 2 | male | 40 | 80 | 1.73 | 26.7 |

Four healthy volunteers (Table 2) participated in the second part of the study for the acquisitions in the sitting posture.

Table 2 Morphological information for subjects participated in the second part of the study

| Subject | Sex | Age [y.o.] | Weight [kgf] | Height [m] | BMI [kg/m²] |
|---|---|---|---|---|---|
| 1 | male | 24 | 65 | 1.8 | 20.5 |
| 2 | female | 34 | 65 | 1.7 | 23 |
| 3 | male | 26 | 75 | 1.8 | 24.5 |
| 4 | male | 22 | 66 | 1.8 | 20.9 |

### 2.2. Measurement in the recumbent position using the Zebris pressure platform

To focus on the pressure distribution in the sacral region, the first set of acquisitions was performed for the participants in the recumbent position. The Zebris FDM pressure platform, manufactured by Zebris Medical GmbH (www.zebris.de), was used for this purpose. This platform has a hard surface with 1920 pressure sensors (40 x 48), each of the 8.475 x 8.475 mm size, distributed over the active surface of 400 x 330 mm. According to the technical specifications, the measuring range is 1–120 N/cm$^2$ with the ± 5% accuracy. Acquisition frequency is 60 Hz.

The two participants lay on their backs with the buttock region being positioned on the platform. The zone of interest was limited to the top region of the sacrum, which is usually loaded in the recumbent position. However, depending on the subject specific anatomical features, the highest local load could occur in slightly different positions. In order to capture the worst-case scenario for each subject, a slow dynamic acquisition was performed with the legs of the subjects moved from supine to lithotomy position.

Three acquisitions were performed, each consisting of 3–4 repetitive cycles of changing legs position. Interface pressure parameters were compared for five leg positions (Table 3).

Table 3 Description of the leg positions for the acquisition in the recumbent posture

| Leg position 1 | Leg position 2 | Leg position 3 | Leg position 4 | Leg position 5 |
|---|---|---|---|---|
| Thighs are lying on the bed. Upper body is partially lifted. | Thighs lifted to ~30° to the bed, lower leg is bent. Upper body is partially lifted. | Thighs lifted to ~60° to the bed, lower leg is bent. Upper body is partially lifted. | Thighs lifted to ~90° to the bed, lower leg is bent. Upper body is partially lifted. | Thighs lifted to ~120° to the bed, lower leg is bent. Upper body is partially lifted. |
|  |  |  |  |  |

## 2.3. Measurement in the sitting position using the Texisense pressure pad

To focus on the pressure distribution in the region of ischial tuberosities, a second set of acquisitions was performed for the participants in the sitting position. The TexiMat pressure pad manufactured by Texisense (www.texisense.com) was used for this purpose. This flexible mat is soft and 100% textile with 1024 pressure sensors (32 x 32) distributed over the active surface of 460 x 460 mm. Each sensor has a size of 5 x 5 mm with a distance of 14.7 mm between two sensors. According to the manufacturer, the measurement range is 0.3–45 kPa with a ± 10% accuracy. The acquisition frequency is 10 Hz.

Participants were asked to statically sit on the stool (without backrest but with armrests) covered with the TexiMat (Figure 2) in order to collect the data on the pressure distribution under the region of ischial tuberosities. At the same time, the force data was collected by the AMTI force sensor attached to the seat.

Figure 2 Subject's position for the acquisitions in sitting posture

### 2.4. Post-processing

For the data acquired with both the FDM and TexiMat the pressure distribution was plotted and the peak pressure, contact area and applied force calculated. Pressure distribution maps were plotted in the MATLAB software after applying the 2D convolution to the data matrix (pressure values for each sensor) with a kernel F:

$$F = \begin{bmatrix} 1 & 1 & 1 \\ 1 & 3 & 1 \\ 1 & 1 & 1 \end{bmatrix}$$

This convolution was applied to smooth the raw data reported by the TexiMat. Figure 3 presents the pressure distribution map before (on the left side) and after (on the right side) the smoothing operation was applied. The same smoothing is done by TexiMat software when the data is presented in the real-time mode. To observe the realistic colour distribution, the colormap is scaled (colours are normalized) for each case.

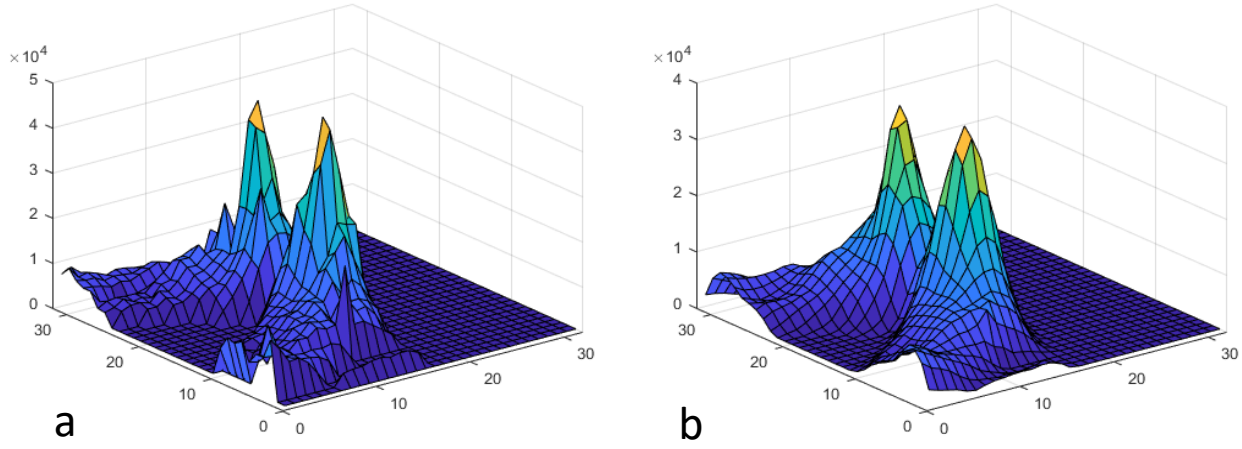


Figure 3 Pressure distribution maps a) raw data without 2D convolution b) data after 2D convolution

The highest value from all sensors for the selected time frame was selected as peak pressure. While the mean pressure per sensor was calculated as the sum of pressures for all sensors divided by the number of sensors with non-zero values.

In addition, the total force at the selected time step was calculated as a sum of pressures for all sensors multiplied by the active area of one sensor (squared distance between sensor's centres). In case of the Zebris this distance is 8.475 mm, while in case of TexiMat this is 14.7 mm.

## 3. Results

### 3.1. Sacral pressures measured in the recumbent position with the Zebris platform

Interface pressure parameters from the Zebris FDM platform (total load applied, peak pressure, mean pressure per sensor and contact area) are provided at five different leg positions for one of the two subjects; namely Subject 1 (Table 4).

Table 4 Total load, peak pressure, mean pressure and contact area at five different legs positions

| Position of the legs | | Pressure distribution map | Total load [N] | Peak pressure [N/cm$^2$] | Mean pressure [N/cm$^2$] | Contact area [cm$^2$] |
|---|---|---|---|---|---|---|
| 1 |  | 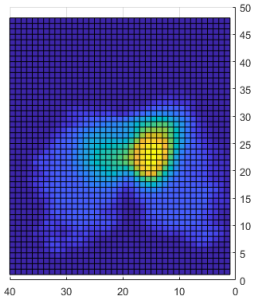 | 739.1 | 5.5 | 1.50 | 476.9 |
| 2 |  | 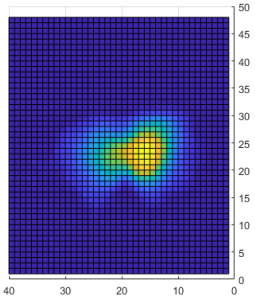 | 763.5 | 9.5 | 3.05 | 250.7 |
| 3 |  | 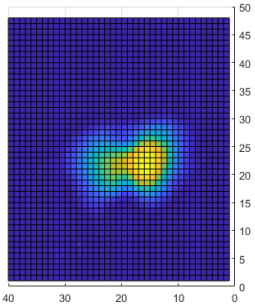 | 708.2 | 9 | 3.35 | 211.2 |
| 4 |  | 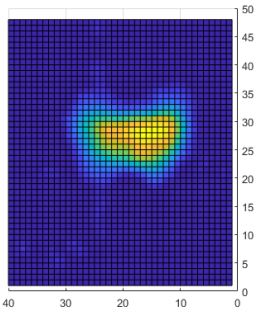 | 665.8 | 7.5 | 2.97 | 224.1 |
| 5 |  | 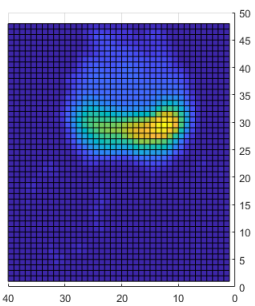 | 743.4 | 7.5 | 2.16 | 343.3 |

The following figures (Figure 4–Figure 6) show the evolution of total force, contact area and peak pressure over time for each of the three acquisitions (3–4 repetitive cycles per acquisition) for both subjects.

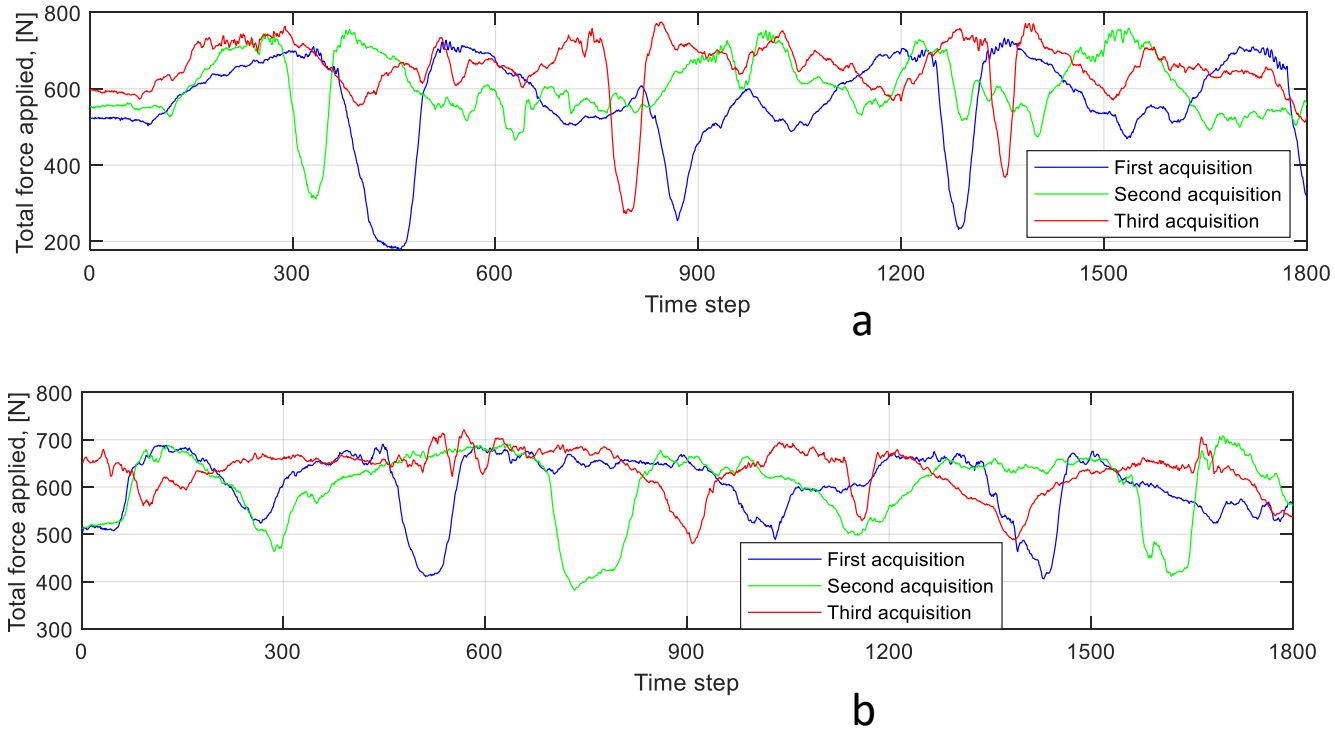


Figure 4 Evolution of the total force for each of 3 acquisitions. a) Subject 1 b) Subject 2

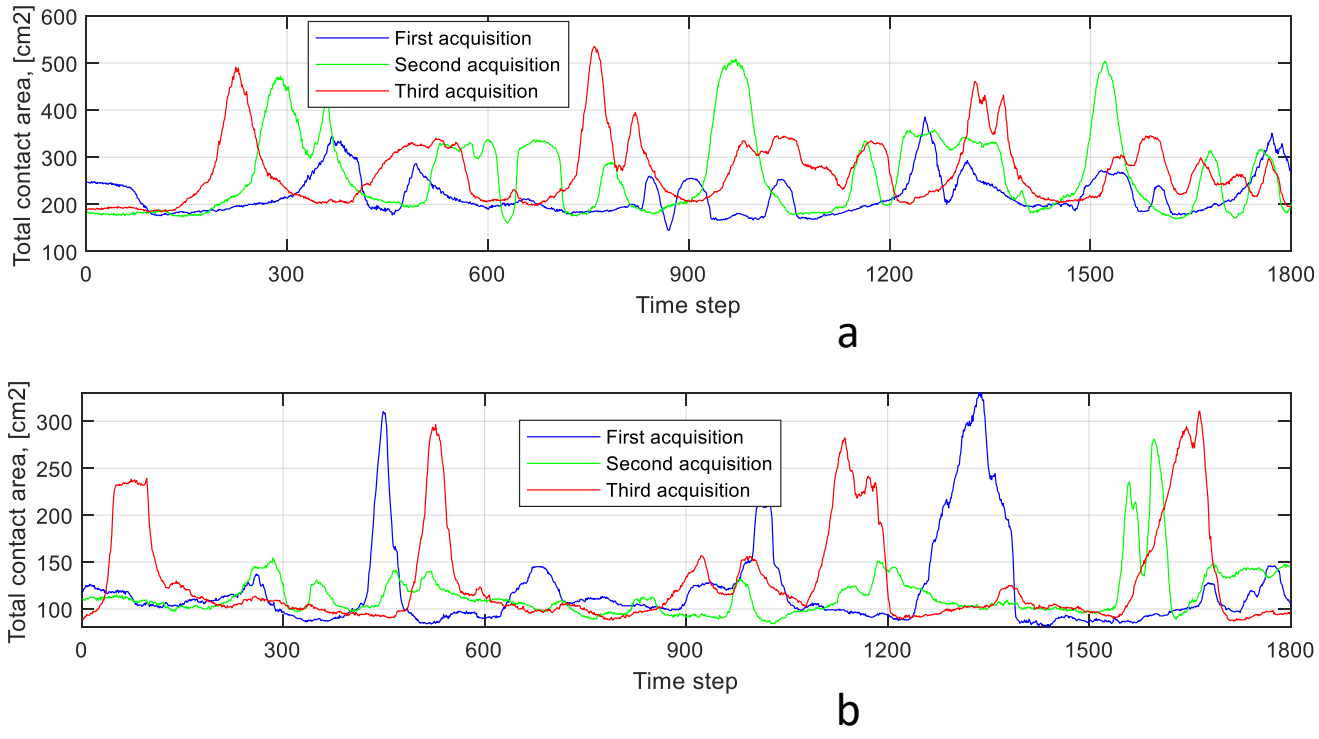


Figure 5 Evolution of total contact area for each of 3 acquisitions. a) Subject 1 b) Subject 2

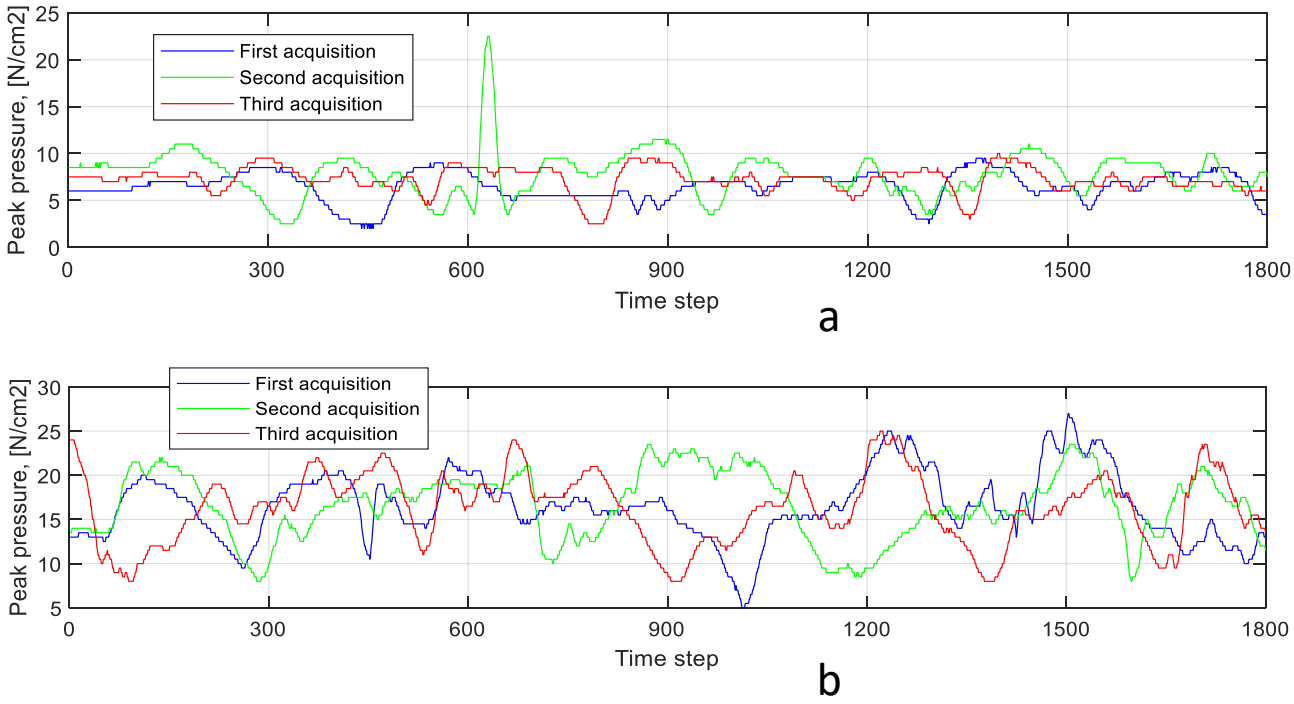


Figure 6 Evolution of the peak pressure for each of 3 acquisitions. a) Subject 1 b) Subject 2

## 3.2. Ischial pressures measured in the sitting position with the Texisense pad

Acquisitions on TexiMat were performed for four subjects in the static sitting position (Figure 7), with the resulting pressure distributions shown in Figure 8. Values of total load, peak pressure, mean pressure and total contact area for each subject are compiled in the Table 5.

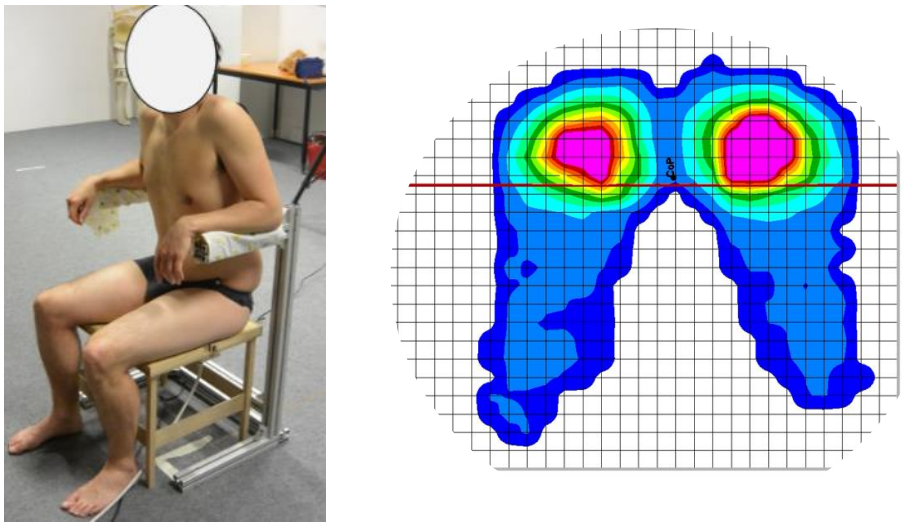

Figure 7 Subject's position in sitting posture and an example of the pressure distribution map

Table 5 Total load, peak pressure and contact area measured by the TexiMat

| Subject # | Total load [N] | Peak pressure [N/cm$^2$] | Mean pressure per sensor [N/cm$^2$] | Contact Area [cm$^2$] |
|---|---|---|---|---|
| 1 | 591.4 | 4.96 | 1.16 | 510.1 |
| 2 | 785.8 | 4.71 | 0.95 | 831.2 |
| 3 | 957.8 | 4.96 | 0.98 | 979.4 |
| 4 | 694.0 | 4.71 | 1.54 | 449.5 |

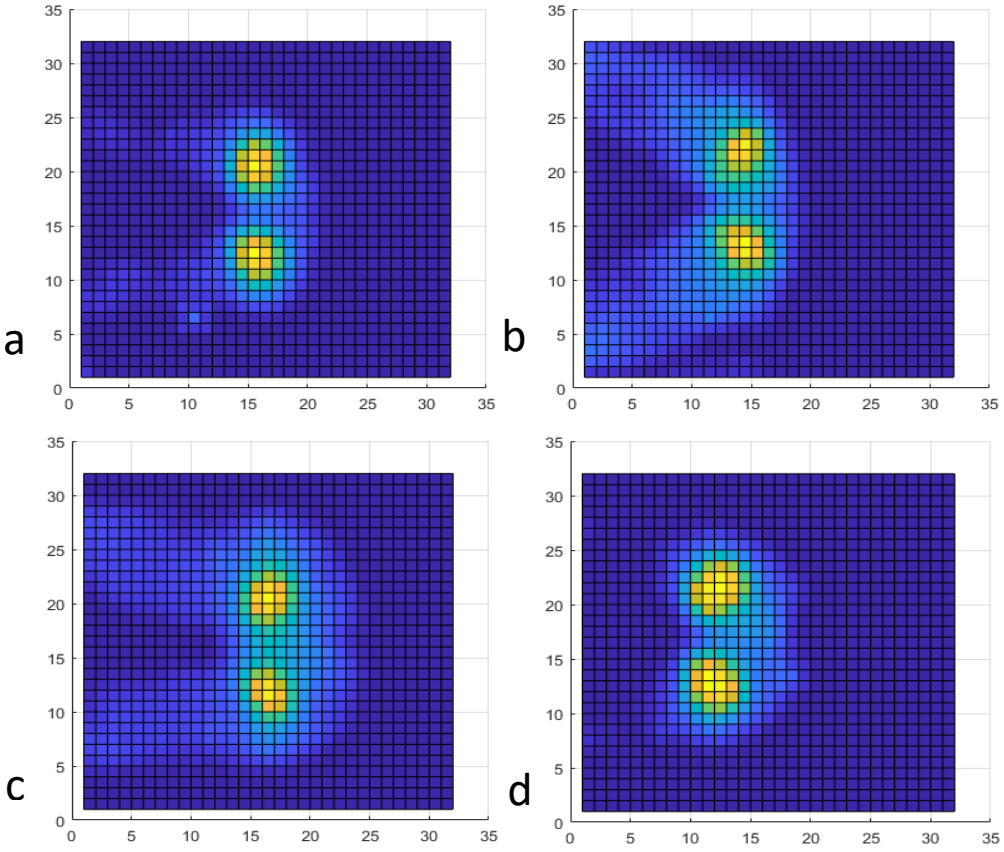


Figure 8 Pressure distribution on the TexiMat in sitting position.
a) Subject 1 b) Subject 2 c) Subject 3 d) Subject 4

In the sitting position, the weight of the individual is distributed between the armrests, legs on the floor and the seat. Therefore, an actual force applied to the seat was measured by the force sensor. Percentage of the total weight of the subject applied to the seat and the force values are listed in Table 6. The relation between the weight applied to the seat and the total force measured by the TexiMat is shown in Figure 9.

Table 6 Force measured by the AMTI force sensor

| Subject # | Seat Force [N] | Seat Weight [kgf] | Seat Weight/Subject Weight [%] |
|---|---|---|---|
| 1 | 450 | 45.9 | 70.6 |
| 2 | 541 | 55.1 | 84.8 |
| 3 | 625 | 63.7 | 84.9 |
| 4 | 496 | 50.6 | 76.6 |

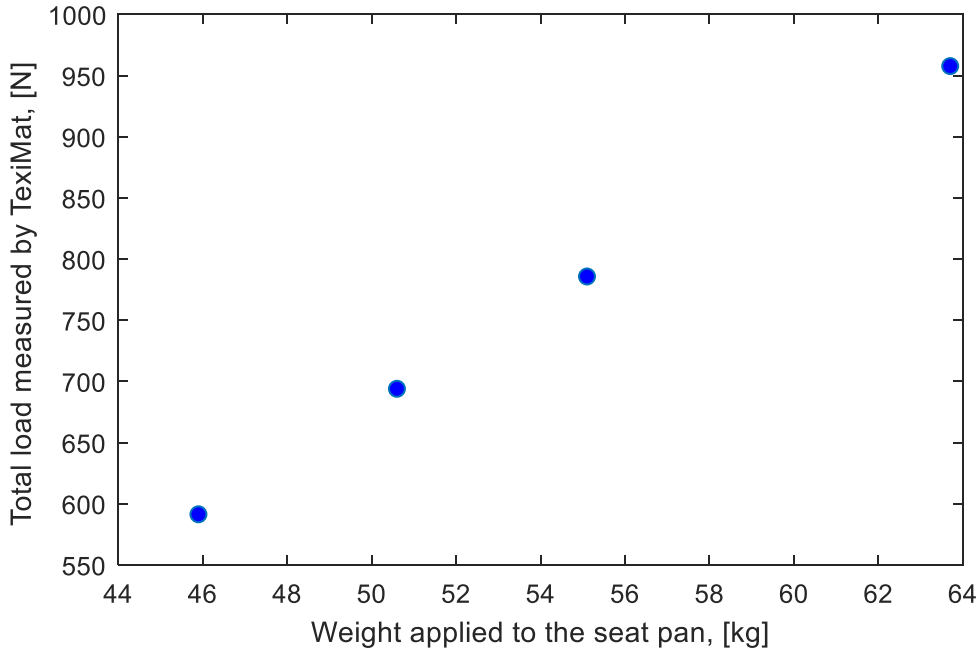


Figure 9 Relation between the weight on the seat pan and the force measured by the TexiMat for four subjects

## 4. Discussion

The objective of this work was to describe the interactions between soft tissues and support surfaces for the healthy sitting and healthy recumbent postures in terms of variation in pressure distribution.

For the acquisitions with the Zebris platform the maximum values of total force and the force variation was higher for the subject 1. This could be related to the higher weight of the subject 1 and to the difference in movement range during the acquisitions between subjects. For the subject 2 smaller contact area in combination with the increased peak pressure was observed. While comparing 5 different leg positions for subject 1, it could be seen that the highest peak pressure occurred at position 2, while highest mean pressure per sensor at position 3, when the smallest contact area was registered. However, from the pressure distribution maps for this subject, it is visible that the region of the top vertebrae of the sacrum is subjected to the higher pressures at position 4. It is also important to mention that these five positions do not correspond to the actual static position of the patient lying in a bed. But the goal in this case was to find the person-specific

position when the sacrum experiences the highest loads. Depending on the anatomy, the sacral vertebrae of another individual could be more exposed to the load when the legs are in different positions.

Similar findings were observed for the acquisitions in the sitting posture with the TexiMat device. For subject 3, for whom the total force was the highest, contact area was also the highest between all the subjects.

The correlation between the weight on the seat pan and the total force measured by the TexiMat was observed. However, the difference in the forces measured by pressure mat and force sensor suggests that the actual active area of the TexiMat sensor could be different from the one used in this study.

Some pressure parameter values found in the literature for the sitting posture are provided below.

In 1972, Hertzberg (31) studied sitting load patterns for young males from the US Airforce seated on the hard surface covered only by thin sheet of latex rubber. He showed that for certain subjects the peak pressure under the ischial tuberosities could rise to more than 41.4 $N/cm^2$.

Conine et al. (32) performed a study with the elderly persons in a wheelchair, establishing a threshold of 0.8 $N/cm^2$ peak pressure, above which the incidence of the PU development significantly increased. Another study by Brienza et al. (10), also focusing on elderly patients, showed peak pressures of 1.5 ± 0.6 $N/cm^2$ in the group that developed PUs in contrast with the peak pressure values of 1 ± 0.3 $N/cm^2$ in the group without the PUs.

Mergl et al. (33) investigated the relation between the discomfort and pressure distribution on the interface between human and a car seat for young healthy individuals. In the buttock region, peak pressure of 2 $N/cm^2$ and mean pressure of 0.5–0.6 $N/cm^2$ were found to be limiting values, above which subjects felt strong discomfort. And in the study of Jackson et al. (34) with glider pilots, the highest peak pressure when the discomfort could be removed by fidgeting was 1.1 $N/cm^2$.

In the thesis of Savonnet (35) pressure maps were acquired for healthy subjects with peak pressure of 1 ± 0.2 $N/cm^2$ and contact area of 1270 ± 310 $cm^2$. In comparison to the current study, peak pressures were lower, while the contact area was larger. This could be also due to the use of backrest.

The reported pressure data mostly concerns the assessment of either wheelchair users (10,32) or subjects in aircraft/car seats (33–35). The thick soft seat pan is common to be used in these cases and subjects are leaning on the backrest and, in some cases, the armrests. All these factors contribute to reducing the pressure on the seat pan.

## 5. Conclusion

In the current study, all subjects (both in recumbent and sitting positions) experienced peak pressures exceeding most of the values found in the studies with wheelchairs or car/plane seats. This could be explained by the difference in the current experimental setup: no cushion below the pressure mat and lack of the backrest for acquisitions in the sitting position.

The same highest values of the mean peak pressure for the sitting measurements were observed for two subjects: for the subject with the lowest BMI & weight and also for the subject with the highest BMI & weight. Therefore, the direct relation between the weight or BMI of the subject and the mean peak pressure couldn't be established based on collected data. These findings support the importance of the subject specific evaluation of the pressure distribution as it is a result of the combination of numerous individual parameters.

## References


1. Ceelen KK, Stekelenburg A, Loerakker S, Strijkers GJ, Bader DL, Nicolay K, et al. Compression-induced damage and internal tissue strains are related. J Biomech. 2008;41(16):3399–404.
2. Traa WA, van Turnhout MC, Nelissen JL, Strijkers GJ, Bader DL, Oomens CWJ. There is an individual tolerance to mechanical loading in compression induced deep tissue injury. Clin Biomech. 2019;63:153–60. https://doi.org/10.1016/j.clinbiomech.2019.02.015
3. Traa WA, van Turnhout MC, Moerman KM, Nelissen JL, Nederveen AJ, Strijkers GJ, et al. MRI based 3D finite element modelling to investigate deep tissue injury. Comput Methods Biomech Biomed Eng. 2018;21(14):760–9. https://doi.org/10.1080/10255842.2018.1517868
4. Garber SL, Rintala DH, Hart KA, Fuhrer MJ. Pressure ulcer risk in spinal cord injury: Predictors of ulcer status over 3 years. Arch Phys Med Rehabil. 2000;81(4):465–71.
5. Gefen A, van Nierop B, Bader DL, Oomens CW. Strain-time cell-death threshold for skeletal muscle in a tissue-engineered model system for deep tissue injury. J Biomech. 2008;41(9):2003–12.
6. Krause JS, Broderick L. Patterns of recurrent pressure ulcers after spinal cord injury: Identification of risk and protective factors 5 or more years after onset. Arch Phys Med Rehabil. 2004;85(8):1257–64.
7. Essex HN, Clark M, Sims J, Warriner A, Cullum N. Health-related quality of life in hospital inpatients with pressure ulceration: Assessment using generic health-related quality of life measures. Wound Repair Regen. 2009;17(6):797–805.
8. Demarré L, Van Lancker A, Van Hecke A, Verhaeghe S, Grypdonck M, Lemey J, et al. The cost of prevention and treatment of pressure ulcers: A systematic review. Int J Nurs Stud. 2015;52(11):1754–74. http://dx.doi.org/10.1016/j.ijnurstu.2015.06.006
9. Ellis M. Pressure ulcer prevention in care home settings. Nurs Older People. 2017;29(3):29–37.
10. Brienza DM, Karg PE, Jo Geyer M, Kelsey S, Trefler E. The relationship between pressure ulcer incidence and buttock-seat cushion interface pressure in at-risk elderly wheelchair users. Arch Phys Med Rehabil. 2001;82(4):529–33.
11. Al-Dirini RMA, Reed MP, Thewlis D. Deformation of the gluteal soft tissues during sitting. Clin Biomech. 2015;30(7):662–8. http://dx.doi.org/10.1016/j.clinbiomech.2015.05.008
12. Loerakker S, Manders E, Strijkers GJ, Nicolay K, Baaijens FPT, Bader DL, et al. The effects of deformation, ischemia, and reperfusion on the development of muscle damage during prolonged loading. J Appl Physiol. 2011;111(4):1168–77.
13. Stekelenburg A, Strijkers GJ, Parusel H, Bader DL, Nicolay K, Oomens CW. Role of ischemia and deformation in the onset of compression-induced deep tissue injury: MRI-based studies in a rat model. J Appl Physiol. 2007;102(5):2002–11.
14. Jiang L, Tu Q, Wang Y, Zhang E. Ischemia-reperfusion injury-induced histological changes affecting early stage pressure ulcer development in a rat model. Ostomy Wound Manag. 2009;55(August):52–6.
15. Peirce SM, Skalak TC, Rodeheaver GT. Ischemia-reperfusion injury in chronic pressure ulcer formation: A skin model in the rat. Wound Repair Regen. 2000;8(1):68–76.
16. Bouten C V., Oomens CW, Baaijens FP, Bader DL. The etiology of pressure ulcers: Skin deep or muscle bound? Arch Phys Med Rehabil. 2003;84(4):616–9.

17. Gawlitta D, Li W, Oomens CWJ, Baaijens FPT, Bader DL, Bouten CVC. The relative contributions of compression and hypoxia to development of muscle tissue damage: An in vitro study. Ann Biomed Eng. 2007;35(2):273–84.
18. Linder-Ganz E, Engelberg S, Scheinowitz M, Gefen A. Pressure-time cell death threshold for albino rat skeletal muscles as related to pressure sore biomechanics. J Biomech. 2006;39(14):2725–32.
19. Stekelenburg A, Oomens CWJ, Strijkers GJ, De Graaf L, Bader DL, Nicolay K. A new MR-compatible loading device to study in vivo muscle damage development in rats due to compressive loading. Med Eng Phys. 2006;28(4):331–8.
20. Loerakker SS, Stekelenburg A, Strijkers GJ, Rijpkema JJM, Baaijens FPT, Bader DL, et al. Temporal effects of mechanical loading on deformation-induced damage in skeletal muscle tissue. Ann Biomed Eng. 2010;38(8):2577–87.
21. Stekelenburg A, Oomens CWJ, Strijkers GJ, Nicolay K, Bader DL. Compression-induced deep tissue injury examined with magnetic resonance imaging and histology. J Appl Physiol. 2006;100(6):1946–54.
22. van Nierop BJ, Stekelenburg A, Loerakker S, Oomens CW, Bader D, Strijkers GJ, et al. Diffusion of water in skeletal muscle tissue is not influenced by compression in a rat model of deep tissue injury. J Biomech. 2010;43(3):570–5. http://dx.doi.org/10.1016/j.jbiomech.2009.07.043
23. Nelissen JL, Sinkus R, Nicolay K, Nederveen AJ, Oomens CWJ, Strijkers GJ. Magnetic resonance elastography of skeletal muscle deep tissue injury. NMR Biomed. 2019;32(6):1–12.
24. Liu Z, Wang J. Influences of sitting posture and interface activity on human physical and psychological reaction. 5th Int Conf Bioinforma Biomed Eng iCBBE 2011. 2011;3–6.
25. Ciaccia FRDAS, Sznelwar LI. An approach to aircraft seat comfort using interface pressure mapping. Work. 2012;41(SUPPL.1):240–5.
26. Hiemstra-van Mastrigt S, Groenesteijn L, Vink P, Kuijt-Evers LFM. Predicting passenger seat comfort and discomfort on the basis of human, context and seat characteristics: a literature review. Ergonomics. 2017;60(7):889–911. http://dx.doi.org/10.1080/00140139.2016.1233356
27. Laszczak P, McGrath M, Tang J, Gao J, Jiang L, Bader DL, et al. A pressure and shear sensor system for stress measurement at lower limb residuum/socket interface. Med Eng Phys. 2016;38(7):695–700.
28. Bader DL, Worsley PR, Gefen A. Bioengineering considerations in the prevention of medical device-related pressure ulcers. Clin Biomech 2019;67(March):70–7. https://doi.org/10.1016/j.clinbiomech.2019.04.018
29. Worsley PR, Rebolledo D, Webb S, Caggiari S, Bader DL. Monitoring the biomechanical and physiological effects of postural changes during leisure chair sitting. J Tissue Viability. 2018;27(1):16–22. https://doi.org/10.1016/j.jtv.2017.10.001
30. Woodhouse M, Worsley PR, Voegeli D, Schoonhoven L, Bader DL. The physiological response of soft tissue to periodic repositioning as a strategy for pressure ulcer prevention. Clin Biomech. 2015;30(2):166–74. http://dx.doi.org/10.1016/j.clinbiomech.2014.12.004
31. Hertzberg HTE. The human buttocks in sitting: pressures, patterns, and palliatives. SAE Tech Pap. 1972 Apr 19;81:39–47. http://www.jstor.org/stable/44720660

32. Conine TA, Hershler C, Daechsel D, Peel C, Pearson A. Pressure ulcer prophylaxis in elderly patients using polyurethane foam or Jay wheelchair cushions. Int J Rhabil Res. 1994;17:123–37.
33. Mergl C, Klendauer M, Mangen C, Bubb H. Predicting long term riding comfort in cars by contact forces between human and seat. SAE Tech Pap. 2005;(June 2005).
34. Jackson C, Emck AJ, Hunston MJ, Jarvis PC. Pressure measurements and comfort of foam safety cushions for confined seating. Aviat Sp Environ Med. 2009;80(6):565–9.
35. Savonnet L. Development of a customizable digital tool for assessing aircraft passenger discomfort and fatigue. PhD thesis, Université de Lyon. 2018.